



<https://theses.gla.ac.uk/>

Theses Digitisation:

<https://www.gla.ac.uk/myglasgow/research/enlighten/theses/digitisation/>

This is a digitised version of the original print thesis.

Copyright and moral rights for this work are retained by the author

A copy can be downloaded for personal non-commercial research or study, without prior permission or charge

This work cannot be reproduced or quoted extensively from without first obtaining permission in writing from the author

The content must not be changed in any way or sold commercially in any format or medium without the formal permission of the author

When referring to this work, full bibliographic details including the author, title, awarding institution and date of the thesis must be given

Enlighten: Theses

<https://theses.gla.ac.uk/>  
[research-enlighten@glasgow.ac.uk](mailto:research-enlighten@glasgow.ac.uk)

# **Autonomous Control for On-Orbit Assembly Using Artificial Potential Functions**

Frank McQuade B.Sc., M.Sc.

This thesis submitted to the Faculty of Engineering, University of Glasgow, for the Degree of Doctor of Philosophy. All aspects of the work presented herein are original in concept except where indicated.

The research was conducted between October 1994 and October 1997 at the Department of Aerospace Engineering, University of Glasgow.

Frank McQuade, November 1997

ProQuest Number: 10391167

All rights reserved

INFORMATION TO ALL USERS

The quality of this reproduction is dependent upon the quality of the copy submitted.

In the unlikely event that the author did not send a complete manuscript and there are missing pages, these will be noted. Also, if material had to be removed, a note will indicate the deletion.



ProQuest 10391167

Published by ProQuest LLC (2017). Copyright of the Dissertation is held by the Author.

All rights reserved.

This work is protected against unauthorized copying under Title 17, United States Code  
Microform Edition © ProQuest LLC.

ProQuest LLC.  
789 East Eisenhower Parkway  
P.O. Box 1346  
Ann Arbor, MI 48106 – 1346

GLASGOW UNIVERSITY  
LIBRARY

1189 (copy 2)

GLASGOW  
UNIVERSITY  
LIBRARY

# Abstract

Current spacecraft mission analysis has highlighted a requirement for the assembly of large structures in Earth Orbit. This thesis investigates an autonomous method of assembly for such large structures. The scheme envisaged is based on Lyapunov's method which is extended to potential function theory. The method forms an analytical solution to the assembly problem by generating high level control commands which are then devolved to individual actuator commands for the assembly vehicles. The application of the method to general assembly problems has allowed the development of a generic global potential function. The application of the global potential function has required the use of a connectivity matrix which contains the information required to assemble the goal structure. Thus, a structure may be modified by altering only the characteristics of the connectivity matrix. The generic assembly method is then applied using a subsumptive type architecture which allows the assembly controller to delegate sub-components of the total structure to secondary controllers. Therefore, the method may then be utilised to construct complex structures, which, when linked to the use of smart components and joints allows the assembly of adaptive structures. These adaptive and variable topology structures which may change their functionality with time may prove useful for future mission applications.

# Acknowledgements

I would like to thank my supervisor and his family, Drs. Colin and Karen McInnes and Calum, who have always extended their friendship and advice. Also, my thanks to Prof. Alan Simpson, for advice and experience which has allowed me to view the world beyond my computer screen.

I would also like to thank the following organisations for their help and assistance in the course of my research. Without their assistance much of the work herein would not have been possible: EPSRC, The Royal Aeronautical Society, The Cross Trust, The Royal Academy of Engineering, Prof. David Akin and the Space Systems Laboratory at the University of Maryland, College Park and last but not least the people of the Department of Aerospace Engineering at the University of Glasgow.

I would like to thank the people in my life. To the guys who have always been by my side, Adam Young, Chris O'Neill, Mark Lande, and Sean McLellan, gentlemen all. I hope you realise how much I have enjoyed your friendship over the years. To the people responsible, the clans Young, O'Neill, Lande and McLellan. To Karen, for her pep talks. To the folks in Glasgow, especially Laurent and Elena, Franck and Marivi, Yamina and Alan, Ingrid, Kerry, Marta, and the rest of the gang. To my extended family, especially my Aunt Winnie and Uncle Billy. Also, to two of the kindest people one could ever meet, Liz Leitch and Emily Garman, for their company, their ability to make me laugh and give me a good kick up the backside when I needed it.

I would like to dedicate this thesis to my family who have been a constant source of inspiration and encouragement to me throughout the years. To my brother, Leslie, and his family, Anne-Marie and Louise, my sister Winnie and especially my parents,

James and Patricia McQuade

*Parents Extraordinaires*

# Contents

<b>Abstract</b>	<b>ii</b>
<b>Acknowledgements</b>	<b>iii</b>
<b>Table of Contents</b>	<b>iv</b>
<b>List of Figures</b>	<b>vii</b>
<b>Nomenclature</b>	<b>xiv</b>
<b>Chapter One: Introduction to On-Orbit Assembly</b>	<b>1</b>
1.1 Introduction	1
1.2 A Brief History of On-Orbit Assembly	2
1.3 State of the Art: Structures	10
1.4 State of the Art: Robotics & Sensors	16
1.5 State of the Art: Assembly Philosophies	20
1.6 Mission Statement	24
<b>Chapter Two: Orbital Mechanics</b>	<b>26</b>
2.1 Introduction	26
2.2 The Two-Body Problem	27
2.3 The Equations of Relative Motion	30
2.4 Two Impulse Rendezvous and the State Transition Matrix	36
2.5 Velocity-Time Optimisation	39
2.6 Point to Point Transfer	41
2.7 Conclusions	47
<b>Chapter Three: Potential Functions</b>	<b>48</b>
3.1 Introduction	48
3.2 Lyapunov's Second Method and Potential Functions	49
3.3 Translation Control	51
3.4 Attitude Control	54
3.5 Conclusions	61

<b>Chapter Four: Obstacle Avoidance</b>	<b>62</b>
4.1 Introduction	62
4.2 Obstacle Representation: Gaussian Distribution	62
4.3 Obstacle Representation: Power Law Distribution	69
4.4 Obstacle Representation: Rectangular Distribution	75
4.5 Obstacle Representation: Superquadratic Distribution	79
4.6 Conclusions	85
<b>Chapter Five: Molecular Dynamics</b>	<b>86</b>
5.1 Introduction	86
5.2 Applications in Molecular Biology	86
5.3 Schrödinger's Equation	88
5.4 Potential Energy Functions	89
5.5 Calculation of Non-Bonded Interactions	91
5.6 Multi-Body Potentials	91
5.7 Conclusions	92
<b>Chapter Six: Structural Assembly</b>	<b>97</b>
6.1 Introduction	97
6.2 Beam Element Definition	97
6.3 Parallel Assembly. Case I: Triangle	101
6.4 Parallel Assembly. Case II: Square	110
6.5 Serial Assembly. Case I: Triangle	113
6.6 Serial Assembly. Case II: Square	116
6.7 Conclusions	120
<b>Chapter Seven: Extended Fabrication</b>	<b>121</b>
7.1 Introduction	121
7.2 General Fabrication	121
7.3 The Connectivity Matrix	125
7.4 The Cube	131
7.5 Carbon 60	146

7.6 Variable Structures	155
7.7 Conclusions	169
<b>Chapter Eight: Control Architecture</b>	<b>170</b>
8.1 Introduction	170
8.2 Subsumption	170
8.3 Case Study: Cube Assembly	171
8.4 Case Study: Truss Assembly	177
8.5 Case Study: Truss Cube Assembly	183
8.6 Informaties	188
8.7 Conclusions	188
<b>Chapter Nine: Conclusion</b>	<b>189</b>
9.1 Review	189
9.2 Mission Statement	191
9.3 Recommendations	193
<b>References</b>	<b>195</b>

# List of Figures

<b>Chapter One: Introduction to On-Orbit Assembly</b>	<b>1</b>
<b>Figure 1.1:</b> <i>Ranger Test Flight Vehicle.</i>	2
<b>Figure 1.2:</b> <i>Agena Vehicle, viewed from Gemini VIII.</i>	3
<b>Figure 1.3:</b> <i>ACCESS Structure.</i>	5
<b>Figure 1.4:</b> <i>EASE Structure.</i>	5
<b>Figure 1.5:</b> <i>International Space Station Alpha.</i>	7
<b>Figure 1.6:</b> <i>Bi-Stem Structure.</i>	13
<b>Figure 1.7:</b> <i>CLCB Structure.</i>	13
<b>Figure 1.8:</b> <i>Inflatable Antenna Experiment.</i>	15
<b>Chapter Two: Orbital Mechanics</b>	<b>26</b>
<b>Figure 2.1:</b> Two-Body Problem.	27
<b>Figure 2.2:</b> Circular Orbit.	29
<b>Figure 2.3:</b> Elliptical Orbit.	31
<b>Figure 2.4:</b> Relative Motion.	31
<b>Figure 2.5:</b> Rotating Co-Ordinate Frame.	32
<b>Figure 2.6:</b> Case I: 70 m Up-range.	36
<b>Figure 2.7:</b> Case II: (-100,50,-50).	37
<b>Figure 2.8.a:</b> Case I: 70 m Up-range to Target Vehicle. Time / $\Delta v$ Cost Function.	42
<b>Figure 2.8.b:</b> Case I: 70 m Up-range to Target Vehicle. Chase Vehicle Trajectory.	43
<b>Figure 2.9.a:</b> Case II: (-100,50,-50) to Target Vehicle. Time / $\Delta v$ Cost Function.	44
<b>Figure 2.9.b:</b> Case II: (-100,50,-50) to Target Vehicle. Chase Vehicle Trajectory.	45
<b>Figure 2.9.c:</b> Case II: (-100,50,-50) to Target Vehicle. Trajectory Variations with Time of Transfer.	45
<b>Figure 2.10.a:</b> Case III: (-100,50,-50) to (100,-100,100) Time / $\Delta v$ Cost Function	46

<b>Figure 2.10.b:</b>	Case III: (-100,50,-50) to Target Vehicle. Chase Vehicle Trajectory.	47
<b>Chapter Three: Potential Functions</b>		<b>48</b>
<b>Figure 3.1:</b>	Potential Function Convergence.	50
<b>Figure 3.2.a:</b>	Discrete Control: Chase Vehicle Trajectory.	53
<b>Figure 3.2.b:</b>	Discrete Control: Potential Function.	53
<b>Figure 3.2.c:</b>	Discrete Control: Potential Function Contours.	54
<b>Figure 3.2.d:</b>	Discrete Control: Chase Vehicle Velocity.	54
<b>Figure 3.3:</b>	Vehicle Attitude Definition.	55
<b>Figure 3.4.a:</b>	Continuous Control: Euler Angles.	59
<b>Figure 3.4.b:</b>	Continuous Control: Body Rates.	59
<b>Figure 3.4.c:</b>	Continuous Control: Control Torques.	60
<b>Figure 3.4.d:</b>	Continuous Control: Potential Function.	60
<b>Chapter Four: Obstacle Avoidance</b>		<b>62</b>
<b>Figure 4.1:</b>	Saddle Point Formation.	64
<b>Figure 4.2.a:</b>	Gaussian Distribution: Chase Vehicle Trajectory.	66
<b>Figure 4.2.b:</b>	Gaussian Distribution: Obstacle.	67
<b>Figure 4.2.c:</b>	Gaussian Distribution: Potential Function Convergence.	67
<b>Figure 4.2.d:</b>	Gaussian Distribution: Potential Function Contours.	68
<b>Figure 4.2.e:</b>	Gaussian Distribution: Chase Vehicle Velocity.	68
<b>Figure 4.3.a:</b>	Power-Law Distribution: Chase Vehicle Trajectory.	71
<b>Figure 4.3.b:</b>	Power-Law Distribution: Obstacle.	71
<b>Figure 4.3.c:</b>	Power-Law Distribution: N=4, Potential Function.	72

<b>Figure 4.3.d:</b>	Power-Law Distribution: N=4, Potential Function Contours.	72
<b>Figure 4.3.e:</b>	Power-Law Distribution: N=10, Potential Function.	73
<b>Figure 4.3.f:</b>	Power-Law Distribution: N=10, Potential Function Contours.	73
<b>Figure 4.3.g:</b>	Power-Law Distribution: N=100, Potential Function.	74
<b>Figure 4.3.h:</b>	Rectangular Distribution: N=100, Potential Function Contours.	74
<b>Figure 4.4.a:</b>	Rectangular Distribution: Chase Vehicle Trajectory.	76
<b>Figure 4.4.b:</b>	Rectangular Distribution: Obstacle.	76
<b>Figure 4.4.c:</b>	Rectangular Distribution: Potential Function.	77
<b>Figure 4.4.d:</b>	Rectangular Distribution: Potential Function.	77
<b>Figure 4.4.e:</b>	Rectangular Distribution: Potential Function Contours.	78
<b>Figure 4.5:</b>	Local Minima Formation.	79
<b>Figure 4.6.a:</b>	Superquadric Distribution: Chase Vehicle Trajectory.	83
<b>Figure 4.6.b:</b>	Superquadric Distribution: Obstacle.	83
<b>Figure 4.6.c:</b>	Superquadric Distribution: Potential Function.	84
<b>Figure 4.6.d:</b>	Superquadric Distribution: Potential Function Contours.	84
<b>Figure 4.6.e:</b>	Superquadric Distribution: Obstacle Potential.	85
<b>Chapter Five: Molecular Dynamics</b>		<b>86</b>
<b>Figure 5.1:</b>	Morse Potential.	90
<b>Figure 5.2a:</b>	Potential Function Behaviour.	92
<b>Figure 5.2.b.i:</b>	Atomic Motion: Time = 0 s.	93
<b>Figure 5.2.b.ii:</b>	Atomic Motion: Time = 1 s.	93
<b>Figure 5.2.b.iii:</b>	Atomic Motion: Time = 2 s.	94
<b>Figure 5.2.b.iv:</b>	Atomic Motion: Time = 3 s.	94
<b>Figure 5.2.b.v:</b>	Atomic Motion: Time = 4 s.	95
<b>Figure 5.2.b.vi:</b>	Atomic Motion: Time = 6 s.	95

<b>Chapter Six: Structural Assembly</b>	<b>97</b>
<b>Figure 6.1:</b>	Beam Element Definition. 98
<b>Figure 6.2:</b>	Beam and Vehicle System. 99
<b>Figure 6.3.a:</b>	Triangle Assembly. 108
<b>Figure 6.3.b:</b>	Potential Function. 108
<b>Figure 6.3.c:</b>	$\Delta v$ Cost. 109
<b>Figure 6.4.a:</b>	Square Assembly. 111
<b>Figure 6.4.b:</b>	Potential Function. 112
<b>Figure 6.4.c:</b>	Total $\Delta v$ Cost. 112
<b>Figure 6.4.d:</b>	$\Delta v$ Cost. 113
<b>Figure 6.5.a:</b>	Triangle Assembly. 115
<b>Figure 6.5.b:</b>	Potential Function. 116
<b>Figure 6.5.c:</b>	$\Delta v$ Cost. 116
<b>Figure 6.6.a:</b>	Square Assembly. 118
<b>Figure 6.6.b:</b>	Potential Function. 118
<b>Figure 6.6.c:</b>	Total $\Delta v$ Cost. 119
<b>Figure 6.6.d:</b>	$\Delta v$ Cost. 119
<b>Chapter Seven: Extended Fabrication</b>	<b>121</b>
<b>Figure 7.1:</b>	Generic beams Connections. 124
<b>Figure 7.2:</b>	Common Beam Connection. 126
<b>Figure 7.3:</b>	Common Node Connection. 128
<b>Figure 7.4:</b>	Connecting Beam. 129
<b>Figure 7.5:</b>	Design Integration. 131
<b>Figure 7.6.a.i:</b>	Parallel Cube Assembly: Time = 0 s. 133
<b>Figure 7.6.a.ii:</b>	Parallel Cube Assembly: Time = 25 s. 134
<b>Figure 7.6.a.iii:</b>	Parallel Cube Assembly: Time = 50 s. 134
<b>Figure 7.6.a.iv:</b>	Parallel Cube Assembly: Time = 75 s. 135
<b>Figure 7.6.a.v:</b>	Parallel Cube Assembly: Time = 100 s. 135
<b>Figure 7.6.a.vi:</b>	Parallel Cube Assembly: Time = 125 s. 136
<b>Figure 7.6.a.vii:</b>	Parallel Cube Assembly: Time = 150 s. 137

<b>Figure 7.6.a.viii:</b>	Parallel Cube Assembly: Time = 500 s.	135
<b>Figure 7.6.b:</b>	Potential Function.	137
<b>Figure 7.6.c:</b>	$\Delta v$ Cost.	138
<b>Figure 7.7.a.i:</b>	Serial Cube Assembly: Time = 0 s.	139
<b>Figure 7.7.a.ii:</b>	Serial Cube Assembly: Time = 25 s.	140
<b>Figure 7.7.a.iii:</b>	Serial Cube Assembly: Time = 50 s.	140
<b>Figure 7.7.a.iv:</b>	Serial Cube Assembly: Time = 75 s.	141
<b>Figure 7.7.a.v:</b>	Serial Cube Assembly: Time = 100 s.	141
<b>Figure 7.7.a.vi:</b>	Serial Cube Assembly: Time = 500 s.	142
<b>Figure 7.7.a.vii:</b>	Serial Cube Assembly: Time = 750 s.	142
<b>Figure 7.7.a.viii:</b>	Serial Cube Assembly: Time = 1000 s.	143
<b>Figure 7.7.a.ix:</b>	Serial Cube Assembly: Time = 1500 s.	143
<b>Figure 7.7.a.x:</b>	Serial Cube Assembly: Time = 2900 s.	144
<b>Figure 7.7.b:</b>	Potential Function.	144
<b>Figure 7.7.c:</b>	$\Delta v$ Cost.	145
<b>Figure 7.8:</b>	Bucky Ball.	151
<b>Figure 7.9.a:</b>	Potential Function.	151
<b>Figure 7.9.b.i:</b>	Bucky Ball Assembly: Time = 0 s.	151
<b>Figure 7.9.b.ii:</b>	Bucky Ball Assembly: Time = 500 s.	152
<b>Figure 7.9.b.iii:</b>	Bucky Ball Assembly: Time = 1000 s.	152
<b>Figure 7.9.b.iv:</b>	Bucky Ball Assembly: Time = 1500 s.	153
<b>Figure 7.9.b.v:</b>	Bucky Ball Assembly: Time = 2000 s.	153
<b>Figure 7.9.b.vi:</b>	Bucky Ball Assembly: Time = 2500 s.	154
<b>Figure 7.9.b.vii:</b>	Bucky Ball Assembly: Time = 3000 s.	154
<b>Figure 7.9.b.viii:</b>	Bucky Ball Assembly: Time = 3250 s.	155
<b>Figure 7.10:</b>	Reflector Structure.	156
<b>Figure 7.11.a:</b>	Potential Function.	158
<b>Figure 7.11.b:</b>	Potential Function.	158
<b>Figure 7.11.c:</b>	Controlled Angle.	159
<b>Figure 7.11.d.i:</b>	Deployment: Time = 0 s.	159
<b>Figure 7.11.d.ii:</b>	Deployment: Time = 500 s.	160

<b>Figure 7.11.d.iii:</b>	Deployment: Time = 1000 s.	160
<b>Figure 7.11.d.iv:</b>	Deployment: Time = 2000 s.	161
<b>Figure 7.11.d.v:</b>	Deployment: Time = 3000 s.	161
<b>Figure 7.11.d.vi:</b>	Deployment: Time = 4000 s.	162
<b>Figure 7.11.d.vii:</b>	Deployment: Time = 5000 s.	162
<b>Figure 7.11.d.viii:</b>	Deployment: Time = 8000 s.	163
<b>Figure 7.12.a:</b>	Potential Function.	164
<b>Figure 7.12.b.i:</b>	Reconfigure: Time = 0 s.	165
<b>Figure 7.12.b.ii:</b>	Reconfigure: Time = 100 s.	165
<b>Figure 7.12.b.iii:</b>	Reconfigure: Time = 200 s.	166
<b>Figure 7.12.b.iv:</b>	Reconfigure: Time = 300 s.	166
<b>Figure 7.12.b.v:</b>	Reconfigure: Time = 400 s.	167
<b>Figure 7.12.b.vi:</b>	Reconfigure: Time = 500 s.	167
<b>Figure 7.12.b.vii:</b>	Reconfigure: Time = 600 s.	168
<b>Figure 7.12.b.viii:</b>	Reconfigure: Time = 1100 s.	168
<b>Chapter Eight: Control Architecture</b>		<b>170</b>
<b>Figure 8.1:</b>	Subsumption Architecture.	171
<b>Figure 8.2:</b>	Cube Assembly.	172
<b>Figure 8.3.a:</b>	Potential Function.	173
<b>Figure 8.3.b.i:</b>	Cube Assembly: Time = 0 s.	173
<b>Figure 8.3.b.ii:</b>	Cube Assembly: Time = 125 s.	174
<b>Figure 8.3.b.iii:</b>	Cube Assembly: Time = 250 s.	174
<b>Figure 8.3.b.iv:</b>	Cube Assembly: Time = 500 s.	175
<b>Figure 8.3.b.v:</b>	Cube Assembly: Time = 675 s.	175
<b>Figure 8.3.b.vi:</b>	Cube Assembly: Time = 750 s.	176
<b>Figure 8.3.b.vii:</b>	Cube Assembly: Time = 1850 s.	176
<b>Figure 8.4:</b>	Truss Structure.	177
<b>Figure 8.5:</b>	Truss Controller Architecture.	177
<b>Figure 8.6.a:</b>	Potential Function.	178
<b>Figure 8.6.b.i:</b>	Truss Assembly: Time = 0 s.	179

<b>Figure 8.6.b.ii:</b>	Truss Assembly: Time = 500 s.	179
<b>Figure 8.6.b.iii:</b>	Truss Assembly: Time = 1000 s.	180
<b>Figure 8.6.b.iv:</b>	Truss Assembly: Time = 2000 s.	180
<b>Figure 8.6.b.v:</b>	Truss Assembly: Time = 2750 s.	181
<b>Figure 8.6.b.vi:</b>	Truss Assembly: Time = 3750 s.	181
<b>Figure 8.6.b.vii:</b>	Truss Assembly: Time = 4750 s.	182
<b>Figure 8.6.b.viii:</b>	Truss Assembly: Time = 5295 s.	182
<b>Figure 8.7:</b>	Truss Cube Controller Architecture.	184
<b>Figure 8.8.i:</b>	Truss Assembly: Time = 0 s.	185
<b>Figure 8.8.ii:</b>	Truss Assembly: Time = 500 s.	185
<b>Figure 8.8.iii:</b>	Truss Assembly: Time = 1000 s.	186
<b>Figure 8.8.iv:</b>	Truss Assembly: Time = 1500 s.	186
<b>Figure 8.8.v:</b>	Truss Assembly: Time = 2000 s.	187
<b>Figure 8.8.vi:</b>	Truss Assembly: Time = 2230 s.	187

# Nomenclature

A	Scaling Function.
A	Control Accelerations.
B	Scaling Constant.
D	Obstacle Characteristic Dimension.
$D_b$	Energy of Equilibrium Bond Length.
E	Energy.
$E_k$	Kinetic Energy.
$E_p$	Potential Energy.
F	Control Force.
G	Universal Gravitational Constant ( $6.673 \times 10^{-11} \text{ m}^3 \cdot \text{kg}^{-2} \cdot \text{s}$ ).
G	Connection Set.
G	Transformation Matrix.
I	Moment of Inertia.
K	Distance to Superquadric Surface.
M	Moment.
N	Number of Atoms within a Molecule.
N	Power Index.
P	Pressure.
R	Universal Gas Constant ( $287 \text{ J} \cdot \text{kg}^{-1} \cdot \text{K}^{-1}$ ).
T	Absolute Temperature.
T	Control Torque.
V	Scalar Potential.
X	Global State Vector.
a,b	Superquadric Characteristic Dimension.
a	Orbit Semi-Major Axis.
$b_o$	Equilibrium Bond Length.
e	Orbit Eccentricity.
$g_t$	Acceleration due to Gravity acting on the Target Vehicle.
$G_c$	Acceleration due to Gravity acting on the Chase Vehicle.

$h,w$	Height and Width of a Superquadric Obstacle.
$h$	Planck's Constant ( $9.110 \times 10^{-31}$ J.s).
$h$	Altitude above Earth's Surface.
$h_a$	Orbit Apogee Altitude.
$h_p$	Orbit Perigee Altitude.
$k_1, k_2$	Scaling Constants.
$l$	Beam Length.
$m$	Mass.
$m_{Earth}$	Earth Mass ( $5.976 \times 10^{24}$ kg).
$u$	Contour Shaping Constant.
$r_{Earth}$	Radius of the Earth (6371 km at the Equator).
$\mathbf{r}$	Position Vector.
$\mathbf{r}_c$	Chase Vehicle Position Vector.
$\mathbf{r}_{Goal}$	Position Vector of Goal.
$\mathbf{r}_t$	Target Vehicle Position Vector.
$\mathbf{F}$	Female Connector Position Vector.
$\mathbf{s}$	Vehicle State Vector.
$t$	Time.
$\mathbf{v}$	Velocity.
$v^*$	Maximum Controlled Vehicle Velocity.
$\mathbf{x}$	Vehicle Position Vector.
$\Delta S$	Change in Entropy.
$\Delta v$	Translational Velocity Cost.
$\Delta \omega$	Rotational Velocity Cost.
$\Delta E$	Change in Energy.
$\Delta G$	Molecular Free Energy.
$\phi$	Beam Elevation.
$\Psi$	Wave Function.
$\Phi$	State Transition Matrix.
$\alpha$	Scaling Constant.
$\beta$	Scaling Constant.

$\varepsilon_{ij}$	Connectivity Matrix.
$\kappa$	Shaping Function or Constant.
$\kappa$	Equilibrium Constant.
$\lambda$	Scaling Constant.
$\mu$	Gravitational Parameter.
$\theta$	Euler Angles.
$\theta$	Beam Azimuth.
$\bar{\theta}$	Vehicle Goal Orientation
$\sigma$	Gaussian Distribution.
$\sigma$	Female Connector.
$\omega$	Orbital Angular Velocity.

# Chapter One: Introduction to On-Orbit Assembly

*For I dipt into the future, far as human eye could see,  
Saw the vision of the world, and all the wonder that would be;*

“Locksley Hall” Alfred, Lord Tennyson

## 1.1 Introduction

Currently, a continuous human presence in space is maintained solely by the continued operation of space station *Mir*. However, the next few years will see this capability expanded with the construction of *International Space Station Alpha* (ISSA). Although a large structure, *International Space Station Alpha* consists mostly of pre-fabricated units that will be assembled on-orbit. The proposed Extra-Vehicular Activity (EVA) required of the astronaut team for both assembly and maintenance is far beyond current experience. However, the use of telerobotics will simplify the assembly of *International Space Station Alpha*. The shuttle will make use of its own robot arm, while a station based manipulator will assist further in the assembly process. Currently, the development of free-flying manipulators is led by the Ranger<sup>1</sup> project at the University of Maryland Space Systems Laboratory. The Ranger vehicle, shown in **Figure 1.1**, is scheduled to fly as a shuttle experiment in 1998 and will provide the first step in developing free-flying assembly vehicles.

This thesis will propose an autonomous assembly method applicable to general on-orbit assembly problems. The particular assembly problem considered here consists of assembling a series of uniform slender beams into regular, periodic structures. Free-flying Ranger-type vehicles are assumed to be used in the assembly process. The beams are envisaged as being fastened using a standardised rigid joint which is easily assembled but provides a rigid connection. The study is presented firstly with an examination of background control methods, consisting of **Chapters 2 to 4**. The extension of these methods to a control algorithm capable of assembling truss structures is discussed in **Chapters 5 to 7**. The general application of the control algorithm is examined in **Chapter 8** with a discussion of the control architecture. Finally, conclusions and recommendations are drawn in **Chapter 9**.



**Figure 1.1:** *Ranger* Test Flight Vehicle (Source: Ref. 1).

## 1.2 A Brief History of On-Orbit Assembly

The simplest form of on-orbit assembly which is carried out on a routine basis is that of rendezvous and docking. The recent *Shuttle* missions to rendezvous and dock with the Russian Space Station *Mir* are a precursor to the more complex task of rendezvous and docking with *International Space Station Alpha*. If the *International Space Station Alpha* is successful, it is clear that the volume and complexity of operations being carried out in low Earth orbit will greatly increase. The following sections describe the history of on-orbit assembly and attempt to highlight the critical development paths.

### 1.2.1 On-Orbit Assembly: 1957-1968

In the late 1950s, the Soviet Union focused world attention on space. The launch of *Sputnik*<sup>2,3</sup> in October 1957 would start the short space race which culminated with US *Apollo* astronaut Dr. Neil Armstrong stepping onto the surface of the moon in July 1969. However, the technologies which were demonstrated and applied in placing Dr. Armstrong onto the lunar surface also have applications in on-orbit assembly. The assembly of the Command and Service Module (CSM) and the Lunar Excursion Module (LEM) into a single vehicle during transit to lunar orbit and the subsequent ascent to rendezvous and dock from the Lunar surface were manually piloted manoeuvres which corresponded to two of the most critical single point failures of the whole mission.

The expertise required of the *Apollo* missions, and the failed Soviet lunar attempts had been in development from as early as 1962. Colonel Yuri Gagarin's launch into low Earth orbit on April 12<sup>th</sup> 1961 aboard *Vostok 1* was the first human flight in Earth orbit. However, as early as August 11<sup>th</sup> 1962 the Russian space programme attempted a rendezvous between the spacecraft *Vostok 3* and *Vostok 4*. Ultimately, these missions were not successful with a closest approach between the craft of 6.5 km. A second attempt was made with the *Vostok 5*

and 6 missions. Again, these missions were not successful, with a closest approach of 5 km being made. Another noteworthy point of the *Vostok 6* mission is that the cosmonaut was Valentina V. Tereshkova, the first woman in space. Political infighting and a lack of direction within the Soviet Union resulted in a failure to capitalise on this early lead. Although the *Voshkod 1* mission of October 1964 and the *Voshkod 2* missions would be successful in demonstrating the first space-walk and multi-crew missions, the next manned mission would not be until the unsuccessful *Soyuz 1* mission of 1967 in which Vladimir Komarov lost his life.

The American preparations for the proposed *Apollo* lunar missions would proceed with the successful *Mercury* program. Following on, the larger and more complex *Gemini* program began to examine on-orbit operations. The *Gemini III* mission of March 1965 would be the first orbit correction conducted by a crew. The *Gemini VI* mission in December of that year would go a step further and successfully manoeuvre to within one foot of the *Gemini VII* spacecraft. However, the first on-orbit assembly was to be carried out by the *Gemini VIII*<sup>4,5</sup> crew in March 1966 when the spacecraft rendezvoused and docked with a passive *Agena* target vehicle, shown in **Figure 1.2**. Coincidentally, the mission commander of *Gemini VIII* was Dr. Neil Armstrong. The remainder of the *Gemini* flights consolidated this technique with four additional dockings over the six months before the first manned *Apollo* missions commenced in October 1968. These missions were all manually piloted by the crew. However, the process of automated docking was later pioneered by the Soviet Union using the *Soyuz* and *Progress* spacecraft.

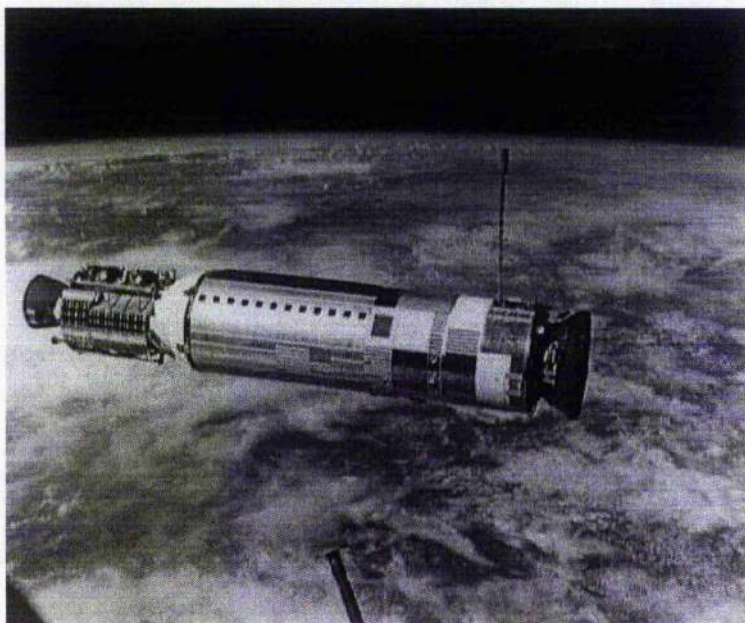


**Figure 1.2:** Agena Vehicle, viewed from *Gemini VIII* (Source: NASA).

### 1.2.2 On-Orbit Assembly: 1968-1986

The completion of the *Apollo* lunar program in December 1972 marked a change of emphasis in both the American and Soviet programs. The launch of the Soviet *Salyut I* space station in April 1971 and the American *Skylab* station in May 1973 marked the commencement of a continuing human space presence which would last until the present day. Although the American *Skylab* program would be short lived, lasting until early in 1974, the Soviet program would continue to gain momentum with a series of five *Salyut* stations throughout the 1970s. In addition, the *Soyuz* program and its derivative *Progress* ferry pioneered the use of automated rendezvous and docking. Although little is known of the technical specifications of these docking methods, the *Igla* rendezvous and docking system flew on the unmanned *Progress* vehicle to later *Salyut* stations as early as 1978. This docking system was initially developed for use onboard the *Salyut 6* and *7* stations. These two stations, launched in September 1977 and April 1982 respectively, represented the second generation of Soviet space station. However, although *Salyut 7* was in operation until early in 1986, these designs were eventually superseded by the third generation *Mir* space station.

Although the American space program moved away from the space station concept in the early 1970s, the flight of the shuttle *Columbia* in April 1981 heralded the possibility of an expansion of space-based operations. Following the *Challenger* disaster of January 1986, that expansion has not yet been fulfilled. However, prior to the disaster, experiments such as the *ACCESS / EASE* mission provided large amounts of data on the possibility of using astronaut construction teams to assemble large structures on orbit. These experiments, flown on the second flight of the shuttle *Atlantis* on mission 61B in November 1985, consisted of assembling two truss structures using a variety of different assembly techniques.

The 'Assembly Concept for Construction of Space Structures' (*ACCESS*)<sup>6</sup> mission, **Figure 1.3**, was principally initiated as a structural mechanics experiment. The objective was to manufacture a 10-bay, 30 m long truss consisting of 96 individual beams and 30 joint clusters. The construction team of two astronauts were held in foot restraints while the truss was rotated and translated to present proper work positions. The MIT lead 'Experimental Assembly of Structures in EVA' (*EASE*)<sup>7</sup> mission, **Figure 1.4**, was intended as an examination of astronaut performance during assembly<sup>8</sup>. The experiment grew from the 'Structural Assembly Demonstration Experiment' (*SADE*)<sup>9,10</sup> and involved two astronauts in the shuttle payload bay constructing a single tetrahedral structure. The astronauts worked with a 'low man', who used foot restraints on the floor of the payload bay, and a 'high man' who worked without restraints at the opposite end of the beam.



**Figure 1.3:** ACCESS Structure (Source: NASA).

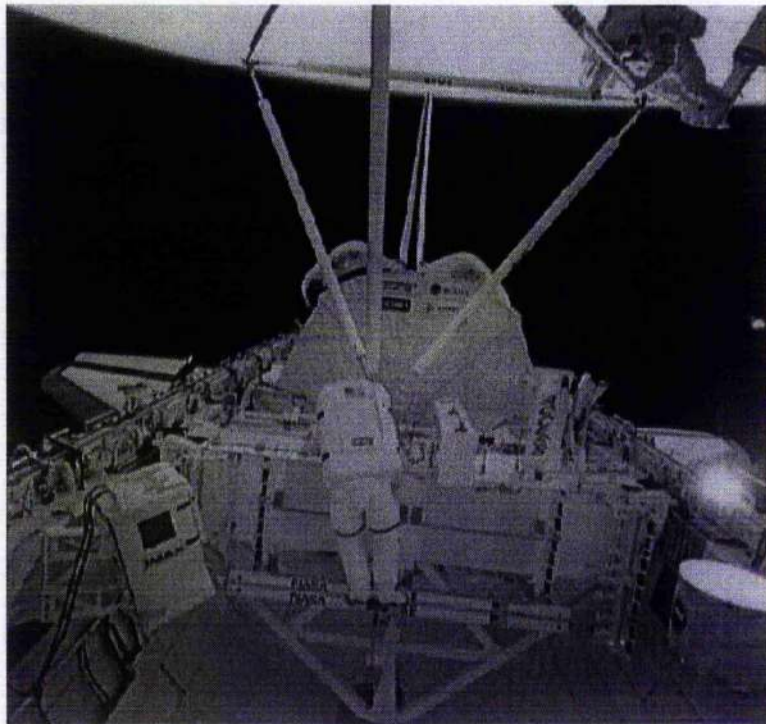


**Figure 1.4:** EASE Structure (Source: NASA).

Although both of these experiments were successful, and the structures were fully assembled by the astronaut team, the infrastructure required to perform even a simple assembly task prompted further research into the field of automated assembly. The MIT team, led by Prof. David Akin, began to examine the general field of robotics and more specifically, telerobotics for assembling *EASE* type structures. Following a switch to the Neutral Buoyancy Facility at the University of Maryland, Prof. Akin and his team began work on a series of robotic vehicles and structures which would eventually lead to the *Ranger* telerobotic vehicle. *Ranger* is due to fly on the *Shuttle* late in 1999 and will be discussed in more detail later.

### 1.2.3 On-Orbit Assembly: 1986-1997

The *Mir* station was launched in February 1986, and represented the first large space structure which would require assembly on-orbit. The main core of the *Mir* station was an upgraded *Salyut* design, however, the following year saw the addition of the *Kvant* module to the station. The *Kvant* module was launched on March 1987 and provided an additional 40 m<sup>3</sup> of working space to the station. The station continued to grow with the addition of the *Kvant-2*, *Kristall*, *Spektr* and *Priroda* modules. In addition, in 1995 a docking adapter was added to allow the American space shuttle to use the *Mir* facilities. The final internal usable volume of the station is now approaching 400 m<sup>3</sup>.

The *Mir* station is the first space station which has been continually manned since its launch. The station has been assembled using a combination of automatic docking techniques and cosmonaut assistance. A significant lesson learned from these additions to the station was that the assembly of cables and plumbing, both internally and externally formed a significant proportion of the assembly procedure. With the launch of the space station in 1986, an upgraded *Soyuz TM* manned spacecraft was introduced. Also, in 1989, the *Progress M* ferry began to service *Mir*. The significance of these spacecraft is that they are both capable of automatic rendezvous and docking using the *Kurs* system. Again, little is known of the technical specification of this system. However, it is clear that the system will be installed on the Russian components of *International Space Station Alpha*. The collision between a *Progress TM* ferry and the *Spektr* module arising from a failed docking procedure in July 1997 has cast doubt on the future of *Mir*. However, the long duration stays of the cosmonauts and the resulting Extra Vehicular Activity (EVA) has provided experience of on-orbit operations which will be vital for the assembly of *International Space Station Alpha*, **Figure 1.5**.

NASA's commitment to the *ACCESS / EASE* missions highlighted their desire to develop the capability to manufacture structures in space. As a consequence, the Automated Structures Assembly Laboratory (ASEL) was initiated at the NASA Langley Research Centre in the late 1980s. Initially, their work focused on two main areas of research. Firstly, telerobotic assembly methods and vehicles, and secondly, the development of a *Space Crane* concept, which is designed to provide a custom construction facility for on-orbit assembly.

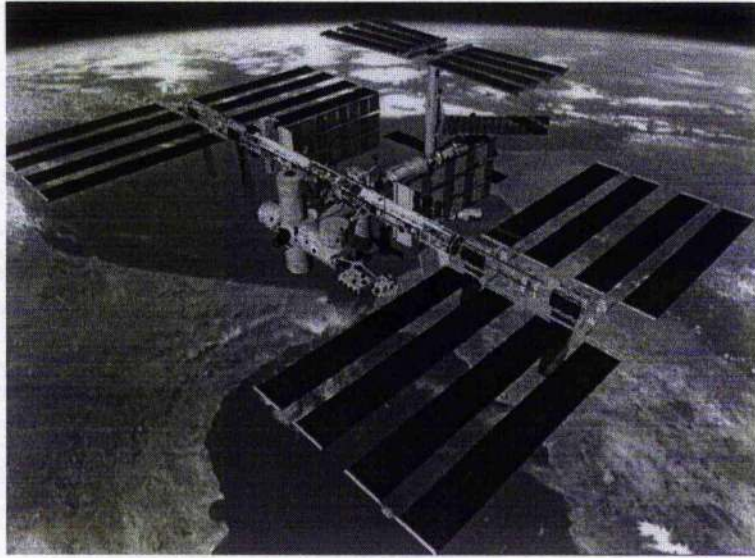


**Figure 1.5:** *International Space Station Alpha* (Source: NASA).

One of the structures that was identified as being required in the near term was that of large scale precision reflectors<sup>11</sup>.

ASEL began its studies in telerobotics and automation by examining the supporting structures required to assemble a large reflector on-orbit. Initially traditional 'pick and place' techniques were applied. This is a technique very similar to that used in terrestrial production lines where robot manipulators pick an object from a predetermined location and place it in another location. This is a fairly rudimentary approach, however, the objectives of the study were principally to develop a proof of concept system, and not to develop new technology. Thus the development needs were formalised as;

- Practical experience of automated systems.
- Software capability for robust systems.
- Proven telerobotic interfaces.

To gain experience, ASEL began experiments using a robot manipulator to construct a honeycomb truss structure consisting of 102 beams of 2 m length. Incorporated within the experiment were error terms in positioning and velocity which were overseen by a human operator capable of telerobotically recovering the manipulator from any errors. Results from the experiment indicated that the system was indeed feasible. In addition, the assembly time per beam was approximately five minutes, including the time spent overcoming errors. This has prompted further research into the assembly of truss structures where experiments have incorporated elements such as machine vision<sup>12</sup>, structure validation<sup>13</sup>, advanced software hierarchies<sup>14</sup> including expert systems<sup>15</sup> and Artificial Intelligence planning architectures<sup>16</sup>.

The second area of research was aimed at the development of on-orbit hardware capable of providing the infrastructure to apply automated construction techniques. The concept that has been developed to fulfill this mission is the *Space Crane*. The crane is assembled from truss elements very similar to that of the *ACCESS* mission which themselves are manufactured from uniform beams. Various joints have been examined including articulated joints, rotary joints and high stiffness joints to provide a vibration damping capability<sup>17</sup>. Much of the analysis has been focused out on the structural properties<sup>18,19</sup> of the *Space Crane*. The process of assembling the *Space Crane* has been largely assumed to be automated with the experience being provided by the reflector assembly studies.

#### 1.2.4 On-Orbit Assembly: 1997-

Following the collapse of the Soviet Union, NASA and the Russian Space Agency (RSA) began a series of experiments which will lead to the construction of *International Space Station Alpha*. Following a formal agreement in 1993<sup>20</sup> a cash-strapped RSA has allowed NASA use of the *Mir* station leading to a series of shuttle missions by the *Atlantis* and *Discovery* orbiters docking with *Mir*. The use of *Mir* has allowed NASA and RSA astronaut / cosmonaut teams to gain experience of joint on-orbit operations with the specific aim of proving technologies for the launch and assembly of *International Space Station Alpha* components, the first of which is due to be launched in 1998.

The *International Space Station Alpha* programme grew from a series of proposals for the American space station *Freedom*<sup>21</sup> and is itself the proof of concept for Large Scale Structures (*LSS*) being assembled on-orbit. As the cost of *Freedom* grew, NASA looked to international partners to assist in financing the station. Currently, the space station will provide working and living quarters for scientists from Japan, Europe, Canada, the USA and Russia. The size and scope of the station is far beyond any previous platform. With a total length of 108 m and a breadth of 74 m, the overall station size is 2.5 times larger than *Mir*<sup>22</sup>. Thus, the station must be assembled on orbit from forty separate launches, which remains the largest engineering challenge of the programme<sup>23</sup>. The main modules of the station have been manufactured in both the USA and Russia. These components will be assembled for the first time on-orbit using a combination of automatic docking procedures (the Russians will assemble the initial components using the *Kurs* docking system), shuttle borne robotic arms and teams of Astronauts / Cosmonauts. The EVA requirement for the station is for 1,000 hours over a period of five years. This requirement is larger than the current total EVA experience of all previous space programmes.

The sections of the station may be categorised as the pressurised modules, solar panels and radiators, the main station truss and external scientific payload. The pressurised modules will all be assembled as discussed previously, in addition, the solar panels and reflectors will all be deployed automatically with assistance from robotic arms, as will the external scientific payload<sup>24</sup>. However, the main truss of the station, onto which the remainder of the station will be attached consists of a framework of beam elements<sup>25</sup>. As a consequence of the

*ACCESS / EASE* experiments, the Hubble refurbishing missions and experience of operations on Mir, the task of assembling the truss on-orbit and installing wiring looms and plumbing connectors was thought to be a task beyond the on-orbit assembly experience currently available. Therefore, the decision has been taken by NASA and the international partners to assemble the framework and install the necessary equipment on the ground to ease the workload of the astronauts.

### 1.2.5 Future Studies

If current population growth continues, conservative estimates place the total world population in excess of 7 billion people by the year 2020. As a consequence, many studies have examined the need for clean power to supply such a large global population. One of the options examined has been the *Solar Power Satellite (SPS)* concept<sup>26</sup>. Originally examined in the late 1960s, a patent for an orbiting solar farm was filed in 1968 by Peter Glaser<sup>27</sup>. The original concepts examined by NASA and other organisations involved massive projects. Some studies have estimated an overall cost of a Geostationary *SPS* approaching \$300 billion in 1997 dollars<sup>28</sup>. This relates to a 5-10 gigawatt output from a 5x10 km satellite. This translates into an installed cost of 5 \$.kW<sup>-1</sup>. Some estimates in manpower have identified a support requirement of over 600 people for a 90 day tour.

Studies carried out in 1995 have presented a much more modest structure<sup>29</sup>. The more recent studies have been based on a modular design called the *Sun Tower* system. The cost of *Sun Tower* is much lower at \$10-\$15 billion in 1997 dollars delivering a power output of 250 megawatts in Medium Earth Orbit (MEO). Examining the baseline costs of solar panels, typical costs of photo-voltaic arrays are in the region 1-2 \$.kW<sup>-1</sup><sup>30</sup>. This results in an installed cost approaching 5 \$.kW<sup>-1</sup>. This can be compared with 1.25 \$.kW<sup>-1</sup> for a conventional power plant. However, in Earth orbit, the energy output from the Sun results in a potential maximum output of 1.365 kW.m<sup>-2</sup><sup>31</sup> from a solar power satellite. Therefore, in the long term, the *SPS* concept may prove commercially attractive. Other applications for advanced modular solar power concepts are in areas such as low thrust electric propulsion. This type of propulsion would allow faster Mars missions and missions to the outer planets. However, the cost of developing the technology is dwarfed when compared to the cost of launch to Low Earth Orbit (LEO).

The cost to LEO is critical to many proposed missions. Early studies of the *International Space Station* in the form of the American *Freedom* station involved provision for the assembly of large telescopes and orbital construction facilities for the assembly of large mass vehicles such as Lunar and Mars transfer vehicles. As the cost of the station grew, the cost of marginal missions such as these became untenable. Thus, most of these facilities did not make the transition to *International Space Station Alpha*. However, as the launch cost to LEO is reduced, these missions may become more attractive and large scale construction facilities will be required for on-orbit assembly.

### 1.3 State of the Art: Structures

Many large spacecraft are limited by the volume of the launch vehicle nose fairing. Therefore, if there is a requirement for a large volume spacecraft, a method of construction is required which will allow a transition to the operational configuration on-orbit. Currently, the structures which allow such transitions may be divided into three distinct classes: erectables, deployables, and inflatables. Each of these structures has associated advantages and disadvantages. The following sections shall explore these in detail.

#### 1.3.1 Erectables

An erectable structure is simply that. This class of structure requires assembly, whether by astronaut EVA or robotic manipulators in-situ. Experience using neutral buoyancy tank simulations has shown that unaided construction techniques are achievable by astronauts. However, these techniques prove to be both demanding and fatiguing for the astronauts<sup>32</sup>. Therefore, various techniques have been developed which will assist astronauts in the assembly of structures on-orbit. Principally, the type of structures envisaged here are that of large load bearing truss structures which themselves are assembled from individual beam elements ranging from 2 m to 6 m in length. To assemble this type of structure, studies and tests have been carried out using a Mobile Work Station (*MWS*) and Swing Arm Beam Erector (*SABER*)<sup>33, 34</sup>.

The *MWS* is a mechanical device consisting of mobile foot restraints and a rail which translates the whole mechanism along the partly assembled truss. The astronauts are held in place by the foot restraints which may themselves be adjusted. However, the prescribed envelope of movement is rather limited. Thus, the astronaut is relieved of some of the fatiguing translation and, in addition, is provided with a mechanism to react against the forces and moments incurred during assembly. Working co-operatively, two astronauts were found to be very efficient in building truss elements consisting of 6 m struts. Average assembly times of approximately 40 second / beam were achieved in neutral buoyancy simulation<sup>6</sup>.

The *SABER* device operates in a similar fashion to that of the *MWS*. However, a fundamental difference is that the astronaut is held in position while the truss element is rotated and translated to present the astronaut with the next work site. Again, this was found to be very efficient with average assembly times of 30 second / beam for a beam length of 2m. Both of these studies culminated in the *ACCESS* mission. The *ACCESS* mission made use of a *SABER* type assembly mechanism where the astronauts were restrained in the shuttle payload bay while a 96 beam, 30 m long element was assembled. The mission was highly successful with an average assembly time of 16 second / beam for a beam length of 1 m<sup>6</sup>.

An exponent of erectable structures is Anthony Coppa<sup>35</sup>. In a series of papers and patents, Coppa has designed a system of interlocking beams which assemble to form a *Coppatruss*. A *Coppatruss* is a linear truss consisting of close packed tetrahedrons. The truss structure and joint mechanisms are very similar to other proposals, however the assembly

method uses a robotic assembler which is self-contained. The assembler utilises a jig structure which will assemble triangles which are then connected to form the truss. The beams which form the triangles are supplied from a cartridge module. Thus, the robot assembler would be supplied with raw materials which are loaded from a cartridge and a *Coppatruss* would automatically result. The need for EVA or free-flying assemblers would therefore be eliminated.

Studies carried out in the late 1980s<sup>6</sup> have highlighted a number of technology needs which are required to allow feasible structures to be assembled on-orbit at a reasonable cost. These are;

- Demonstration of rapid EVA assembly techniques.
- Development and demonstration of automated assembly techniques.
- Development and demonstration of a large stiff space crane.
- Validated hardware and assembly design costing algorithms.

In addition, the following areas have been identified as critical issues for large spacecraft operations<sup>36</sup>;

- Validated dynamic analysis.
- Validated accuracy prediction methods.
- Space qualified passive damping concepts.
- Demonstrated active control concepts.
- Demonstrated adaptive structures.
- Demonstrated structural integrity monitoring concepts.
- Validated design costing algorithms.

The erectable structure is recognised as a principal technology for the assembly and servicing of large spacecraft in the future. However, at this moment in time, the emphasis has altered from astronaut focused operations to remote teleoperated vehicles.

### *1.3.2 Deployables*

Deployable structures are considered to be the only practical method of constructing some of the very light structures in use today<sup>37, 6</sup>. A deployable structure is one which, following insertion into orbit, will begin to deploy itself on cue from a ground signal. One

example of this would be a solar panel unfolding itself. Their reliability has led to their inclusion on most spacecraft in the form of furlable booms, lattice columns and solar array wings. However, these different tasks may be reduced to the following structural types;

- Long Slender Beams.
- Deployable Reflectors.

Long slender beams are used in many different applications. For example, the solar wings of the *Hubble Space Telescope* (HST) are deployed using a long slender beam which, as it deploys, drags the remainder of the solar panel with it. The *Voyager* spacecraft also made use of a long slender beam to deploy science packages, as have many other missions. Of all the applications, the four main types of long slender beams may be categorised as;

- Storable Tubular Expendable Member (STEM).
- Continuous Longeron Coilable Booms (CLCB).
- Articulated Linear Trusses and Fold-Out Beams.
- Deployable Reflectors.

STEM structures, or more commonly, bi-stem structures are deployable in a fashion similar to that of a carpenter's measuring tape. The stem itself is stored in a flat roll which may be deployed using the potential energy of the flattened material or a small motor for more precise deployment rates. A bi-stem uses two stems interlinked to form a complete tube as shown in **Figure 1.6**. The bi-stem is the more common structure which allows greater bending stiffness and mechanical damping behaviour. Many hundreds of these structures have flown in spacecraft with a tube diameter in the region of 1-5 cm. The longest structure ever deployed was a stem unit flown on the *Radio Astronomy Explorer* (RAE) in the late 1960s. Four units were flown, each being over 250 m in length. The stem and bi-stem structures are not useful for very precise structures, however, their low cost and high packing efficiency make them very attractive.

CLCBs are widely used on spacecraft and are considered to be a mature technology with very predictable characteristics. Invented in 1972 by the Astro Aerospace Corporation, and more commonly known as the *Astromast*, the CLCB is a linear truss structure with a triangular cross section. The structure may be deployed from a very compact configuration with a typical stowed length less than 2 - 3% of the total deployed length. **Figure 1.7** shows a typical CLCB. The structure is made up of triangular elements joined by linear elements with a pretensioned diagonal which stores enough internal potential energy to allow a self

deployment once in orbit. A controlled deployment is possible by using a lanyard cable attached to the end-most unit which may be played out to the desired length. Typical widths of the structure are between 15 cm and 75 cm. The maximum practical width is estimated at 1 m due to the internal energy of the diagonals growing dangerously large.

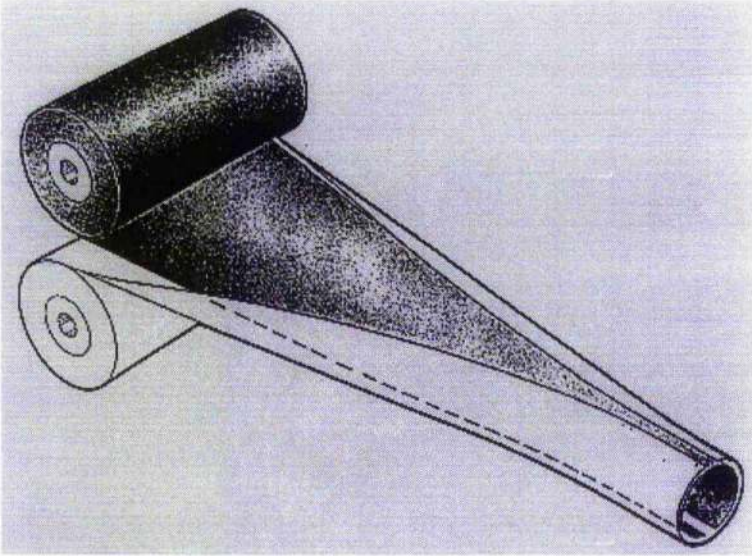


**Figure 1.6:** *Bi-Stem* Structure (Source: Ref. 6).

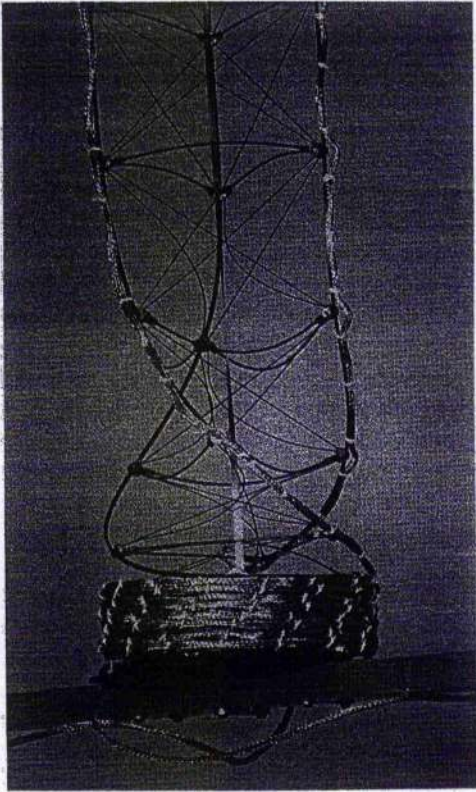


**Figure 1.7:** *CLCB* Structure (Source: Ref. 6).

Articulated trusses are essentially similar to the trusses considered in the ACCESS / EASE missions. However, instead of manual construction, these structures make use of scissors and pantograph mechanisms to deploy. Thus, from a relatively close packed configuration, it is possible to deploy a large strong linear truss. However, the only practical precision example of this type of structure to have flown is on the *Seasat* and *ERS 2* synthetic aperture radar (SAR) payloads. This example was manufactured by the Astro Aerospace Corporation, the principal developers of CLCBs. The advantages of using this type of structure is their high strength and their ease of deployment. In addition, if a surface is added to one of the faces of the deployed structure, a stable platform is provided with good support properties. However, the disadvantages are their mechanical complexity and their relatively poor packing efficiency. Careful consideration must be given to the application of this type of structure.

Deployable reflectors are used on-board spacecraft for a number of tasks. Applications include remote sensing and communications. Since a wide range of power and frequencies must be supported by these structures, a variety of different types have emerged, which may be divided into two classes;

- Single piece reflectors.
- Moderate precision deployable mesh reflectors.

Single piece reflectors are very similar in size to that of a typical TV satellite dish. Their small size allow them to be launched fully formed. Therefore, it is possible to manufacture these out of relatively common composite or metallic materials. In addition, due to their manufacture occurring at a single point in time, the accuracy of the reflector may be very precisely defined. In orbit, these dishes are deployed in a single action. Simply, they will be manoeuvred from a stowed to an operational configuration. Also, since the receptor or feed of the dish may be pre-installed, the housing for the reflector need only point the instrument in the necessary direction.

If a mission demands a larger dish, then a deployable mesh reflector will be used. These reflectors are quite common, having flown on several missions. However, the most well know case is the *Galileo* high gain antenna which failed to deploy during transit to Jupiter. These large reflectors must be deployed, or unfurled in orbit. This is usually carried out using an umbrella type assembly where the reflecting mesh material is attached at various points. On deployment of the mechanism, the mesh will also unfurl, thus forming the necessary parabola. However, due to the limited attachment points of the material to the supporting structure, the surface accuracy of the reflector remains at best moderate. The mesh material itself requires careful design in that it must appear solid to the impinging radiation. Therefore, the mesh must be woven to a very high specification so that each mesh cell is

smaller than that of the wavelength of the incoming radiation. Typical materials are synthetic or metallic fibres and typical reflector diameters range from 5 m to 15 m.

### 1.3.3 Inflatables

Inflatable structures have been the subject of much attention since the beginning of the space programme<sup>6</sup>. Principally, their advantage is their high packing efficiency and ease of deployment. They have been flown extensively on spacecraft such as *Echo I*, *Echo II*, *Pageos*, *Explorer IX*, and *Explorer XIX*. Recent experiments such as the Inflatable Antenna Experiment (*IAE*), **Figure 1.8**, have highlighted this area as a promising technique for the deployment of large space structures<sup>38, 39</sup>. Generally inflatables are considered for applications which do not require highly precise shapes. This is due to the difficulties associated with manufacturing the thin polymers and fabrics used. In addition, due to the inherent high coefficient of thermal expansion of polymers, the contours of the structure will change with temperature. Currently, there are two classes of inflatable structures in use;

- Pressure Stabilised Inflatables.
- Rigidised Inflatables.

Pressure stabilised inflatables are commonly used as antennas or concentrators. Due to their low mass and packaged volume, their launch costs are distinctly lower than other classes of structure. Typically, an inflatable structure will be an order of magnitude lower mass and packaged volume than deployed structures. A typical example of this type of structure is the antenna used on the *Echo II* passive communications satellite. In general, these structures have demonstrated excellent performance. Their large continuous surfaces

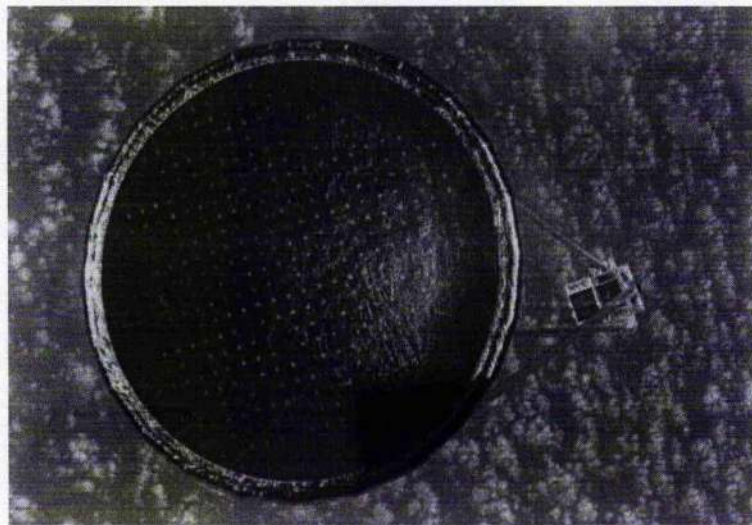


**Figure 1.8:** *Inflatable Antenna Experiment* (Source: NASA).

mean good thermal properties, typically being isothermal to within 10 Kelvin. In addition, having been used extensively on military systems in space, they appear to be very reliable with few failure modes.

Dynamically, structural deformations cannot occur without the internal volume of the inflatable changing. The volume change is opposed by the internal pressure and so results in a stable structure where resonance problems are unlikely. In addition, the fabrics used have exhibited a large damping coefficient, thus resulting in a rapid damping of disturbances with a typical surface accuracy of a 0.1-1 mm and an operational pressure in the range of  $10^{-3}$ - $10^{-5}$  atmospheres. At such low pressures, it is possible to use a gas reservoir which can maintain internal pressure for an operational lifetime of order 10 years.

Rigidised inflatables are similar to pressure stabilised inflatables with one major difference. These inflatables are treated such that they will become rigid in space, thus allowing them to function as load bearing structures. This type of structure was used in the *Echo II* and *Explorer* missions. The type of material used here was a laminate of aluminium and polyester which sets following inflation. Currently, two materials are used. The first uses a space curing resin which is enclosed by two impermeable films. On exposure to space, the resin will harden. A second material used is a Gelatin / Fabric Composite. These fabrics work by impregnating a carrier material with gelatin. On exposure to space a solvent, usually water is released from the material thus hardening the film. It has been shown that this type of structure has a good performance coupled with minimal degradation over time.

#### *1.3.4 Conclusion*

Due to their unique nature, design and development dominates the cost of current spacecraft production<sup>40</sup>. In contrast, a civil engineering project has a design and development cost of less than 10% of the total project cost<sup>6</sup>. To make large structures affordable, two areas have been highlighted as critical technologies. Firstly, the development of off-the-shelf building block components. And secondly, a method of construction and validation which will minimise the cost of system integration<sup>41</sup>. However, for large space structures, acceptance by the space community will firstly require the demonstration of a validated method of assembly<sup>42</sup>. In addition, the costs of such large structures mean that two questions must be addressed; whether the structure will be deployed, or assembled, as expected and as a consequence, whether the structure will operate as expected. Therefore, with the limited experience of large space structures available today, the risks are seen by many to be too high at present.

#### **1.4 State of the Art: Robotics & Sensors**

Currently, there is a wealth of research material concerning the development of robotics and sensors. There is, however, limited research in robotics specifically designed for operations in space<sup>43</sup>. However, NASA is actively promoting robotics and telerobotics with a

number of projects including *Mars Pathfinder* and demonstration robots such as *Dante*<sup>44, 45</sup>. At the forefront of this research is the *Ranger* project and the *Inspektor* class of robot. However, the development of robotic vehicles in other fields will have a beneficial influence on space robotics in that the terrestrial technology is reaching maturity.

#### 1.4.1 *Ranger*

The *Ranger* vehicle is currently being designed and constructed in the Space Systems Laboratory at the University of Maryland. The project originated as a consequence of the earlier *EASE* mission. The *EASE* mission highlighted the difficulties faced by astronauts on a construction EVA. Therefore, the Space Systems Laboratory began development of the first dextrous space telerobot. A precursor of the *Ranger* vehicle was the *Beam Assembly Telerobot (BAT)*<sup>46</sup> which was a vehicle developed for testing in a neutral buoyancy tank to demonstrate the core technologies required of the *Ranger* vehicle. Principally the BAT vehicle made use of two dextrous robotic arms to bring together and connect two beams.

Following the successful demonstration of BAT, the *Ranger* vehicle was proposed for development with a total budget of \$10 million in 1997 dollars<sup>1</sup>. The prototype *Ranger NBV* (Neutral Buoyancy Vehicle) neared completion in 1995<sup>47</sup>. Tests and development continued in the neutral buoyancy tank at the University of Maryland until 1997 when an agreement was reached with NASA to fly the vehicle on the shuttle late in 1998<sup>48, 49, 50, 51</sup>. The vehicle which will fly on the shuttle, the *Ranger SFX* (Space Flight Experiment) will have a final mass of 800 Kg and is approximately the size of an original *Mercury* capsule.

The principal objective of the *Ranger* experiment is to calibrate and validate ground neutral buoyancy tests with the on-orbit performance, thus allowing future development to occur on the ground. Other objectives include determining the capabilities and limitations of space telerobotic systems. This will be carried out using a series of servicing tasks ranging from the straightforward to the complex. The technologies which will be demonstrated are the robotic manipulator control algorithms, a full immersion virtual environment interface<sup>52</sup> for the operator, obstacle detection<sup>53</sup>, obstacle avoidance<sup>54</sup> and adaptive flight control methods. Thus, this vehicle will represent a proof of concept demonstration for the construction problem which will be discussed later in this thesis. If this experiment is successful, then real on-orbit assembly experiments could be carried out sooner rather than later.

#### 1.4.2 *Remote Inspection Robots*

Another class of robots which has attracted much attention is that of remote inspection vehicles. These vehicles have been designed to fly free from *International Space Station Alpha* and the *Space Shuttle* to inspect the surface of the vehicles in inaccessible sites. Currently, there are several studies examining these types of vehicles. The first is the NASA developed Autonomous EVA Robotic Camera (AERCam), *Sprint*<sup>55</sup>. *Sprint* is a teleoperated vehicle which is due to fly at *Mir* in 1998<sup>56</sup>. The vehicle consists of a stable platform capable

of both translation and rotation. The sensor suite onboard the vehicle will consist of a camera and lighting system in addition to a communication module for control purposes. Although the initial vehicle will be tightly controlled by an astronaut, later generations are planned which will elaborate on the original vehicle by including various degrees of autonomy<sup>57, 58</sup>.

European studies are also proceeding, principally with the *Inspector* vehicle currently being developed by Daimler-Benz. Essentially this vehicle is identical to the *Sprint* vehicle in concept, the only differences being in the engineering design. However, the final *Inspector* vehicle is designed to be fully autonomous, moving between predetermined way-points with minimal intervention from the astronaut controller. A third vehicle, called *Scamp*, is currently being used as a test-bed for a second generation vehicle at the University of Maryland. The principal objective of the *Scamp* vehicle is to demonstrate telerobotic interfaces. Currently, a computer vision obstacle avoidance algorithm has been developed which will run from a desktop PC, thus proving the control architecture of these vehicles is not prohibitive.

One of the major design specifications of these vehicles is that they will not translate quickly enough to damage another vehicle if there is a collision. Therefore, the translation capability of the vehicle is provided by a modest propulsion system. Any translation between two way-points may consist of relatively long periods of acceleration and deceleration. In addition, since any control system will be based on visual cues, conventional optimal control methods will not be applicable. New, control algorithms such as the potential field techniques developed at the University of Glasgow will also require extensive testing before being certified for operations near any manned habitat in orbit.

#### 1.4.3 Sensors

Any free-flying robotic vehicle which is designed to work on-orbit either alone or with a group of similar vehicles will require a wide range of capabilities. With regard to sensors, although the robot may carry many different types of sensors, these may be reduced to just two classes. The first class of sensor, herein referred to as *Formation* sensors, would be used to determine the robot's place within the environment. An example of this would be the robot determining its relationship to the other working robots. The second class of sensor, herein referred to as *Proximity* sensors, is designed for the detection and manipulation of any objects within the immediate proximity of the robot vehicle. An example of this would be a gripper arm reaching out and grasping a component.

Formation sensors are typically based on utilising the Global Positioning System (GPS) or GPS-like systems. This method has been proposed for use with the Spacecraft Interferometer Concept at the Jet Propulsion Laboratory<sup>59</sup> which makes use of a GPS-like technique. The interferometer concept requires that each spacecraft is positioned very accurately relative to one another over large distances. The method envisaged here is the *Autonomous Formation Flying* (AFF) system which allows the calculation of the relative distance and angles between spacecraft. The method requires each spacecraft to transmit a

phase and pseudo-range signal which is received by multiple antennas on the other spacecraft. The multiple antennae on each spacecraft allows complete solid angle coverage. Thus each spacecraft can calculate its position relative to the others with high precision. The accuracy possible with this method is estimated to be 1 cm in range and 1 arcmin in relative angle.

Currently, there are a large variety of proximity sensors available commercially. There are also many applications, typically where robots are utilised. Although many of the sensors available are designed to perform the same task, the method by which they do so is varied. However, it is possible to classify the range of sensors into four main groups. These are;

- Laser and photo-electric triangulation.
- Optical reflection intensity.
- Optical and microwave time of flight.
- Inductive and capacitive.

Laser and photo-electric triangulation sensors work in a manner where they emit a narrow beam of light at an offset angle from the spacecraft. This beam of light is then reflected back from the target object with the location of the returned beam allowing the calculation of the range-to-target. Experimentally, this type of sensor promises extended range and lower sensitivity to the surface properties of the target. However, they are rather complex, so much so that data handling is processed by a neural network. In addition, certain types of laser emitters can cause problems with eye safety and so their use may be limited to environments where humans are not present. Due to sensor geometry, a typical range for this class of sensor is 3-50 cm.

Optical reflection intensity sensors operate as their name would suggest. A beam of light is emitted from the spacecraft to the target object and the intensity of the reflection is measured. Currently, this is the most widely used sensor, however, it is very susceptible to environmental and target surface conditions. Ranges vary from as little as 10 cm to 350 cm. A similar class of sensor is that of optical and microwave time of flight sensors. These sensors work in a similar fashion to that of reflection intensity sensors, however they measure the time between emission and return of the carrier beam. The principal advantage of using this sensor is that it can perform over a wide range of distances, typically from 15 cm to 15 m. However, the sensor is expensive and the resolution is limited to only 15 cm.

Inductive and capacitive sensors are commonly used in two areas; production lines and metal detectors. They have a very limited range, and the resolution is limited to detecting object presence rather than range. These sensors utilise two plates or coils. A current is passed across the coils, and the presence of a metallic object will distort the signal. They have a very

limited range, typically less than 1 cm. Research is currently attempting to extend the range of this type of sensor for use in the end effectors of robot arms.

A study carried out at the Jet Propulsion Laboratory for NASA<sup>60</sup> concluded that the sensors which were best suited to space operations were the;

- Idec/Izumi SA1D triangulation sensor.
- Sick DME2000 laser time of flight sensor.
- Capacitec 410SCBNC capacitance sensor.

Of these three sensors, the DME2000 laser time of flight sensor gave the best overall performance. However, a more cost effective choice would be the SA1D triangulation sensor which is better for measuring point-to-point distances. For application to area coverage, such as a sleeve for a robot manipulator, the capacitance sensors give better performance. The best of these is the 410SCBNC sensor. An ideal application of this sensor would be on working surfaces such as grippers.

## **1.5 State of the Art: Assembly Philosophies**

Currently, there are numerous control methodologies available to the engineer. However, for the scope of this study, Lyapunov's method and the associated potential function method shall be considered the method of choice. Although Lyapunov's method was originally formulated at the turn of the century, it is only recently that it has received widespread attention. A number of studies exist applying Lyapunov's method, which will be discussed further in **Chapter 3**. However, a brief introduction shall be provided here and the application to spacecraft systems discussed.

### *1.5.1 Control via Lyapunov's Second Method*

Lyapunov's second method may be described more as a philosophy than a strictly defined method. The method is applied by firstly specifying some goal condition or state. From any initial condition or state, if the system moves towards the goal, then the system is converging and, in principle, no control action is required. Alternatively, if the system is moving away from the goal, then the system is divergent and a control action is required to ensure that the system is again moving towards the goal and is convergent. There are many differing methods of formulating and applying these control actions.

The potential function, or energy, method is one such method of deriving control inputs. Each condition or state within the system domain is assigned a positive 'potential' value. The potential is assigned so that if the system diverges from the goal, the potential will increase with time, and if convergent, then the potential will decrease until the potential

vanishes at the solution. A common analogy is that if the potential magnitudes were plotted throughout the domain, a 'salad bowl' paraboloid geometry would result with the goal at the bottom of the bowl. Thus, if a marble were to be dropped into the bowl, every possible outcome would result in the marble reaching the bottom of the bowl.

Obstacles may be included in the domain by adding areas of high potential in the region of the obstacle. However, the addition of the high potential may cause the formation of a local minimum. A local minimum is a region within the domain where, if that condition is reached, the potential function would be uniformly increasing in every direction. Returning to the 'salad bowl' analogy, this would be the equivalent of fixing an obstacle to the side of the bowl such that it was possible for the marble to be trapped behind it, thus preventing the marble falling to the goal condition. The formation of local minima has proved to be a stumbling block in many applications of the potential function method. Therefore, the application of obstacle potentials and the resulting local minima shall be examined in greater depth in **Chapter 4**.

Although the application of potential functions to spacecraft control is well documented, much of the work has concentrated on robot manipulators<sup>61</sup>. The expansion of the technique to include areas such as spacecraft orbit and attitude control has been carried out by the research team lead by McInnes at the University of Glasgow<sup>62</sup>. Much of this work has concentrated on areas such as proximity manoeuvring<sup>63</sup>, large angle slew manoeuvres<sup>64</sup>, terminal descent guidance for remote landers<sup>65</sup>, constellation and formation keeping<sup>66</sup> and rendezvous and docking<sup>67</sup>.

### *1.5.2 Automated Docking Methods*

Many automated docking schemes are currently in use or in development. Of the methods available, they include radar, laser and visual based systems. However, of interest to this study is the application of automated control algorithms. Lyapunov's theorem provides a method which demonstrates the flexibility required for such complex problems. The two principal proponents of Lyapunov's method and its application to spacecraft rendezvous and docking are Wang at the Jet Propulsion Laboratory and St. John-Olcayto and McInnes at the University of Glasgow. Wang<sup>68</sup> has examined a generic docking case where an active body is closing to dock with a static body. For this case, both are assumed to be 6 degree of freedom bodies which are controlled in both attitude and position. The method, when applied, relies on shaping the closure rate between docking adapters situated on each body. A control input is then derived which will ensure this closure rate is always negative definite in both attitude and position. Strictly speaking this method represents a pure application of Lyapunov's second method, however, the approach does not utilise a potential function. The method has been expanded to include a simple collision avoidance scheme and has been applied to many different problems, including the interaction<sup>69, 70</sup> and formation keeping<sup>71, 72</sup> of groups of micro-spacecraft.

An extensive study<sup>73</sup> carried out at the University of Glasgow on behalf of the European Space Agency has examined the application of potential functions to the rendezvous and docking problem. The study was aimed at deriving an advanced control algorithm for the *Automated Transfer Vehicle* (ATV) which ESA is developing to re-supply the ISSA. The dynamic model provides a very accurate simulation of the ATV incorporating elements such as sensor noise, thruster execution errors and collision avoidance. Based on this model, several control algorithms have been developed using potential functions and Laplace Navigation. In addition, two classes of obstacle potentials have been examined, the Gaussian potential, and the power-law potential. Both of these potentials are examined in greater detail in **Chapter 4**.

Laplace Navigation utilises fluid potential flow theory so that goal conditions may be defined using sinks, and obstacles formed using sources. A distinct advantage over conventional potential function methods is that the addition of an obstacle source will not form a local minima. This may be verified using Laplace's equation. If a potential function is chosen such that it satisfies Laplace's equation

$$\nabla^2 V = 0 \tag{1.1}$$

where  $V$  is the potential function, the potential function will not contain any local minima as the second derivative shall always be zero. Therefore no maxima or minima may form other than at the solution or boundaries of the problem. In addition, the use of irrotational vortices may be used to specify the direction in which an obstacle is negotiated. The disadvantage of Laplace Navigation is the computational demands posed by the grid solution to the Laplace equation. Thus the method may prove difficult to apply to rapidly changing environments.

### *1.5.3 Controlling Groups of Small Robotic Vehicles*

The automated rendezvous and docking methods which have been described have been expanded to include both formation-keeping and path planning. However, there are many other control methods which have been applied to the problem of controlling groups of vehicles in different environments. The few which shall be discussed here are relevant to the problem of on-orbit assembly not because of their robot navigation strategies, but more so their application to the problem and the control architecture which has been derived.

The group of robotic vehicles envisaged here is typified by the work of Bay<sup>74</sup> and the *Army-Ant* group of robots. The *Army-Ant* group study was designed to examine the properties of a group of homogenous robotic vehicles. The robots were designed to be capable of working as a group to perform tasks such as lifting, transporting and placing pallets and oversized objects within a warehouse environment. The criteria for the experiment is that each robot should cost less than \$2,000 and as a group demonstrate;

- Robustness.
- Flexibility.
- Small Size.
- Simplicity.
- Emergent Group Behaviour.

The last element is critical, the *army-ant* concept is very dependent upon the group capability being greater than the sum of the individual capabilities. Thus, the design of the individual control mechanism must incorporate emergent group behaviour. Currently, the robot control scheme is based on each robot following a self-elected leader. Any given robot may elect itself leader by detecting the objective before its compatriots. The remainder of the robots will follow the exact movements of the leader. Although Bay has proposed this concept and begun development of the robotic vehicles in question, the study has not reached fruition as yet. However, it is interesting to note the comparisons which may be drawn between this study and the field of animal behaviour.

Niwa<sup>75</sup> has examined the behaviour of fish schooling and developed a mathematical model of the school behaviour. Within this study, it is assumed that no individual leader exists within the school of fish. Rather, the behaviour of any individual fish within the group is based on the behaviour of its nearest neighbour in terms of separation and velocity, both of which have strong correlations to the average size of the individual fish within the school. Thus, based on a very simple set of rules, it may be assumed that no individual will lead the school, but rather the school itself is the leader, and that the school is behaving as a single organism. It is this type of emergent behaviour which is critical to the development of behavioural models for groups of robotic vehicles.

Noreils and Chatila<sup>76</sup> proposed a very detailed examination of task execution for a single mobile robot. The study addressed issues such as planning, control, reactivity and robustness where the robot control architecture was split into three very distinct control levels, these are;

- Planning.
- Control.
- Function.

The planning level consists of a task plan. Although complex strategies are envisaged, the task plan consisted of a simple list of goals divided into very explicit tasks. The control level consists of a more complex management scheme. This scheme has four components, a supervisor, executive, error recovery management and surveillance manager. The objective of

this control level is to translate global strategies formulated by the planning level into specific operations. The functional level consists of series of modules performing specific tasks such as sensors and translation. Each module within the functional level provides a capability for the robot. The modules will exchange information with the other modules and also the control level. This type of architecture incorporates the advantage that tasks and events, errors and problems are dealt with at the lowest level of the architecture. In fact, this is a common approach to robot control, with the layered control method originally proposed by Brooks<sup>77</sup>. The interaction between the layers ensures the architecture's ability to react to external stimuli. As an event occurs which cannot be processed by a control layer, that stimuli is passed to a higher control layer which subsumes the task. This control method is commonly called a subsumption architecture and is discussed further in **Chapter 8**.

Driven by a need for higher precision assembly of electronic components, Hollis<sup>78</sup> at Carnegie Mellon University has developed an alternative control method for a group of construction robots. The robots operate in groups of up to forty on a conventional air table. The robots float on a steady cushion of air to provide the very high degree of accuracy that wheels could not. Steering is provided by on-board magnetic thrusters. Power is supplied via a cable which also provides a communication capability between the robots. Two types of robots exist in the domain. A courier robot and a manipulator. The manipulator is generally stationary, but will rotate between the task and a parts bin. The courier robots restock the parts bins. This is a complex system with courier robots travelling throughout the domain. However, to simplify the communication and software management problem, an overseer is not used, but rather levels of protocols are pre-programmed into the individual robots to deal with specific events.

The Hollis system corresponds to a decentralised scheme where the management structure is very shallow. The subsumption architecture of Brooks however, represents a very deep management structure. These two methods correspond to the two extremes of robot control. For this study, a compromise shall be made where central task planning shall be required. However, the individual elements of the group will retain a large degree of autonomy. Considering the task of path planning, strategies to consider external events have been formalised. One such study<sup>79</sup> proposes a taxonomy to formulate strategies. However, much of the work on on-orbit assembly strategies have focused on structural characteristics. Hamernik *et al*<sup>80</sup> have devised a strategy based on vibration damping in structures by the optimal placing of damping beams. However, it may said that the strategy must be formulated for specific tasks. Current research may yet provide a generic strategy for the autonomous assembly of space structures.

## **1.6 Mission Statement**

The objective of this study is to provide a method which will allow the autonomous assembly of components in space. The problem has been approached in three broad areas consisting of;

- The development of a control algorithm.
- The development of a model to test the control algorithm.
- The derivation of an architecture to simplify information handling.

The autonomous assembly problem is assumed to be carried out using autonomous free-flying vehicles such as a production model of the *Ranger* vehicle.

The control of the assembly vehicles and the development of control algorithms will firstly focus on the control of a single vehicle in both position and attitude. This will then be expanded to the control of a group of vehicles in both position and attitude. Finally, the control algorithm will be expanded to allow a series of components to be assembled by a group of vehicles to produce a predetermined structure.

The model which will be used to evaluate the control algorithms will be based on a model of a single assembly vehicle as a point mass. For each point mass a state vector shall be defined for position, velocity, attitude and attitude rates. There shall be no external forces acting on the vehicle other than control forces and those derived from the orbital mechanics of the problem. The model of the single vehicle is then expanded to include a number of identical vehicles. The components within the model shall be assumed to be active only when manoeuvred by a controlling vehicle. However, when inactive, their dynamics shall again be propagated by the orbital mechanics of the problem.

The control architecture shall be developed in such a manner that the assembly process may be reduced to a series of connections carried out in a specific order. This will require a method of information handling such that each assembly vehicle shall have access to a database of the connections required to assemble the desired structure. In practice, this will take the form of a connectivity matrix in which connections between specific components are represented by a binary flag. In addition, management of the assembly process shall be developed to simplify the assembly of complex structures. This will entail the reduction of a large group of vehicles into smaller teams with limited tasks. This will reduce the demands on each individual vehicle in terms of communication bandwidth and sensor range.

Therefore, concisely, the objective of this study is;

*To provide an on-orbit assembly method which will incorporate a practical and robust algorithm for individual vehicle control within a larger co-operative group. The emphasis shall be on providing a practical application of the control method which will allow further development to a prototype article.*

# Chapter Two: Orbital Mechanics

*Orbital Mechanics is just Newton's Law of Gravitation. However, one has to know this law very well.*

A.E.Roy

## 2.1 Introduction

The development of a method to control an engineering system demands an analysis of the system and its environment. This will involve the development of a model to simulate that system. This chapter will aim to provide an analysis, model and optimised solution to the problem of on-orbit manoeuvring. Thus, in future chapters, the model developed here may provide a datum against which any orbital manoeuvring algorithms may be compared. The chapter will aim to solve this problem in three broad areas;

- To develop a dynamic model of an Earth orbiting spacecraft.
- To develop a model of an orbiting spacecraft relative to a rotating co-ordinate frame.
- Solve the above problem to provide an optimised two impulse transfer between points relative to the rotating co-ordinate frame.

The model of the Earth orbiting spacecraft is based on the well known two-body problem. The use of a rotating co-ordinate frame will allow an analysis of the motion of a second spacecraft orbiting relative to the datum spacecraft. This is an essential part of any model devised for the analysis of the rendezvous and docking problem which is dealt with in **Chapter 3**. Using the rotating co-ordinate frame, an analysis is provided which allows optimal two-impulse transfers between two points relative to the datum spacecraft. This will allow any proposed rendezvous and docking control method to be compared to the optimal solution.

## 2.2 The Two-Body Problem

Currently engineering simulations are available which describe orbit propagation with a high degree of fidelity. However, the two-body problem is the basis of many simple orbit simulations. The two-body problem requires certain assumptions to be made which allows a closed form solution to the equations of motion for the orbiting spacecraft. These assumptions are;

- The Earth and orbiting spacecraft may be modelled as point masses.
- The analysis will not include the effects of aerodynamic forces.
- The only external force is gravity and may be expressed to first order as an inverse square force field.

Using these assumptions, the two bodies, the Earth and the spacecraft may be located in a coordinate frame as shown in **Figure 2.1**.

### 2.2.1 Equations of Motion

Examining **Figure 2.1**, a mass is defined to represent the Earth with mass  $m_1$  at position vector  $r_1$ . A second mass is defined to represent the spacecraft with mass  $m_2$  at position vector  $r_2$ . The force which attracts the two bodies may be expressed using Newton's second law as

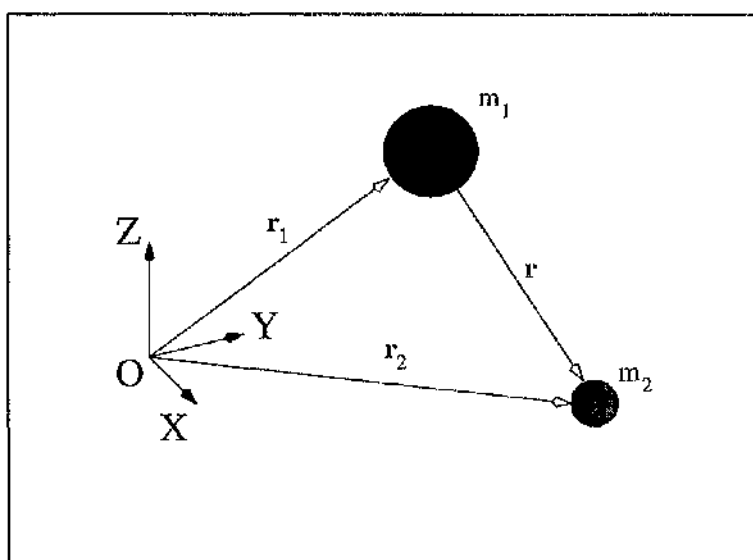


Figure 2.1: Two-Body Problem.

$$m_1 \ddot{\mathbf{r}}_1 = G \frac{m_1 m_2}{r^3} \mathbf{r} \quad (2.1)$$

for mass  $m_1$  and

$$m_2 \ddot{\mathbf{r}}_2 = -G \frac{m_1 m_2}{r^3} \mathbf{r} \quad (2.2)$$

for mass  $m_2$ . Dividing **Equation 2.1** by  $m_1$  and **Equation 2.2** by  $m_2$  and subtracting **Equation 2.2** from **Equation 2.1** the relative acceleration of the two masses is given by

$$\ddot{\mathbf{r}} = -G \frac{(m_1 + m_2)}{r^3} \mathbf{r} \quad (2.3)$$

where  $\mathbf{r} = \mathbf{r}_2 - \mathbf{r}_1$  is the position of  $m_2$  relative to  $m_1$ .

The gravitational parameter is defined as

$$\mu = Gm_{Earth} \quad (2.4)$$

where  $G$  is the *Universal Gravitational Constant* ( $6.673 \times 10^{-11} \text{ m}^3.\text{kg}^{-2}.\text{s}$ ) and  $m_{Earth}$  is the mass of the Earth ( $5.976 \times 10^{24} \text{ kg}$ ). In addition, making the assumption that  $m_1$  is very much larger than  $m_2$  then the two-body relative equation of motion may be written as

$$\ddot{\mathbf{r}} + \mu \frac{\mathbf{r}}{r^3} = 0 \quad (2.5)$$

To propagate the orbit described by **Equation 2.5** a numerical integrator, such as Runge-Kutta to the fourth order<sup>81</sup>, may be applied.

### 2.2.2 The Circular Orbit

Using a numerical integrator, the equations of motion of the spacecraft may be easily solved. However, this is an initial value problem which requires initial conditions. The following initial conditions are applied. The initial velocity  $v_o$  of the spacecraft is defined using

$$v_o = \sqrt{\frac{\mu}{r_o}} \quad (2.6)$$

where the initial radius of the spacecraft,  $r_o$  is given by

$$r_o = r_{Earth} + h_{Vehicle} \quad (2.7)$$

The initial altitude of the spacecraft,  $h_{Vehicle}$  is defined as 300 km and  $r_{Earth}$  is defined as 6371 km at the equator. The integration proceeds with

$$x_o = r_o \quad (2.8)$$

$$\dot{y}_o = v_o \quad (2.9)$$

Using these initial conditions in conjunction with the Runge-Kutta 4<sup>th</sup> order integrator, the orbit shown in **Figure 2.2** results. As can be seen, the orbit is of constant altitude and results in an orbit period of 86 minutes.

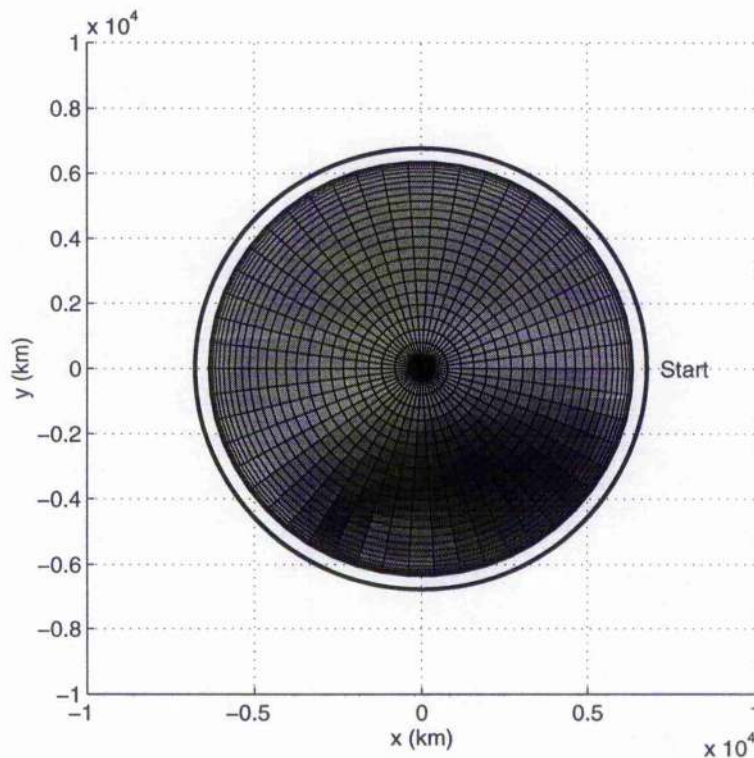


**Figure 2.2:** Circular Orbit.

### 2.2.3 The Elliptical Orbit

The motion of the spacecraft may be easily expanded to include elliptical orbits. The elliptical case differs from that of the circular case in one aspect only, the initial velocity  $v_o$ . Defining the shape of the orbit using the apogee altitude,  $h_a$ , and perigee altitude,  $h_p$ , the semi-major axis of the ellipse may then be calculated from

$$a = r_{Earth} + \frac{1}{2}(h_a + h_p) \quad (2.10)$$

Using a perigee altitude identical to that of the circular case and defining the apogee altitude as 2500 km yields a semi-major axis of 7771 km. Thus the initial velocity of the spacecraft may be calculated using

$$v_o = \sqrt{\frac{\mu}{r_o} \left( \frac{1+e}{1-e} \right)} \quad (2.11)$$

where  $e$  is the *eccentricity* of the orbit, defined from the semi-major axis of the ellipse using

$$e = 1 - \frac{r_o}{a} \quad (2.12)$$

Integrating the equations of motion in conjunction with these initial conditions results in the orbit shown in **Figure 2.3**. The orbit forms the ellipse, with the altitude varying as a function of time. The orbit period of 113 minutes for this case is longer than the circular case. Thus the relative motion of the two spacecraft, one in the circular orbit, the second in an ellipse can be rather complex. This relative motion is shown in **Figure 2.4**.

### 2.3 The Equations of Relative Motion

Consider a spacecraft orbiting the Earth in a circular orbit. If this spacecraft is assumed to be a target with a separate chase vehicle attempting to rendezvous, then an appropriate co-ordinate frame must be chosen. Although the two-body problem made use of an inertially fixed Earth centred co-ordinate frame, this frame of reference is not adequate to describe the relative motion. Therefore, a rotating co-ordinate frame attached to the target vehicle must be used.

#### 2.3.1 The Equations of Relative Motion

The use of a rotating co-ordinate frame, centred on the target spacecraft, as shown in **Figure 2.5**, allows the derivation of a set of equations of relative motion. Examining the position vectors of the target vehicle  $\mathbf{r}_t$ , and the chase vehicle  $\mathbf{r}_c$  in Earth-centred co-ordinates allows the formulation of the equation

$$\mathbf{r}_c = \mathbf{r}_t + \mathbf{r} \quad (2.13)$$

where  $\mathbf{r}$  is the position vector of the chase vehicle relative to the target spacecraft.

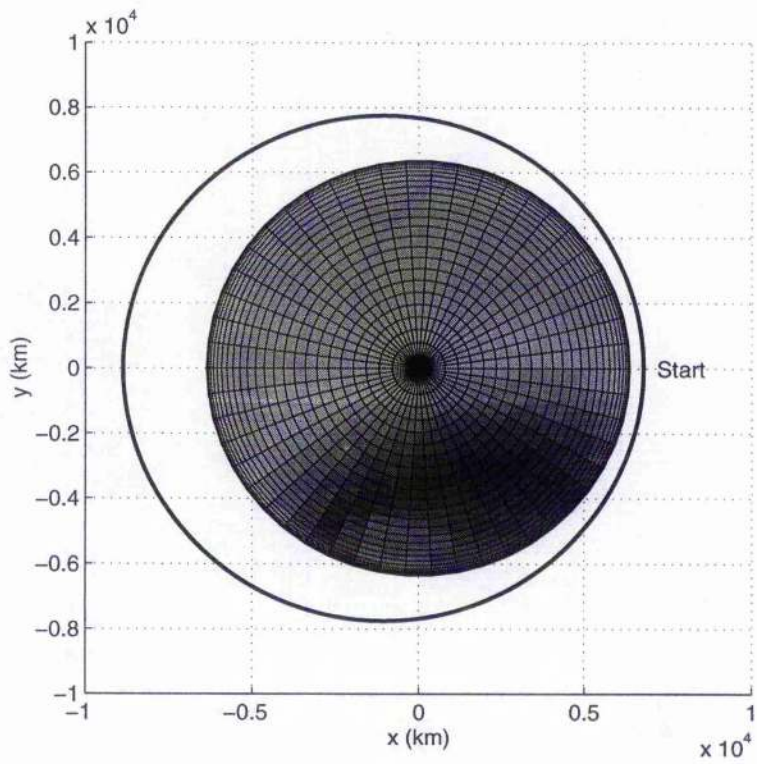


**Figure 2.3:** Elliptical Orbit.

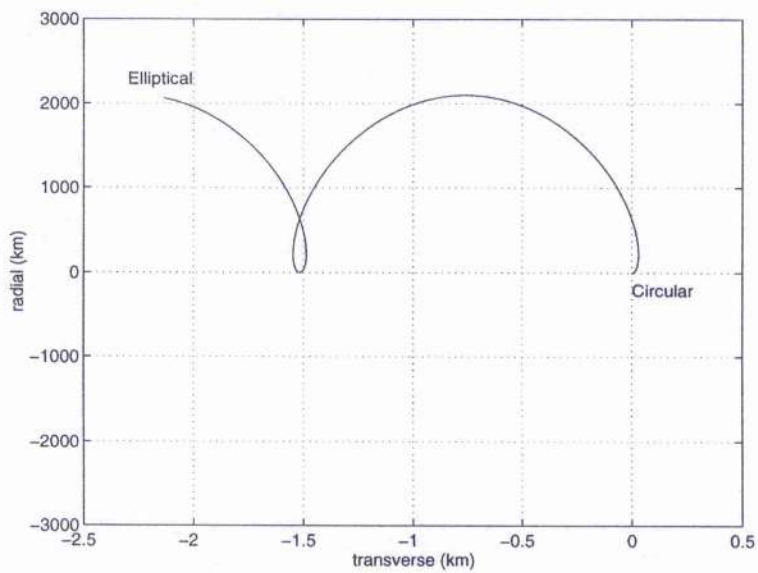


**Figure 2.4:** Relative Motion.

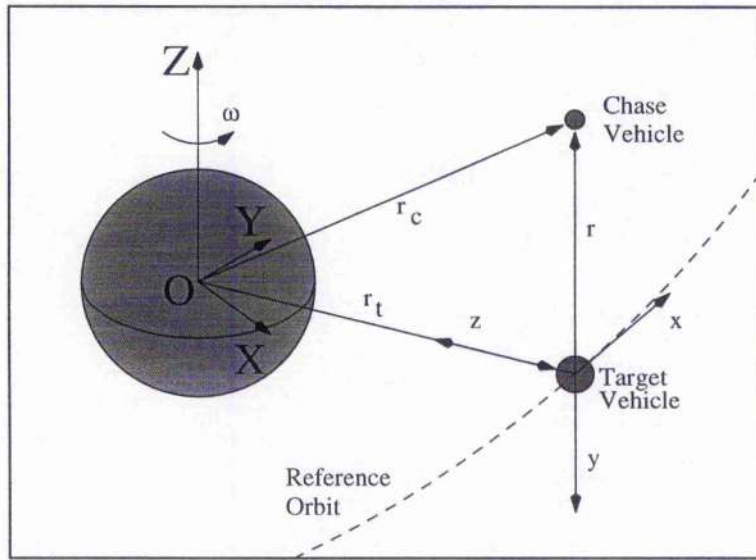


Figure 2.5: Rotating Co-ordinate Frame.

Considering the vector  $\mathbf{r}$ , if the target vehicle is defined as the origin of a rotating co-ordinate frame, then differentiating  $\mathbf{r}$  with respect to the Earth-centred inertial co-ordinate frame results in

$$\frac{d}{dt} \mathbf{r} = \frac{\partial}{\partial t} \mathbf{r} + \boldsymbol{\omega} \times \mathbf{r} \quad (2.14)$$

where  $\partial$  indicates a differentiation in the rotating frame of reference and  $\boldsymbol{\omega}$  is the orbital angular velocity of the rotating frame. Further differentiation gives the relative acceleration

$$\frac{d^2}{dt^2} \mathbf{r} = \frac{\partial^2}{\partial t^2} \mathbf{r} + 2(\boldsymbol{\omega} \times \dot{\mathbf{r}}) + \dot{\boldsymbol{\omega}} \times \mathbf{r} + \boldsymbol{\omega} \times (\boldsymbol{\omega} \times \mathbf{r}) \quad (2.15)$$

If **Equation 2.15** is used to with **Equation 2.13**, the acceleration of the chase vehicle, may be obtained as

$$\ddot{\mathbf{r}}_c = \ddot{\mathbf{r}}_t + \ddot{\mathbf{r}} + 2(\boldsymbol{\omega} \times \dot{\mathbf{r}}) + \dot{\boldsymbol{\omega}} \times \mathbf{r} + \boldsymbol{\omega} \times (\boldsymbol{\omega} \times \mathbf{r}) \quad (2.16)$$

If the relative motion of the chase is to be described in target spacecraft centred Cartesian co-ordinates, then the relative position vector  $\mathbf{r}$  may be expressed as

$$\mathbf{r} = x\mathbf{i} + y\mathbf{j} + z\mathbf{k} \quad (2.17)$$

and the Earth-centred position vector of the target spacecraft becomes

$$\mathbf{r}_t = -r_t \mathbf{k} \quad (2.18)$$

Thus, substituting **Equations 2.17** and **2.18** into **Equation 2.13**, the position vector of the chase vehicle may be expressed as

$$\mathbf{r}_c = x\mathbf{i} + y\mathbf{j} + (z - r_t)\mathbf{k} \quad (2.19)$$

Consider now the acceleration due to gravity,  $\mathbf{g}_t$ , acting on the target spacecraft

$$\ddot{\mathbf{r}}_t = \mathbf{g}_t \quad (2.20)$$

and also for the chase vehicle

$$\ddot{\mathbf{r}}_c = \mathbf{g}_c + \mathbf{A} \quad (2.21)$$

where  $\mathbf{A}$  represents the control acceleration applied to the spacecraft and  $\mathbf{g}_c$  is the acceleration due to gravity acting on the chase vehicle. Using direction cosines  $\mathbf{g}_c$  may be expressed as

$$\mathbf{g}_c = \left( -|\mathbf{g}_c| \frac{x}{r_c} \right) \mathbf{i} + \left( -|\mathbf{g}_c| \frac{y}{r_c} \right) \mathbf{j} + \left( |\mathbf{g}_c| \frac{z - r_t}{r_c} \right) \mathbf{k} \quad (2.22)$$

Finally **Equation 2.16** may be resolved into  $x$ ,  $y$  and  $z$  components by defining the angular velocity vector as

$$\boldsymbol{\omega} = \omega \mathbf{j} \quad (2.23)$$

Performing the necessary operations, results the series of differential equations

$$\ddot{x} = -g_c \frac{x}{r_c} + A_x + 2\omega \dot{z} + \dot{\omega} z + \omega^2 x \quad (2.24.a)$$

$$\ddot{y} = -g_c \frac{y}{r_c} + A_y \quad (2.24.b)$$

$$\ddot{z} = +g_c \frac{z-r_t}{r_c} + A_z - g_t - 2\omega\dot{x} - \dot{\omega}x + \omega^2 z \quad (2.24.c)$$

These equations represent the non-linear equations of relative motion. Typically, these equations are solved using a numerical integration method. However, the equations are often linearised to provide closed form analytic solutions.

### 2.3.2 The Clohessy-Wiltshire Equations of Motion

The Clohessy-Wiltshire<sup>82</sup> equations represent a linearised model of the non-linear equations of relative motion. The equations may be linearised on the assumption that the orbital radius of the target spacecraft is very much larger than the distance from the target spacecraft to the chase spacecraft, or

$$|r_t| \gg |r| \quad (2.25)$$

Therefore, the equations may be linearised using the following relations

$$r = \left[ x^2 + y^2 + (z+r_t)^2 \right]^{1/2} \approx r_t \left( 1 + \frac{z}{r_t} \right) \quad (2.26.a)$$

$$g = \frac{g_t r_t^2}{r^2} \approx g_t \left( 1 - \frac{2z}{r_t} \right) \quad (2.26.b)$$

$$-g \frac{x}{r} \approx -g_t \frac{x}{r_t} \quad (2.26.c)$$

$$-g \frac{y}{r} \approx -g_t \frac{y}{r_t} \quad (2.26.d)$$

$$-g \left( \frac{z+r_t}{r} \right) \approx -g_t \left( 1 - \frac{2z}{r_t} \right) \quad (2.26.e)$$

Using **Equations 2.26**, **Equations 2.24** may linearised to give

$$\ddot{x} = -g \frac{x}{r} + A_x + 2\omega\dot{z} + \dot{\omega}z + \omega^2 x \quad (2.27.a)$$

$$\ddot{y} = -g \frac{y}{r} + A_y \quad (2.27.b)$$

$$\ddot{z} = +g \left( 1 + \frac{2z}{r} \right) + A_z - g - 2\omega\dot{x} - \dot{\omega}x + \omega^2 z \quad (2.27.c)$$

**Equations 2.27** correspond to the linearised equations of relative motion. However, the linearised equations may be further simplified by considering the unforced case where the control accelerations are zero

$$A_x = A_y = A_z = 0 \quad (2.28)$$

In addition, if the target spacecraft is in a circular orbit, then  $\omega$  may be written as

$$\omega = \sqrt{\frac{g}{r}} \quad (2.29)$$

where  $\dot{\omega}$  is now zero. Therefore **Equations 2.27** may be rewritten to produce the commonly encountered Clohessy-Wiltshire equations of motion

$$\ddot{x} - 2\omega\dot{z} = 0 \quad (2.30.a)$$

$$\ddot{y} + \omega^2 y = 0 \quad (2.30.b)$$

$$\ddot{z} - 3\omega^2 z + 2\omega\dot{x} = 0 \quad (2.30.c)$$

The Clohessy-Wiltshire equations of relative motion have been extensively applied to rendezvous and docking problems. Again, these equations may be numerically integrated to determine the relative motion of the chase vehicle. However, as will be seen, closed form solutions are also available. The following two case studies examine typical relative motion characteristics. Then, in the following sections an orbit transfer scheme shall be examined. Therefore the two case studies may be considered as reference trajectories for later use.

### 2.3.3 Case I: 70 m Up-range

The chase vehicle will be located 70 m from the target spacecraft in the  $x$ -direction. Therefore, the initial relative position vector  $\mathbf{r}$  is defined as (70, 0, 0) and the chase vehicle is located in an identical circular orbit to that of the target vehicle. Therefore, as shown in

**Figure 2.6**, there is no relative motion of the chase spacecraft and the target spacecraft as they co-orbit the Earth. If the two spacecraft are to rendezvous, active manoeuvring by the chase vehicle will clearly be required.

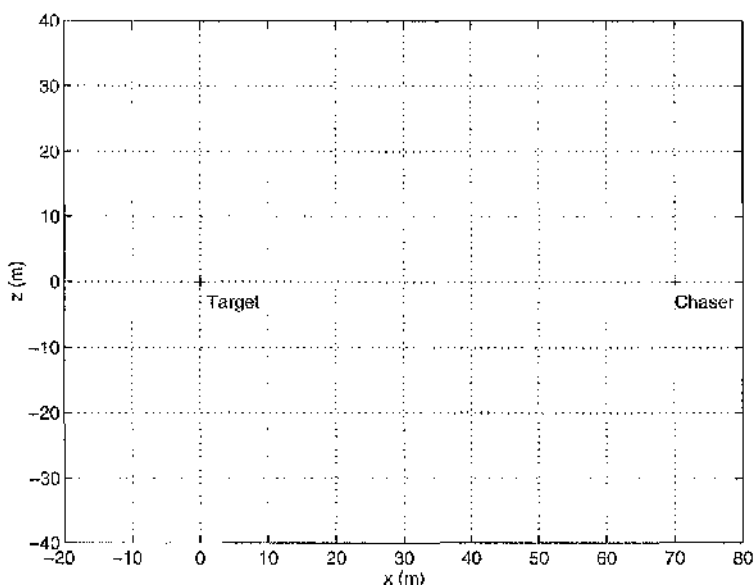


**Figure 2.6:** Case I: 70 m Up-range.

### 2.3.4 Case II: (-100,50,-50)

The second case study examines a more interesting trajectory where the chase vehicle is offset from the target in all three axes. From the initial point (-100,50,-50) the chase vehicle proceeds to drift away from the target spacecraft. Examining **Figure 2.7**, the motion displays a periodic nature with the motion over two full orbits clear. This, results in the chase vehicle being located over 3 km downrange from the target spacecraft after 167 minutes. These cases highlight the need for active manoeuvring of the chase vehicle to ensure successful rendezvous with the target vehicle.

## 2.4 Two Impulse Rendezvous and the State Transition Matrix

The rendezvous of the chase vehicle to the target vehicle will require a control input to the chase vehicle. The most efficient transfer is the two-impulse transfer. The two-impulse transfer involves the chase vehicle propulsion system performing a controlled impulse which sets the vehicle on a trajectory which intersects the target vehicle. On arrival at the target vehicle, the propulsion system will again perform an impulse to bring the chase vehicle to rest. The calculation of the impulse magnitude and direction, or more commonly the two-impulse rendezvous problem<sup>83</sup> is based on a solution to the linearised equations of motion.

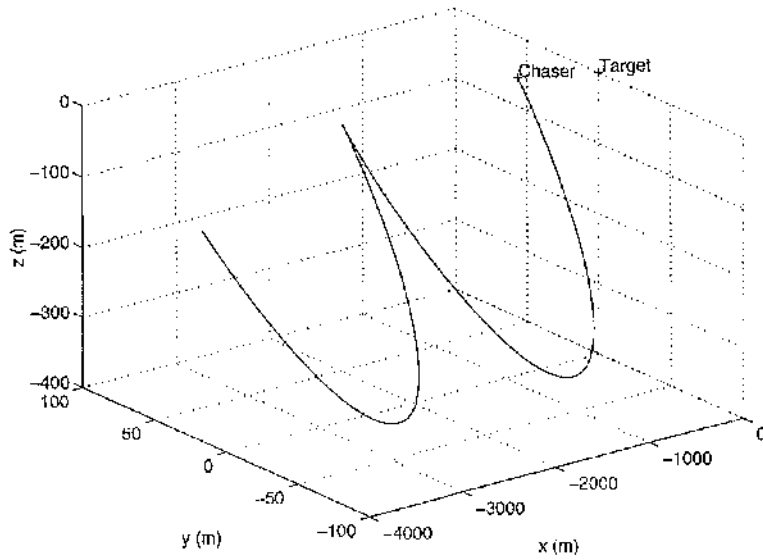


Figure 2.7: Case II: (-100,50,-50).

Examining, **Equations 2.30**, it is apparent that the  $x$  and  $z$  components are closely coupled. However, the  $y$  component is de-coupled and may be solved by expressing the equation as the solution of a simple harmonic oscillator

$$y(t) = y_o \cos(\omega t) + \frac{\dot{y}_o}{\omega} \sin(\omega t) \quad (2.31.a)$$

which may be differentiated to yield

$$\dot{y}(t) = -y_o \omega \sin(\omega t) + \dot{y}_o \cos(\omega t) \quad (2.31.b)$$

Thus, the  $y$ -position and velocity components may be calculated from the initial position and velocity. The  $x$  and  $z$  terms are closely coupled, however a solution exists in the form of a simple harmonic oscillator, but with the addition of a forcing term

$$x(t) = -2 \frac{\dot{z}_o}{\omega} \cos(\omega t) + \left( 4 \frac{\dot{x}_o}{\omega} - 6z_o \right) \sin(\omega t) - (3\dot{x}_o - 6\omega z_o)t + x_o + \frac{2\dot{z}_o}{\omega} \quad (2.31.c)$$

which is differentiated to give

$$\dot{x}(t) = 2\dot{z}_o \sin(\omega t) + (4\dot{x}_o - 6\omega z_o) \cos(\omega t) - (3\dot{x}_o - 6\omega z_o) \quad (2.31.d)$$

In addition, the  $z$ -component is given by

$$z(t) = 4z_o - 2\frac{\dot{x}_o}{\omega} + \frac{\dot{z}_o}{\omega} \sin(\omega t) - \left(2\frac{\dot{x}_o}{\omega} - 3z_o\right) \cos(\omega t) \quad (2.31.e)$$

and again differentiating yields

$$\dot{z}(t) = z_o \cos(\omega t) + (3\omega z_o - 2\dot{x}_o) \sin(\omega t) \quad (2.31.f)$$

Now, the trajectory of the chase vehicle relative to the target vehicle may be described by the above equations. Re-arranging **Equations 2.31**, the motion of the chase may be described using the *State Transition Matrix*  $\Phi$  where state of the chase vehicle at some time  $t$  may be described by

$$\mathbf{s}(t) = \Phi \mathbf{s}_o \quad (2.32)$$

where the state vector  $\mathbf{x}$  is defined as

$$\mathbf{s} = \{\mathbf{x}, \dot{\mathbf{x}}\}^T \quad (2.33.a)$$

where

$$\mathbf{x} = \{x, y, z\} \quad (2.33.b)$$

and

$$\dot{\mathbf{x}} = \{\dot{x}, \dot{y}, \dot{z}\} \quad (2.33.c)$$

and the state transition matrix  $\Phi$  is given by

$$\Phi = \begin{pmatrix} 1 & 0 & 6(\omega t - \sin(\omega t)) & \frac{4}{\omega} \sin(\omega t) - 3t & 0 & \frac{2}{\omega}(1 - \cos(\omega t)) \\ 0 & \cos(\omega t) & 0 & 0 & \frac{1}{\omega} \sin(\omega t) & 0 \\ 0 & 0 & 4 - 3\cos(\omega t) & \frac{2}{\omega}(\cos(\omega t) - 1) & 0 & \frac{1}{\omega} \sin(\omega t) \\ 0 & 0 & 6\omega(1 - \cos(\omega t)) & 4\cos(\omega t) - 3 & 0 & 2\sin(\omega t) \\ 0 & -\omega \sin(\omega t) & 0 & 0 & \cos(\omega t) & 0 \\ 0 & 0 & 3\omega \sin(\omega t) & -2\sin(\omega t) & 0 & \cos(\omega t) \end{pmatrix} \quad (2.34)$$

For rendezvous trajectories the initial and final positions may be used to calculate the required initial velocity and the final velocity at the target. Thus the magnitude of both the initial and final impulses may be calculated. The sum of both impulse magnitudes measured in change of velocity, or  $\Delta v$  may be used as a measure of the cost of the transfer. Multiple solutions do exist for the transfer corresponding to an infinite number of possible trajectories. Therefore, to obtain an optimal solution, the minimum  $\Delta v$  transfer may be calculated.

## 2.5 Velocity-Time Optimisation

The optimisation method for the transfer is derived from the state transition matrix. This requires a direct method of calculation of the total  $\Delta v$  which may be obtained by arranging the state transition matrix in four quadrants

$$\Phi = \begin{Bmatrix} \mathbf{A} & \mathbf{B} \\ \mathbf{C} & \mathbf{D} \end{Bmatrix} \quad (2.35)$$

where  $\mathbf{A}$ ,  $\mathbf{B}$ ,  $\mathbf{C}$  and  $\mathbf{D}$  are given by

$$\mathbf{A} = \begin{Bmatrix} 1 & 0 & 6(\omega t - \sin(\omega t)) \\ 0 & \cos(\omega t) & 0 \\ 0 & 0 & 4 - 3\cos(\omega t) \end{Bmatrix} \quad (2.36.a)$$

$$\mathbf{B} = \begin{Bmatrix} \frac{4}{\omega} \sin(\omega t) - 3t & 0 & \frac{2}{\omega} (1 - \cos(\omega t)) \\ 0 & \frac{1}{\omega} \sin(\omega t) & 0 \\ \frac{2}{\omega} (\cos(\omega t) - 1) & 0 & \frac{1}{\omega} \sin(\omega t) \end{Bmatrix} \quad (2.36.b)$$

$$\mathbf{C} = \begin{Bmatrix} 0 & 0 & 6\omega(1 - \cos(\omega t)) \\ 0 & -\omega \sin(\omega t) & 0 \\ 0 & 0 & 3\omega \sin(\omega t) \end{Bmatrix} \quad (2.36.c)$$

$$\mathbf{D} = \begin{Bmatrix} 4\cos(\omega t) - 3 & 0 & 2\sin(\omega t) \\ 0 & \cos(\omega t) & 0 \\ -2\sin(\omega t) & 0 & \cos(\omega t) \end{Bmatrix} \quad (2.36.d)$$

Using the four quadrants, it becomes possible to re-write the state-transition matrix in two sections corresponding to some final position and velocity

$$\mathbf{x}_f = \mathbf{A}\mathbf{x}_o + \mathbf{B}\dot{\mathbf{x}}_o \quad (2.37.a)$$

$$\dot{\mathbf{x}}_f = \mathbf{C}\mathbf{x}_o + \mathbf{D}\dot{\mathbf{x}}_o \quad (2.37.b)$$

at some final time  $t_f$ . To calculate the required initial velocity to intercept the target, **Equation 2.37.a** may be re-arranged to give

$$\dot{\mathbf{x}}_o = \mathbf{B}^{-1}(\mathbf{x}_f - \mathbf{A}\mathbf{x}_o) \quad (2.38)$$

where the inverse of  $\mathbf{B}$  is given by

$$\mathbf{B}^{-1} = \left\{ \begin{array}{cc} \frac{-\omega \cos(\omega t/2)}{3\omega t \cos(\omega t/2) - 8 \sin(\omega t/2)} & 0 \\ 0 & \frac{\omega}{\sin(\omega t)} \end{array} \right\} \left\{ \begin{array}{cc} \frac{2\omega \sin(\omega t/2)}{3\omega t \cos(\omega t/2) - 8 \sin(\omega t/2)} & 0 \\ \frac{\omega(3\omega t - 4 \sin(\omega t/2))}{2 \sin(\omega t/2)(3\omega t \cos(\omega t/2) - 8 \sin(\omega t/2))} & 0 \end{array} \right\} \quad (2.39)$$

Therefore, the final velocity at the target may be calculated directly from the initial and final positions by substituting **Equation 2.38** into **Equation 2.37.b** to give

$$\dot{\mathbf{x}}_f = \mathbf{C}\mathbf{x}_o + \mathbf{D}[\mathbf{B}^{-1}(\mathbf{x}_f - \mathbf{A}\mathbf{x}_o)] \quad (2.40)$$

The impulse magnitudes may now be calculated. If the chase vehicle is starting from, and finishing at rest relative to the target vehicle, then the  $\Delta v$  is given merely by the initial and final velocities

$$\Delta v_o = |\dot{\mathbf{x}}_o| \quad (2.41.a)$$

and

$$\Delta v_f = |\dot{\mathbf{x}}_f| \quad (2.41.b)$$

where the total  $\Delta v$  of the transfer is given by

$$\Delta v = \Delta v_o + \Delta v_f \quad (2.42)$$

Therefore, knowing the vectors,  $\mathbf{x}_o$  and  $\mathbf{x}_f$  the total  $\Delta v$  of the manoeuvre may be calculated as a function of transfer time  $t_f$ . Therefore, using a simple functional minimisation algorithm, the transfer time may be optimised for a minimum  $\Delta v$ . However, this cost function contains many minima, therefore care must be taken when choosing a minimisation algorithm.

## 2.6 Point to Point Transfer

The optimisation of the two-impulse transfer results in a minimum  $\Delta v$  value. However, the  $\Delta v$  and the associated trajectory will vary radically for a small change in the time of transfer. The following three cases aim to provide solutions to a variety of problems to highlight the benefits and drawbacks of the trajectory optimisation using the state transition matrix.

### 2.6.1 Case I: 70 m Up-range to Target Vehicle

Examining an identical case to that of **Section 2.3.3**, the objective of this transfer is to move the chase vehicle from 70 m up-range to rendezvous with target vehicle. Thus, using the state transition matrix in conjunction with the initial and final position vectors

$$\mathbf{x}_o = \{70, 0, 0\}^T \quad \mathbf{x}_f = \{0, 0, 0\}^T \quad (2.43)$$

a minimisation algorithm may be used to calculate the optimal rendezvous trajectory.

Examining **Figure 2.8.a**, the values of  $\Delta v$  are plotted against time  $t_f$ . The plot displays the periodic nature of the function. As can be seen the function does not have a single minimum, thus problems may be encountered with minimisation algorithms such as Newton's or Fibonacci's method. The minimisation was carried out in this case using a sorting algorithm to choose the minimum value of a sampled data set. i.e. the function was sampled every second for  $2 \times 10^4$  s to produce a data set. The minimum value was then chosen from that data set. This technique is computationally intensive, however since the analysis is carried out only once, the loss in efficiency is acceptable.

Therefore, performing the analysis for these conditions results in an optimal time of transfer time of

$$t = 16259 \text{ s} \quad (2.44)$$

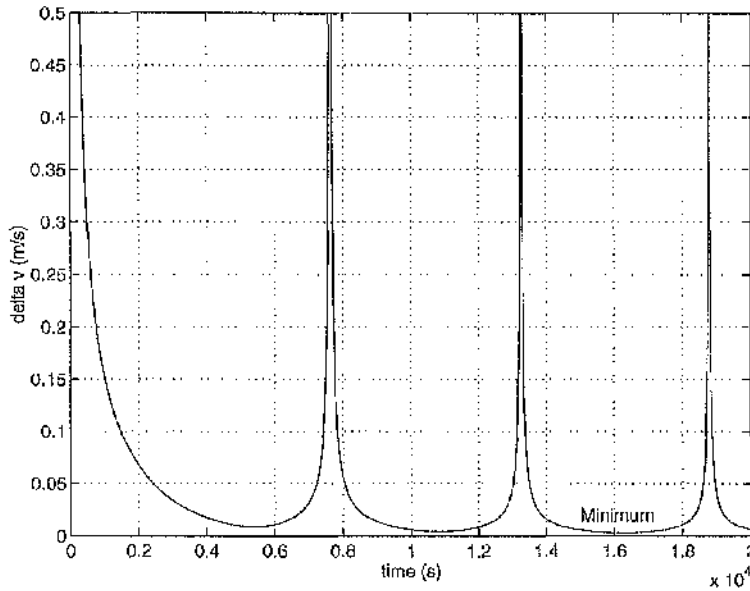


Figure 2.8.a: Case I: (70,0,0) to Target Vehicle: Time /  $\Delta v$  Cost Function.

with an initial and final velocity vector of

$$\dot{\mathbf{x}}_o = \dot{\mathbf{x}}_f = \begin{pmatrix} 1.433 \times 10^{-3} \\ 0 \\ 0 \end{pmatrix} \quad (2.45)$$

giving an optimised  $\Delta v$  of

$$\Delta v = 2.866 \times 10^{-3} \text{ m.s}^{-1} \quad (2.46)$$

where

$$\Delta v_o = \Delta v_f = 1.433 \times 10^{-3} \text{ m.s}^{-1} \quad (2.47)$$

Using these parameters with the Clohessy-Wiltshire equations results in the trajectory shown in **Figure 2.8.b**. It is apparent that the first impulse results in the chase vehicle drifting backwards in its orbit until such a time as it arrives at the target vehicle whereupon a second impulse is used to bring the chase vehicle to rest. The transfer time also corresponds to approximately three orbit periods with the drift per orbit also seen.

The transfer modelled here corresponds to the problem of orbit phasing. Orbit phasing is the movement of vehicle along its own orbit. As can be seen in **Figure 2.8.a**, the minimum  $\Delta v$  value per orbit cycle is decreasing as the time of transfer increases. If the optimisation

were carried out over a longer period of time then the minimum  $\Delta v$  would always occur in the longest possible orbit period.

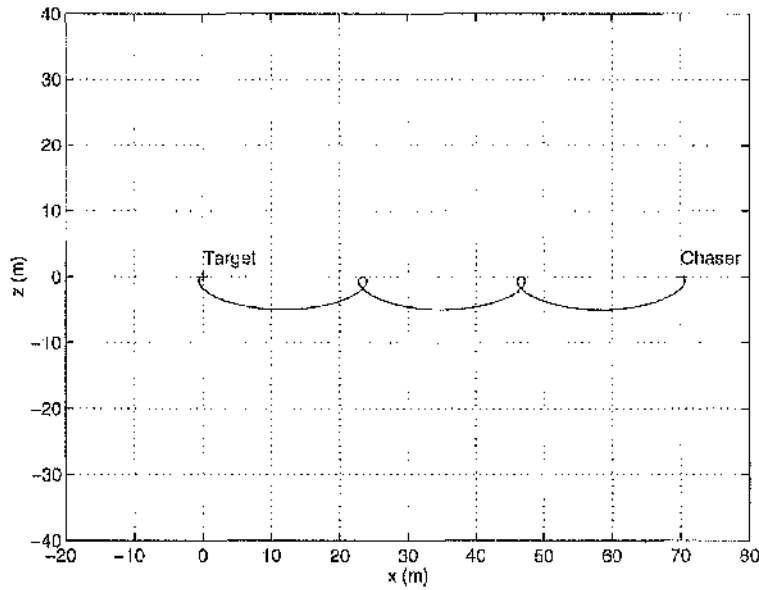


Figure 2.8.b: Case I: (70,0,0) to Target Vehicle: Chase Vehicle Trajectory.

### 2.6.2 Case II: (-100,50,-50) to Target Vehicle

Examining an identical case to that of **Section 2.3.4**, the objective of this transfer is to move the chase vehicle from a displaced position along all three axes to the target vehicle. Therefore, the initial and final position vectors are given as

$$\mathbf{x}_o = \{-100, 50, -50\}^T \qquad \mathbf{x}_f = \{0, 0, 0\}^T \qquad (2.48)$$

The optimisation of the transfer produces the cost function plot shown in **Figure 2.9.a**. When comparing this plot against that of the previous case study, it is observed that the curve is more complex. However, using the same minimisation algorithm the minimum value of  $\Delta v$  is obtained for a time of

$$t = 3592 \text{ s} \qquad (2.49)$$

Using this value in conjunction with the initial and final position vectors, the initial and final velocity vectors are obtained as

$$\dot{\mathbf{x}}_o = \begin{pmatrix} -0.112 \\ -3.566 \times 10^{-2} \\ -2.343 \times 10^{-2} \end{pmatrix} \quad \dot{\mathbf{x}}_f = \begin{pmatrix} 3.414 \times 10^{-3} \\ 1.366 \times 10^{-2} \\ -5.579 \times 10^{-2} \end{pmatrix} \quad (2.50)$$

thus producing an optimal  $\Delta v$  of

$$\Delta v = 0.178 \text{ m.s}^{-1} \quad (2.51)$$

where

$$\Delta v_o = 0.120 \text{ m.s}^{-1} \quad \Delta v_f = 5.754 \times 10^{-2} \text{ m.s}^{-1} \quad (2.52)$$

Propagating the orbit using these values results in the trajectory shown in **Figure 2.9.b**. The trajectory followed by the vehicle reflects the complexity of the problem with the chase vehicle looping over and above the target vehicle before the final orbit matching impulse. The final transfer time is very important to the path chosen by the optimisation algorithm. To demonstrate the variety of the possible paths, **Figure 2.9.c** displays three different trajectories for small variations in the final  $\Delta v$ . This may have an application in manoeuvring around obstacles, however guaranteeing a safe path may only be achieved using intermediate waypoints. The use of waypoints rather than direct transfers to the target vehicle is demonstrated in the following section.

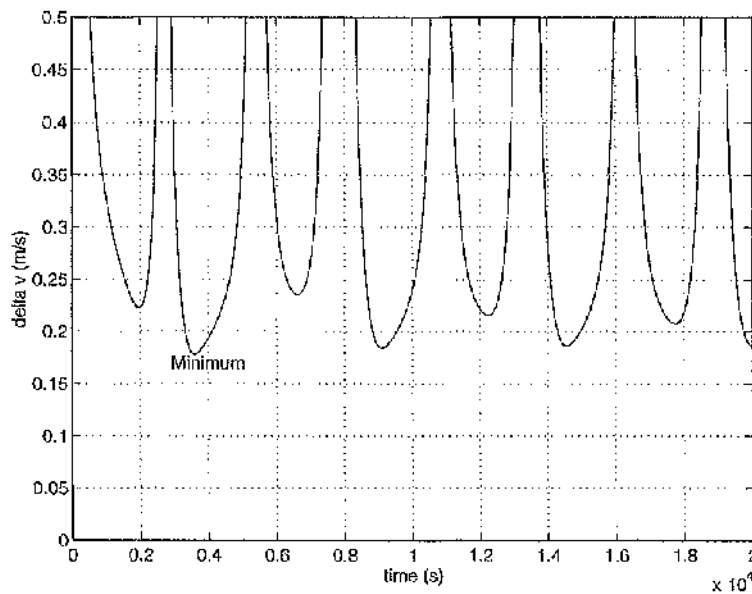


**Figure 2.9.a:** Case II: (-100,50,-50) to Target Vehicle: Time /  $\Delta v$  Cost Function.

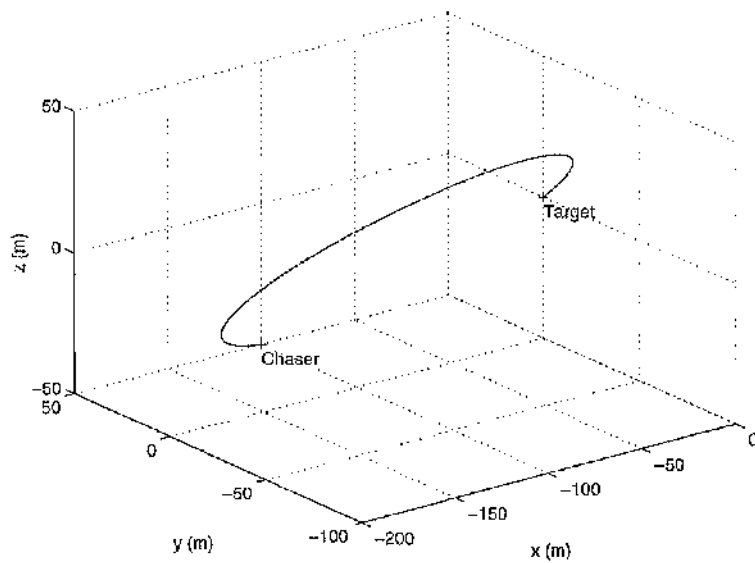


Figure 2.9.b: Case II: (-100,50,-50) to Target Vehicle: Chase Vehicle Trajectory.

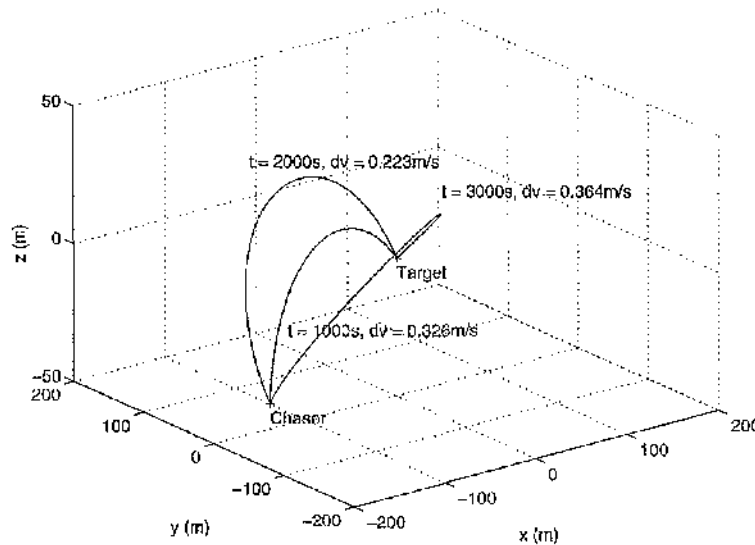


Figure 2.9.c: Case II: (-100,50,-50) to Target Vehicle: Trajectories Variations with Time of Transfer.

### 2.6.3 Case III: (-100,50,-50) to (100,-100,100)

The possibility of using the state transition matrix to manoeuvre the chase vehicle between two points would allow these points to be linked in to a series of manoeuvres to shape the path followed by the chase vehicle to the goal location or target vehicle. However, the scope of this example is to demonstrate the possibility of using the state transition matrix to transfer from a generic point  $A$  to point  $B$  relative to the target vehicle. Therefore, using the state transition matrix in conjunction with the initial and final positions

$$\mathbf{x}_o = \{-100, 50, -50\}^T \qquad \mathbf{x}_f = \{100, -100, 100\}^T \qquad (2.53)$$

produces the cost function plot shown in **Figure 2.10.a**. Again the function has a complex form, however the minimisation algorithm produces a minimum value of  $\Delta v$  for a transfer time of

$$t = 3440 \text{ s} \tag{2.54}$$

Using this value for transfer time, the following initial and final velocity vectors are obtained

$$\dot{\mathbf{x}}_o = \begin{pmatrix} -0.132 \\ 0.104 \\ -3.017 \times 10^{-2} \end{pmatrix} \quad \dot{\mathbf{x}}_f = \begin{pmatrix} 0.215 \\ 0.147 \\ -4.772 \times 10^{-2} \end{pmatrix} \tag{2.55}$$

with an optimised  $\Delta v$  of

$$\Delta v = 0.435 \text{ m.s}^{-1} \tag{2.56}$$

where

$$\Delta v_o = 0.170 \text{ m.s}^{-1} \quad \Delta v_f = 0.265 \text{ m.s}^{-1} \tag{2.57}$$

The trajectory which results from these parameters is shown in **Figure 2.10.b**. As can be seen, the trajectory successfully manoeuvres the chase vehicle between the two points. It

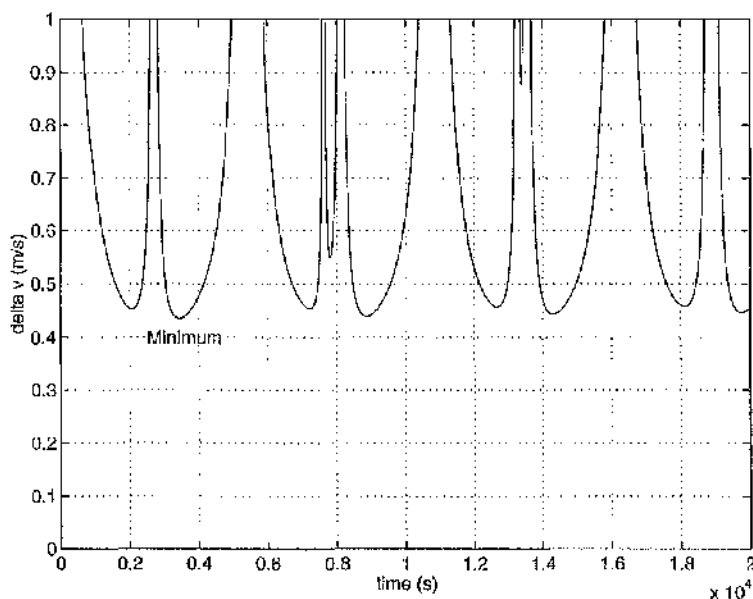


**Figure 2.10.a:** Case III: (-100,50,-50) to (100,-100,100): Time /  $\Delta v$  Cost Function.

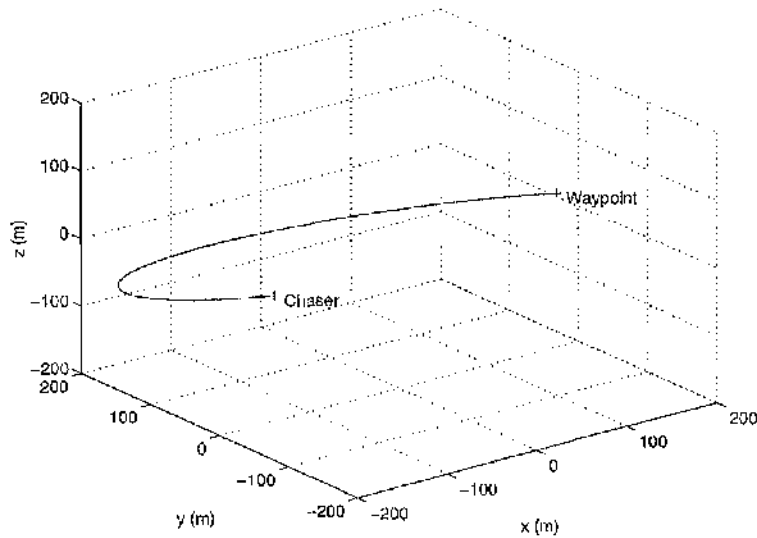


**Figure 2.10.b:** Case III: (-100,50,-50) to (100,-100,100). The Chase Vehicle Trajectory.

should be noted that the transfer time was lower than that of the previous case, even though the distance travelled was higher. However, the total  $\Delta v$  was correspondingly higher. This results demonstrates that, although the transfer is successfully optimised, the result from the state transition matrix and the dynamics resulting from the Clohessy-Wiltshire equations may not always produce the expected result.

## 2.7 Conclusions

The main conclusion to draw from the linearisation and optimisation of the Clohessy-Wiltshire equations is that the solution will provide the optimal datum value for a transfer between two points. However, there are drawbacks to the method. Principally, the flexibility of the two impulse transfer must be called into question when considering the possibility of obstacle avoidance. i.e. the optimisation of a transfer would be compromised if a mid-course correction was required.

The very nature of the linearised equations of motion will limit the types of transfer envisaged here. The linearisation of the equations and the assumption that the distance from the target to the centre of the Earth is very much larger than the distance to the chase vehicle results in the limitation of the method to transfers under  $10^3$  m. Therefore it may be stated that in conclusion, the state transition method provides an optimal solution to the  $\Delta v$  minimisation problem, and thus provides a datum against which other, more flexible methods, may be measured.

# Chapter Three: Potential Functions

## 3.1 Introduction

Having established in **Chapter 1** the requirements for a control methodology for on-orbit assembly it is now possible to define a set of specifications;

- The control method must be closed-loop, with particular attention paid to the smooth convergence of vehicles to the desired configuration.
- The complexity of the hardware, and software must be minimal. Current space qualified computer technology is not as advanced as terrestrial technology.
- The control methodology must be fully autonomous. There are large cost savings to be made by eliminating human operators from the control loop.
- The control methodology must be stable. With the current cost of placing hardware on orbit, the loss of hardware through control system action or inaction is unacceptable.

Therefore, with these specifications a robust, non-linear, low complexity control methodology is required. One such methodology is generated using *Lyapunov's Second Method*.

Lyapunov's second method is not new, having originally appeared in the Russian literature in 1892. It was not until 1907 that the a French translation appeared in Western literature. The method, although used extensively in Russian control problems, did not achieve widespread popularity in the West. Eventually translated into English in 1947, the method became more widespread culminating in the definitive papers by Kalman and Bertram<sup>84, 85</sup> in which the method was applied to a wide variety of control problems.

Although typically described as a method, Lyapunov's method as described by Kalman and Bertram is far from a rigorous mathematical technique. In fact, the method should be more properly defined as an approach to control problems. However, it should be

noted that Lyapunov's *theorem* may be formed as an explicit proof. Lyapunov originally described the objective of the technique as;

*'To answer questions of stability of differential equations, utilising the given form of the equations but without specific knowledge of the solutions.'*

Since Kalman and Bertram's paper of 1960, Lyapunov's method has been extensively applied to stability problems for both spacecraft and terrestrial control problems. The flexibility of the method is ideally suited to complex non-linear spacecraft control problems<sup>86, 87</sup>.

### 3.2 Lyapunov's Second Method and Potential Functions

The objective of Lyapunov's Second Method is to ensure the stability of a system of differential equations describing a dynamical system. In physical terms, the method has been described by Kalman & Bertram as the following reasoning;

*'If the rate of change  $dE(x)/dt$  of the energy  $E(x)$  of an isolated physical system is negative for every possible state  $x$ , except for a single equilibrium state  $x_e$ , then the energy will continually decrease until it finally assumes its minimum value  $E(x_e)$ .'*

This statement corresponds to the intuitive definition of all stability problems. i.e. any dissipative system perturbed from its equilibrium state will always return to it.

In mathematical terms, this may be expressed as;

*'A dynamical system is stable (in the sense that it returns to equilibrium after any perturbation) if and only if there exists a 'Lyapunov function,' i.e. some scalar function  $V(x)$  of the state with the properties:*

$$i) V(x) > 0, \dot{V}(x) < 0 \quad \text{when } x \neq x_e \quad (3.1)$$

*and*

$$ii) V(x) = \dot{V}(x) = 0 \quad \text{when } x = x_e \quad (3.2)$$

An extended form of the Lyapunov function, termed a potential function will be used in the subsequent analyses. It is this function that may be defined analytically and used to drive the state vector of a dynamical system to the desired goal. However, the mechanism which forces convergence is based on the rate of change of the potential function. Examining **Figure 3.1**, if the rate of change of the potential,  $\dot{V}(\mathbf{x})$  is negative, then the state vector will converge to the goal point at the global minimum of the potential function. However, if  $\dot{V}(\mathbf{x})$  is positive, then the state vector will diverge from the goal point. In this case control intervention is required to render  $\dot{V}(\mathbf{x})$  negative.

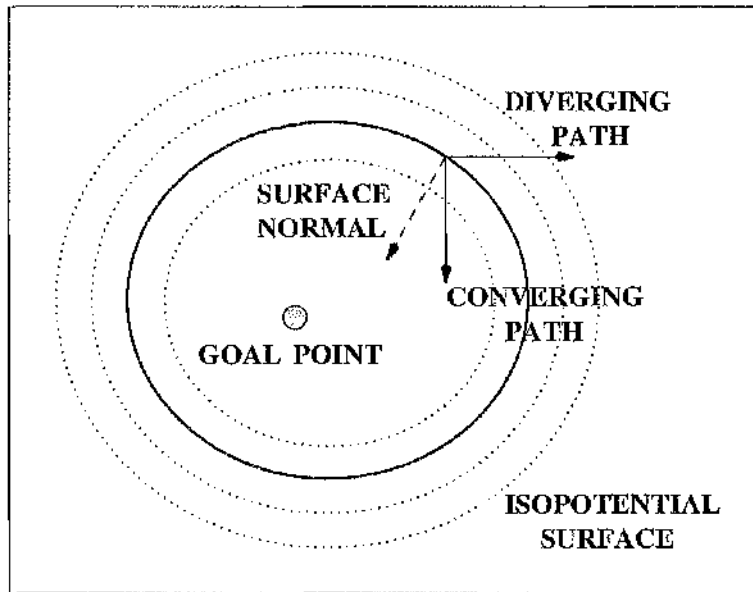


**Figure 3.1:** Potential Function Stability.

Therefore, it is possible to derive a methodology to force convergence of any system to a desired goal. Defining a potential function based on the state vector  $\mathbf{x}$ , which takes the form

$$V = f(\mathbf{x}) \tag{3.3}$$

differentiating the potential function with respect to time results in

$$\dot{V} = \nabla f \cdot \dot{\mathbf{x}} \tag{3.4}$$

Therefore, with an analytical definition of  $\dot{V}$ , it is possible to calculate the control inputs required to bring the dynamical system to the desired goal point. In the following sections, two methods of control are explored. The first is a continuous control method, the second is a discrete method. The continuous method ensures that the rate of change of potential is

continuously negative by implementing a control action at every time step. The discrete method differs in that control intervention is only implemented when the rate of change of the potential is zero or positive, thus allowing the system more freedom of action. The analysis and comparison of both methods is examined using two case studies. The first is a translation control problem, and the second an attitude control problem.

### 3.3 Translation Control

Consider now the problem of a single manoeuvring chase vehicle attempting to close to a target goal point relative to a circular reference orbit. This problem has been previously examined in **Section 2.6**. Rather than use the optimal two-impulse transfer, the discrete form of the potential function method shall be applied and compared to the optimal solution.

#### 3.3.1 Potential Function Definition

To guarantee that the vehicle will translate from its initial position to the goal point, control intervention is clearly required. Therefore, the problem requires a potential function based on the location of the chase vehicle and the goal point. Defining the position vector of the chase vehicle as  $\mathbf{r}$ , and the goal point as  $\mathbf{r}_{Goal}$  then a simple quadratic potential function may be defined of the form

$$V = \frac{\lambda}{2} (\mathbf{r} - \mathbf{r}_{Goal}) \cdot (\mathbf{r} - \mathbf{r}_{Goal}) \quad (3.5)$$

where  $\lambda$  is a scaling constant. Thus the function ensures that the potential  $V$  is positive for every position except at the solution, where  $(\mathbf{r} - \mathbf{r}_{Goal})$  vanishes.

In addition, to conform with the conventional definition of Lyapunov functions, the rate of change of potential  $\dot{V}$  must be negative definite along any trajectory except at the goal. Therefore, differentiating the potential function gives

$$\dot{V} = \lambda (\mathbf{r} - \mathbf{r}_{Goal}) \cdot \mathbf{v} \quad (3.6)$$

where  $\mathbf{v}$  is the velocity vector of the chase vehicle. Thus, to ensure that the chase vehicle converges to the goal point, the control method must ensure that the rate of change of potential is always negative definite.

#### 3.3.2 Example: Discrete Control

The discrete control method differs from the continuous case in that control intervention is required only if the rate of change of the potential is zero or positive. Returning to **Figure 3.1**, the internal normal of any isopotential surface will, in every case,

point to a lower potential. Therefore, the rate of change of the potential shall be guaranteed negative definite if the desired vehicle velocity vector is given by

$$\mathbf{v}_{Desired} = -\kappa \frac{\nabla V}{|\nabla V|} \quad \text{if} \quad \dot{V} \geq 0 \quad (3.7)$$

where  $\kappa$  is a constant and  $\nabla V/|\nabla V|$  is the unit vector normal to the isopotential surface. Substituting the gradient of the potential  $V$  in **Equation 3.7**, the desired vehicle velocity vector then becomes

$$\mathbf{v}_{Desired} = -\kappa \frac{(\mathbf{r} - \mathbf{r}_{Goal})}{|\mathbf{r} - \mathbf{r}_{Goal}|} \quad (3.8)$$

so that  $\dot{V}(\mathbf{x})$  is always rendered negative definite.

The constant  $\kappa$  in **Equation 3.8** may also be represented by a shaping function. The term is used to shape the magnitude of the velocity of the vehicle as the goal is approached. Therefore, a function which will scale the magnitude of the impulses as the potential decreases is given by

$$\kappa = v^* \{1 - \exp(-\beta V)\} \quad (3.9)$$

where  $v^*$  represents the maximum controlled velocity of the vehicle, in this case  $0.1 \text{ m.s}^{-1}$ , and  $\beta$  is a constant, typically defined as unity. Examining the case given in **Section 2.6.1**, using the initial positions given in **Equation 2.43.b**, the trajectory of the chase vehicle may be propagated to produce **Figure 3.2.a**. The intervention of the controller is clearly visible as the path of the vehicle is shaped with four course correcting impulses implemented by the chase vehicle. The behaviour of the potential function is plotted in **Figure 3.2.b** where the control impulses are clearly visible as is the smooth convergence as the potential reduces in an exponential manner to the goal. Examining **Figure 3.2.c**, the potential function is combined with the vehicle trajectory to show the descent of the vehicle down the potential well. This plot is useful in highlighting that control intervention will result in the vehicle following the internal normal of the isopotential surface.

The velocity profile is shown in **Figure 3.2.d**, and the maximum controlled velocity of  $0.1 \text{ m.s}^{-1}$  is clearly shown as the course corrections reset the velocity. The total  $\Delta v$  cost of the transfer is  $3.356 \times 10^{-3} \text{ m.s}^{-1}$ . When compared to the value of  $2.866 \times 10^{-3} \text{ m.s}^{-1}$  obtained from the two-impulse transfer, it is obvious that the transfer is less efficient. However, the

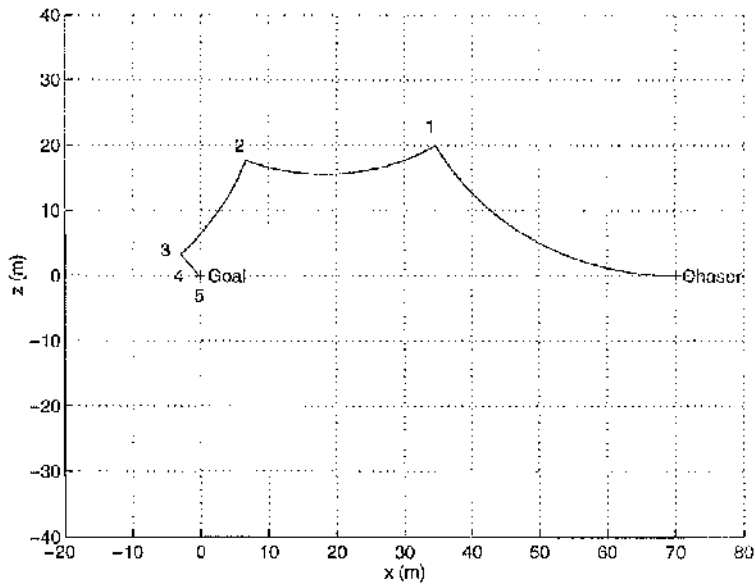


Figure 3.2.a: Discrete Control: Chase Vehicle Trajectory.

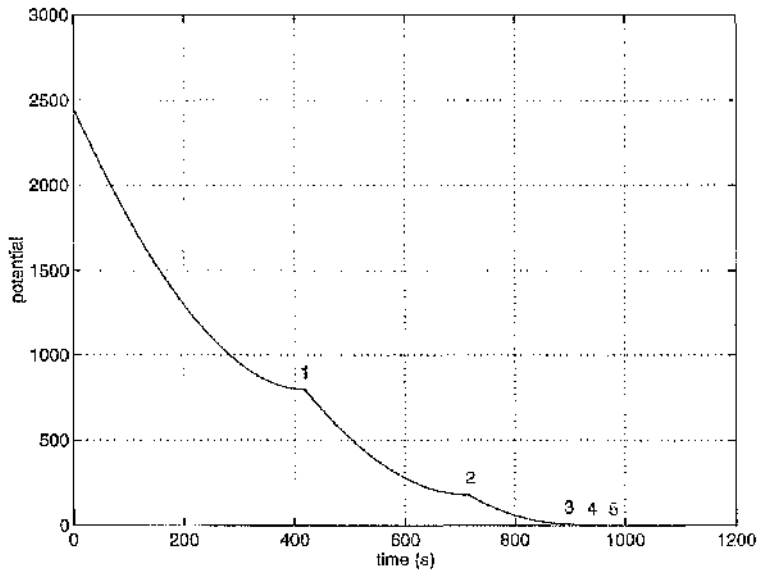


Figure 3.2.b: Discrete Control: Potential Function.

flexibility offered by the potential function method, especially when used in conjunction with a collision avoidance technique, outweighs the inefficiencies. It should be noted that currently, if the rate of change of potential is greater than or equal to zero, then control intervention is triggered. However, if the trigger was modified such that control intervention occurred when

$$\dot{V}(\mathbf{x}) \geq f(V) \tag{3.10}$$

then the point of control intervention may be varied throughout the convergence process. This capability allows path shaping such as minimal intervention at large distances from the goal

but as the vehicle nears the solution, control intervention increases. This provides a degree of control which will be crucial as the technique is expanded upon.

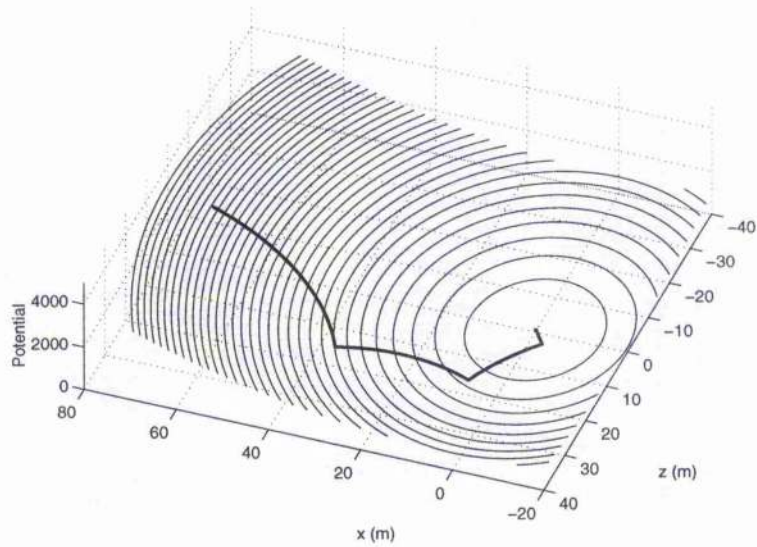


Figure 3.2.c: Discrete Control: Potential Function Contours.

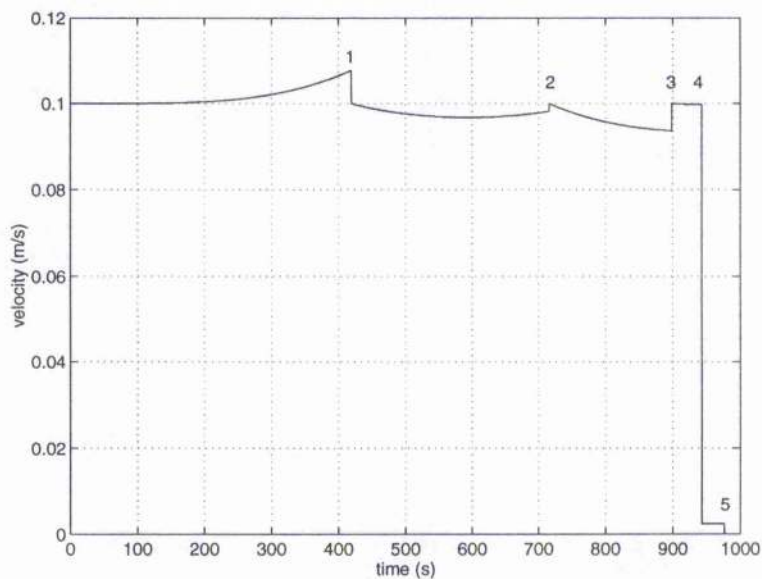


Figure 3.2.d: Discrete Control: Chase Vehicle Velocity.

### 3.4 Attitude Control

Many space based systems require the use of accurate pointing, whether as part of an antenna mechanism or indeed a complete structure such as the *Hubble Space Telescope* (HST). The control mechanism for changing the attitude of the structure may take the form of momentum wheels which may be controlled continuously for minimal energy expenditure.

The problem of pointing a body, as shown in **Figure 3.3**, may be accomplished by examining the attitude dynamics, represented by Euler's equations, viz.

$$I_1 \dot{\omega}_1 + (I_3 - I_2) \omega_2 \omega_3 = T_1 \quad (3.11.a)$$

$$I_2 \dot{\omega}_2 + (I_1 - I_3) \omega_1 \omega_3 = T_2 \quad (3.11.b)$$

$$I_3 \dot{\omega}_3 + (I_2 - I_1) \omega_2 \omega_1 = T_3 \quad (3.11.c)$$

where the body has moments of inertia  $I_1$ ,  $I_2$ , and  $I_3$  with continuous control torques  $T_1$ ,  $T_2$  and  $T_3$  applied. The Euler angles may be related to the body rates,  $\omega_1$ ,  $\omega_2$  and  $\omega_3$ , through the kinematic relations

$$\dot{\theta}_i = \sum_{j=1}^3 G_{ij} \omega_j \quad (3.12)$$

where  $G_{ij}$  is the transformation matrix

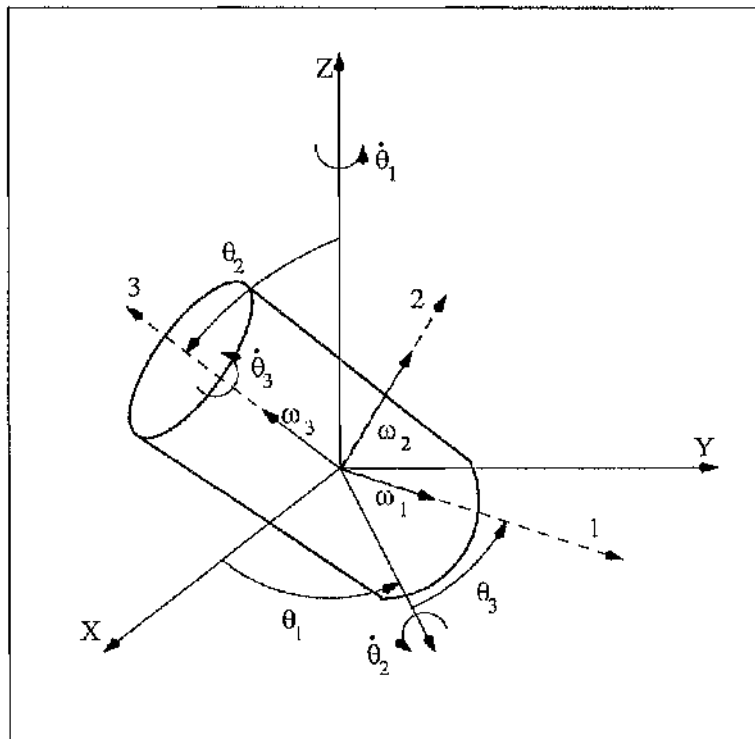


**Figure 3.3:** Vehicle Attitude Definition.

$$G_{ij} = \begin{Bmatrix} 1 & \sin \theta_1 \tan \theta_2 & \cos \theta_1 \tan \theta_2 \\ 0 & \cos \theta_1 & -\sin \theta_1 \\ 0 & \sin \theta_1 \sec \theta_2 & \cos \theta_1 \sec \theta_2 \end{Bmatrix} \quad (3.13)$$

Thus, with the dynamics of the body defined, it is now possible to control the body attitude through the use of a potential function.

### 3.4.1 Potential Function Derivation

The desired solution or goal point for this problem is to bring the body to rest at some goal orientation. Therefore, the terms which must be controlled are the body rates and the Euler angles. To this end, the potential function will take the form

$$V = V_{Euler} + V_{Rates} \quad (3.14)$$

The Euler angle potential function will take the form of a quadratic potential with a single goal point, viz

$$V_{Euler} = \frac{\alpha}{2} \sum_{i=1}^3 (\theta_i - \bar{\theta}_i)^2 \quad (3.15)$$

where  $\bar{\theta}_i$  is the goal orientation and  $\alpha$  is a scaling constant. The body rate potential is a simpler function with the goal corresponding to null body rates. Therefore, this potential function will take the form

$$V_{Rates} = \frac{1}{2} \sum_{i=1}^3 I_i \omega_i^2 \quad (3.16)$$

The total potential, being the sum of the Euler and body rates potentials will then take the form

$$V = \frac{1}{2} \sum_{i=1}^3 I_i \omega_i^2 + \frac{\alpha}{2} \sum_{i=1}^3 (\theta_i - \bar{\theta}_i)^2 \quad (3.17)$$

For this problem, a continuous control implementation will be used. To comply with Lyapunov's method, the rate of change of potential  $\dot{V}$  must be rendered negative definite. Therefore, differentiating the potential results in

$$\dot{V} = \sum_{i=1}^3 I_i \omega_i \dot{\omega}_i + \alpha \sum_{i=1}^3 (\theta_i - \bar{\theta}_i) \dot{\theta}_i \quad (3.18)$$

Rearranging and substituting **Equations 3.11** and **Equations 3.13** into the rate of change of potential and simplifying leads to the equation

$$\dot{V} = \sum_{i=1}^3 \omega_i T_i + \alpha \sum_{i=1}^3 (\theta_i - \bar{\theta}_i) \sum_{j=1}^3 G_{ij} \omega_j \quad (3.19)$$

This equation will now be used to generate a set of control laws.

### 3.4.3 Example: Continuous Control

Using the kinematic relations given by **Equations 3.7**, a control torque which will render  $\dot{V}$  negative definite may be derived of the form

$$T_i = -\kappa \omega_i - \alpha \sum_{j=1}^3 G_{ij}^{-1} (\theta_j - \bar{\theta}_j) \quad (3.20)$$

where  $\kappa$  is a positive definite shaping function. When the control torque is substituted into **Equation 3.19** then  $\dot{V}$  takes the form

$$\dot{V} = -\kappa \sum_{i=1}^3 \omega_i^2 \quad (3.21)$$

Thus the control torques which will rotate the body to the goal attitude are available in analytical form. To evaluate the performance of the controller, a case study will be considered.

To implement the continuous control potential function, the equations of motion of the body must first be defined. Rearranging **Equations 3.11** it is found that

$$\dot{\omega}_1 = \frac{T_1}{I_1} - \frac{(I_3 - I_2)}{I_1} \omega_2 \omega_3 \quad (3.22.a)$$

$$\dot{\omega}_2 = \frac{T_2}{I_2} - \frac{(I_1 - I_3)}{I_2} \omega_1 \omega_3 \quad (3.22.b)$$

$$\dot{\omega}_3 = \frac{T_3}{I_3} - \frac{(I_2 - I_1)}{I_3} \omega_2 \omega_1 \quad (3.22.c)$$

and expressing in full the kinematic relations as given in **Equation 3.12**, yields

$$\dot{\theta}_1 = \omega_1 + \omega_2 \sin \theta_1 \tan \theta_2 + \omega_3 \cos \theta_1 \tan \theta_2 \quad (3.23.a)$$

$$\dot{\theta}_2 = \omega_2 \cos \theta_1 - \omega_3 \sin \theta_1 \quad (3.23.b)$$

$$\dot{\theta}_3 = \omega_2 \sin \theta_1 \sec \theta_2 + \omega_3 \cos \theta_1 \sec \theta_2 \quad (3.23.c)$$

Then, a system of six simultaneous differential equations results which fully characterises the rotation of the body.

The physical characteristics of the body will be defined as a solid cylinder of 1m radius and 4 m length. In addition, assuming a mass of 240 kg, the moments of inertia  $I_1$ ,  $I_2$  and  $I_3$  may be calculated from

$$I_1 = I_2 = \frac{1}{4} mr^2 + \frac{1}{12} ml^2 = 335 \text{ kg.m}^2, \quad I_3 = \frac{1}{2} mr^2 = 30 \text{ kg.m}^2 \quad (3.24)$$

The initial conditions will now be defined as

$$\omega_1 = \omega_2 = \omega_3 = 0 \quad (3.25.a)$$

with initial Euler angles

$$(\theta_1, \theta_2, \theta_3) = (0, 1, \pi) \quad (3.25.b)$$

and final, goal conditions

$$\omega_1 = \omega_2 = \omega_3 = 0 \quad (3.26.a)$$

with Euler angles

$$(\bar{\theta}_1, \bar{\theta}_2, \bar{\theta}_3) = (0, 0, 0) \quad (3.26.b)$$

When used in conjunction with the initial conditions, **Equations 3.22** and **Equation 3.23**, may be integrated numerically using a Runge-Kutta scheme. The control torques are implemented as given in **Equation 3.20** with  $\kappa = 10$  and  $\alpha = 1$ .

The Euler angles representing the attitude of the body are shown in **Figure 3.4.a**. The influence of the controller may be clearly seen as the three angles are slowly damped to the goal. Thus, the potential function drives the body to the desired orientation. In addition, the body rates shown in **Figure 3.4.b** can also be seen to converge to the goal as they are damped.

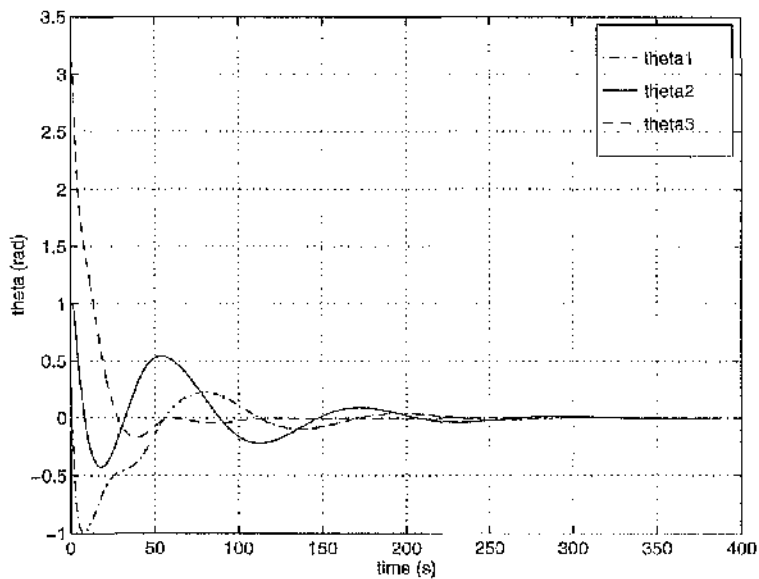


**Figure 3.4.a:** Continuous Control: Euler Angles.

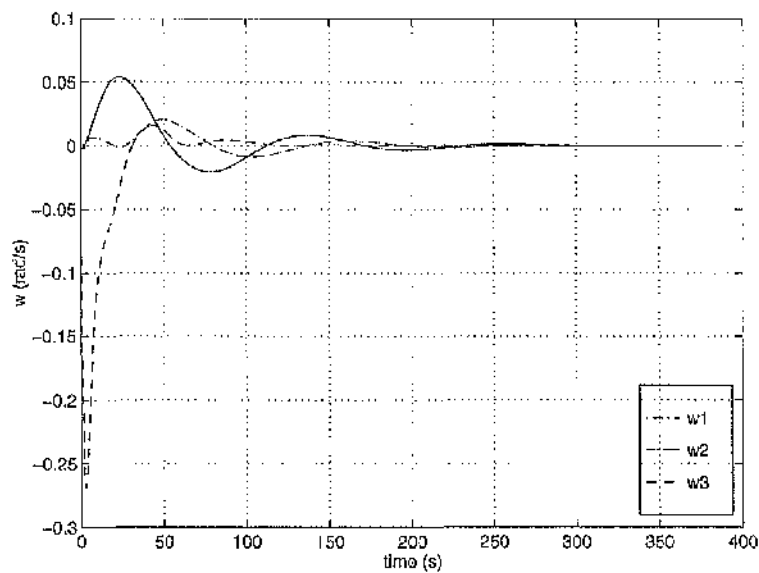


**Figure 3.4.b:** Continuous Control: Body Rates.

The control torques are shown in **Figure 3.4.c**. Again, the torques are seen to decay as the goal attitude is approached, allowing a smooth convergence.

The strong coupling of the motion about each body axis is also apparent. As axes 2 and 3 are controlled, axis 1 is displaced as a consequence. However, the potential function brings the body to the goal attitude. The potential function is shown in **Figure 3.4.d**. As the potential reduces to zero, it is clear that the rate of change of potential remains negative definite, thus complying with Lyapunov's theorem and guaranteeing convergence. Therefore, the potential function method has been demonstrated to successfully control a complex non-

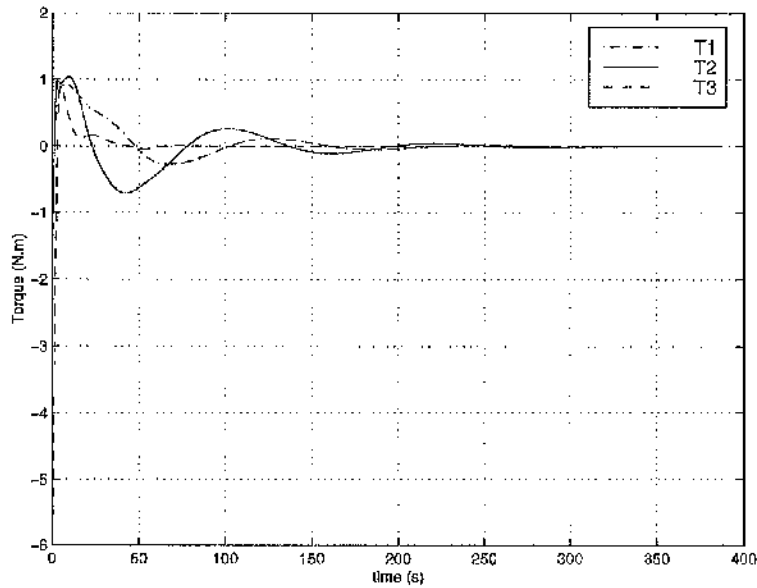


**Figure 3.3.c:** Continuous Control: Control Torques.

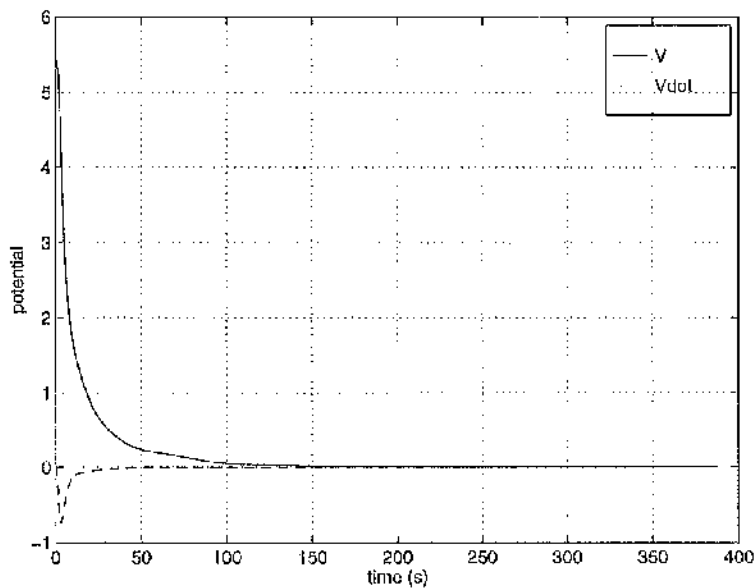


**Figure 3.3.d:** Continuous Control: Potential Function.

linear problem by continuously controlling the rate of change of potential. However, this is not always an optimal solution. For a problem in which control intervention is minimal, such as a translational problem where excessive fuel expenditure is undesirable, then the discretised method is more suitable.

### 3.5 Conclusions

It has been shown that the use of Lyapunov's second method meets the specifications of the spacecraft control methodology previously defined. Specifically, it may be said that if a dynamical system allows the definition of a Lyapunov function, then stability may be guaranteed through an appropriate choice of controls. Thus, to summarise the specifications required, Lyapunov's second method provides;

- A closed-loop control method allowing stable convergence to the desired configuration.
- The complexity of the control software is minimal. The problem of controlling a complex non-linear spacecraft system is reduced to the analytical derivation of a potential function.
- Using appropriate sensors and actuators, the method appears suitable for autonomous, on-board applications.

The control method examined here meets the criteria defined for a spacecraft control methodology. Although two different implementations were examined, the continuous and discrete methods, both proved satisfactory. Also, the use of the quadratic potential function has proven to be satisfactorily applied in both cases. In general, the continuous method has been applied to attitude control problems while translation problems have been discrete. However, with the use of low thrust propulsion systems, the continuous method may also be applied to translation problems. Lastly, the method is not wholly practical without consideration of obstacles within the spacecraft path. This problem, and various techniques for obstacle avoidance, will be examined in the following chapter.

# Chapter Four: Obstacle Avoidance

*Obstacles are made to be overcome.*

Anon.

## 4.1 Introduction

In the previous chapter, the application of potential function methods to spacecraft translation control was discussed. However, for a real system, collision avoidance will be required to enforce the separation between the controlled vehicle and any obstacles which may be present. Using the cases discussed in **Section 2.6.1** and **Section 3.3**, where the chase vehicle is located 70 m up-range from the target vehicle, an obstacle will now be added. To provide an obstacle avoidance capability within the potential function, obstacles may be represented by identifying regions of high potential, thus preventing approach of the vehicle. Considering **Equation 3.5**, a quadratic potential with the addition of an obstacle potential takes the form

$$V = V_{Goal} + V_{Obs} \quad (4.1)$$

where  $V_{Goal}$  corresponds to the attractive potential described in **Chapter 3** and  $V_{Obs}$  corresponds to the obstacle potential. The exact form of  $V_{Obs}$  may be defined using a variety of methods. In addition,  $V_{Obs}$  may encompass either a single or multiple obstacles.

This chapter will examine four different methods of defining the obstacle potential. The four methods are the Gaussian, Power-Law, Rectangular and Superquadric obstacles. The advantages and disadvantages of each shall also be discussed.

## 4.2 Obstacle Representation: Gaussian Distribution

To represent an obstacle within the potential field, the region of high potential may be defined using a *Gaussian Potential Function*. Thus, an inaccessible area is created within the potential field due to the increase in potential as the obstacle is approached. It is this increase, and the manner in which it does so, that is critical to the application to collision avoidance.

#### 4.2.1 Object Definition

A Gaussian potential function is based on the very common Gaussian probability distribution. The general form of the function is given by

$$V_{Obs} = A \exp\left\{-\frac{1}{\sigma}|\mathbf{r} - \mathbf{r}_{Obs}|^2\right\} \quad (4.2)$$

where  $A$  is a scaling parameter,  $\sigma$  is the standard deviation of the distribution and  $\mathbf{r}_{Obs}$  is the position vector of the obstacle. The values of  $A$  and  $\sigma$  are critical in the definition of the obstacle potential. If an object is not completely encompassed by the obstacle potential, a collision could result. Therefore, a rigorous method of sizing the obstacle potential is required. A method is available, based on the assumption of a one-dimensional problem where the attractive or goal potential is given by

$$V_{Goal} = \frac{\lambda}{2}(x - x_{Goal})^2 \quad (4.3)$$

The obstacle potential is then given by the one dimensional form of **Equation 4.2**, which may be expressed as

$$V_{Obs} = A \exp\left\{-\frac{1}{\sigma}|x - x_{Obs}|^2\right\} \quad (4.4)$$

thus resulting in the total potential

$$V = \frac{\lambda}{2}(x - x_{Goal})^2 + A \exp\left\{-\frac{(x - x_{Obs})^2}{\sigma}\right\} \quad (4.5)$$

Examining **Figure 4.1**, the addition of an arbitrary goal and obstacle potential are plotted. The addition of the goal and obstacle potentials may be clearly seen. However, the addition does create a local minimum. The formation of local minima can cause problems in the application of potential functions. However, if the one-dimensional problem is expanded to multiple dimensions, the local minimum here becomes a saddle point. Therefore, the position of the saddle point, and its distance from the centre of the obstacle is critical when considering the size of the obstacle potential. Defining the distance  $D$  as the characteristic dimension of the obstacle such that

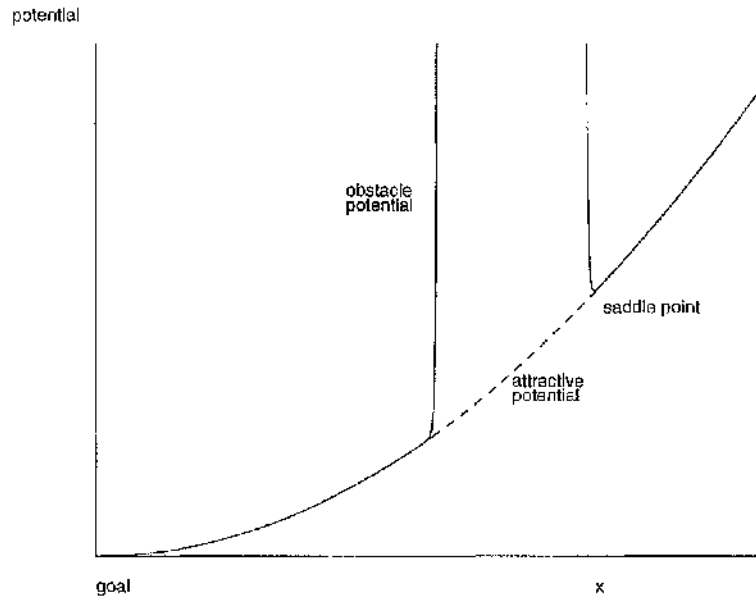


**Figure 4.1:** Saddle Point Formation.

$$D = x_{Saddle} - x_{Obs} \quad (4.6)$$

then  $A$  and  $\sigma$  must be chosen such that  $D$  is larger than the size of the object to be avoided.

Considering the properties of the total potential function at the saddle point, then it may be said that

$$\frac{dV}{dx} = 0 \quad \text{when} \quad x = x_{min} \quad (4.7)$$

and that the value of  $x$  may be written as

$$x_{min} \equiv x_{Saddle} \quad (4.8)$$

Therefore, differentiating **Equation 4.5** with respect to  $x$  and substituting using **Equations 4.7** and **4.8** yields

$$\lambda(x_{Saddle} - x_{Goal}) - \frac{2A}{\sigma} D \exp\left\{-\frac{D^2}{\sigma}\right\} = 0 \quad (4.9)$$

which may be re-arranged to give

$$A = \frac{\lambda\sigma(D + x_{Obs} - x_{Goal})}{2D \exp\left\{-\frac{D^2}{\sigma}\right\}} \quad (4.10)$$

where  $\sigma$  is the standard deviation which may be calculated using the statistical form

$$D = 3\sigma \quad (4.11)$$

where  $D$  encompasses 98% of the Gaussian distribution.

Even though this evaluation of  $A$  is only valid for one dimensional problems it can form the basis to calculate  $A$  for higher dimensional problems. Therefore, for a higher dimensional potential function of the form given in **Equation 4.2** the value of  $A$  becomes

$$A = \frac{\lambda\sigma(D + |\mathbf{r}_{obs}| - |\mathbf{r}_{Goal}|)}{2D \exp\left\{-\frac{D^2}{\sigma}\right\}} \quad (4.12)$$

where  $\mathbf{r}_{Goal}$  and  $\mathbf{r}_{Obs}$  again represent the position vector of the goal and obstacle respectively.

#### 4.2.2 Example

The case study defined in **Section 2.3.3** will now be considered with the addition of a single obstacle and with the initial positions of the chase and target vehicles given by

$$\mathbf{r} = \{70, 0, 0\} \quad \mathbf{r}_{Goal} = \{0, 0, 0\} \quad (4.13)$$

Then, the repulsive component of the total potential takes the form of **Equation 4.2** with a constant  $A$  value defined by **Equation 4.12** resulting in a total potential function of the form

$$V = \frac{\lambda}{2}(\mathbf{r} - \mathbf{r}_{Goal})^2 + \frac{\lambda\sigma(D + |\mathbf{r}_{obs}| - |\mathbf{r}_{Goal}|)}{2D \exp\left\{-\frac{D^2}{\sigma}\right\}} \exp\left\{-\frac{(\mathbf{r} - \mathbf{r}_{Obs})^2}{\sigma}\right\} \quad (4.14)$$

where  $\lambda$  is a constant, typically defined as unity. The characteristic dimension of the obstacle, and the width of the potential function are defined as

$$D=10 \text{ m}$$

$$\sigma = 3.33$$

$$(4.15)$$

with the position of the obstacle defined as

$$\mathbf{r}_{Obs} = \{50,0,0\}$$

$$(4.16)$$

Thus, the obstacle represented here is a 10 m diameter sphere located between the chase vehicle and the target vehicle.

Propagating the motion of the chase vehicle, the trajectory is shown in **Figure 4.2.a**. Although the chase vehicle does converge to the target vehicle, examining the region immediately surrounding the obstacle shown in **Figure 4.2.b** highlights the intensive manoeuvring required by the chase vehicle between points 1 and 2. As can be seen, the chase vehicle path does enter into the obstacle area. The cause of the infringement is that the characteristic dimension is derived in one dimension. There will be a variation in the obstacle width throughout the circumference of the obstacle. However the encroachment is minimal and separation would be enforced by incorporating an additional safety zone surrounding the physical object.

Examining the potential function, the convergence of the total potential to the target vehicle is shown in **Figure 4.2.c** and in contour form in **Figure 4.2.d**. As can be seen, the shaped potential function demonstrates the manner in which the obstacle is avoided. In addition, the contour plot clearly displays control intervention when the rate of

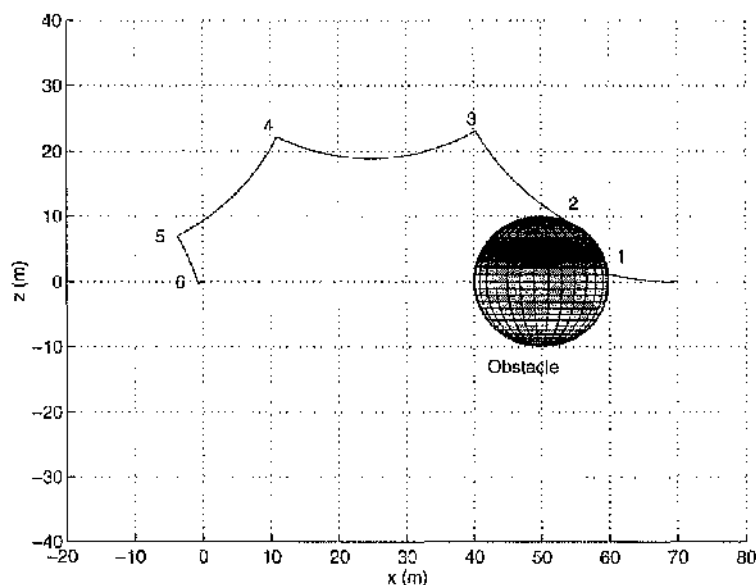


**Figure 4.2.a:** Gaussian Distribution: Chase Vehicle Trajectory.

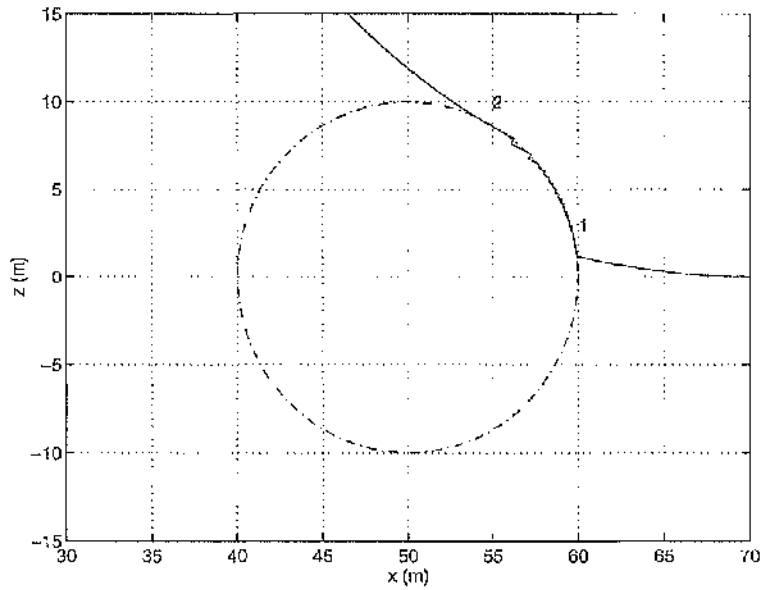


**Figure 4.2.b:** Gaussian Distribution: Obstacle.

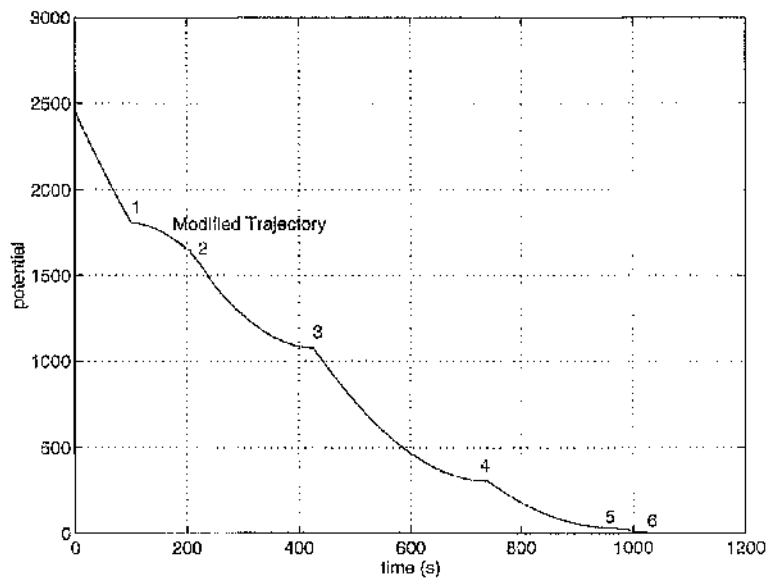


**Figure 4.2.c:** Gaussian Distribution: Potential Function.

change potential becomes positive. Thus, the potential is successfully reduced and vanishes at the origin. The velocity profile, shown in **Figure 4.2.e**, again displays the effect of control intervention. The purely impulsive path corrections demonstrated in **Section 3.3.3** are still apparent, however in avoiding the object, the required changes between points 1 and 2 are almost continuous, thus resulting in a larger  $\Delta v$  of  $2.538 \times 10^{-2} \text{ m.s}^{-1}$ .

Thus, in summary;

- The Gaussian function does produce an obstacle in the potential field which is successfully negotiated.
- The chase vehicle avoids the core areas of the obstacle, but in doing so grazes the surface.
- The saddle point of the total potential is unstable and is successfully negotiated to allow convergence to the goal point.

The only problem encountered with this method is a computational one. The Gaussian obstacle has an exponential decay and the use of the transcendental exponential

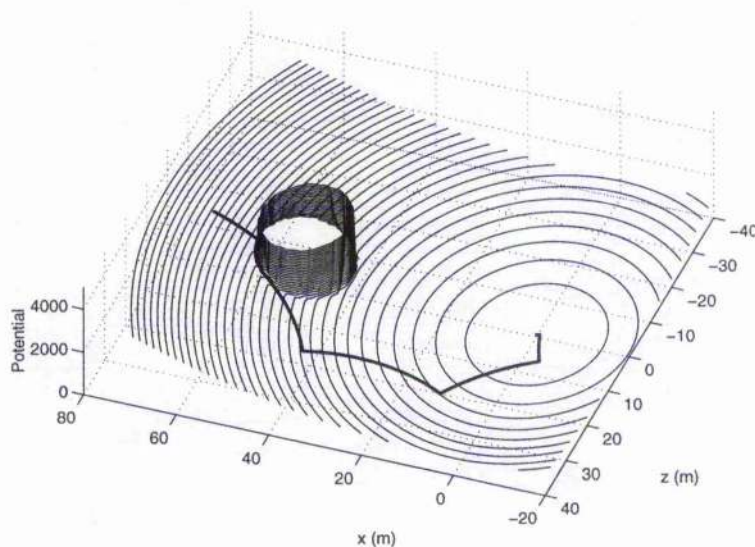


**Figure 4.2.d:** Gaussian Distribution: Potential Function Contours.

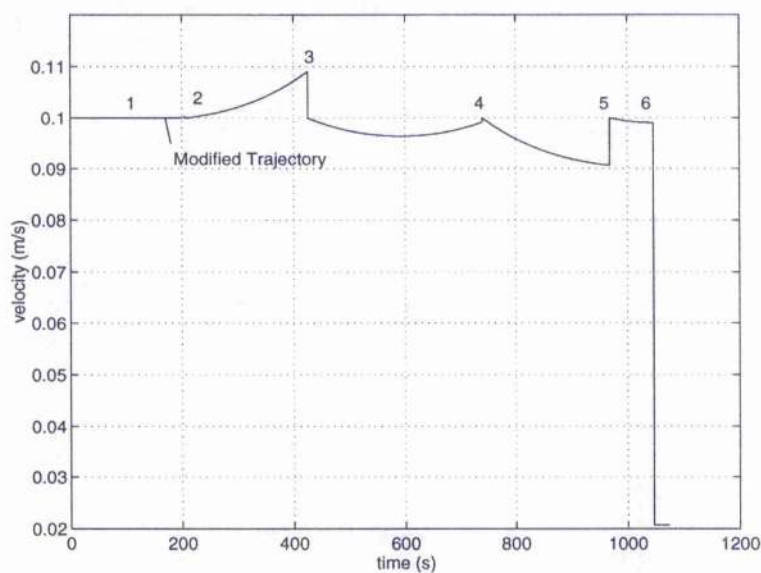


**Figure 4.2.e:** Gaussian Distribution: Chase Vehicle Velocity.

function is expensive to implement computationally. This problem becomes more pronounced the larger the number of obstacles within the vehicle space. This is the principal reason which leads to the use of geometrically decaying functions such as the power-law potential function.

### 4.3 Obstacle Representation: Power Law Distribution

The power-law obstacle originated in the field of molecular dynamics which will be discussed in **Chapter 5**. The computational demands of modelling molecular behaviour required a method of obstacle representation which did not require any complex mathematical operations such as the exponential function within the Gaussian representation. Thus, the principal reason for applying the spherical power-law obstacle is to reduce the computational demands in calculating the obstacle potential for a complex environment. Therefore, to that end, by eliminating the exponential from the function, the need to perform a computationally expensive operation is eliminated. The precise obstacle definition of the method will also be examined. However, in every other respect, the application is similar to the Gaussian obstacle.

#### 4.3.1 Obstacle Definition

As with the Gaussian distribution, considering the problem in one dimension the power-law obstacle potential takes the general form

$$V_{Obs} = \frac{A}{(x - x_{Obs})^{2N}} \quad (4.17)$$

where  $A$  and  $N$  are constants. The function results in the potential strength  $V_{Obs}$  varying only with distance from the object centre and when extended to three dimensions forms a spherical obstacle. In three dimensions, the obstacle potential becomes

$$V_{Obs} = \frac{A}{|\mathbf{r} - \mathbf{r}_{Obs}|^{2N}} \quad (4.18)$$

where  $\mathbf{r}$  and  $\mathbf{r}_{Obs}$  are the position vector of the chase vehicle and obstacle respectively. The value of the parameter  $A$  is critical in determining the diameter of the obstacle. However,  $A$  may be determined in a similar fashion to that of the Gaussian potential. Assuming the one-dimensional problem, as shown in **Figure 4.1**, with a goal potential given by **Equation 4.3**, the total potential is given as

$$V = \frac{\lambda}{2}(x - x_{Goal})^2 + \frac{A}{(x - x_{Obs})^{2N}} \quad (4.19)$$

At the saddle point, **Equations 4.7** and **4.8** still hold, therefore, differentiating the potential with respect to  $x$  and substituting for the characteristic dimension  $D$  given in **Equation 4.6** yields

$$(D + x_{Obs} - x_{Goal}) - \frac{2NA}{\lambda D^{2N+1}} = 0 \quad (4.20)$$

which may be re-arranged for  $A$  to yield

$$A = \frac{\lambda(D + x_{Obs} - x_{Goal})D^{2N+1}}{2N} \quad (4.21)$$

where  $N$  is of a sufficiently high value to ensure collision avoidance.

Again, even though this evaluation of  $A$  is only valid for one dimensional problems it can form the basis to calculate  $A$  for higher dimensional problems. Therefore, for a higher dimensional obstacle potential as in **Equation 4.18**, the value of  $A$  is given by

$$A = \frac{\lambda(D + |\mathbf{r}_{Obs}| - |\mathbf{r}_{Goal}|)D^{2N+1}}{2N} \quad (4.22)$$

again, where  $\mathbf{r}_{Goal}$  and  $\mathbf{r}_{Obs}$  represent the position vector of the goal and obstacle respectively.

#### 4.3.2 Example

The previous case study with the initial conditions of the chase and target vehicles given by **Equation 4.13**, is used to evaluate the obstacle potential. Again, the position of the obstacle is given by **Equation 4.16** and the obstacle radius is set at 10 m. In addition, the power  $N$  is arbitrarily defined as

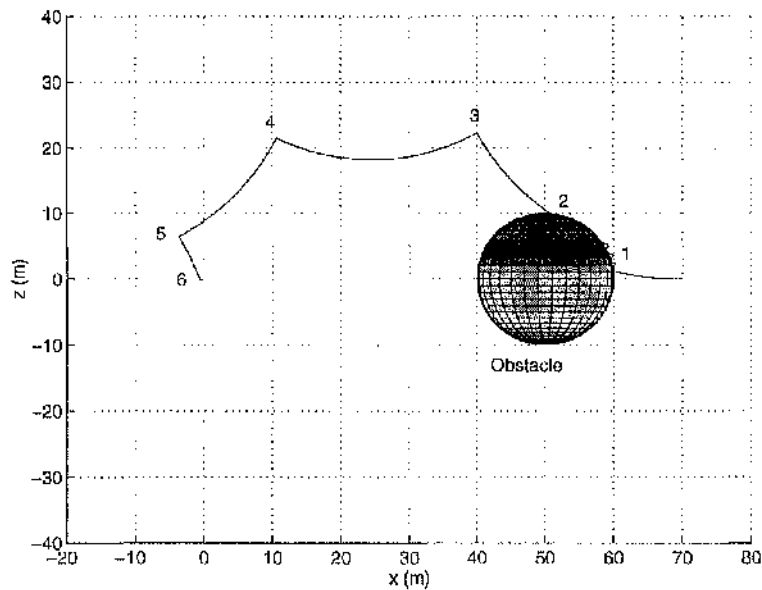
$$N = 4 \quad (4.23)$$

Using a quadratic goal potential, the total potential will then take the form

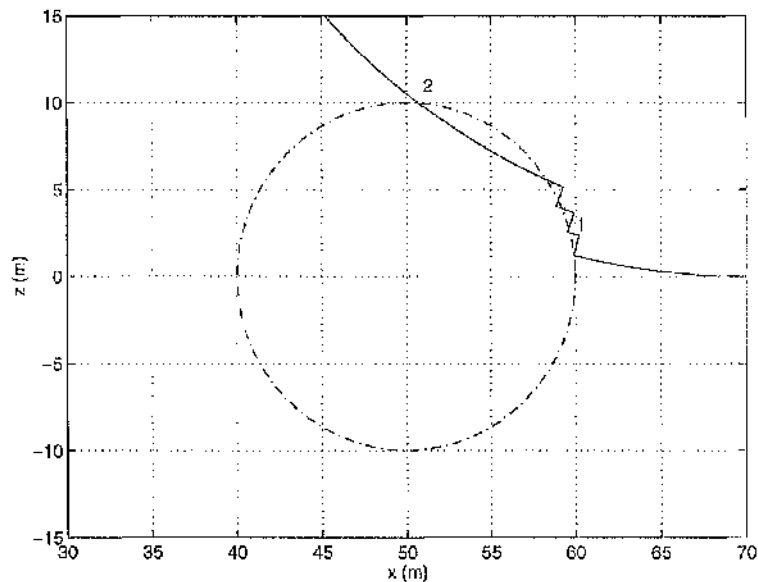
$$V = \frac{\lambda}{2} |\mathbf{r} - \mathbf{r}_{Goal}|^2 + \frac{\lambda(D + |\mathbf{r}_{obs}| - |\mathbf{r}_{Goal}|)D^{2N+1}}{2N|\mathbf{r} - \mathbf{r}_{Goal}|^{2N}} \quad (4.24)$$

where  $\lambda$  again, is a constant, typically defined as unity.

Propagating the trajectory of the chase vehicle and examining **Figure 4.3.a**, the path of the vehicle is shown as it successfully manoeuvres to the goal. However, examining the path around the obstacle, **Figure 4.3.b** displays a clear incursion of the



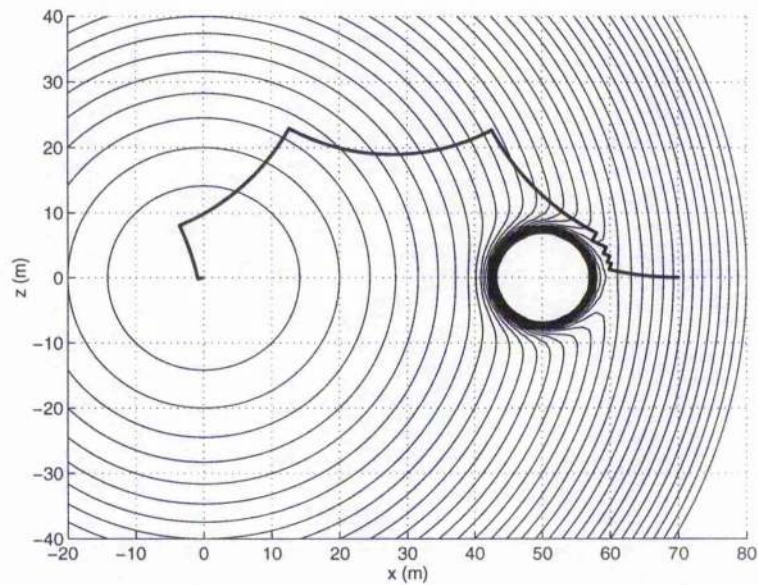
**Figure 4.3.a:** Power-Law Distribution: Chase Vehicle Trajectory



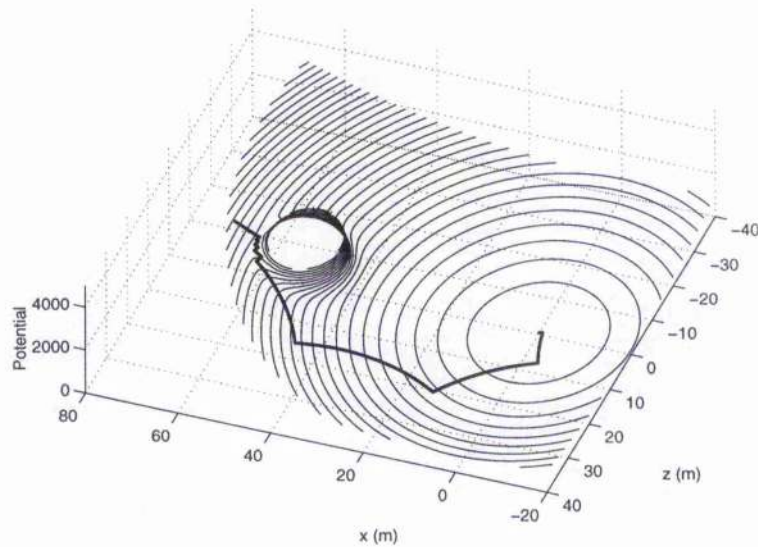
**Figure 4.3.b:** Power-Law Distribution: Obstacle.

vehicle into the obstacle area. This is obviously undesirable, however, the contour form of the potential, shown in **Figure 4.3.c** and **Figure 4.3.d** shows that the obstacle potential does not fully encompass the desired obstacle area. Although the saddle point is clearly at the characteristic dimension from the obstacle centre, this radius is not maintained around the circumference of the obstacle.

The problem of variation in radius around the circumference of the obstacle potential may be countered by using a higher value of  $N$ . The contour plots shown in **Figure 4.3.e** and **Figure 4.3.f** display improved obstacle avoidance with  $N=10$ . The larger value of  $N$  leads to a sharper definition of the obstacle which in turn leads to minimal incursion into the obstacle area. Therefore, the precise definition of the obstacle and the



**Figure 4.3.c:** Power-Law Distribution:  $N=4$ , The Potential Function.



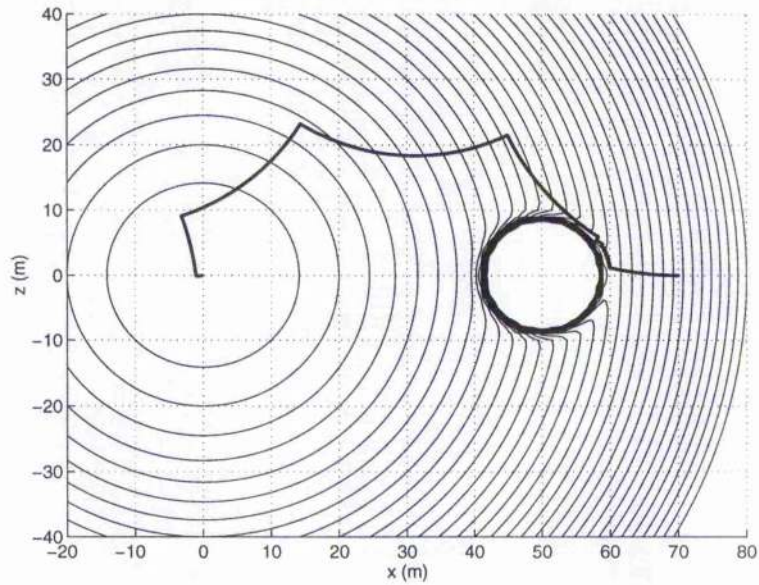


**Figure 4.3.e:** Power-Law Distribution:  $N=10$ , The Potential Function.

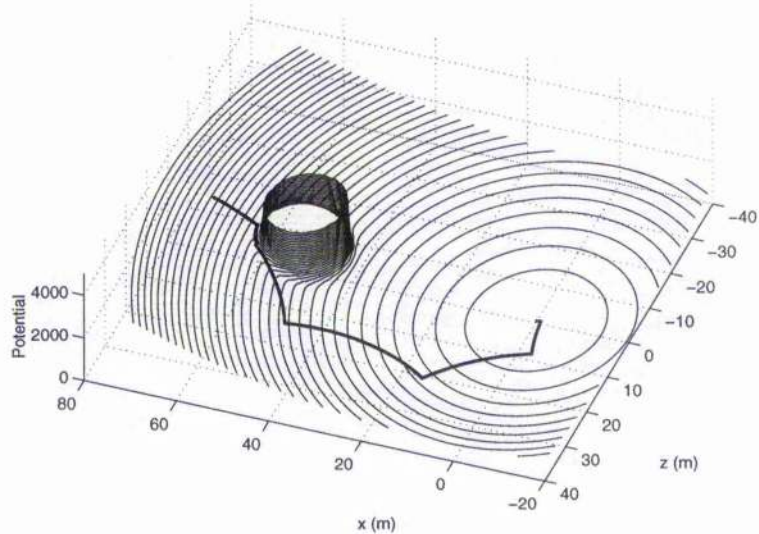


**Figure 4.3.f:** Power-Law Distribution:  $N=10$ , The Potential Well.

prediction of obstacle avoidance with the power-law function is related directly to the value of  $N$ . Increasing the value of  $N$  to 100, the contour plots in **Figure 4.3.g** and **Figure 4.3.h** show precise obstacle avoidance with the chase closely following the contour of the obstacle.

The principal motivation for using the power-law function is to provide a computationally efficient method to implement obstacle representation in a potential function. However, although the method is more efficient, the obstacle is not as clearly defined as the Gaussian distribution. Thus the choice of method will clearly vary depending on the application. Therefore, in summary;

- The Power-Law function does produce an obstacle in the potential field which is successfully negotiated.
- The characteristic dimension is not uniform around the circumference of the obstacle. The variation is very dependent on the value of  $N$  and can lead to the vehicle encroaching into the obstacle area. Therefore, a buffer zone would be required.
- The saddle point of the total potential is unstable and successfully negotiated to allow convergence to the goal point.

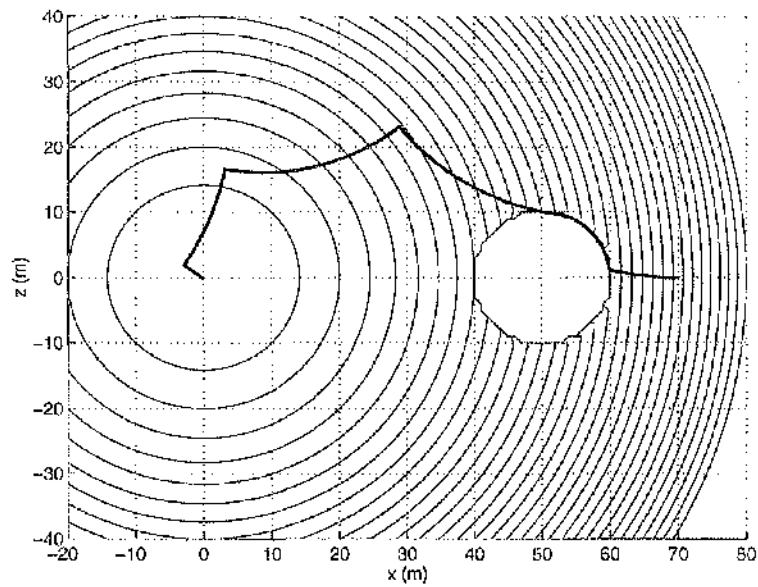


**Figure 4.3.g:** Power-Law Distribution:  $N=100$ , Potential Function.

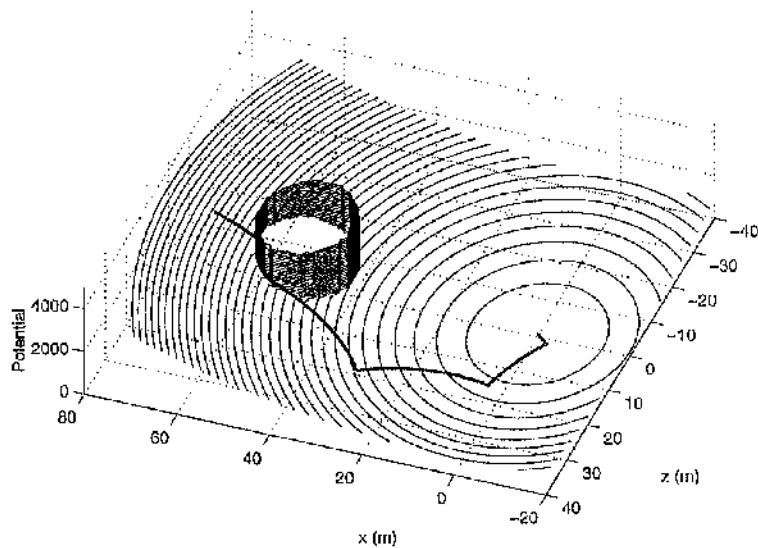


**Figure 4.3.h:** Power-Law Distribution:  $N=100$ , Potential Function Contours.

Until now, the only obstacles examined have been, or could be, enclosed by a spherical obstacle potential. In the following sections the obstacle representation is extended to include rectangular obstacles.

#### 4.4 Obstacle Representation: Rectangular Distribution

Until now the primary consideration has been the definition of obstacles within the potential function. This will now be extended to represent a specific obstacle geometry. The spherical potential functions have been shown to define the obstacle area well. However, these potential functions are inefficient in the definition of irregular objects and can prevent a straightforward path to the goal point in otherwise free space. The logical solution to this problem is to map the obstacle's physical attributes more precisely into the potential space. One of the more useful representations is that of the rectangle. A rectangular potential may be used as building blocks if two or more obstacles are added together to represent a more complex shape. There are many definitions of rectangular obstacle potentials or *Flat-Sided Potential Functions* such as FIRAS<sup>88</sup>. However the following definition is an extension of the spherical power-law distribution and describes the implementation of the rectangular potential as adequately as the more complex functions.

##### 4.4.1 Obstacle Definition

The rectangular power-law potential function in one dimension takes the general form given in **Equation 4.17**. However when extending this to three dimensions, the obstacle potential is defined by the function

$$V_{Obs} = \frac{A}{(x - x_{Obs})^{2N} + (y - y_{Obs})^{2N} + (z - z_{Obs})^{2N}} \quad (4.25)$$

where  $A$  and  $N$  are constants. The characteristic dimension  $D$  is defined in the same manner as for the spherical case and therefore the constant  $A$  is given by **Equation 4.22** while  $N$  is of sufficiently high value to ensure obstacle avoidance. Therefore, combining the different elements results in a total potential of the form

$$V = \frac{\lambda}{2} |\mathbf{r} - \mathbf{r}_{Goal}|^2 + \frac{\lambda(D + |\mathbf{r}_{obs}| - |\mathbf{r}_{Goal}|)D^{2N+1}}{2N[(x - x_{Obs})^{2N} + (y - y_{Obs})^{2N} + (z - z_{Obs})^{2N}]} \quad (4.26)$$

which may be used to shape the vehicle path.

#### 4.4.2 Example

The previous case study will again be used with the initial conditions given by **Equation 4.13**. The total potential is defined by **Equation 4.26**, with an obstacle of side 20m located 50m along the positive  $x$ -axis. This corresponds to a characteristic dimension of 10m with a power  $N = 4$ . Examining the results shown in the **Figures 4.4**, the critical element shown is the failure of the chase vehicle to converge to the goal. Examining **Figure 4.4.a**, the path of the chase vehicle is shown as it manoeuvres towards the obstacle. However, considering the obstacle in more detail, as shown in **Figure 4.4.b**,

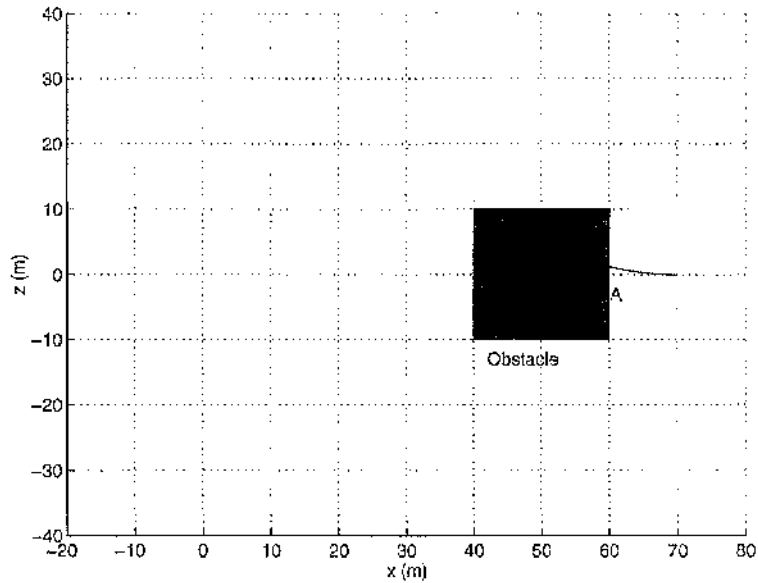


**Figure 4.4.a:** Rectangular Distribution: Chase Vehicle Trajectory.

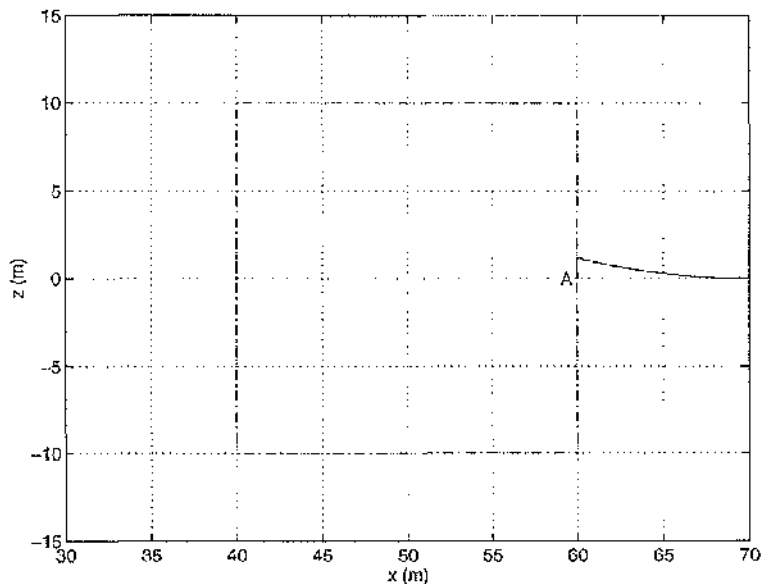


**Figure 4.4.b:** Rectangular Distribution: Obstacle.

the chase vehicle converges to a point directly behind the obstacle. The behaviour of the total potential function, shown in **Figure 4.4.c** shows the failure to converge with the potential becoming constant at a non-zero value.

The failure to converge to the goal is as a direct consequence of the formation of a *local minimum* directly behind the obstacle. The local minimum is clearly visible by examining the contour plots of the total potential in **Figure 4.4.d** and **Figure 4.4.e**. When

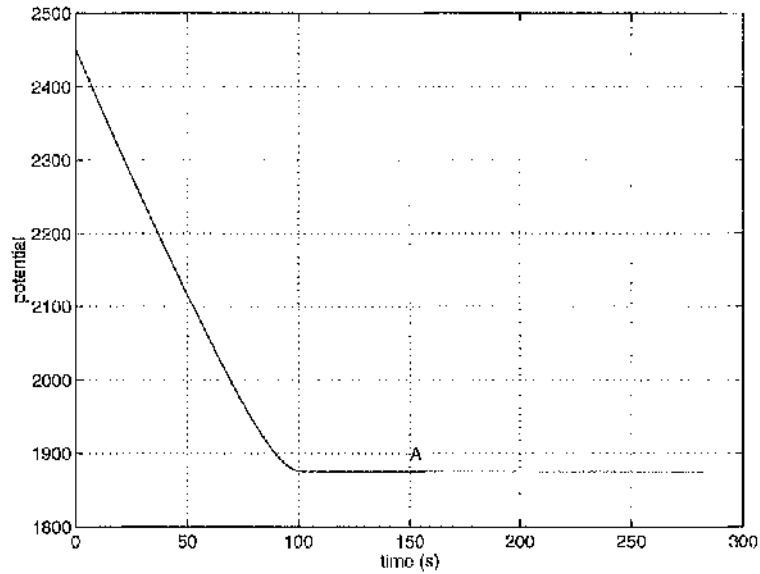


**Figure 4.4.c:** Rectangular Distribution: Potential Function.

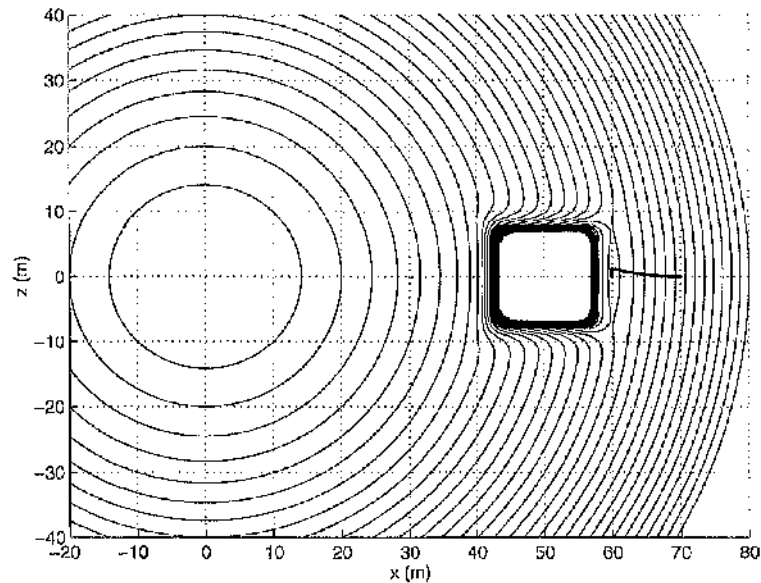


**Figure 4.4.d:** Rectangular Distribution: Potential Function.

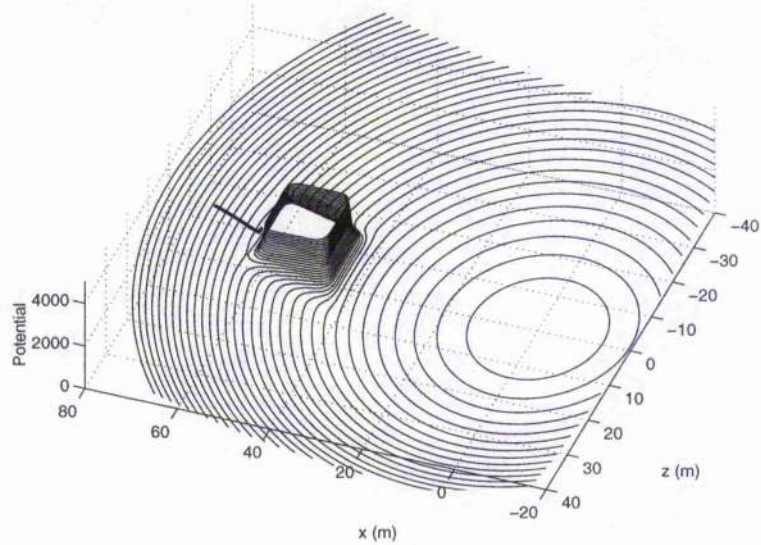


**Figure 4.4.e:** Rectangular Distribution: Potential Function Contours.

considering the method by which the obstacle potential is defined, it becomes apparent that the addition of any flat sided potential and any goal potential will result in the formation of a local minimum. Examining **Figure 4.5** the goal potential contour and the obstacle potential contour will always be coincident at points *B* and *C*. This will always indicate the formation of a local minimum at point *A*. Therefore, the case study demonstrates that, although the flat sided potential works well, when used in conjunction with a goal potential, local minima will form. In summary;

- The rectangular power-law function does produce an obstacle in the potential field which prohibits the chase vehicle entering into that area, but also forms a local minimum.
- The characteristic dimension is not constant around the circumference of the obstacle. As with the spherical power-law, the variation of the characteristic dimension is a strong function of  $N$ .
- The saddle point of the total potential becomes a local minimum and is not negotiated. This is not affected by the value of  $N$  and demonstrates the inapplicability of flat sided potentials to this type of problem.

The problem of representing rectangular objects is not as straightforward as may be envisaged. Applying a simple flat sided potential will result in the creation of a local minimum. However, this may be addressed by using a class of obstacle potentials known as *Superquadrics*.

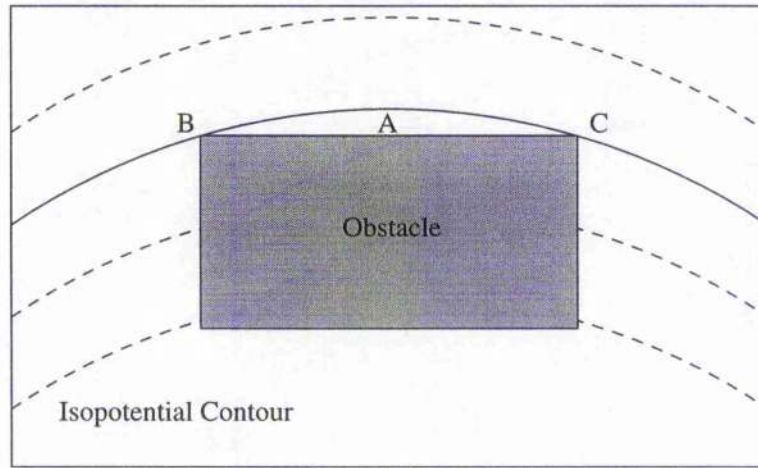


Figure 4.5: Local Minima Formation.

#### 4.5 Obstacle Representation: Superquadric Distribution

Superquadrics are a class of geometries that were initially employed in the field of computer graphics<sup>89</sup>. These functions are ideal for representing objects such as rectangles or ellipses as mathematical functions. Their use in collision avoidance was originally proposed for use by space manipulators using potential field methods<sup>90,91</sup>. The crucial element of a superquadric potential function is that the contours of the function change shape as the distance from the obstacle increases. For example, a square obstacle will be mapped to a square potential at the obstacle surface. However, as the distance to the obstacle increases, the contour of the repulsive potential will change shape to form an ellipse at the intersection of the attractive and repulsive potentials. It is this characteristic that makes superquadrics useful in as much as local minima may be eliminated. However, to obtain such a result requires a much more complex analysis than the other methods presented here.

##### 4.5.1 Obstacle Definition

The general form of the superquadric in two dimensions is given by

$$\left(\frac{x}{a}\right)^{2n} + \left(\frac{b}{a}\right)^2 \left(\frac{y}{b}\right)^{2n} = 1 \quad \text{where } n \geq 1 \quad (4.27)$$

The resulting geometric shape is often called an  $n$ -ellipse where  $a$  and  $b$  are the semi major, and minor axes of the ellipse respectively. For this function to be applied to a specific rectangular obstacle, then the ellipse must touch the corners of the obstacle, and also minimise the area between the obstacle and the ellipse which leads to

$$a = \frac{w}{2} \left( \frac{1}{2^{2n}} \right) \qquad b = \frac{h}{2} \left( \frac{1}{2^{2n}} \right) \qquad (4.28)$$

where  $w$  and  $h$  are the  $x$  and  $y$  dimensions of the rectangle respectively.

At the surface of the obstacle, the contour of the potential must match the obstacle shape. Thus  $n$  must be equal to infinity at the surface for this requirement to be satisfied. Likewise, moving away from the surface, the contours must be elliptical in the limit. Therefore a function may be derived which will define the distance to the obstacle surface and, in addition, define the potential contour value at that distance. It may be shown that such a function is given by<sup>90</sup>

$$K = \left[ \left( \frac{x}{a} \right)^{2n} + \left( \frac{y}{b} \right)^{2n} \right]^{\frac{1}{2n}} - 1 \qquad (4.29)$$

where  $K$  is the distance to the obstacle surface. The value  $n$ , which defines the contour shape, must vary from infinity to unity while  $K$  varies from zero to infinity, thus  $n$  is defined as

$$n = \frac{1}{1 - \exp(-\alpha K)} \qquad (4.30)$$

where  $\alpha$  is a constant.

Following the definition of the form of the isopotential contours, all that remains is to assign a potential value to them. The potential magnitude must decrease with distance, and the function which is most commonly applied is the Yukawa<sup>90</sup> potential of the form

$$V_{Obs} = A \frac{\exp(-\alpha K)}{K} \qquad (4.31)$$

where  $A$  is a scaling factor, and unless stated otherwise, is defined as unity. The definition of the potential, and the isopotential contours leads to a non-linear problem with co-dependency of  $K$  and  $n$ . The method to solve this problem and apply the potential is best demonstrated by example.

#### 4.5.2 Example

The solution to the problem of assigning values to  $K$  and  $n$  may be carried out using the bisection method. However, to do so requires the manipulation of **Equation 4.30** to

$$K_1 = -\frac{1}{\alpha} \ln \left[ 1 - \frac{1}{n} \right] \quad (4.32)$$

and, when used in conjunction with **Equation 4.29**, is re-written as

$$K_2 = \left[ \left( \frac{x}{a} \right)^{2n} + \left( \frac{b}{a} \right)^2 \left( \frac{z}{b} \right)^{2n} \right]^{\frac{1}{2n}} - 1 \quad (4.33)$$

Clearly,  $K_1$  and  $K_2$  must be equal. The difference between the two functions yields an error term, viz

$$\varepsilon = K_1 - K_2 \quad (4.34)$$

which may be solved for  $n$  using the bisection method. Thus  $K$  may be recalculated for the new  $n$  value. The process is then iterated until convergence. Obtaining  $K$  then allows the calculation of the total potential which takes the form

$$V = \frac{\lambda}{2} |\mathbf{r} - \mathbf{r}_{Goal}|^2 + A \frac{\exp(-\alpha K)}{K} \quad (4.35)$$

where  $A$  is unity and  $\alpha$  is set high enough to ensure that no local minima form at the saddle point. Methods for calculating an optimal setting of  $\alpha$  are also available<sup>90</sup>. However, for this example, the saddle point position need not be optimised, and so a value is chosen of sufficiently high magnitude, in this case  $\alpha = 45$ .

Applying this obstacle potential in conjunction with a quadratic goal potential requires the definition of the characteristic dimension of the obstacle. In this case a square obstacle will be considered with

$$h = w = 20 \text{ m} \quad (4.36)$$

Simulating the chase vehicle motion yields the results shown in the series of **Figures 4.6**. As can be seen, the chase vehicle does negotiate the obstacle and converge to the goal. Examining **Figure 4.6.a**, the path of the chase vehicle is shown as it successfully negotiates the obstacle. The obstacle avoidance is shown in more detail in **Figure 4.6.b**, as the chase vehicle easily clears the obstacle.

The contour plots shown in **Figures 4.6.c** and **4.6.d** display the contours of the total potential. As can be seen, the local minimum visible in the flat-sided potential does not form, thus allowing the chase vehicle to travel around the obstacle. However, the resolution of the contour map does not show the true form of the obstacle. Examining **Figure 4.6.e**, only the obstacle potential is shown with the path of the chase vehicle. As can be clearly seen, the path does closely follow the contour of the obstacle. Thus, in summary;

- The superquadric function does produce an obstacle in the potential field which allows convergence to the goal by eliminating the local minima formed by the flat-sided power-law. In addition the saddle which is formed is unstable, again allowing convergence.
- The height and width of the obstacle are very clearly defined, making the obstacle definition substantially simpler than previous methods for complex geometries.
- The complexity of the method is not a significant factor when considering single obstacles, however, as the complexity of the environment increases, then the computational demands will also increase.

The superquadric potential does provide the best means of defining non-spherical obstacles within the potential field. However, it does so at the expense of complexity. Therefore, for any obstacle avoidance potential, careful consideration of the specific problem would be required before applying this function. The complexity is also substantially increased if the parameter  $\alpha$  was calculated to fully guarantee the elimination of local minima with an analysis of the saddle point in three dimensions. Current methods are computationally demanding. Applying these techniques would effectively double the computational requirements of the method.

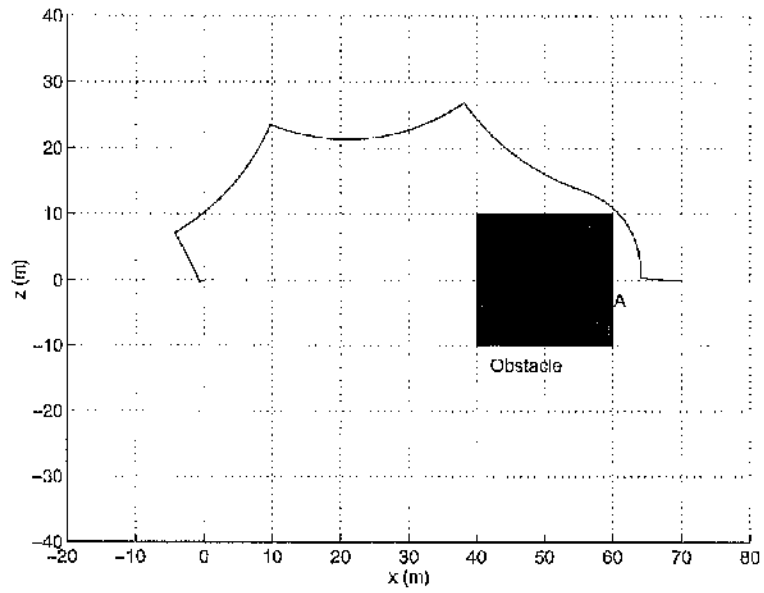


Figure 4.6.a: Superquadric Distribution: Chase Vehicle Trajectory.

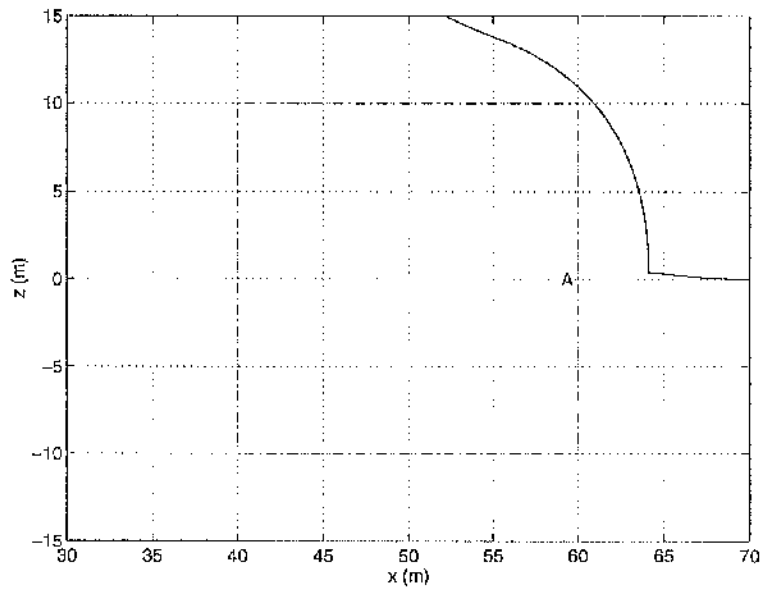
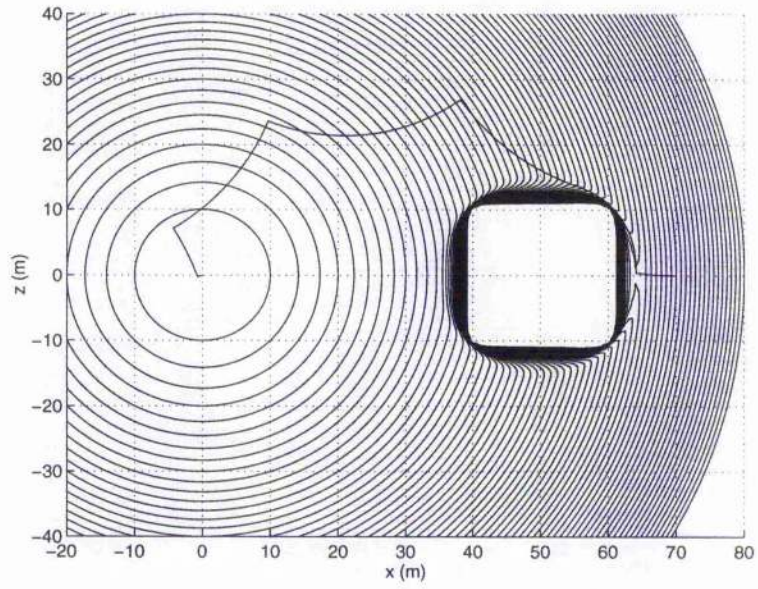
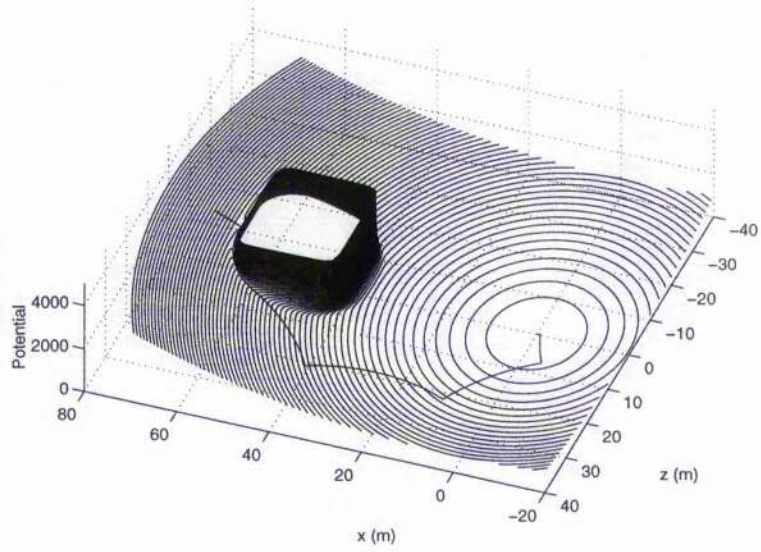


Figure 4.6.b: Superquadric Distribution: Obstacle.



**Figure 4.6.c:** Superquadric Distribution: Potential Function.



**Figure 4.6.d:** Superquadric Distribution: Potential Function Contours.

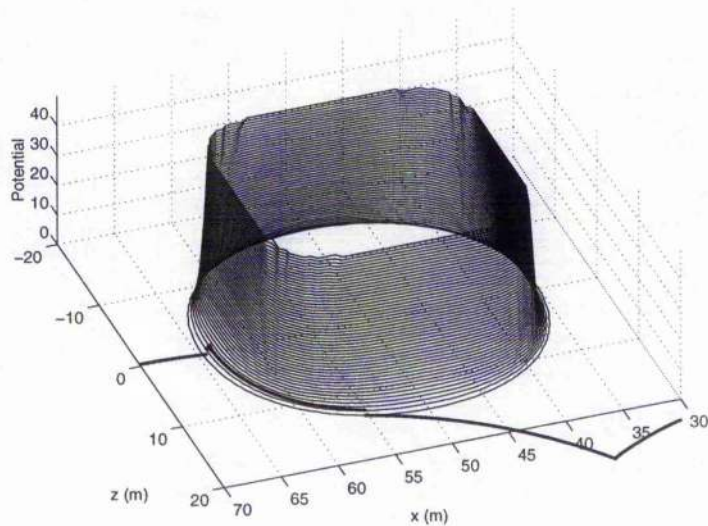


**Figure 4.6.e:** Superquadric Distribution: Obstacle Potential.

## 4.6 Conclusions

Of the four methods of defining obstacle potentials, only one method, the flat-sided power law potential was unsuccessfully negotiated by the chase vehicle. The remaining three methods created obstacle potentials that, when added to an attractive potential, did not generate local minima. Each method has its own merits, however, some have more general applications than others. The Gaussian method for a spherical obstacle offered the best all round performance and with specific regard to the balance of computational complexity and accuracy. The ability to exactly define the characteristic dimension of the obstacle and guarantee minimal incursions into that space in conjunction with easily definable parameters makes this function more applicable to general problems.

The spherical power-law potential demonstrated good results, however the sensitivity of the method to the value of the parameter  $N$  made it difficult to determine the interface between the goal and obstacle potentials. Thus, incursions into the obstacle area could not be prohibited. The advantage of this method is its computational simplicity. For such an easily applied method, the performance is reasonable, and would be applicable to problems where computing power was limited. Finally, the superquadric was by far the most complex of the four methods with parameters that are obtained from non-linear problems. However, the performance is excellent and very efficient in the use of space as the potential function maps itself on to the contours of the body. This method would be applicable to complex geometries where there were significant restrictions on movement. Thus, in conclusion, the ability to model and successfully negotiate obstacles has been demonstrated. The ability to create obstacles and shape the chase vehicle path to the goal point is one of the principal reasons for the use of potential function methods in the remainder of this thesis.

# Chapter Five: Molecular Dynamics

*Equilibria in biological systems are governed by their tendency to move towards states of lower free energy*

T.P. Flores & D.S. Moss

## 5.1 Introduction

In everyday life, construction surrounds us in many different forms. From the easily detected human activity on a construction project, to the almost imperceptible regeneration of our own bodies. The natural world has been producing structures far more complex and beautiful than any human construction. Therefore, this chapter looks at some of the rules which have been developed by human science to examine and duplicate nature's methods of construction. The methods applied to the study and simulation of molecular chemistry make use of potential functions. This chapter intends to demonstrate the relevance of potential function methods to physical problems. In addition, the molecular potentials will be simplified and applied to a multi-body problem with the aim of demonstrating that a stable structure may be constructed using potential function methods. This will demonstrate the underlying principles of potential function construction methods discussed in the following chapter.

## 5.2 Applications in Molecular Biology

The science of molecular biology has grown from the desire to manufacture molecules and chemicals with specific features. Within this objective, to examine how molecules are constructed, the science of *Molecular Dynamics*<sup>92,93,94</sup> has been developed. The principal tenet of this field is that a molecule will reach a state of equilibrium when the free energy within the molecule is minimised.

### 5.2.1 Energy Minimisation

The free energy within a molecule is given by the equation

$$\Delta G = -RT \ln \kappa \quad (5.1)$$

where  $\Delta G$  is the Gibbs Free Energy,  $R$  is the Universal Gas constant,  $T$  is the absolute temperature and  $\kappa$  is the equilibrium constant for a chemical reaction with constant pressure and temperature. However, explicitly defining the change in free energy of the system then

$$\Delta G = \Delta E + P\Delta V - T\Delta S \quad (5.2)$$

where  $\Delta E$  is the change in internal energy of the system,  $P$  the Pressure,  $V$  the Volume and  $\Delta S$  the Entropy.

However, if the assumption is made that system under scrutiny is well-ordered at a modest temperature and pressure, then the  $\Delta E$  term will dominate thus resulting in the free energy taking the form

$$\Delta G \approx \Delta E \quad (5.3)$$

Therefore, it is possible to minimise the internal energy and thus the Gibbs free energy of the system and to maximise the stability of the resulting structure. To minimise the internal energy of the system, the energy must be considered of the form

$$E = E_k + E_p \quad (5.4)$$

where the subscripts  $k$  and  $p$  represent kinetic and potential energy respectively. Thus, since the kinetic energy of the system is a function of temperature alone, the problem will reduce to minimising the potential energy of the system.

### 5.2.2. Computational Issues

In a real, biological system, the assumption that a system is well-ordered is not valid. Therefore, the  $T\Delta S$  term may not be disregarded. The result of this is that the complete free energy must be calculated to determine the stability of a system. This in itself is a much harder task. To simulate such a system requires a great deal of expertise and computing power. We can assume that both position and velocity are simultaneously defined. This assumption is only valid for heavier atoms and molecules i.e. Carbon atoms. However, for smaller, lighter particles, a quantum-mechanical treatment is required. The computational power required to implement even such a simplified model is extreme. For every pico-second of simulated time, 1 hour of processor time on a Cray X-MP is required. Thus the practical limit for simulated time is restricted to approximately 1 nano-second.

### 5.3 Schrödinger's Equation

When considering a construction problem or a civil engineering project, the measurement of the position of the components which make up the problem is relatively straightforward. The use of modern techniques such as laser ranging allows the accurate positioning of large elements to millimetre accuracy. However, when considering assembly problems on a quantum level, the positioning of sub-atomic particles with certainty is not possible. Heisenberg's Uncertainty Principle states that the position of a sub-atomic particle and its velocity may not be simultaneously measured with infinite precision. In 1926, Schrödinger developed a formulation of non-relativistic quantum mechanics which forms the basis for calculations in quantum chemistry.

Schrödinger's equation provides a probability wave function,  $\psi(\mathbf{r}, t)$ , which allows a prediction of the location and velocity of sub-atomic particles of the form

$$-\frac{\hbar^2}{2} \sum_{j=1}^N \frac{1}{m_j} \frac{\partial^2}{\partial \mathbf{r}_j^2} \psi(\mathbf{r}, t) + V(\mathbf{r}, t)\psi(\mathbf{r}, t) = i\hbar \frac{\partial}{\partial t} \psi(\mathbf{r}, t) \quad (5.5)$$

for a system of  $N$  molecules with position  $\mathbf{r}_i$ , mass  $m_i$ , wave function  $\psi(\mathbf{r}, t)$ , and potential field  $V(\mathbf{r}, t)$ . If the molecule potential field could be fully described, then the wave function would be obtained from Schrödinger's equation. However, this equation cannot be solved even for the simplest of molecules, such as the Hydrogen pair,  $\text{H}_2$ . However, approximations which simplify Schrödinger's equation into other forms do exist, the most prominent of these being the Born-Oppenheimer approximation.

Originally formulated in 1927, the Born-Oppenheimer approximation allows the electronic and nuclear distributions of a molecule to be treated separately. As a consequence, the motion of nuclei and electrons may also be treated as separate. Since even the lightest nucleus has a much larger inertia than that of an electron, the characteristic speeds and frequencies of nuclear motion are much lower than that of electron motion. Thus, it may be assumed that the electrons will form a shell surrounding the nucleus and the total potential energy of the molecule may be calculated based solely on the position of the nuclei. This allows an accurate model of the potential energy surface for up to 10-20 atoms.

The potential field in which the atoms exist is crucial in molecular dynamics. The atomic force, and the total energy of the system are both dependent on the potential field. The total energy of the system may be written as

$$E = \frac{1}{2} \sum_{i=1}^N m_i v_i^2 + V(\mathbf{r}) \quad (5.6)$$

In practice, the calculation of kinetic energy is relatively straightforward to compute. However, the calculation of the potential energy component is not straightforward, and key parameters must be derived experimentally.

#### 5.4 Potential Energy Functions

Deriving the potential energy function requires a representation of all the terms which influence atomic bonding. In practice these are covalent bond stretching, bond angle bending, harmonic dihedral bending, sinusoidal dihedral torsions, and non-bonded (Van Der Waals, and Coulombic) interactions. Therefore the total potential may be written as a summation of these components

$$V = V_{Bonds} + V_{Angles} + V_{Torsions} + V_{NBI} \quad (5.7)$$

where the non-bonded interaction,  $V_{NBI}$  is given by

$$V_{NBI} = V_{VanDerWaals} + V_{Electrostatic} + V_{Hydrogen} \quad (5.8)$$

Computationally, the definition and application of the full potential function would be too expensive. Therefore, in an effort to demonstrate the multi-body interactions envisaged here, a reduced potential function is used. The reduced potential function is formulated using only the principal potentials, the bond potential in conjunction with the repulsive component of the Van Der Waals potential. Thus a new potential is derived of the form.

$$V = V_{Bonds} + V_{Repulsive} \quad (5.9)$$

Thus, having identified the elements to be included within the total potential, it is now possible to proceed and define the potentials associated with each element.

##### 5.5.1 Bond Potentials

The potential function which describes bond properties, and specifically the tensile properties of the bond is typically a function called the Morse potential. The Morse potential function gives a good estimate of the tensile properties and is defined as

$$V_{Bonds} = \sum_{i=1}^{N_b} \left[ D_{b_i} \left( 1 - \exp \left\{ -\alpha_i (b_i - b_{o_i}) \right\} \right)^2 - D_{b_i} \right] \quad (5.10)$$

where  $D_{b_i}$  is the energy at the equilibrium bond length  $b_{o_i}$ ,  $\alpha_n$  is used as a gain to produce the desired molecular vibration spectrum and  $N_b$  is the total number of bonds.

Although the Morse potential gives excellent results, the bond potential may be further simplified for bond lengths close to the equilibrium value. The potential is that of a quadratic harmonic approximation of the form

$$V_{Bonds} = \frac{1}{2} \sum_{i=1}^{N_b} K_{b_i} (b_i - \bar{b}_i)^2 \quad (5.11)$$

where  $\bar{b}_i$  is the equilibrium bond length and  $K_{b_i} = 2D_{b_i} \alpha_i^2$ . The two curves are shown in **Figure 5.1**.

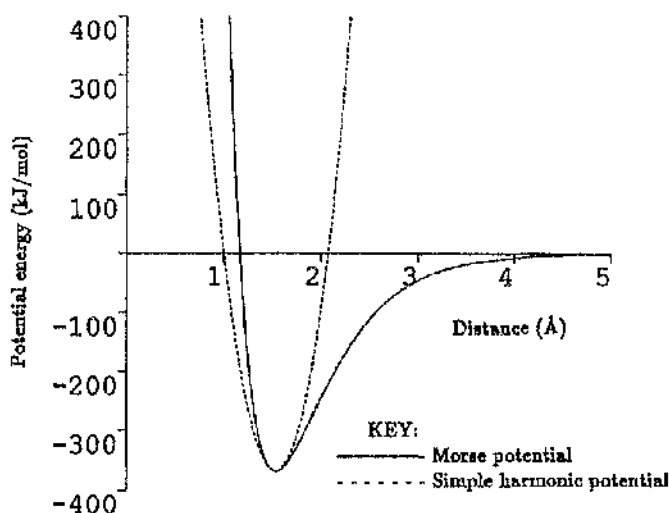


**Figure 5.1:** The Morse Potential (Adapted from Ref. 92).

### 5.5.2 Repulsive Components

When atoms come close together, their electron clouds overlap and produce a repulsive force. This repulsive force increases as the separation decreases. Therefore, for a computationally expensive problem such as this, a spherical power-law function is applied. The choice of the power-law potential is further supported by Lennard and Jones<sup>92</sup> who determined that the power-law is sufficient for an arbitrarily high index. Thus, the potential energy function takes the form

$$V_{Repulsive} = \sum_{i < j}^{N_{atoms}} \frac{A_{ij}}{r_{ij}^n} \quad (5.12)$$

where  $r_{ij}$  is the distance between the centres of the nuclei and  $A_{ij}$  is a scaling constant.

## 5.5 Calculation of Non-Bonded Interactions

The calculation of long range interactions between two atoms is expensive. Therefore, the computational cost of determining the non-bonded interactions between every pair of atoms within a system is unreasonably high with the computation time increasing with  $N^2$ . Therefore, to reduce computing times, a cut-off radius  $R_{cut}$  is introduced. Within this radius, all of the forces between atomic pairs are calculated, however, outside of the radius all interactions are considered negligible.  $R_{cut}$  is generally lower than 8 Angstroms. However, the electrostatic forces are still significant until almost 15 Angstroms. This quandary is overcome by treating local atoms as charge groups. If a particular charge group centroid is within the  $R_{cut}$  distance, then the group is included within the calculation.

## 5.6 Multi-Body potentials

The application of the potential function control methods to a multi-body problem may be demonstrated by applying a molecular potential with Lyapunov's method. Thus, a problem with a *molecule* consisting of a number of generic *atoms* will be used to demonstrate that the minimisation of the potential energy within the molecule produces a stable structure.

### 5.6.1 Problem Definition

A *molecule* will now be defined consisting of six *atoms* with each atom's optimal state corresponding to a bond to every other atom. Thus each atom will be bonded to five other atoms. Therefore, using the attractive and repulsive components defined in **Equations 5.11** and **5.12** the total potential of the molecule takes the form

$$V = \frac{1}{2} \sum_{i=1}^{N_{Bonds}} K_{b_i} (b_i - \bar{b}_i)^2 + \sum_{i < j}^{N_{Atoms}} \frac{A_{ij}}{r_{ij}^{12}} \quad (5.13)$$

where  $K_{b_i}$  and  $A_{ij}$  in this case are defined as unity for every bond and atom and  $n$  has been arbitrarily defined as 12. If the radius of each atom is one unit, and the goal bond length,  $\bar{b}$ , is defined as two units, then the final configuration will result in every atom touching each other. This is the only condition imposed on the molecule. Aside from this criteria, the final state of the molecule remains undefined.

### 5.6.2. Example

The potential function is minimised using the discrete control method at every integration time step. Thus, an internal normal is calculated at each isopotential surface.

However, since translation costs are clearly irrelevant, as propulsion is not an issue, the method is applied continuously with no trigger mechanism. Therefore, simulating the molecule starting from some random initial position yields the results shown in **Figures 5.2**. Examining **Figure 5.2.a**, the potential function is shown. As expected the potential function is minimised, however, it should be noted that the potential does not vanish. Examining both components of the potential function, it is possible to identify the cause of the residual potential. The first component is non-zero due to the physical configuration of the molecule. If all the atoms are attempting to reach the desired bond length, then physically this is not possible. Instead the atoms will settle to an equilibrium position where all the bond lengths in the molecule are as close to the goal bond length as possible. In addition, although the repulsive potential is very small, by its very nature, it can never be zero. Therefore, a small residual is present.

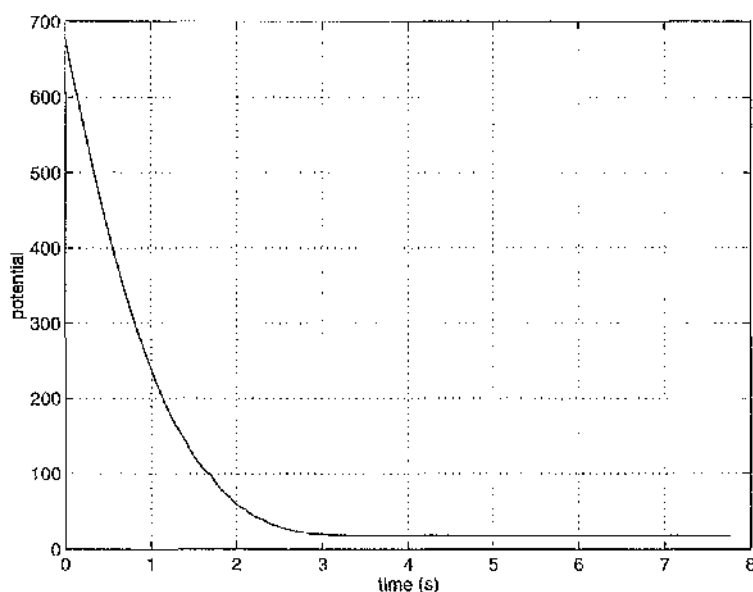


**Figure 5.2.a:** The Potential Function Behaviour.

The motion of the atoms are shown in **Figure 5.2.b**. As can be seen the atoms form the shape which fills the least volume corresponding to the minimum energy configuration. In addition, the three larger equilibrium bond lengths correspond to the atoms at opposite ends of the molecule. Thus, it has been demonstrated that potential functions are capable of forming stable structures from multi-body systems.

## 5.7 Conclusions

The use of potential functions has been expanded to include multi-body systems.

The science of molecular dynamics has been briefly reviewed and the behaviour of large molecules used to provide insight to multi-body system dynamics. The validity of potential

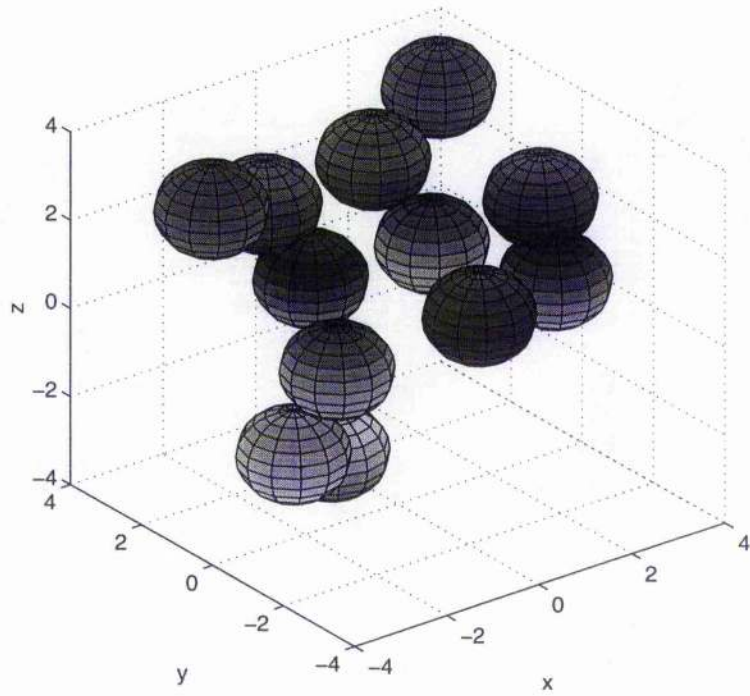


**Figure 5.2.b.i:** The Atomic Motion: Time = 0 s.

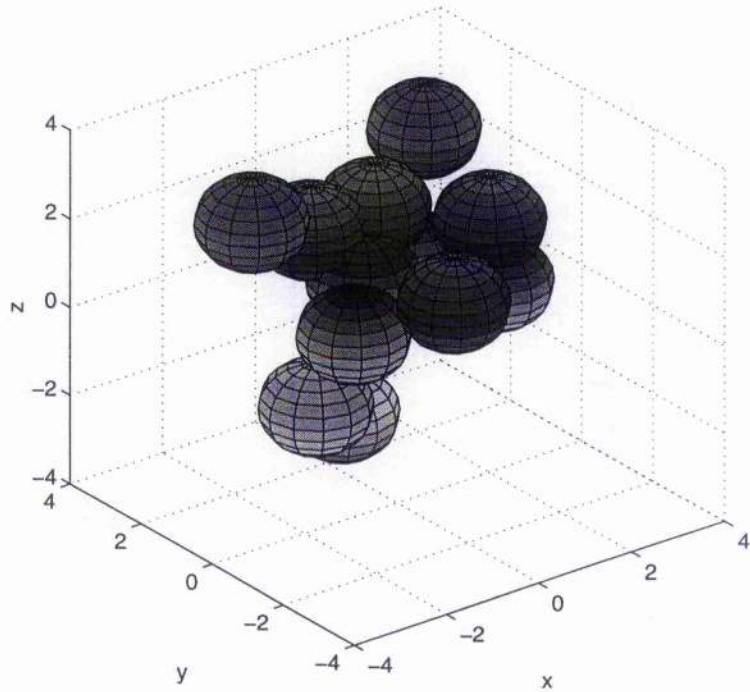


**Figure 5.2.b.ii:** The Atomic Motion: Time = 1 s.

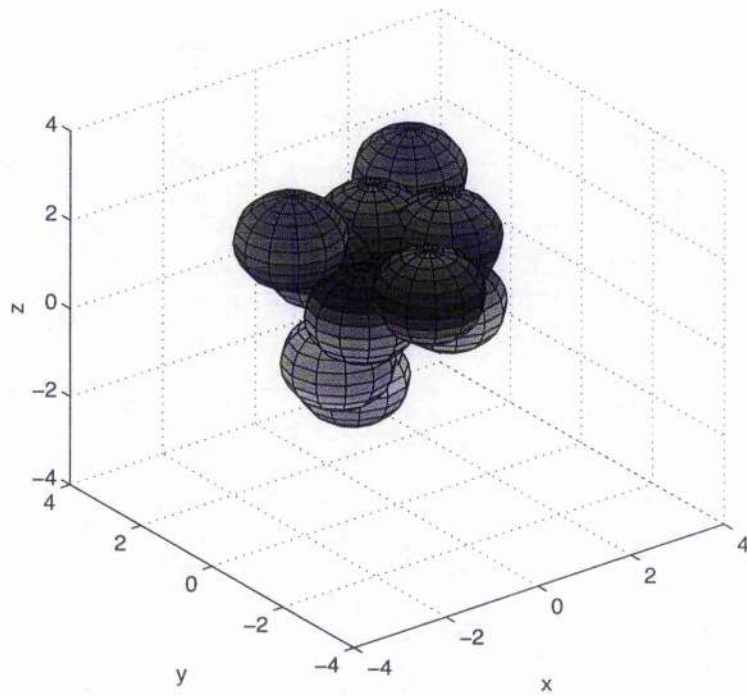


**Figure 5.2.b.iii:** The Atomic Motion: Time = 2 s.

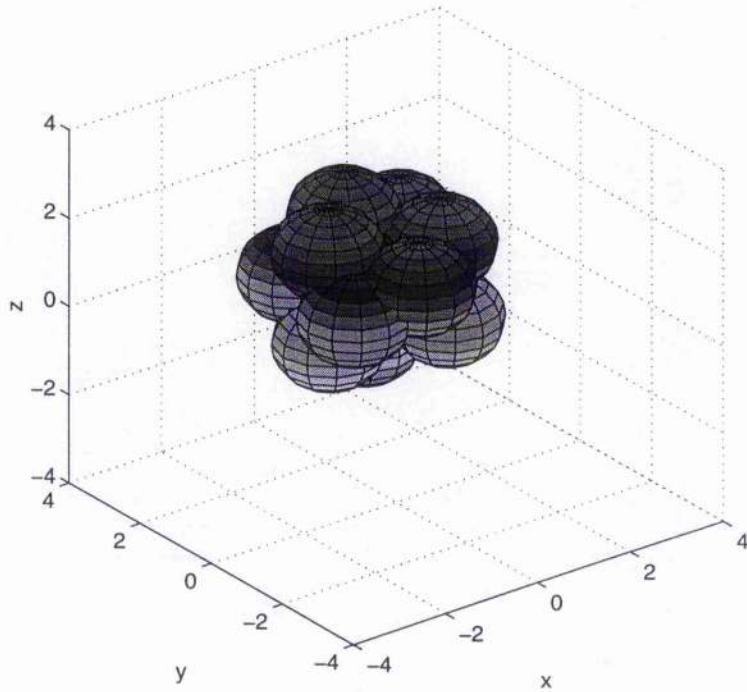


**Figure 5.2.b.iv:** The Atomic Motion: Time = 3 s.

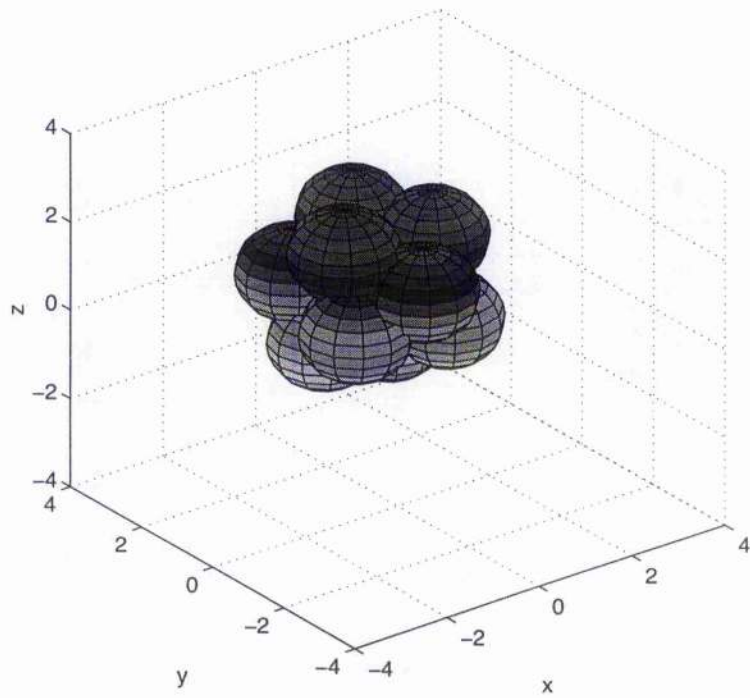


**Figure 5.2.b.v:** The Atomic Motion: Time = 4 s.

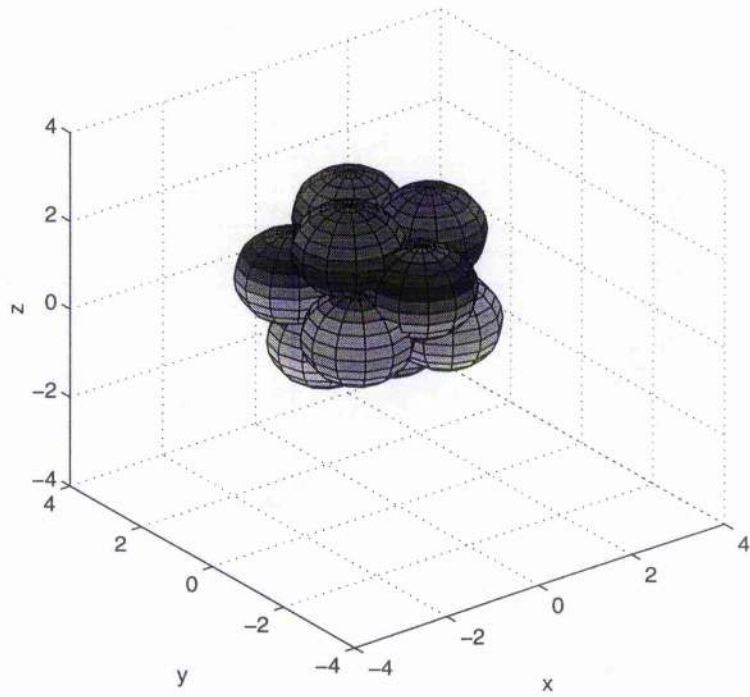


**Figure 5.2.b.vi:** The Atomic Motion: Time = 6 s.

functions for assembly has been seen through physical analogies from molecular dynamics. Thus, in summary;

- For a well-ordered system, stability is directly related to potential energy. A consequence of this is that the probability of a stable structure is increased as the complexity of the structure is reduced. This will become increasingly more important as a structure grows in size.
- Multi-element attractive and repulsive potential functions can be generated.
- Computational requirements may be reduced by introducing a cut-off radius.
- The goal configuration may not be physically possible. However, the method will force the configuration of the bodies to the minimum energy state.

The purpose of this chapter has been to demonstrate the foundation elements of a potential function method which may be used to assemble stable structures from multi-body systems. This has been done using a physical analogy with molecular dynamics. The following chapter shall expand on this by extending the methods from atom building blocks to beam elements capable of forming useful engineering structures.

# Chapter Six: Structural Assembly

## 6.1 Introduction

The previous chapter has demonstrated the application of potential functions to multi-body systems and their use in forming minimum energy configurations. The purpose of this chapter is to expand on this to demonstrate the application of the method to autonomous assembly of engineering structures<sup>95,96,97</sup>. Therefore, applying the lessons learned from molecular dynamics to the assembly problem, a stable building block from which larger structures may be assembled is required. The logical choice for such a building block is a beam element. Two distinct applications of the potential function method will now be examined. These are the *Parallel* and *Serial* implementations<sup>98</sup>. The parallel method involves a simultaneous effort with all the beam elements to form a stable structure. The serial method is a more practical implementation, with only a sub-set of the total number of beams within the structure being active at any one instant. The application of both methods will be demonstrated using two structures, a simple pin-jointed triangle and square.

## 6.2 Beam Element Definition

For the type of pin-jointed structures envisaged here, it is assumed that the beam element is capable of perfect translation and rotation to a given position and orientation. As a consequence, the detailed mechanics of translation and rotation may be ignored. However, the connectors placed at the end of each beam must be modelled and in addition, the centre of mass of the beam must also be identified. Thus, including the assumptions stated here, it is now possible to proceed and define the characteristics of the beam. The beam element is defined as a uniform beam of length  $l$  and, as shown in **Figure 6.1**, has connectors placed at either end. The end connectors are used to join the beams together with each beam having a male and female connector. Thus, defining the position vector of the *male* connector of the  $i^{\text{th}}$  beam as

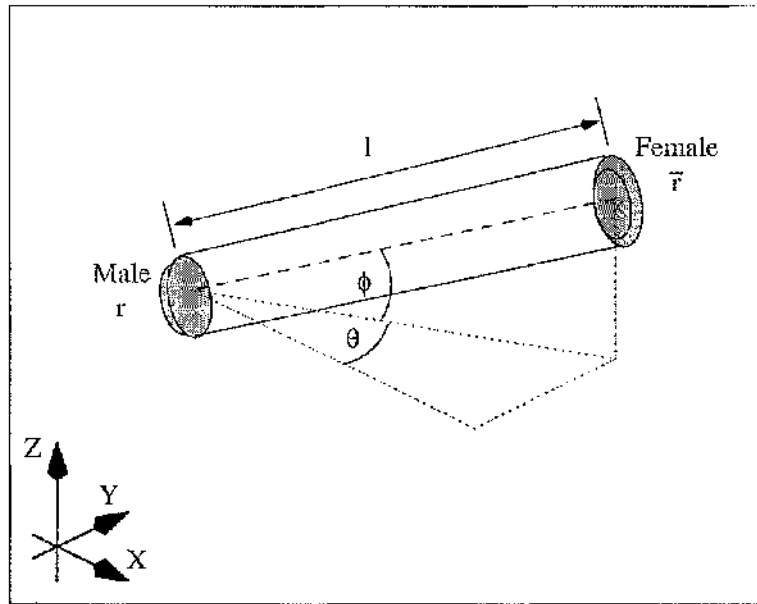


Figure 6.1: Beam Element Definition.

$$\mathbf{r}_i = \{x_i, y_i, z_i\} \quad (6.1)$$

then the female connector of the  $i^{\text{th}}$  beam may be described by the position vector

$$\bar{\mathbf{r}}_i = \{x_i + l \cos \theta_i \cos \phi_i, y_i + l \sin \theta_i \cos \phi_i, z_i + l \sin \phi_i\} \quad (6.2)$$

where  $\theta_i$  and  $\phi_i$  define the orientation of the beam in azimuth and elevation. For the case studies envisaged here, typically the length  $l$  of the beam is 2 m, of similar length to those used in the ACCESS experiment described in **Section 1.2.2**.

If collision avoidance between the beams is to be enforced, then the distance between the centre of mass of two colliding beams must be defined. Thus, the centre of mass of each beam is given as the point halfway along the length of the beam. This may be described by the position vector

$$\mathbf{r}_{iCM} = \left\{ x_i + \frac{l}{2} \cos \theta_i \cos \phi_i, y_i + \frac{l}{2} \sin \theta_i \cos \phi_i, z_i + \frac{l}{2} \sin \phi_i \right\} \quad (6.3)$$

Thus, with the basic properties of the beam elements, the complete location and orientation of the male and female connectors and the centre of mass of the  $i^{\text{th}}$  beam may be described using the state vector

$$\mathbf{x}_i = \{x_i, y_i, z_i, \theta_i, \phi_i\} \quad (6.4)$$

The application of the parallel and serial methods to the problem of assembling individual beam elements into useful structures demands a method of translating and rotating the beam elements into their final positions. This may be done by two methods, the first involves the use of a free-flying robot capable of grappling, rotating and translating the elements. In addition, the free-flyer must demonstrate the dexterity to assemble and manipulate the joints which will connect the beams together. The type of vehicle envisaged here is similar to that of the *Ranger* vehicle previously discussed in **Section 1.4.1**. The second method is to include sensors and actuators within the construction of each beam. In effect this creates a *smart* beam capable of carrying out the assembly tasks completely autonomously. However, this type of beam could only be considered to operate efficiently within the parallel assembly regime. In addition, it may be noted that such a set of smart beams could provide a fully re-configurable structure as will be discussed later in **Chapter 7**.

The measure of  $\Delta v$ , based on the assumptions made earlier regarding the properties of the beams, provides an approximate indication of cost for beam translation. The cost of beam rotation, however, is more complex. Considering the mechanism of beam rotation, a controlling vehicle will be required to implement an impulse thus applying a torque to the beam. Examining **Figure 6.2**, the moment applied around the centre of mass of the beam is given by

$$M = I\dot{\omega} \quad (6.5)$$

where  $I$  is the moment of inertia of the beam and free-flying vehicle combined which may be expressed as

$$I = \frac{1}{12}ml^2 + I_v \quad (6.6)$$

where  $I_v$  is the moment of inertia of the free-flying vehicle. The moment caused by the controlling force  $F$ , is also given by

$$M = F \frac{d}{2} \quad (6.7)$$

where  $d$  is the characteristic dimension of the free-flyer. Re-arranging **Equation 6.5** and **Equation 6.7** results in

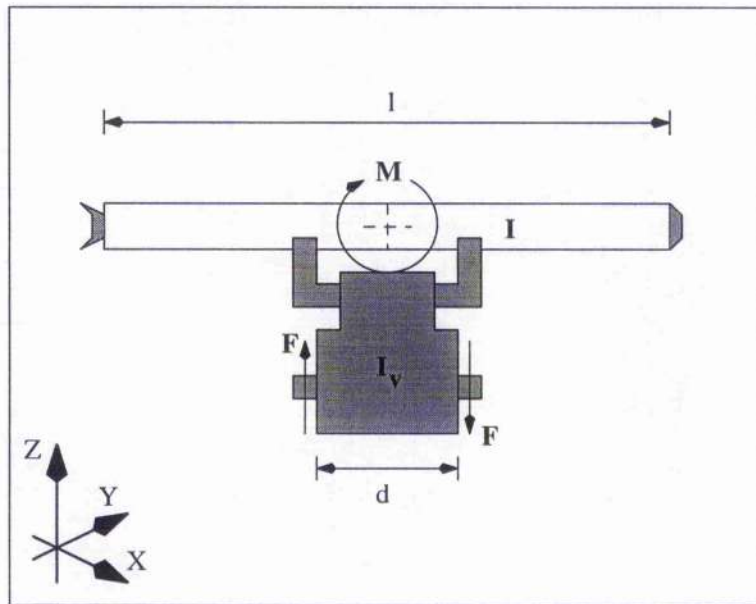


Figure 6.2: Beam and Vehicle System.

$$I\Delta\omega = \frac{d}{2}F\Delta t \quad (6.8)$$

or

$$I\Delta\omega = \frac{d}{2}\Delta v \quad (6.9)$$

which gives an approximate relation between  $\Delta v$  and  $\Delta\omega$  as

$$\Delta v = \frac{2I}{d}\Delta\omega \quad (6.10)$$

The beam/free-flyer model which is developed here is a rudimentary one. If the model were to be developed further, account must be taken of the free-flying vehicle moment of inertia, sensor models and thruster actuation models. For the purpose of illustration in this thesis, the properties of the beam and free-flyer are chosen such that the manoeuvring impulse for rotation will be equivalent to that of a manoeuvring impulse for translation. Therefore, for current purposes, the cost of implementing one radian per second of rotation is equivalent to one metre per second of translation and so all manoeuvring impulses may be measured in terms of  $\Delta v$ . With these assumptions it is then possible to quantify the motion of the beams.

### 6.3 Parallel Assembly. Case I: Triangle

The simplest geometrical shape of any consequence in engineering structures is the triangle. Replacing the atomic model of **Chapter 5** with that of the beam element, it is possible to proceed and develop a potential function which may be used to assemble the triangle.

#### 6.3.1 Potential Function Definition

The only major difference between the structural assembly potential and the atomic potential is the emphasis on the connections between the elements. Thus, the total potential will take the form

$$V = V_{Connection} + V_{Obs} \quad (6.11)$$

where  $V_{Connection}$  replaces the  $V_{Bonds}$  term and  $V_{Obs}$  replaces the  $V_{Repulsive}$  term in **Equation 5.9**. The  $V_{Bonds}$  term is based solely on minimising the distance between the centres of the atoms while  $V_{Obs}$  term prevents unwanted collisions. However, for the  $V_{Connection}$  term in structural assembly, the potential is based on minimising the distance between the male and female connectors of the beams. Therefore, for the triangle the connection potential will take the form

$$V_{Connection} = \frac{1}{2} \left[ |\mathbf{r}_1 - \bar{\mathbf{r}}_3|^2 + |\mathbf{r}_2 - \bar{\mathbf{r}}_1|^2 + |\mathbf{r}_3 - \bar{\mathbf{r}}_2|^2 \right] \quad (6.12)$$

which, by including the definition of the male and female connectors, may be expressed in scalar form as

$$\begin{aligned} V_{Connection} = \frac{1}{2} & \left[ (x_1 - x_3 - l \cos \theta_3 \cos \phi_3)^2 + (x_2 - x_1 - l \cos \theta_1 \cos \phi_1)^2 \right. \\ & + (x_3 - x_2 - l \cos \theta_2 \cos \phi_2)^2 + (y_1 - y_3 + l \sin \theta_3 \cos \phi_3)^2 \\ & + (y_2 - y_1 + l \sin \theta_1 \cos \phi_1)^2 + (y_3 - y_2 + l \sin \theta_2 \cos \phi_2)^2 \\ & + (z_1 - z_3 + l \sin \phi_3)^2 + (z_2 - z_1 + l \sin \phi_1)^2 \\ & \left. + (z_3 - z_2 + l \sin \phi_2)^2 \right] \quad (6.13) \end{aligned}$$

Thus, the goal is reached when the male connector of beam one is connected to the female connector of beam three, beam two is connected to beam one and beam three is connected to beam two, thus forming the triangle.

The repulsive component is formed by adding a spherical Gaussian obstacle potential located at the centre of mass of each beam. The Gaussian obstacle potential has

been used in this case as opposed to the power-law obstacle due to of the ease in defining the obstacle boundary. In addition, with only three beams considered here, this is not a computationally intensive problem, therefore the Gaussian potential is a logical choice. The potential is sized to fully enclose the entire beam, thus preventing collision. However, since the obstacle locations are continually moving, the magnitude of the repulsive potential is scaled to the separation between each beam and every other beam, viz

$$V_{Obs} = A \sum_{i=1}^{N_{beams}} \sum_{j=1, j \neq i}^{N_{beams}} \exp\{-B|\mathbf{r}_{CGi} - \mathbf{r}_{CGj}|\} \quad (6.14.a)$$

where the distance between the two centres of mass may be expressed in scalar form as

$$\begin{aligned} |\mathbf{r}_{CGi} - \mathbf{r}_{CGj}| = & \left[ \left( x_i + \frac{l}{2} \cos \theta_i \cos \phi_i - x_j - \frac{l}{2} \cos \theta_j \cos \phi_j \right)^2 \right. \\ & + \left( y_i + \frac{l}{2} \sin \theta_i \cos \phi_i - y_j - \frac{l}{2} \sin \theta_j \cos \phi_j \right)^2 \\ & \left. + \left( z_i + \frac{l}{2} \sin \phi_i - z_j - \frac{l}{2} \sin \phi_j \right)^2 \right]^{\frac{1}{2}} \end{aligned} \quad (6.14.b)$$

### 6.3.2 Example

The triangular structure is composed of three beam elements. Each beam element is connected to the other two beams via a male and female connector. The potential function which describes the problem is derived by incorporating **Equations 6.12** and **6.14** into **Equation 6.11**, thus resulting in the equation

$$\begin{aligned} V = & \frac{1}{2} \left[ |\mathbf{r}_1 - \bar{\mathbf{r}}_2|^2 + |\mathbf{r}_2 - \bar{\mathbf{r}}_3|^2 + |\mathbf{r}_3 - \bar{\mathbf{r}}_1|^2 \right] \\ & + A \sum_{i=1}^{N_{beams}} \sum_{j=1, j \neq i}^{N_{beams}} \exp\{-B|\mathbf{r}_{iCM} - \mathbf{r}_{jCM}|\} \end{aligned} \quad (6.15)$$

To derive the control inputs for the individual beams, the translational and rotational components may be obtained from the gradient of the potential as described in **Chapter 3**. Differentiating the connection potential for the  $x$ -component of each beam gives

$$\frac{\partial}{\partial x_1} [V_{Connection}] = (x_1 - \bar{x}_3) - (x_2 - \bar{x}_1) \quad (6.16.a)$$

$$\frac{\partial}{\partial x_2} [V_{Connection}] = (x_2 - \bar{x}_1) - (x_3 - \bar{x}_2) \quad (6.16.b)$$

$$\frac{\partial}{\partial x_3} [V_{Connection}] = (x_3 - \bar{x}_2) - (x_1 - \bar{x}_3) \quad (6.16.c)$$

and for the  $y$ -component

$$\frac{\partial}{\partial y_1} [V_{Connection}] = (y_1 - \bar{y}_3) - (y_2 - \bar{y}_1) \quad (6.16.d)$$

$$\frac{\partial}{\partial y_2} [V_{Connection}] = (y_2 - \bar{y}_1) - (y_3 - \bar{y}_2) \quad (6.16.e)$$

$$\frac{\partial}{\partial y_3} [V_{Connection}] = (y_3 - \bar{y}_2) - (y_1 - \bar{y}_3) \quad (6.16.f)$$

and the  $z$ -component

$$\frac{\partial}{\partial z_1} [V_{Connection}] = (z_1 - \bar{z}_3) - (z_2 - \bar{z}_1) \quad (6.16.g)$$

$$\frac{\partial}{\partial z_2} [V_{Connection}] = (z_2 - \bar{z}_1) - (z_3 - \bar{z}_2) \quad (6.16.h)$$

$$\frac{\partial}{\partial z_3} [V_{Connection}] = (z_3 - \bar{z}_2) - (z_1 - \bar{z}_3) \quad (6.16.i)$$

The rotational components may be derived in the same manner, viz

$$\frac{\partial}{\partial \theta_1} [V_{Connection}] = (x_2 - \bar{x}_1) \cdot l \sin \theta_1 \cos \phi_1 - (y_2 - \bar{y}_1) \cdot l \cos \theta_1 \cos \phi_1 \quad (6.16.j)$$

$$\frac{\partial}{\partial \theta_2} [V_{Connection}] = (x_3 - \bar{x}_2) \cdot l \sin \theta_2 \cos \phi_2 - (y_3 - \bar{y}_2) \cdot l \cos \theta_2 \cos \phi_2 \quad (6.16.k)$$

$$\frac{\partial}{\partial \theta_3} [V_{Connection}] = (x_1 - \bar{x}_3) \cdot l \sin \theta_3 \cos \phi_3 - (y_1 - \bar{y}_3) \cdot l \cos \theta_3 \cos \phi_3 \quad (6.16.l)$$

$$\begin{aligned} \frac{\partial}{\partial \phi_1} [V_{Connection}] &= (x_2 - \bar{x}_1) \cdot l \cos \theta_1 \sin \phi_1 + (y_2 - \bar{y}_1) \cdot l \sin \theta_1 \sin \phi_1 \\ &\quad - (z_2 - \bar{z}_1) \cdot l \cos \phi_1 \end{aligned} \quad (6.16.m)$$

$$\begin{aligned} \frac{\partial}{\partial \phi_2} [V_{Connection}] &= (x_3 - \bar{x}_2) \cdot l \cos \theta_2 \sin \phi_2 + (y_3 - \bar{y}_2) \cdot l \sin \theta_2 \sin \phi_2 \\ &\quad - (z_3 - \bar{z}_2) \cdot l \cos \phi_2 \end{aligned} \quad (6.16.n)$$

$$\begin{aligned} \frac{\partial}{\partial \phi_3} [V_{Connection}] &= (x_1 - \bar{x}_3) \cdot l \cos \theta_3 \sin \phi_3 + (y_1 - \bar{y}_3) \cdot l \sin \theta_3 \sin \phi_3 \\ &\quad - (z_1 - \bar{z}_3) \cdot l \cos \phi_3 \end{aligned} \quad (6.16.o)$$

The components of the obstacle potential function may be obtained from **Equation 6.12** as

$$\frac{\partial}{\partial x_i} [V_{Obs}] = -A \cdot B \cdot \left[ \begin{aligned} &\sum_{j=1, j \neq i}^{N_{Obst}} (x_{CG_j} - x_{CG_i}) \cdot \exp\{-B|\mathbf{r}_{CG_i} - \mathbf{r}_{CG_j}|\} + \\ &\sum_{j=1, j \neq i}^{N_{Obst}} (x_{CG_j} - x_{CG_i}) \cdot \exp\{-B|\mathbf{r}_{CG_j} - \mathbf{r}_{CG_i}|\} \end{aligned} \right] \quad (6.17.a)$$

$$\frac{\partial}{\partial y_i} [V_{Obs}] = -A \cdot B \cdot \left[ \begin{aligned} &\sum_{j=1, j \neq i}^{N_{Obst}} (y_{CG_j} - y_{CG_i}) \cdot \exp\{-B|\mathbf{r}_{CG_i} - \mathbf{r}_{CG_j}|\} + \\ &\sum_{j=1, j \neq i}^{N_{Obst}} (y_{CG_j} - y_{CG_i}) \cdot \exp\{-B|\mathbf{r}_{CG_j} - \mathbf{r}_{CG_i}|\} \end{aligned} \right] \quad (6.17.b)$$

$$\frac{\partial}{\partial z_i} [V_{Obs}] = -A \cdot B \cdot \left[ \begin{array}{l} \sum_{j=1, j \neq i}^{N_{Beams}} (z_{CG_i} - z_{CG_j}) \cdot \exp\{-B|\mathbf{r}_{CG_i} - \mathbf{r}_{CG_j}|\} + \\ \sum_{j=1, j \neq i}^{N_{Beams}} (z_{CG_j} - z_{CG_i}) \cdot \exp\{-B|\mathbf{r}_{CG_j} - \mathbf{r}_{CG_i}|\} \end{array} \right] \quad (6.17.c)$$

The rotational components, again are obtained by differentiating the obstacle potential in a similar fashion, viz

$$\frac{\partial}{\partial \theta_i} [V_{Obs}] = -A \cdot B \cdot \left[ \begin{array}{l} \sum_{j=1, j \neq i}^{N_{Beams}} \left\{ \begin{array}{l} (\sin \theta_j \cos \phi_j) \cdot (x_{CG_i} - x_{CG_j}) - \\ (\cos \theta_j \cos \phi_j) \cdot (y_{CG_i} - y_{CG_j}) \end{array} \right\} \cdot \exp\{-B|\mathbf{r}_{CG_i} - \mathbf{r}_{CG_j}|\} - \\ \sum_{j=1, j \neq i}^{N_{Beams}} \left\{ \begin{array}{l} (\sin \theta_i \cos \phi_i) \cdot (x_{CG_j} - x_{CG_i}) - \\ (\cos \theta_i \cos \phi_i) \cdot (y_{CG_j} - y_{CG_i}) \end{array} \right\} \cdot \exp\{-B|\mathbf{r}_{CG_j} - \mathbf{r}_{CG_i}|\} \end{array} \right] \quad (6.17.d)$$

$$\frac{\partial}{\partial \phi_i} [V_{Obs}] = -A \cdot B \cdot \left[ \begin{array}{l} \sum_{j=1, j \neq i}^{N_{Beams}} \left\{ \begin{array}{l} (x_{CG_i} - x_{CG_j}) \cdot (\cos \theta_i \cos \phi_i) + \\ (y_{CG_i} - y_{CG_j}) \cdot (\cos \theta_i \cos \phi_i) - \\ (z_{CG_i} - z_{CG_j}) \cdot (\cos \phi_i) \end{array} \right\} \cdot \exp\{-B|\mathbf{r}_{CG_i} - \mathbf{r}_{CG_j}|\} - \\ \sum_{j=1, j \neq i}^{N_{Beams}} \left\{ \begin{array}{l} (x_{CG_j} - x_{CG_i}) \cdot (\cos \theta_j \cos \phi_j) + \\ (y_{CG_j} - y_{CG_i}) \cdot (\cos \theta_j \cos \phi_j) - \\ (z_{CG_j} - z_{CG_i}) \cdot (\cos \phi_j) \end{array} \right\} \cdot \exp\{-B|\mathbf{r}_{CG_j} - \mathbf{r}_{CG_i}|\} \end{array} \right] \quad (6.17.e)$$

The desired velocities of the individual beams may now be calculated using **Equation 3.7** and the components of the potential gradient derived above using

$$\dot{x}_i|_{Desired} = -\kappa \frac{\partial V / \partial x_i}{|VV|} \quad \text{where} \quad \frac{\partial V}{\partial x_i} = \frac{\partial}{\partial x_i} [V_{Connection}] + \frac{\partial}{\partial x_i} [V_{Obs}] \quad (6.18.a)$$

$$\dot{y}_i|_{Desired} = -\kappa \frac{\partial V / \partial y_i}{|\nabla V|} \quad \text{where} \quad \frac{\partial V}{\partial y_i} = \frac{\partial}{\partial y_i} [V_{Connection}] + \frac{\partial}{\partial y_i} [V_{Obs}] \quad (6.18.b)$$

$$\dot{z}_i|_{Desired} = -\kappa \frac{\partial V / \partial z_i}{|\nabla V|} \quad \text{where} \quad \frac{\partial V}{\partial z_i} = \frac{\partial}{\partial z_i} [V_{Connection}] + \frac{\partial}{\partial z_i} [V_{Obs}] \quad (6.18.c)$$

The required angular velocities are then derived in the same manner as

$$\dot{\theta}_i|_{Desired} = -\kappa \frac{\partial V / \partial \theta_i}{|\nabla V|} \quad \text{where} \quad \frac{\partial V}{\partial \theta_i} = \frac{\partial}{\partial \theta_i} [V_{Connection}] + \frac{\partial}{\partial \theta_i} [V_{Obs}] \quad (6.18.d)$$

$$\dot{\phi}_i|_{Desired} = -\kappa \frac{\partial V / \partial \phi_i}{|\nabla V|} \quad \text{where} \quad \frac{\partial V}{\partial \phi_i} = \frac{\partial}{\partial \phi_i} [V_{Connection}] + \frac{\partial}{\partial \phi_i} [V_{Obs}] \quad (6.18.e)$$

where the normed gradient of the total potential is given by

$$|\nabla V| = \left\{ \sum_{i=1}^{N_{beams}} \left[ \left( \frac{\partial V}{\partial x_i} \right)^2 + \left( \frac{\partial V}{\partial y_i} \right)^2 + \left( \frac{\partial V}{\partial z_i} \right)^2 + \left( \frac{\partial V}{\partial \theta_i} \right)^2 + \left( \frac{\partial V}{\partial \phi_i} \right)^2 \right] \right\}^{\frac{1}{2}} \quad (6.19)$$

and  $\kappa$  is defined by **Equation 3.9**. The translational  $\Delta v$  cost of the individual beams may be calculated from

$$\Delta v_i = \left| \dot{x}_i - [\dot{x}_i]_{Desired} \right| + \left| \dot{y}_i - [\dot{y}_i]_{Desired} \right| + \left| \dot{z}_i - [\dot{z}_i]_{Desired} \right| \quad (6.20.a)$$

and the angular rotation cost,  $\Delta \omega$  may be calculated from

$$\Delta \omega_i = \left| \dot{\theta}_i - [\dot{\theta}_i]_{Desired} \right| + \left| \dot{\phi}_i - [\dot{\phi}_i]_{Desired} \right| \quad (6.20.b)$$

The approximate relationship between  $\Delta v$  and  $\Delta \omega$  defined in **Equation 6.10** may then be used to determine the assembly cost of a given structure. Intervention by the controller is governed by the trigger mechanism described in **Section 3.3.2**. For the structural assembly case, the trigger mechanism used is given as

$$\dot{V}(\mathbf{x}) \geq -V \quad (6.21)$$

Thus, convergence is assured in at least an exponential manner. This may be seen when **Equation 6.21** is integrated to give

$$V \geq V_0 \exp(-t) \quad (6.22)$$

Therefore, the controller has the capability to make large course corrections more often if the potential is large. However, as the potential decreases, control intervention becomes less frequent as the requirement for large course corrections decreases.

When considering the application of collision avoidance to structural assembly, a contradiction emerges. Collisions between elements are clearly undesirable, however, the elements must also be brought into contact for connection at the appropriate time. Examining the total potential, the two components must vanish at the global minimum. Therefore, the repulsive component must be scaled to allow convergence at the appropriate time. This may be carried out by relating the repulsive term to the connection term by a modification of the constant  $A$  in **Equation 6.14** to take the form

$$A = k_1 \{1 - \exp(-k_2 V_{Connection})\} \quad (6.23)$$

where  $k_1$  and  $k_2$  are scaling constants. Therefore, as  $V_{Connection}$  vanishes at the goal, it can be seen that  $V_{Obs}$  now vanishes. Substituting the term for  $A$ , in **Equation 6.14**, three constants,  $B$ ,  $k_1$ , and  $k_2$  appear which must be chosen to ensure collision avoidance. This is far from a straightforward task. The three values currently used are

$$B = 1.1 \quad (6.24.a)$$

$$k_1 = 550 \quad (6.24.b)$$

$$k_2 = 0.0081 \quad (6.24.c)$$

These values have been chosen following an extensive parameter search and will ensure collision avoidance.

Implementing this potential function in free space with the three beams equally spaced along the x-axis on the x-y plane results in the assembly sequence shown in **Figure 6.3.a**. Examining the assembly procedure, the beams do converge to the goal configuration after approximately 120 s. It should be noted that the beams do not converge in an even manner to the solution. Although the physical contraction of the beam spacing to the solution appears straightforward, the interaction of the potential function components is more complex. Examining **Figure 6.3.b** the total potential function is shown. In addition, the individual components of the potential are also plotted. Considering the total potential,

the rate of change is continuously negative definite and so conforms with Lyapunov's method. However, the two components, the connection and repulsive potentials, are not constrained directly and their interaction is more complex. The connection potential can be seen to be continuously decreasing. In contrast though, the repulsive component varies considerably. Initially, the beams are placed too close to each other, therefore, as the beams converge to the solution, the repulsive component begins to grow. Thus, the

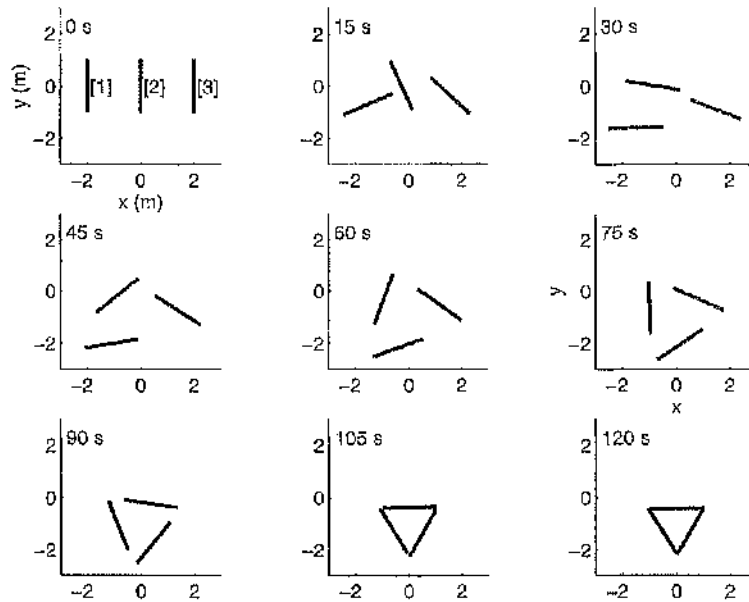


Figure 6.3.a: Triangle Assembly.

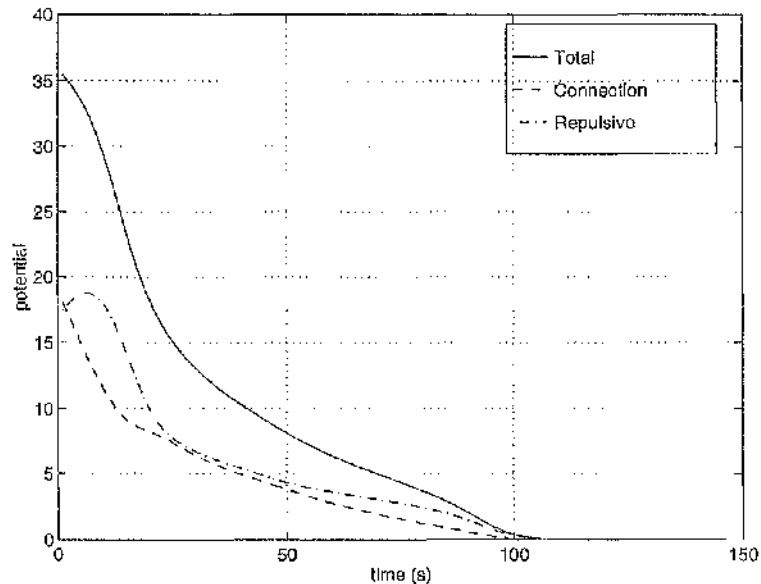


Figure 6.3.b: Potential Function.

repulsive component maintains beam separation while the beams manoeuvre to the correct orientation. Thus, the obstacle potential moderates the pace at which the beams converge to the goal.

The cost of assembly in terms of total  $\Delta v$ , for all the beams is shown in **Figure 6.3.c.i** to **6.3.c.iv**. Examining **Figure 6.3.c.i**, the total cost of assembly including both translation and rotation is shown for all three beams. As can be seen, the cost to each beam is approximately  $5 \text{ m.s}^{-1}$ . This value is reasonable, but higher than desired. Examining the translation and rotation components in **Figures 6.3.c.ii** to **6.3.c.iv**, a value of  $3 \text{ m.s}^{-1}$  for translation and  $2 \text{ m.s}^{-1}$  for rotation is typical. Again, these values are acceptable, although it would be clearly desirable if they were lower.

Therefore, summarising the results;

- The parallel assembly of the triangle has been completed successfully.
- The total potential function behaviour is stable with successful convergence, however the behaviour of the individual components of the total potential are more complex.
- The cost of assembly is reasonable. However, this area will require further study.

The assembly of the triangle has been accomplished. However, this structure may

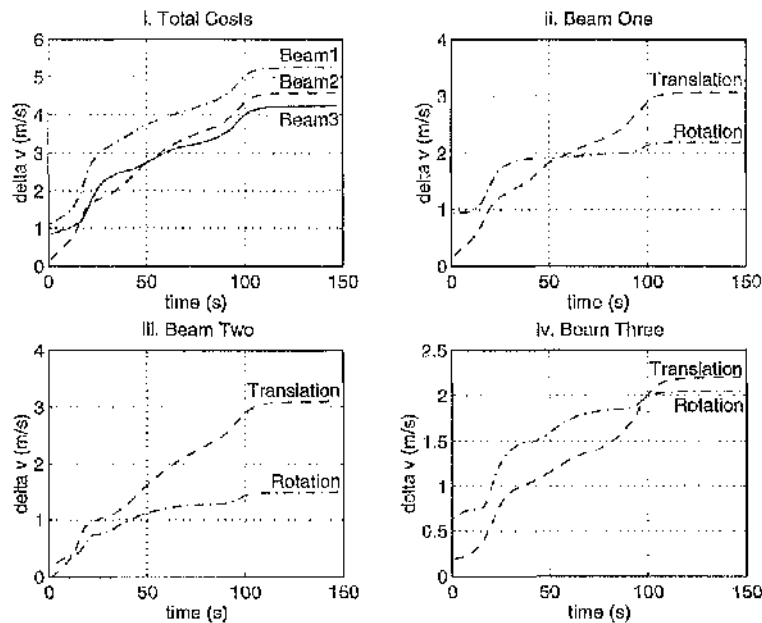


**Figure 6.3.c:**  $\Delta v$  Cost.

be said to be the simplest useful construct and can be regarded as a starting point only. Therefore a more complex structure, the square, will now be examined. This structure adds complexity by demanding not only an additional beam element, but also that the elements be connected together at a specific angle.

#### 6.4 Parallel Assembly. Case II: Square

Considering the final configuration of the elements of a square, it can be seen that it differs from that of the triangle in that the triangular structure is unique with beam elements of identical length resulting in an equilateral triangle. However, this does not hold for more complex structures. Even with a simple structure such as a square, many different solutions are possible which meet the goal as the potential vanishes. For example, the basic rhombus will also satisfy the connection requirements.

##### 6.4.1 Potential Function Definition

To overcome the problem of connection angle, the total potential function must be modified and an additional term added to the potential. This results in a potential function of the form

$$V = V_{Connection} + V_{Obs} + V_{Angle} \quad (6.25)$$

In addition, the connection potential must be modified to account for the four beams in the square structure. Thus, the modified connection potential will take the form

$$V_{Connection} = \frac{1}{2} \left[ |r_1 - \bar{r}_4|^2 + |r_2 - \bar{r}_1|^2 + |r_3 - \bar{r}_2|^2 + |r_4 - \bar{r}_3|^2 \right] \quad (6.26)$$

where the male connector of beam one is connected to the female connector of beam four, beam two to one, beam three to two and finally beam four to beam three.

To obtain the square as a solution, a further criterion must be added to the potential function. This addition must constrain the angle at which the beams connect. The angles which define the orientation of the  $i^{\text{th}}$  beam are  $\theta_i$  and  $\phi_i$ . Therefore, to constrain the angles at which the beams are connected, a quadratic potential may be defined of the form

$$V_{Angle} = f(\theta_i, \phi_i) \quad (6.27)$$

For the case of the square, the orientation of each beam must differ from its neighbours by  $\pi/2$  while the elevation of each beam is constrained to zero. Thus, the potential function takes the form

$$V_{Angle} = \frac{1}{2} \left[ \left\{ (\theta_1 - \theta_4) - \frac{\pi}{2} \right\}^2 + \left\{ (\theta_2 - \theta_1) - \frac{\pi}{2} \right\}^2 + \left\{ (\theta_3 - \theta_2) - \frac{\pi}{2} \right\}^2 + \left\{ (\theta_4 - \theta_3) + \frac{3\pi}{2} \right\}^2 + \phi_1^2 + \phi_2^2 + \phi_3^2 + \phi_4^2 \right] \quad (6.28)$$

where the goal is reached when the orientation of each beam differs from its neighbour by  $\pi/2$  and the elevation is zero. It should be noted however, that to complete a structure such as a square, although three angles are  $\pi/2$ , the final corner angle is  $-3\pi/2$ . This characteristic is simply a geometric property of the square.

#### 6.4.2 Example

Simulating the assembly process with the above potential function produces the results shown in **Figures 6.4**. The physical convergence of the beams is shown in **Figure 6.4.a**. Again, convergence occurs at approximately 350 s. Following an initial phase of manoeuvring to reposition the beams, the square is safely formed without collision. Examining the potential function shown in **Figure 6.4.b**, the manoeuvring phase is apparent where the connection potential convergence is retarded by the repulsive potential. The repulsive potential increases to a point such that separation is maintained until the beams are positioned to allow a safe connection phase from 250 to 350 s.

The cost of assembly, again measured in terms of  $\Delta v$  is shown in **Figure 6.4.c**. The total cost of assembly ranges from 4 to 7 m.s<sup>-1</sup>. This is consistent with the cost of assembling the triangle in the previous section. However, surprisingly, the majority of the

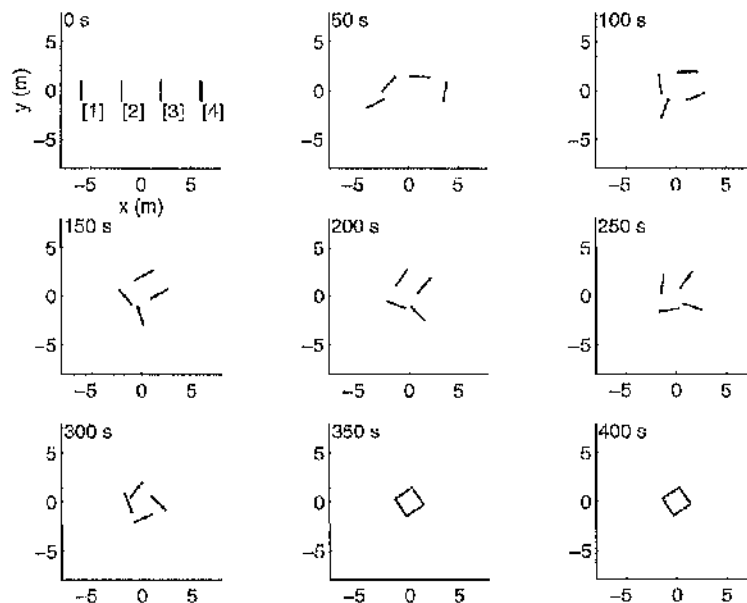


**Figure 6.4.a:** Square Assembly.

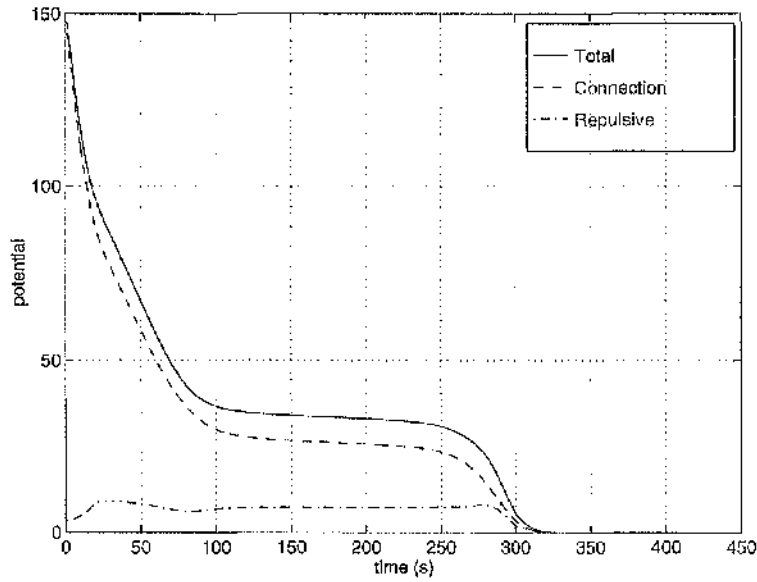


Figure 6.4.b: Potential Function.

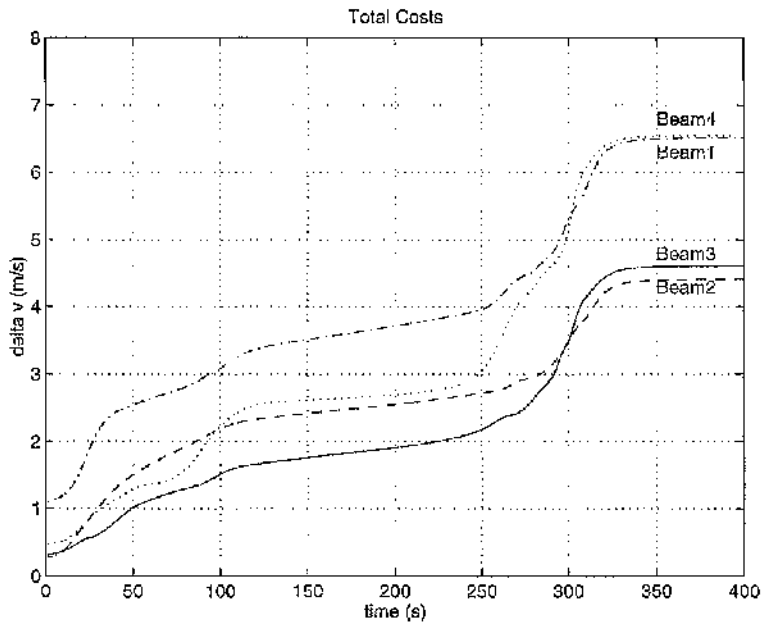


Figure 6.4.c: Total  $\Delta v$  Cost.

$\Delta v$  cost per beam is in the connection phase. Individually, the translation and rotational components of each beam are shown in **Figures 6.4.d.i to iv**. Again, the  $\Delta v$  cost is higher in the connection phase. However, most of the cost is in the translational component. This is consistent with the manoeuvring phase as the bulk of manoeuvring is in the rotational component as the beams re-orientate themselves to allow convergence, whereupon the beams may then translate safely to their final position.

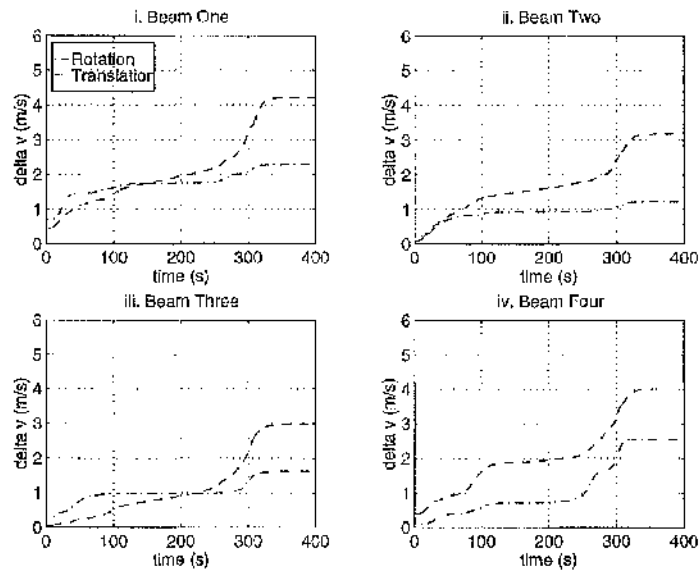


Figure 6.4.d:  $\Delta v$  Cost.

Summarising the results;

- The parallel assembly of the square has been successfully completed.
- The total potential function monotonically decreases. However, the individual components again are more complex with the addition of the angle constraining potential.
- The cost of assembly is reasonable. However the rotational and translation components have different characteristics.

The advantage of a parallel implementation is the simplicity of application. The elements are all active and the final configuration is achieved by using the total potential. However, this is not always practical and has led to the development of a serial implementation to deal with the construction of larger structures.

### 6.5 Serial Assembly. Case 1: Triangle

Until now, it had been assumed that each beam element was grappled by a vehicle which was capable of implementing the translational and rotational changes required by the controller. However, if the assembly of larger structures is considered, then this assumption becomes less practical. It would seem more desirable to utilise only a few vehicles performing repetitive tasks rather than a large number of vehicles performing a single task. Therefore, in this section, it will be assumed that for the three beam elements, there will only be two vehicles available to implement the controller commands. And so, if the controller is to drive the potential function to the goal, the construction sequence must

be implemented serially, rather than in parallel. This serial implementation may be achieved using virtual elements.

### 6.5.1 Virtual Elements

The controller may accomplish the serial assembly of a structure by assuming the existence of one or more *Virtual Elements*. The virtual element is a fictitious beam element which replaces any uncontrolled beam elements. At this point, the total potential may be minimised resulting in a structure consisting of real and virtual beam elements. The virtual elements may then be replaced by real elements as and when controlling vehicles become available. This is carried out by re-starting the convergence of the potential function.

### 6.5.2 Potential Function Definition

As a demonstration of the virtual element technique, the construction of the triangle manufactured in **Section 6.3** will now be extended into a two phase process. Initially beam elements one and two will be assembled in phase one before assembling the final beam element three in phase two. Therefore, the potential function given in **Equation 6.15** will be implemented with the only modification being to the connection potential which will take the form

$$V_{Connection} = \frac{1}{2} \left[ |\mathbf{r}_1 - \bar{\mathbf{r}}_2|^2 + |\mathbf{r}_2 - \bar{\mathbf{r}}_v|^2 + |\mathbf{r}_v - \bar{\mathbf{r}}_1|^2 \right] \quad (6.29)$$

where  $\mathbf{r}_v$  corresponds to the virtual element. The repulsive potential remains identical to that of **Equation 6.14** as the virtual element has no need for any collision avoidance. Following the convergence of the potential to the goal configuration, the virtual beam will be replaced by the third physical beam element. Considering the two controlling vehicles, their objectives during the first phase is to assemble beams one and two, when both vehicles are assigned to these two beams. However during the second phase, one vehicle remains with the partly assembled structure while the second will complete the structure by connecting beam element three.

### 6.5.3 Example

The assembly process will now be simulated using the potential function given in **Equation 6.11**, with the connection potential defined in **Equation 6.29** and the repulsive potential defined in **Equation 6.15**. The initial positions of the beams are such that the three beams are equally spaced along the x-axis at 2 m intervals. Examining **Figure 6.5.a**, the successful assembly of the triangle is shown where the two phases of construction may be clearly seen. Examining the behaviour of the total potential, the two phases of construction become even more apparent. The total potential is shown in **Figure 6.5.b** and,

starting from the initial perturbed state, the potential successfully converges in 100 s. At approximately 130 s the virtual element is replaced with the real third element and the potential is perturbed again. The potential then reconverges to the goal after approximately 200 s. The  $\Delta v$  cost of assembling the triangle is shown in **Figure 6.5.c.i** with the cost to each beam of approximately  $5 \text{ m.s}^{-1}$  being of a value similar to that for the parallel triangle. In fact, ignoring the delayed assembly of beam three, all three components have a  $\Delta v$  profile similar to that of the parallel triangle. Therefore, in this case, it may be said that there is no  $\Delta v$  penalty in moving from the parallel to serial implementation.

Summarising the results;

- The serial assembly of the triangle has been completed successfully.
- The cost of assembly is reasonable. The  $\Delta v$  profile is similar to the parallel implementation.

Thus, the serial implementation of the triangle assembly has been successful. The use of virtual elements in assembly has also been demonstrated. However the technique is unwieldy with the potential function being re-configured many times over. Therefore the following section shall examine the possibility of streamlining this process.

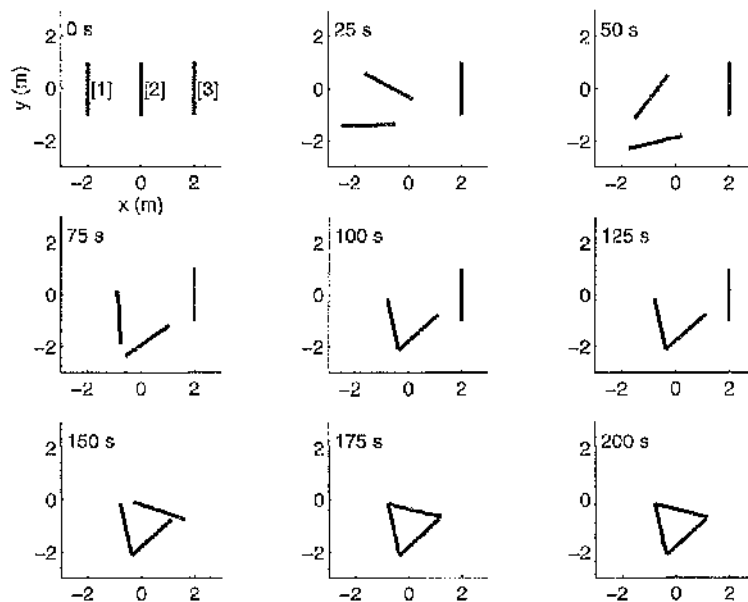


**Figure 6.5.a:** Triangle Assembly.

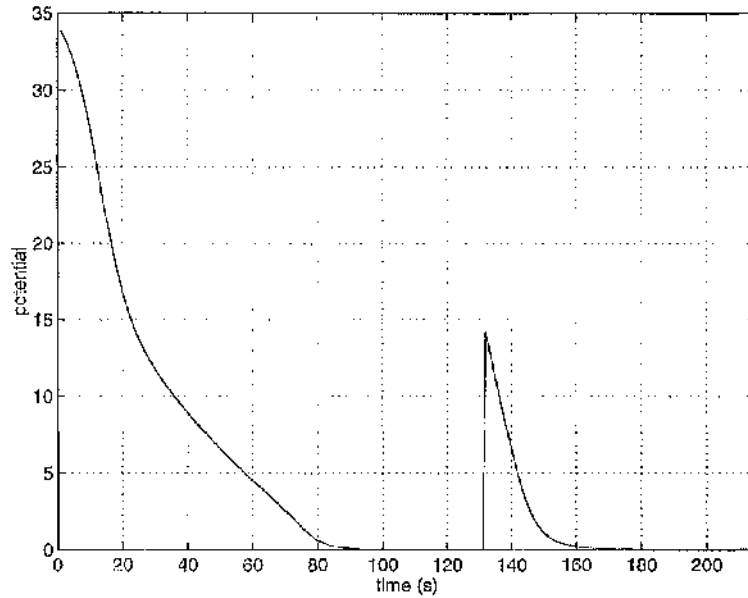


Figure 6.5.b: Potential Function.

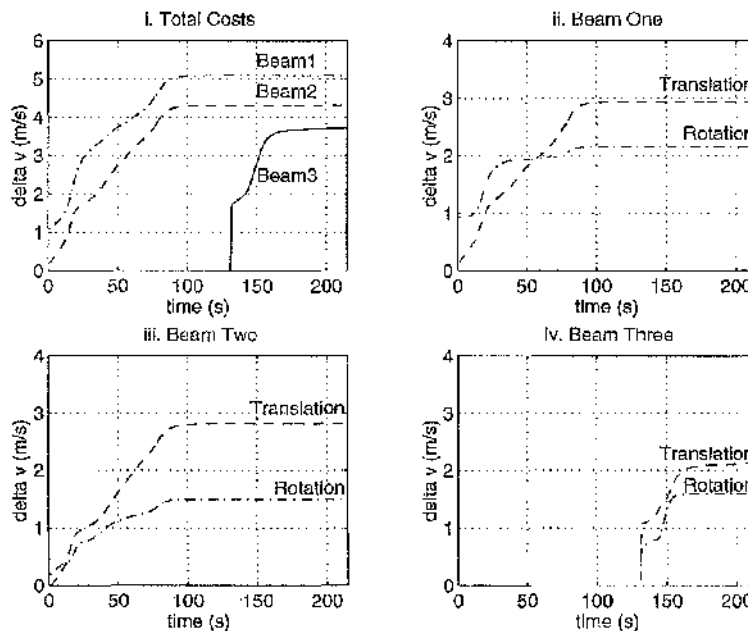


Figure 6.5.c:  $\Delta v$  Cost.

### 6.6 Serial Assembly. Case II: Square

The formation of the triangle structure using virtual elements provides only one method of implementing a serial construction. The virtual element method essentially manufactures the complete structure many times over using these fictitious elements. However, it is more efficient to build the structure over a series of steps using potential functions which relate only to the active beams. This technique will again be demonstrated using the square structure of **Section 6.4** as an example. The fundamental difference

between this method and previous methods is that the connection potential will be modified many times throughout construction.

### 6.6.1 Potential Function Definition

The total potential function for the serial construction of the square is identical to that of the parallel implementation given in **Equation 6.25**. However, a modification of the potential function is made such that the connection potential takes the form

$$V_{\text{Connection}} = \begin{cases} \frac{1}{2} |\mathbf{r}_1 - \bar{\mathbf{r}}_2|^2 & t_o \geq t > t_1 \\ \frac{1}{2} |\mathbf{r}_2 - \bar{\mathbf{r}}_3|^2 & t_1 \geq t > t_2 \\ \frac{1}{2} |\mathbf{r}_3 - \bar{\mathbf{r}}_4|^2 & t_2 \geq t > t_3 \\ \frac{1}{2} |\mathbf{r}_4 - \bar{\mathbf{r}}_1|^2 & t_3 \geq t \geq t_f \end{cases} \quad (6.30)$$

where  $t_o$  is the initial time, and  $t_1$ ,  $t_2$ ,  $t_3$ , and  $t_f$  represent critical points in the manufacture where beam elements are added to the structure. In addition, the initial left hand beam element of the square will be held in place such that the female connector of the other elements will connect to the partially formed structure. For example, during phase one, beam element one will be held stationary while beam element two will manoeuvre to form the connection. The order of manufacture of the square is that beam two shall connect to beam one, beam three to beam two and beam four to beam three thus completing the structure.

### 6.6.2 Example

Using the potential given in **Equation 6.25** with the connection potential given in **Equation 6.30**, the overall results of the test case are shown in **Figures 6.6**. The assembly of the square is shown in **Figure 6.6.a**. Starting from an initial position on the x-axis, the beam elements are split into two groups. Beam one is located at the origin and represents the site of the final structure. The remainder of the beams are distributed along the x-axis and represent a beam store from which the controlling vehicles will retrieve the construction elements. The order of assembly and the assembly phases are clearly shown with beam one stationary and beam two manoeuvring to form the first connection. Following on, beam three then connects to the growing structure and finally beam four completes the square.

The behaviour of the total potential is shown in **Figure 6.6.b**. The perturbation of the potential from equilibrium is seen with three peaks shown. The first peak corresponds to phase one and the second and third peaks at 3100 s and 6900 s correspond to the second

and third phases. There is no perturbation for the final phase as all the beams concerned are already in their correct positions. The total  $\Delta v$  costs for the beams are shown in **Figure 6.6.c**. As expected the total costs are reasonable with values up to  $5 \text{ m.s}^{-1}$ . The first beam which is immobile obviously results in a null cost. However, as the complexity of the structure grows, and the manoeuvring required grows then the  $\Delta v$  cost will also grow. This is apparent when considering the growth of  $\Delta v$  from beam two to beam four.

Examining **Figures 6.6.d.i** to **iv** the individual components of the  $\Delta v$  costs are shown. Again, beam one has no corresponding cost, however the remaining beams do have

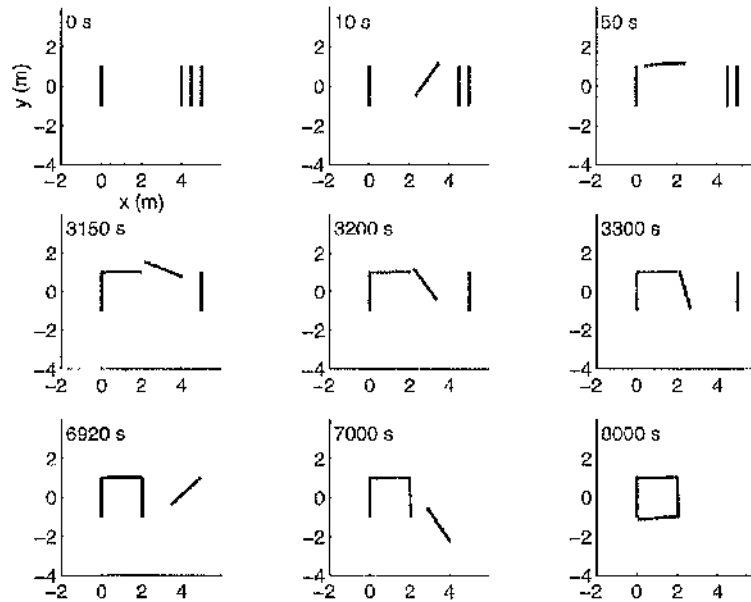


**Figure 6.6.a:** Square Assembly.

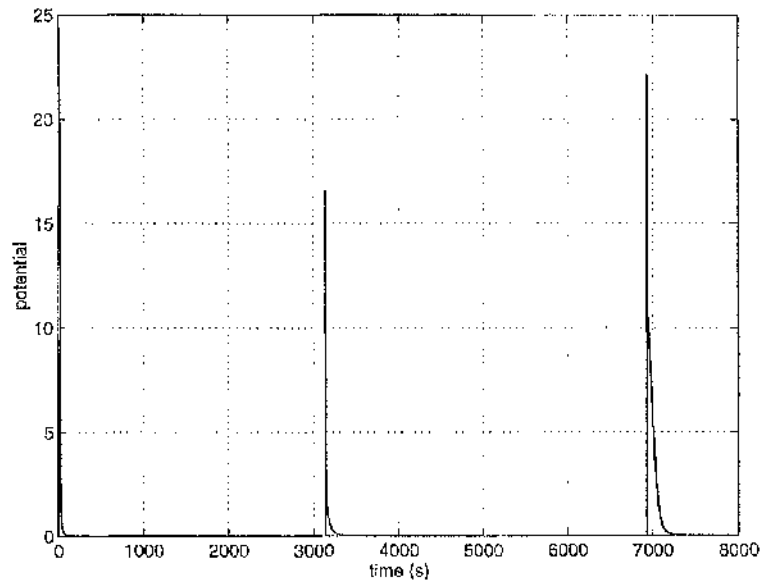


**Figure 6.6.b:** Potential Function.

the expected increase in cost. Although beams two and three have a larger translational cost than rotational cost, beam four has a larger rotational cost than translational. This highlights the active manoeuvring required of the final beam.

Summarising the results;

- The serial assembly of the square has been completed successfully.
- The potential function behaviour is again stable with the individual components merging smoothly to form a total potential.

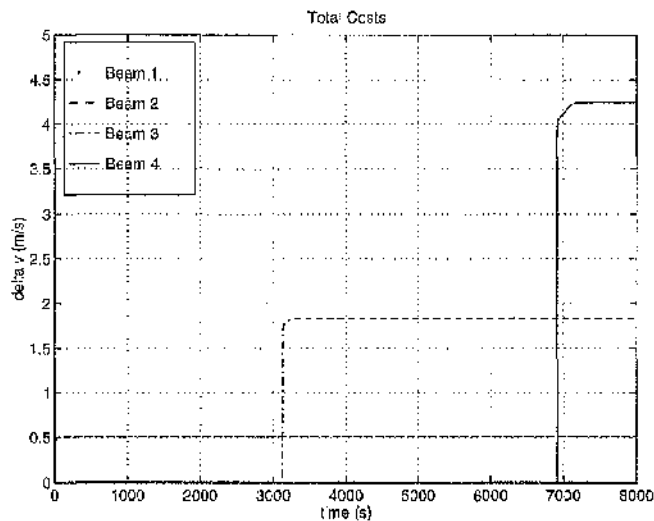


Figure 6.6.c: Total  $\Delta v$  Cost.

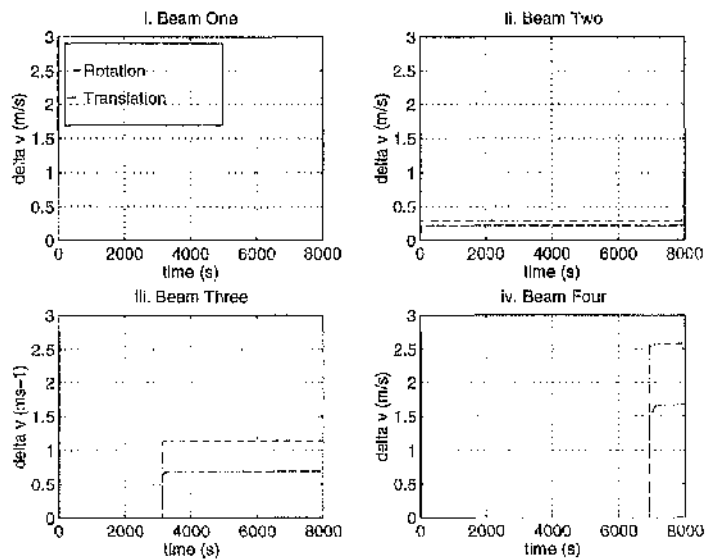


Figure 6.6.d:  $\Delta v$  Cost.

- The cost of assembly is reasonable. However, this will again require further study with an optimisation strategy required. Again, the  $\Delta v$  profile is similar to the parallel implementation.
- As the complexity of a serial structure grows the  $\Delta v$  cost of the final beams will grow correspondingly.

Following the manufacture of the square structure, it is clear the change from a serial implementation to a parallel implementation is not only more practical, but advantageous in terms of the complexity and  $\Delta v$  profile.

## 6.7 Conclusions

Using multi-body potentials and expanding them to include connection constraints has demonstrated the feasibility of using potential functions to manufacture specific structures. The parallel and serial implementation of the construction of the triangle and square have been successful. However, problems and limitations of each method have been highlighted. Thus, in conclusion;

- The parallel method is the ideal approach to using potential functions for manufacture. However, the number of controlling vehicles required to assemble the components quickly increases with the complexity of the structure. Thus for larger structures, the serial implementation becomes more relevant.
- The serial approach has proved successful. The use of virtual elements and a multi-component connection potential have allowed convergence to the goal configuration. However, with this type of structure, the configurations of intermediate structures must be analysed for stability during manufacture.
- Expanding the potential function to include connection constraints has been successful.
- The cost of assembly is reasonable, however the lack of a truly optimal strategy highlights the possibility of reducing this cost.

Following on from the molecular dynamics simulation of **Chapter 5**, the manufacture of the triangle and square by parallel and serial methods has validated the use of multi-body potential functions. However, the potential functions described here have been very specific. The following chapters will examine the possibility of extending this technique to more general structures.

# Chapter Seven: Extended Fabrication

## 7.1 Introduction

Following on from the specific assembly problems described in **Chapter 6**, the objective is now to expand on these to form an overall strategy for assembly of pre-defined structures. The assembly potential functions which have been examined until now have taken the form

$$V = V_{Connection} + V_{Obs} + V_{Angle} \quad (7.1)$$

In this chapter, the above structure shall be maintained, however, each component shall be expanded upon to form a more generalised approach to component assembly. In addition, the two-dimensional case studies examined in **Chapter 6** shall be expanded to include complex three-dimensional structures.

The generalisation of component assembly will expand on the potential function given in **Equation 7.1** to produce a *Global Potential Function*. The global potential function itself shall be based on a *Global State Vector* which comprises of the beam state vector described in **Section 6.2** for every beam within the goal structure. Thus, using these global parameters it is possible to compactly describe the components within the environment. However, a method of describing the goal structure is now required. To describe the goal structure, a *Connectivity Matrix* is used. The connectivity matrix is an  $N_{Beams} \times N_{Beams}$  matrix, where  $N_{Beams}$  is the total number of beams within the structure, which describes the connections within that structure. Therefore it becomes possible to assemble different structures with changes only to the connectivity matrix.

## 7.2 General Fabrication

Expanding the potential function method to general assembly problems demands the representation of a multi-element environment. For complex assembly problems, there will be multiple free-flying vehicles, not just multiple obstacles. In addition, each vehicle must also be aware of the position of every other vehicle. Therefore, each vehicle can be defined by a

state vector  $\mathbf{x}_i$  as defined in **Section 6.2**. Using the state vector of each vehicle, it then becomes possible to define a *Global State Vector*  $\mathbf{X}$ , which corresponds to a system consisting of  $N_{Beams}$  elements, viz.

$$\mathbf{X} = \{ \mathbf{x}_1, \mathbf{x}_2, \dots, \mathbf{x}_{N_{Beams}} \} \quad (7.2)$$

Therefore, the derivation of the global state vector now allows the construction of a *Global Potential Function* representing every element of the assembly process. The global potential function must be defined in such a manner as to correspond with the conventional definition of Lyapunov's method. Thus, the global potential function  $V$  may be described as a function of the global state vector, viz.

$$V = f(\mathbf{X}) \quad (7.3)$$

In particular,  $V$  is constructed such that

$$V \rightarrow 0 \quad \text{as} \quad \mathbf{X} \rightarrow \mathbf{X}_e \quad (7.4)$$

where  $\mathbf{X}_e$  is the desired final state of the elements corresponding to the assembled configuration of the structure. Therefore, utilising the same control function and conventions established in **Chapter 6**, the desired transitional and rotational velocities of all the individual free-flying vehicles may be calculated from a potential function taking the form of **Equation 7.1**.

### 7.2.1 The Control Inputs

If the individual vehicle state vector consists of both translational and rotational components (i.e. a full six degree of freedom problem) then the state vector of the  $i^{\text{th}}$  beam is given by

$$\mathbf{x}_i = \{ \mathbf{r}_i, \theta_i \} \quad (7.5)$$

where  $\theta_i$  is the attitude vector of the vehicle. Using this state vector in conjunction with the discrete method of calculating the controls, the desired translational velocity  $\mathbf{v}_i$  and angular velocity  $\omega_i$  of the  $i^{\text{th}}$  vehicle is given by

$$\mathbf{v}_i |_{Desired} = -\kappa \frac{\nabla_{\mathbf{r}_i} V}{|\nabla V|} \quad \text{where} \quad \nabla_{\mathbf{r}_i} V = -\kappa \frac{\partial V}{\partial \mathbf{r}_i} \quad (7.6)$$

and

$$\omega_i|_{Desired} = -\kappa \frac{\nabla_{\theta_i} V}{|\nabla V|} \quad \text{where} \quad \nabla_{\theta_i} V = -\kappa \frac{\partial V}{\partial \theta_i} \quad (7.7)$$

as detailed in **Section 6.3**.

Thus, the global potential function supplies the desired translational and rotational rates for each vehicle within the global state vector. These rates may then be used by the controller to supply actuator commands to each individual vehicle. The convergence of the controller is, in principle, guaranteed by Lyapunov's theorem. However, as demonstrated in **Section 4.4**, for complex problems local minima do exist in the potential function. It has been found however, that these local minima are not problematic in dynamic systems. It was found in **Chapter 4** that local minima can occur in two-dimensional potential functions. However, in three dimensions these local minima may in fact be unstable saddle points. In addition, since each element is in relative motion, and is repelled by its neighbours, any local minima may only be short-lived. Similarly, the discrete nature of the controller results in a quasi-stochastic 'noise' which may also eject elements from any local minima which form.

### 7.2.2 The Connection Potential

The assembly of simple two-dimensional structures has been demonstrated in **Chapter 6**. To extend the method to include an arbitrary number of beams, as shown in **Figure 7.1**, it then becomes possible to define a potential function encompassing all the connections within a structure. Thus, the enhanced global potential function takes the form

$$V_{Connection} = \frac{1}{2} \sum_{i=1}^{N_{beams}} \sum_{j=1}^{N_{beams}} \varepsilon_{ij} (\mathbf{r}_i - \bar{\mathbf{r}}_j) \cdot (\mathbf{r}_i - \bar{\mathbf{r}}_j) \quad (7.8)$$

where  $\mathbf{r}_i$  and  $\bar{\mathbf{r}}_j$  correspond to the male and female end connectors of the  $i^{\text{th}}$  beam. The manner in which the elements are connected is determined by the connectivity matrix  $\varepsilon_{ij}$  which is constructed from the logic

$$\varepsilon_{ij} = \begin{cases} 1 & \text{Connection between } \bar{\mathbf{r}}_i \text{ and } \mathbf{r}_j \\ 0 & \text{No connection between } \bar{\mathbf{r}}_i \text{ and } \mathbf{r}_j \end{cases} \quad (7.9)$$

where  $(i, j)$  corresponds to the matrix element of column  $i$  and row  $j$ , read from the top left of the connectivity matrix. Thus, a sparse matrix is obtained which consists solely of binary elements. For example, the connectivity matrix which corresponds to four beams formed into a square is given by

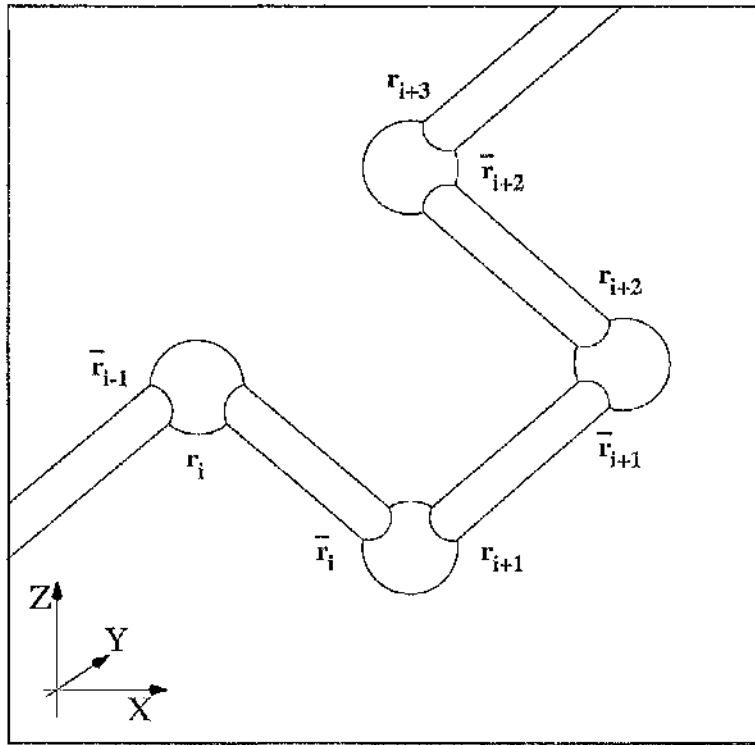


Figure 7.1: Generic Beam Connections.

$$\varepsilon_{ij} = \begin{matrix} & \xrightarrow{i} \\ \downarrow j & \begin{pmatrix} 0 & 1 & 0 & 0 \\ 0 & 0 & 1 & 0 \\ 0 & 0 & 0 & 1 \\ 1 & 0 & 0 & 0 \end{pmatrix} \end{matrix} \quad (7.10)$$

which corresponds to beam one connecting to beam four, beam two to one, beam three to two and beam four to three, thus resulting in the square.

### 7.2.3 The Obstacle Potential

For a large global state vector, consisting of many distinct objects, the repulsive component must contain every possible combination resulting in a collision. Therefore, a term must appear in the global potential relating every object to every other object within the global state vector. As in **Chapter 6**, choosing a Gaussian obstacle potential, the *Global Obstacle Potential* is given as

$$V_{Obs} = A \sum_{i=1}^{N_{Beams}} \sum_{j=1, j \neq i}^{N_{Beams}} \exp\left\{-B|\mathbf{r}_{CGi} - \mathbf{r}_{CGj}|^2\right\} \quad (7.11)$$

where  $\mathbf{r}_{CG}$  corresponds to the position of the centre of mass of each object within the global state vector and  $A$  is defined in **Equation 6.23**.

### 7.2.4 The Angle Potential

Finally, it had been considered in **Chapter 6** that the angle potential would maintain the angular separation between two beam elements. However, it is possible to express the angle potential in a more general form which will place the  $i^{\text{th}}$  beam in a specific orientation. Thus, expressing the angle potential as

$$V_{Angle} = \frac{1}{2} \sum_{i=1}^{N_{Beams}} \sum_{j=1}^{N_{Beams}} \varepsilon_{ij} (\theta_i - \bar{\theta}_i)^2 + \frac{1}{2} \sum_{i=1}^{N_{Beams}} \sum_{j=1}^{N_{Beams}} \varepsilon_{ij} (\phi_i - \bar{\phi}_i)^2 \quad (7.12)$$

results in a potential where the  $i^{\text{th}}$  beam is manoeuvred to a specific orientation  $(\bar{\theta}_i, \bar{\phi}_i)$ . The purpose in doing so is that the target orientation may now be expressed in an explicit fashion independent of any other parameters. However, in some cases, the orientation of the  $i^{\text{th}}$  beam may also be related to the orientation of the  $j^{\text{th}}$  beam element. The consequence of defining beam orientations in such a manner is that the relative positioning of the beams may be important, and not the individual orientation of the beams i.e. for the construction of the square in **Section 6.4** the beam orientations are not specified, but, the relative orientations are. Thus, it is possible to express the target orientation as

$$\bar{\theta}_i = f(\theta_j) \quad (7.13.a)$$

and

$$\bar{\phi}_i = g(\phi_j) \quad (7.13.b)$$

The advantage to such a definition is that the attitude of any beam element need not be individually defined, thus allowing easy assembly of more complex structures.

### 7.3 The Connectivity Matrix

The development of the general potential function, **Equation. 7.8**, alters the emphasis on design from that of the potential function to that of the connectivity matrix. The connectivity matrix becomes all important and determines the exact form of the final structure. Therefore it is important to establish conventions for the design of the connectivity matrix to optimise assembly. As the size of the structure grows, then the size of the connectivity matrix will also grow. Thus, as the matrix becomes large, the manual development of the connections becomes impractical. However, the problem does lend itself

to the use of design tools such as CAD or rapid prototyping packages which include the rules and conventions of assembly. As examined in the following sections, this allows the development, storage and copying of empirical connectivity matrices for use as building blocks within larger, more complex, structures.

### 7.3.1 Common Beams

When two structures have common beams, as shown in **Figure 7.2**, where two square structures are joined along a common beam, the desired operation is as follows

$$\varepsilon_{ij}|_{goal} = \varepsilon_{ij}|_{square1} \oplus \varepsilon_{ij}|_{square2} \quad (7.14)$$

where  $\oplus$  is used to denote an appropriate union of the two matrices. Thus, knowing the square structure connectivity matrix, which takes the form

$$\varepsilon_{ij}|_{square} = \begin{pmatrix} 0 & 1 & 0 & 0 \\ 0 & 0 & 1 & 0 \\ 0 & 0 & 0 & 1 \\ 1 & 0 & 0 & 0 \end{pmatrix} \quad (7.15)$$

the goal connectivity matrix may then be derived.

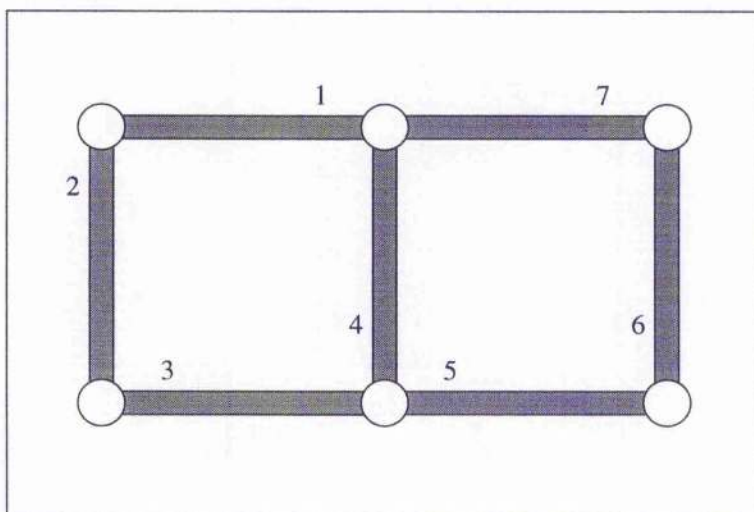


**Figure 7.2:** Common Beam Connection.

The matrix for the complete structure may be derived by first creating an  $N_{Beams} \times N_{Beams}$  null matrix, where  $N_{Beams}$  is the total number of elements within the completed structure. Examining **Figure 7.2**, for the structure envisaged here,  $N_{Beams}$  will clearly be seven. In addition, if one of the squares is assumed to be added to the other, then the original

square connectivity matrix may be mapped onto the upper left quadrant of the basic matrix, viz.

$$\varepsilon_{ij}|_{goal} = \begin{bmatrix} 0 & 1 & 0 & 0 & 0 & 0 & 0 \\ 0 & 0 & 1 & 0 & 0 & 0 & 0 \\ 0 & 0 & 0 & 1 & 0 & 0 & 0 \\ 1 & 0 & 0 & 0 & 0 & 0 & 0 \\ 0 & 0 & 0 & 0 & 0 & 0 & 0 \\ 0 & 0 & 0 & 0 & 0 & 0 & 0 \\ 0 & 0 & 0 & 0 & 0 & 0 & 0 \end{bmatrix} \quad (7.16.a)$$

where the highlighted section corresponds to the square connectivity matrix. In this case, the common element is beam four. Therefore, the addition of the second square connectivity matrix to Equation 7.16.a will incorporate changes to row and column four. This is carried out by adding the second matrix to the larger matrix at element (4,4), viz.

$$\varepsilon_{ij}|_{goal} = \begin{bmatrix} 0 & 1 & 0 & 0 & 0 & 0 & 0 \\ 0 & 0 & 1 & 0 & 0 & 0 & 0 \\ 0 & 0 & 0 & 1 & 0 & 0 & 0 \\ 1 & 0 & 0 & 0 & 1 & 0 & 0 \\ 0 & 0 & 0 & 0 & 0 & 1 & 0 \\ 0 & 0 & 0 & 0 & 0 & 0 & 1 \\ 0 & 0 & 0 & 1 & 0 & 0 & 0 \end{bmatrix} \quad (7.16.b)$$

thus giving the complete connectivity matrix.

### 7.3.2 Common Nodes

A common node connection, as shown in Figure 7.3, is a simple connection between two structures involving multiple connections between beams. The corresponding operation to achieve the goal connectivity matrix is given by

$$\varepsilon_{ij}|_{goal} = \varepsilon_{ij}|_{triangle1} \otimes \varepsilon_{ij}|_{triangle2} \quad (7.17)$$

where  $\otimes$  is used to denote an appropriate union of the two matrices and the connectivity matrix corresponding to a triangle is given by

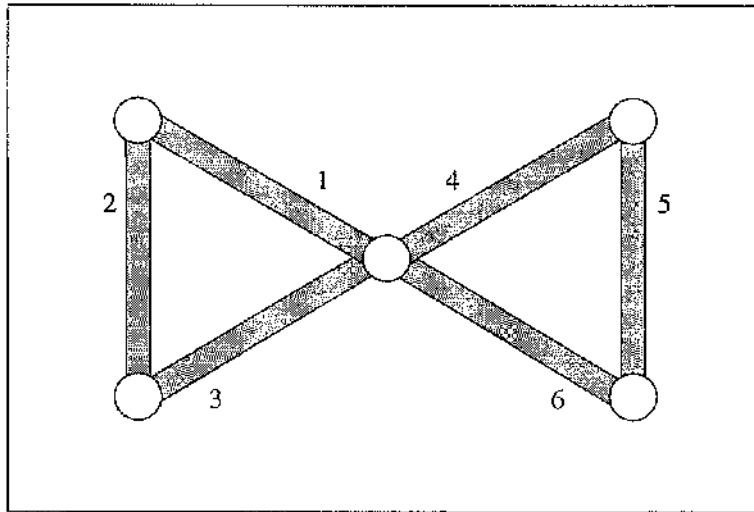


Figure 7.3: Common Node Connection.

$$\varepsilon_{ij}|_{triangle} = \begin{Bmatrix} 0 & 1 & 0 \\ 0 & 0 & 1 \\ 1 & 0 & 0 \end{Bmatrix} \quad (7.18)$$

Again, examining **Figure 7.3**, the goal structure consists of six beam elements, therefore, using an identical technique as for the common beam connection a null  $6 \times 6$  matrix is generated. The two triangle connectivity matrices are then added to the null matrix in such a manner that there are no connections between the two structures, viz.

$$\varepsilon_{ij}|_{goal} = \begin{Bmatrix} 0 & 1 & 0 & 0 & 0 & 0 \\ 0 & 0 & 1 & 0 & 0 & 0 \\ 1 & 0 & 0 & 0 & 0 & 0 \\ 0 & 0 & 0 & 0 & 1 & 0 \\ 0 & 0 & 0 & 0 & 0 & 1 \\ 0 & 0 & 0 & 1 & 0 & 0 \end{Bmatrix} \quad (7.19)$$

The information regarding which node connection to join the structures may then be added. The convention that the male connector corresponds to the  $i^{\text{th}}$  column and the female connector corresponds to the  $j^{\text{th}}$  row will be used. Examining the goal structure, male connectors one and four are connected to female connectors three and six, thus resulting in the additions to the connectivity matrix given by

$$\varepsilon_{ij}|_{goal} = \begin{Bmatrix} 0 & 1 & 0 & 0 & 0 & 0 \\ 0 & 0 & 1 & 0 & 0 & 0 \\ 1 & 0 & 0 & \mathbf{1} & 0 & 0 \\ 0 & 0 & 0 & 0 & 1 & 0 \\ 0 & 0 & 0 & 0 & 0 & 1 \\ \mathbf{1} & 0 & 0 & 1 & 0 & 0 \end{Bmatrix} \quad (7.20)$$

where the highlighted elements correspond to the connections between the structures, thus generating the goal connectivity matrix.

### 7.3.3 Connecting Beams

A structure which demands the connection of two smaller structures using a beam is shown in **Figure 7.4**. The connectivity matrix, may again be generated using a null  $N_{Beams} \times N_{Beams}$  matrix, where  $N_{Beams}$  for this case is 7. The two triangles in the goal structure are connected together using a single additional beam. The operation required to construct the goal connectivity matrix is defined as

$$\varepsilon_{ij}|_{goal} = \varepsilon_{ij}|_{triangle1} \otimes \varepsilon_{ij}|_{beam} \otimes \varepsilon_{ij}|_{triangle2} \quad (7.21)$$

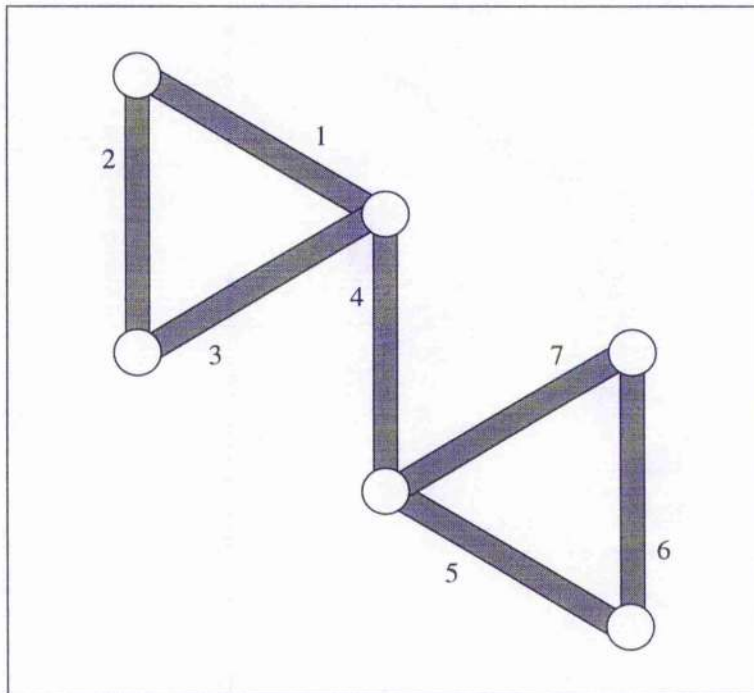


**Figure 7.4:** Connecting Beam.

The two triangular structures may then be added to the null matrix in such a fashion that they are unconnected. This results in the matrix

$$\varepsilon_{ij}|_{goal} = \begin{pmatrix} 0 & 1 & 0 & 0 & 0 & 0 & 0 \\ 0 & 0 & 1 & 0 & 0 & 0 & 0 \\ 1 & 0 & 0 & 0 & 0 & 0 & 0 \\ 0 & 0 & 0 & 0 & 0 & 0 & 0 \\ 0 & 0 & 0 & 0 & 0 & 1 & 0 \\ 0 & 0 & 0 & 0 & 0 & 0 & 1 \\ 0 & 0 & 0 & 0 & 1 & 0 & 0 \end{pmatrix} \quad (7.22)$$

where the highlighted areas represent the two triangle matrices, given in **Equation 7.18**.

The information regarding the positioning of the connecting beam is now required. The first structure must be connected to the second structure via two nodes by a joining member. In essence, this type of connection is a common node connection performed for two nodes simultaneously. In this case, the connecting beam is beam four with the male connector of beam four joined to the female connector of beam three. In addition, the male connector of beam five is connected to the female connector of beam four. This results in the additions to the goal matrix shown by the highlighted areas, viz.

$$\varepsilon_{ij}|_{goal} = \begin{pmatrix} 0 & 1 & 0 & 0 & 0 & 0 & 0 \\ 0 & 0 & 1 & 0 & 0 & 0 & 0 \\ 1 & 0 & 0 & 1 & 0 & 0 & 0 \\ 0 & 0 & 0 & 0 & 1 & 0 & 0 \\ 0 & 0 & 0 & 0 & 0 & 1 & 0 \\ 0 & 0 & 0 & 0 & 0 & 0 & 1 \\ 0 & 0 & 0 & 0 & 1 & 0 & 0 \end{pmatrix} \quad (7.23)$$

Although the three methods described above are all capable of deriving the connectivity matrix analytically, each method requires detailed information regarding the type and specific node information of the connection. This can be a very time consuming process, but may be automated using a graphical interface such as a CAD package. This allows the development, storage and copying of different structures which may be used in a final goal structure. The package is then capable of developing the complete connectivity matrix. Thus, the complete design system, shown in **Figure 7.5** will be capable of taking a developed CAD model, and processing the complete connectivity matrix. Through Lyapunov's method this will then result directly in actuator commands to the controlling vehicles for the assembly of the structure.

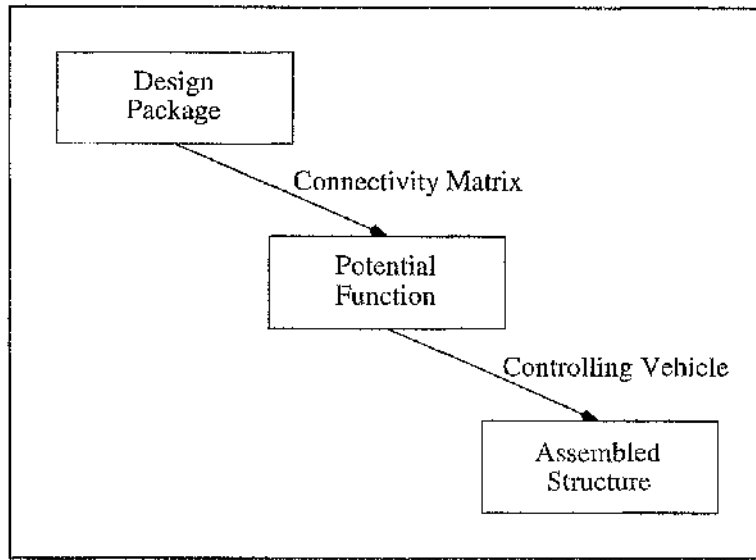


**Figure 7.5:** Design Integration.

As the size of the connectivity matrix grows, it becomes impractical to connect every beam in a single effort, Therefore, as discussed in **Chapter 6**, a method of serial manufacturing is required. Within the connectivity matrix, the serial assembly of a structure will result in the activation of only a fraction of the total matrix. If the total potential of the matrix is calculated, the potential will never converge since there will be inactive beam elements. Two methods of circumventing this problem are examined within the following examples and in **Chapter 8**. In the following examples, techniques are examined which group the active components of a structure into specific areas of the total matrix which are dealt with in a serial fashion. The second method, examined in **Chapter 8** makes use of multiple connectivity matrices and their interaction in which all the elements are active.

## 7.4 The Cube

When assembled, the cube forms a building block structure which may be used to assemble more complex structures. Therefore, this structure will be examined in detail with both a serial and parallel implementation. However, if the structure is assembled using a global potential, then the connectivity matrix must be carefully designed.

### 7.4.1 The Connectivity Matrix

The basic cube structure may be assembled using twelve beams connected together. Thus, the connectivity matrix will consist of a  $12 \times 12$  matrix. However, the structure may also be considered to be assembled from even simpler structures. If the cube is considered to be assembled from two facing squares with four connecting beams joining the corners, then the connectivity matrix of the cube will take the form

$$\varepsilon_{ij} = \left\{ \begin{array}{ccc} \varepsilon_{ij}^{Square1} & \varepsilon_{ij}^{Connecting} & [0] \\ [0] & [0] & \varepsilon_{ij}^{Connecting} \\ [0] & [0] & \varepsilon_{ij}^{Square2} \end{array} \right\} \quad (7.24)$$

where  $[0]$  is a  $4 \times 4$  null matrix. Expressing the connectivity matrix in full gives

$$\varepsilon_{ij} = \left\{ \begin{array}{cccccccccccc} 0 & 1 & 0 & 0 & 1 & 0 & 0 & 0 & 0 & 0 & 0 & 0 \\ 0 & 0 & 1 & 0 & 0 & 1 & 0 & 0 & 0 & 0 & 0 & 0 \\ 0 & 0 & 0 & 1 & 0 & 0 & 1 & 0 & 0 & 0 & 0 & 0 \\ 1 & 0 & 0 & 0 & 0 & 0 & 0 & 1 & 0 & 0 & 0 & 0 \\ 0 & 0 & 0 & 0 & 0 & 0 & 0 & 0 & 1 & 0 & 0 & 0 \\ 0 & 0 & 0 & 0 & 0 & 0 & 0 & 0 & 0 & 1 & 0 & 0 \\ 0 & 0 & 0 & 0 & 0 & 0 & 0 & 0 & 0 & 0 & 1 & 0 \\ 0 & 0 & 0 & 0 & 0 & 0 & 0 & 0 & 0 & 0 & 0 & 1 \\ 0 & 0 & 0 & 0 & 0 & 0 & 0 & 0 & 0 & 1 & 0 & 0 \\ 0 & 0 & 0 & 0 & 0 & 0 & 0 & 0 & 0 & 0 & 1 & 0 \\ 0 & 0 & 0 & 0 & 0 & 0 & 0 & 0 & 0 & 0 & 0 & 1 \\ 0 & 0 & 0 & 0 & 0 & 0 & 0 & 0 & 1 & 0 & 0 & 0 \end{array} \right\} \quad (7.25)$$

Thus, with the connectivity matrix, the global state vector and the global potential function, the cube may be assembled. In the following examples, the cube shall be assembled in both a parallel and serial manner.

#### 7.4.2 Parallel Cube

The parallel assembly method implements the connectivity matrix of the cube, given in **Equation 7.25** in a single effort using the global potential function

$$V = \frac{1}{2} \sum_{i=1}^{N_{Beams}} \sum_{j=1}^{N_{Beams}} \varepsilon_{ij} (\mathbf{r}_i - \bar{\mathbf{r}}_j) \cdot (\mathbf{r}_i - \bar{\mathbf{r}}_j) + A \sum_{i=1}^{N_{Beams}} \sum_{j=1, j \neq i}^{N_{Beams}} \exp \left[ -B |\mathbf{r}_{CGi} - \mathbf{r}_{CGj}|^2 \right] \quad (7.26)$$

$$\frac{1}{2} \sum_{i=1}^{N_{Beams}} \sum_{j=1}^{N_{Beams}} \varepsilon_{ij} (\theta_i - \bar{\theta}_j)^2 + \frac{1}{2} \sum_{i=1}^{N_{Beams}} \sum_{j=1}^{N_{Beams}} \varepsilon_{ij} (\phi_i - \bar{\phi}_j)^2$$

where  $A$  is again defined in **Equation 6.13** and the final two terms representing the angular constraints are given as

$$(\bar{\theta}_i, \bar{\phi}_i) = (\pi/2, \phi_{i-1} + \pi/2) \quad (7.27.a)$$

which forms two square sections in the  $y-z$  plane while the connecting structure is defined using

$$(\bar{\theta}_i, \bar{\phi}_i) = (0,0) \quad (7.27.b)$$

Thus, assembly can proceed with the use of twelve controlling vehicles manoeuvring the twelve beams into the final configuration.

Propagating the assembly of the beams, the results are shown in **Figures 7.6**. The assembly of the beams into the cube is shown in **Figure 7.6.a**. As can be seen the beams converge to the goal structure in approximately 800 s. This is also shown in **Figure 7.6.b** where the behaviour of the potential function is plotted and the smooth asymptotic convergence is clear. However, of more interest is the cost shown in **Figure 7.6.c** where the  $\Delta v$  cost of every beam element is shown. The maximum  $\Delta v$  cost of any beam is  $0.27 \text{ m}\cdot\text{s}^{-1}$  with an average value of approximately  $0.2 \text{ m}\cdot\text{s}^{-1}$ . This is a reasonable value, however, the comparison between this value and a serial implementation of the cube will provide a clearer measure of the  $\Delta v$ .

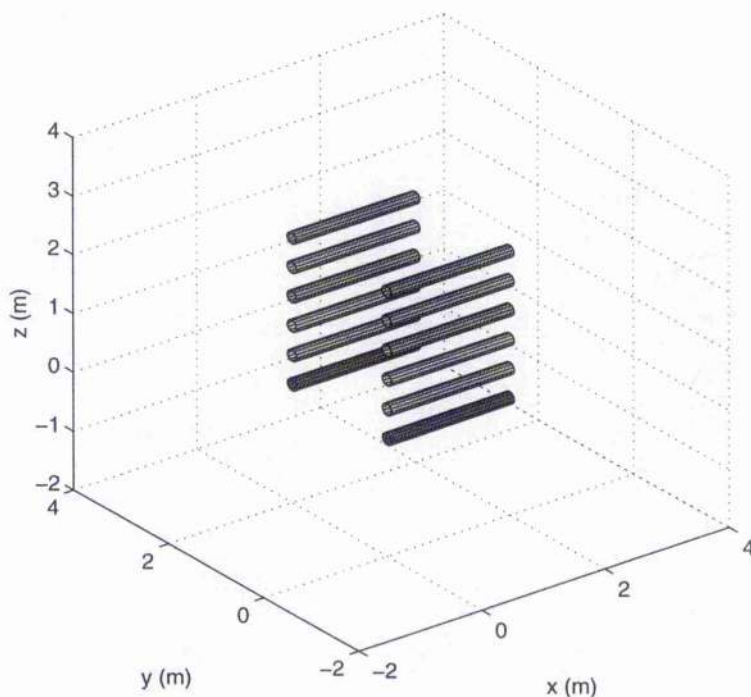


**Figure 7.6.a.i:** Parallel Cube Assembly: Time = 0 s.

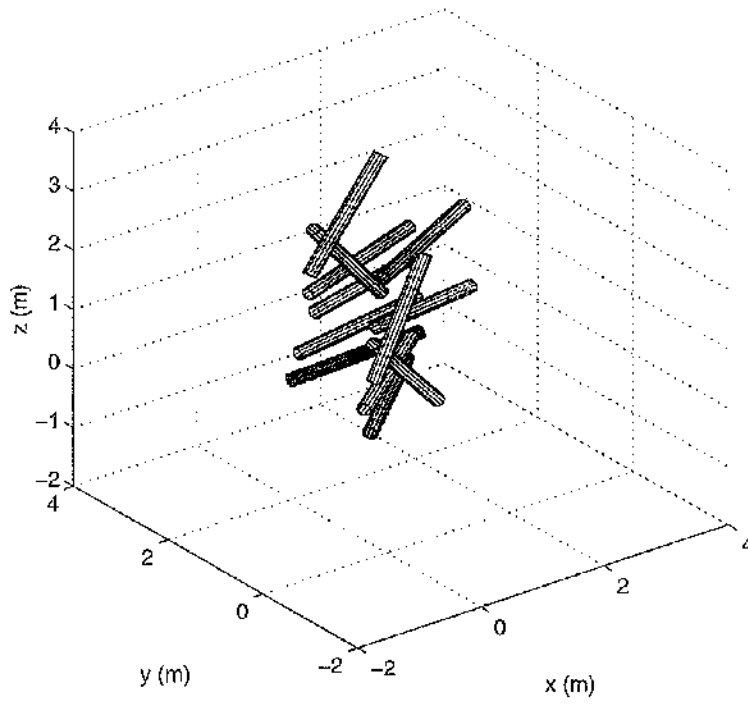


Figure 7.6.a.ii: Parallel Cube Assembly; Time = 25 s.

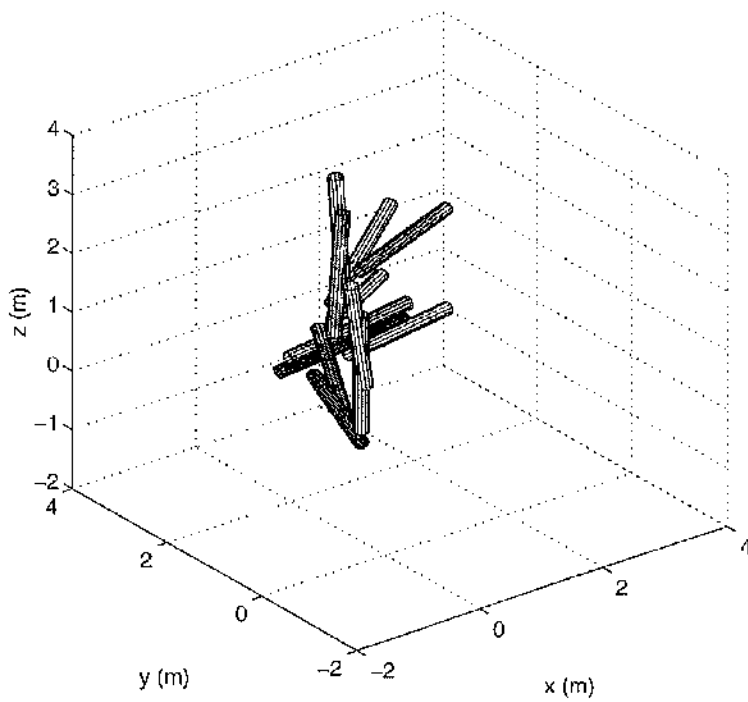


Figure 7.6.a.iii: Parallel Cube Assembly; Time = 50 s.

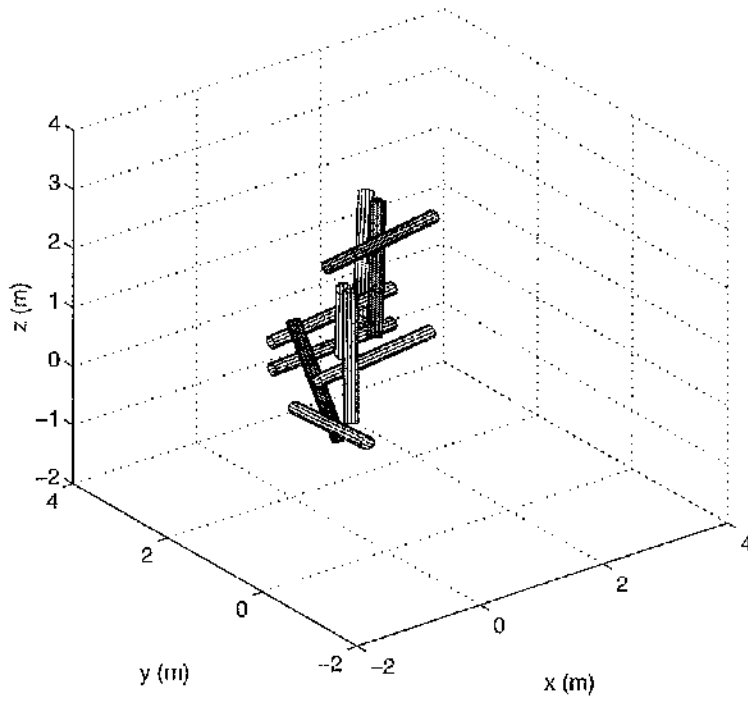


Figure 7.6.a.iv: Parallel Cube Assembly: Time = 75 s.

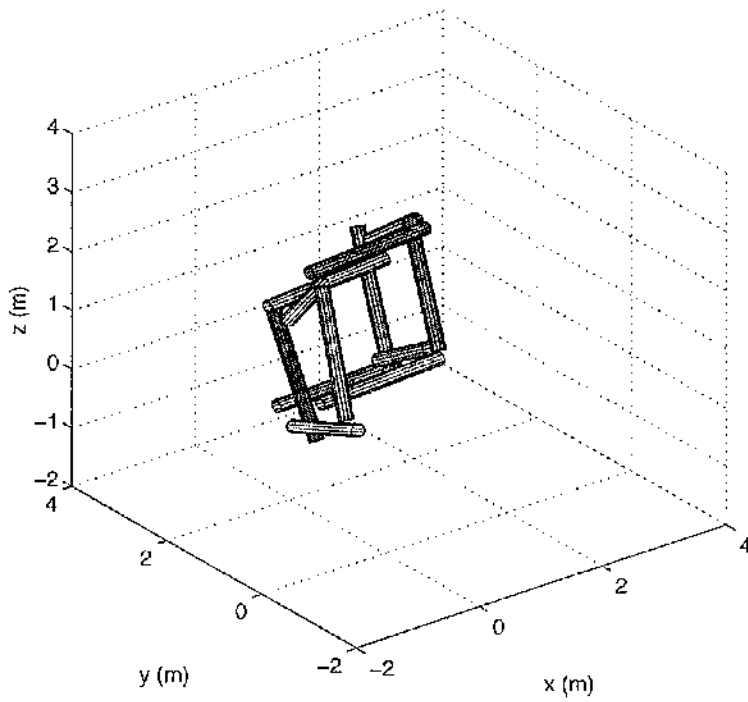


Figure 7.6.a.v: Parallel Cube Assembly: Time = 100 s.

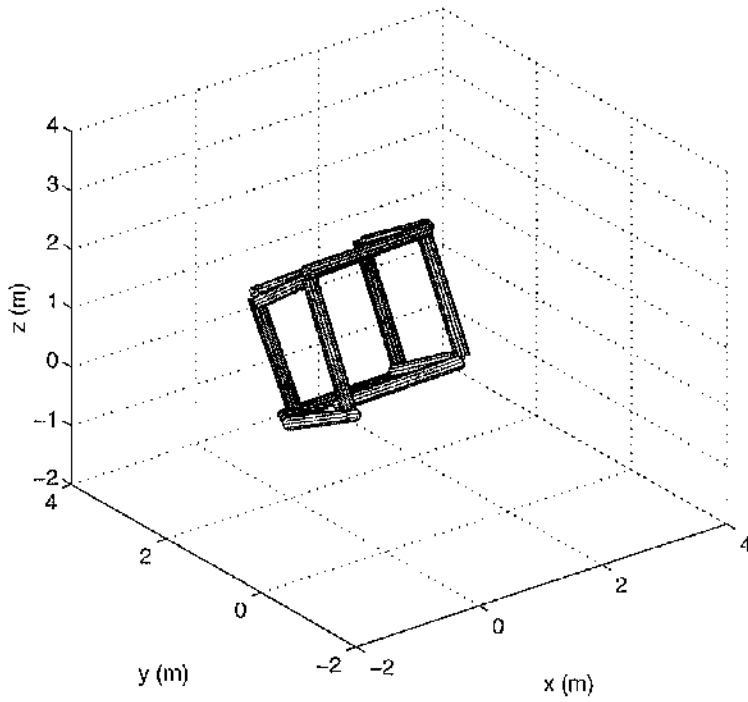


Figure 7.6.a.vi: Parallel Cube Assembly: Time = 125 s.

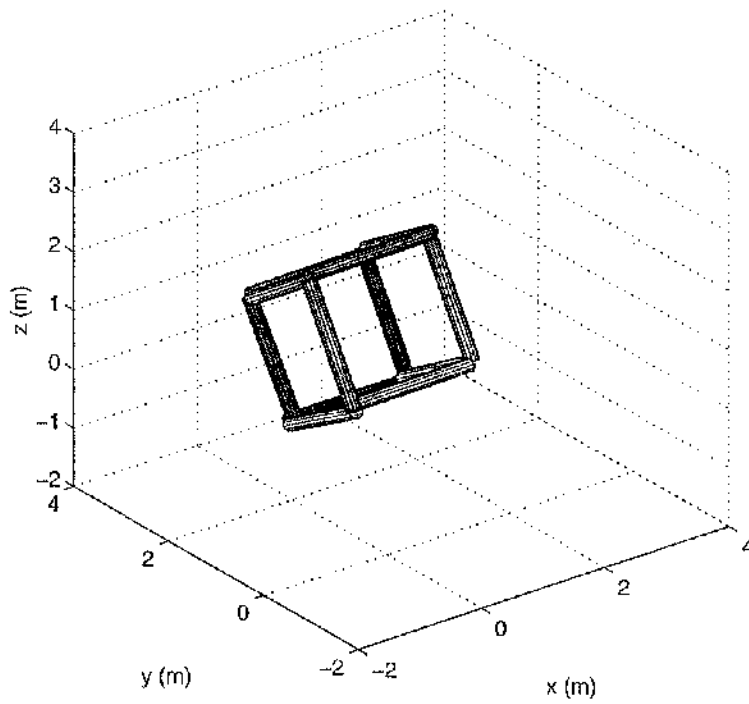
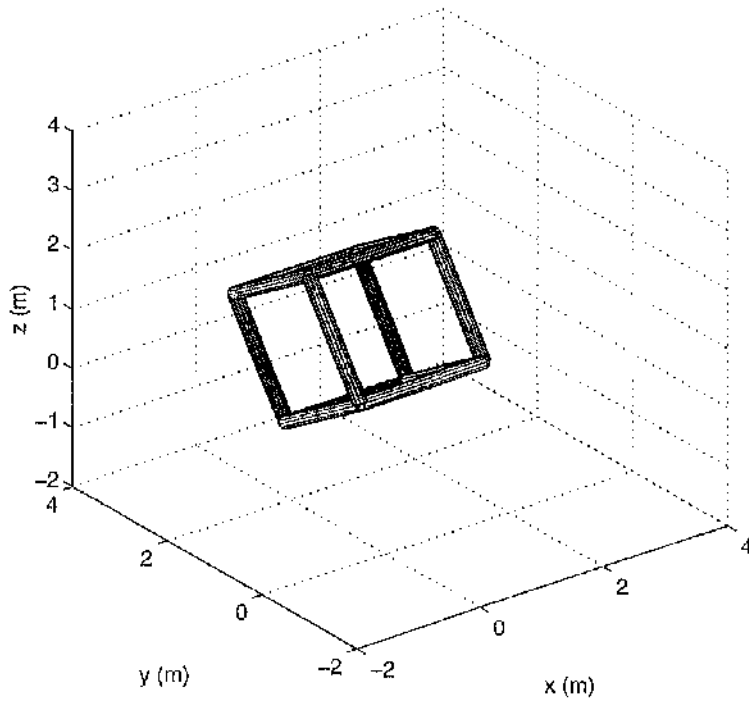
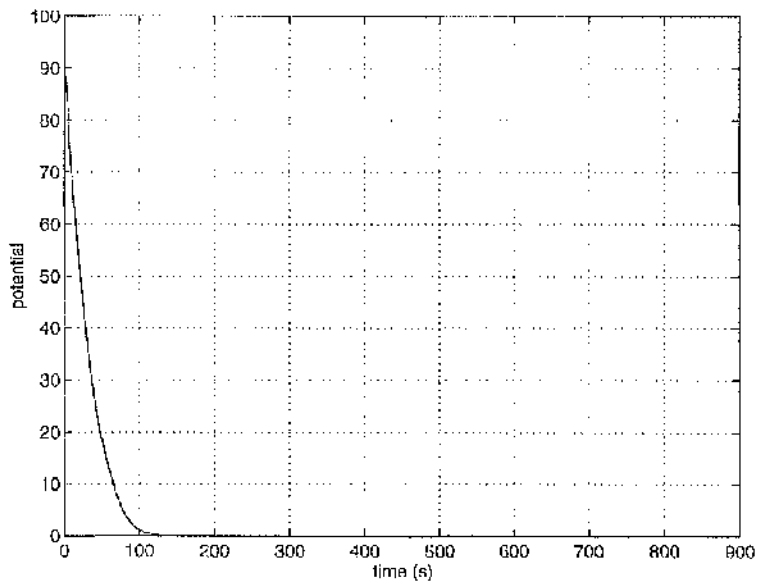


Figure 7.6.a.vii: Parallel Cube Assembly: Time = 150 s.



**Figure 7.6.a.viii:** Parallel Cube Assembly: Time = 500 s.



**Figure 7.6.b:** Potential Function.



**7.7.a.** As can be seen, the beams do converge, in three phases, to the desired cube structure. However, the time of assembly is now 2800 s with the three phases completing in 200, 1000 and 2800 s respectively. This is shown in **Figure 7.7.b** where the potential function is plotted and the three phases are clear with each phase converging in a smooth and stable manner. The  $\Delta v$  cost, shown in **Figure 7.7.c** again demonstrates a slightly higher  $\Delta v$  value than the parallel case. The maximum  $\Delta v$  cost of any beam is  $0.4 \text{ m.s}^{-1}$  with an average value of  $0.25 \text{ m.s}^{-1}$ . However, the total cost of assembly is borne over four vehicles rather than twelve, thus the average propellant requirement of every vehicle is higher than that of the parallel case.

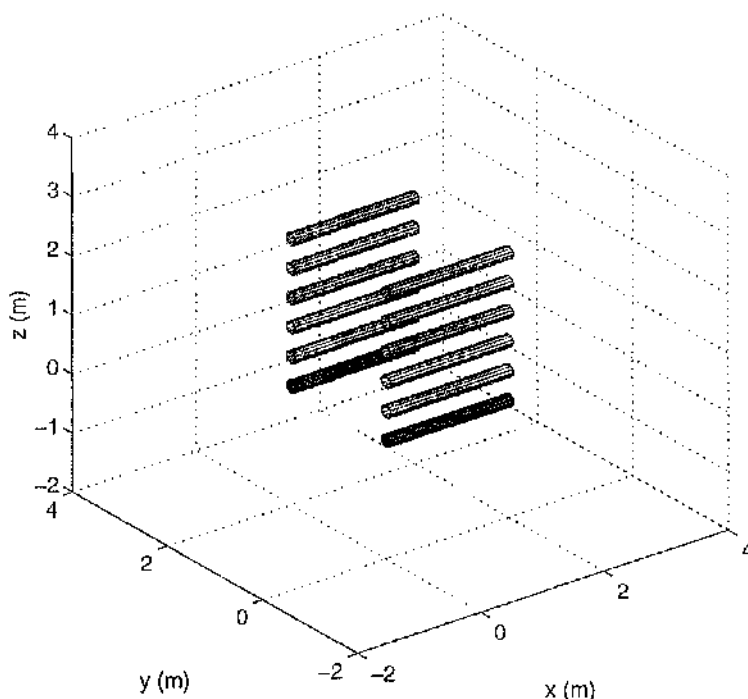


**Figure 7.7.a.i:** Serial Cube Assembly: Time = 0 s.

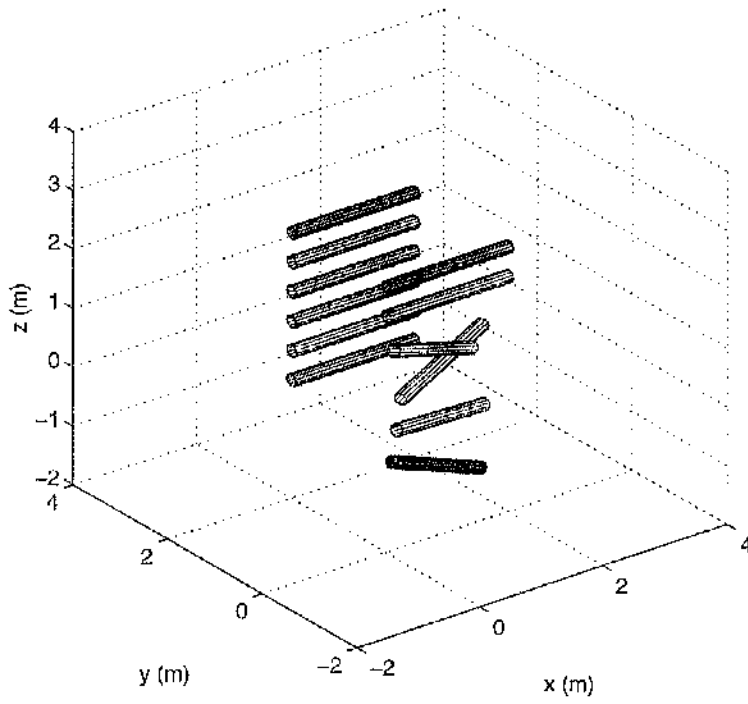


Figure 7.7.a.ii: Serial Cube Assembly: Time = 25 s.

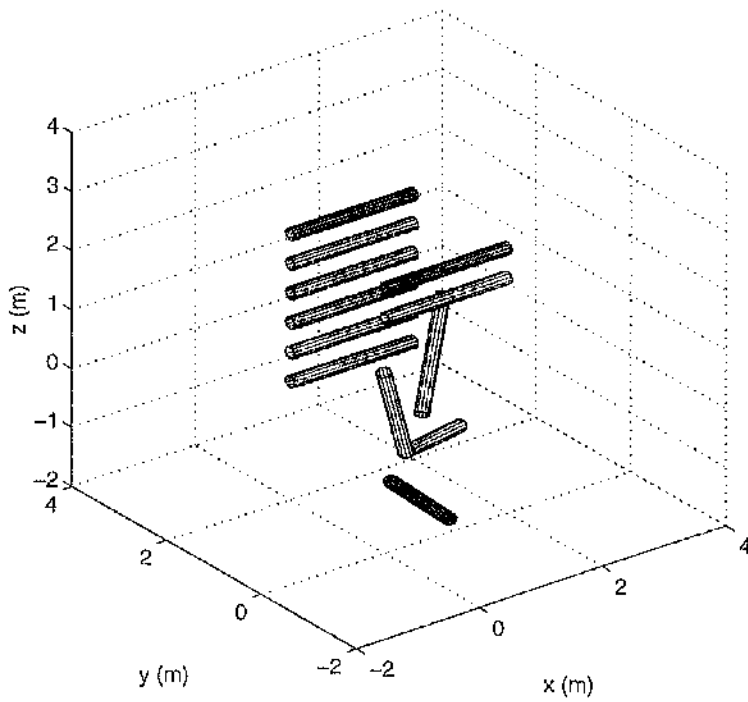


Figure 7.7.a.iii: Serial Cube Assembly: Time = 50 s.

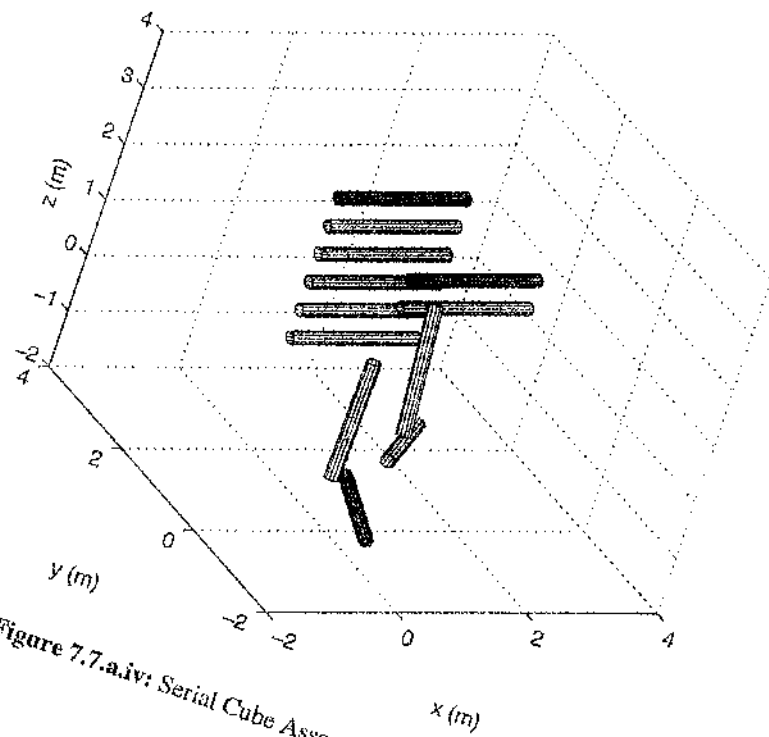


Figure 7.7.a.iv: Serial Cube Assembly: Time = 75 s.

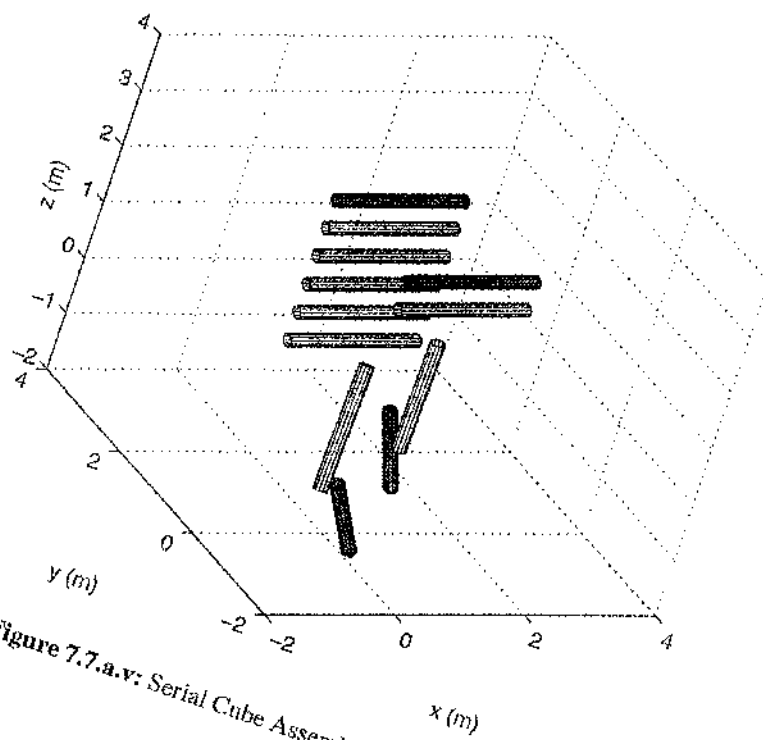
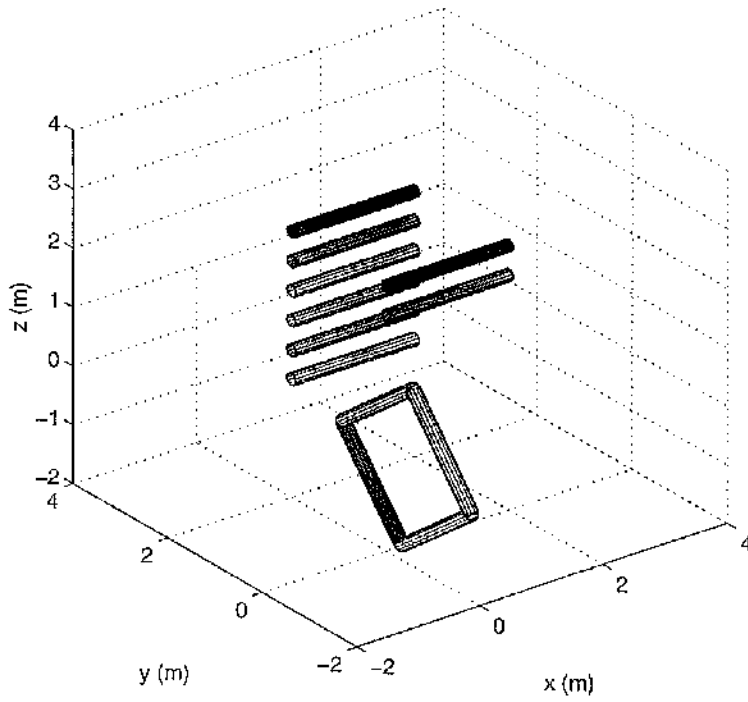
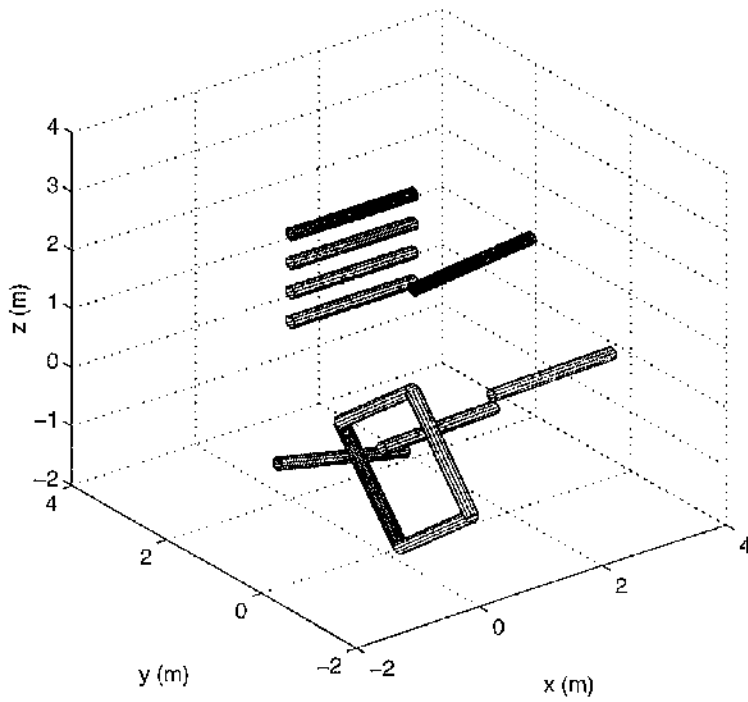


Figure 7.7.a.v: Serial Cube Assembly: Time = 100 s.



**Figure 7.7.a.vi:** Serial Cube Assembly: Time = 500 s.



**Figure 7.7.a.vii:** Serial Cube Assembly: Time = 750 s.

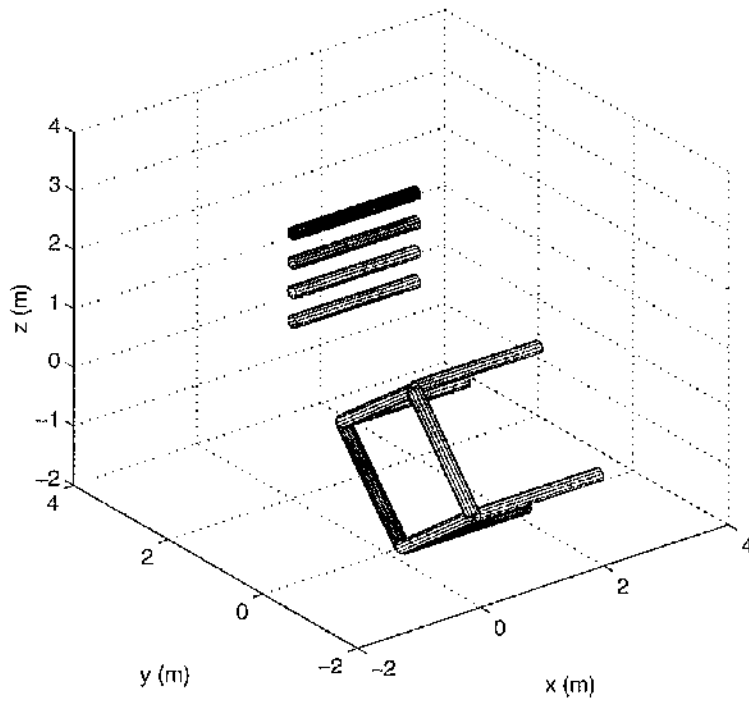


Figure 7.7.a.viii: Serial Cube Assembly: Time = 1000 s.

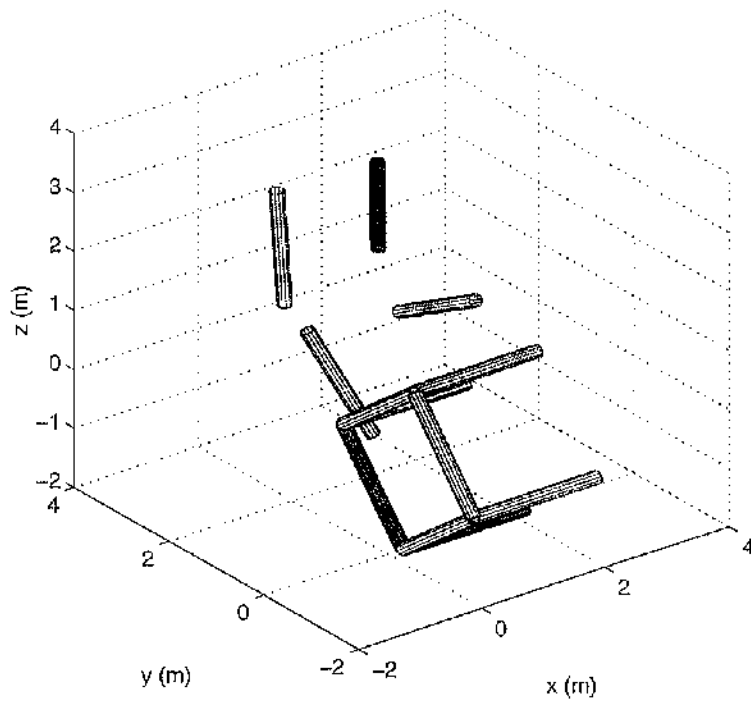


Figure 7.7.a.ix: Serial Cube Assembly: Time = 1500 s.

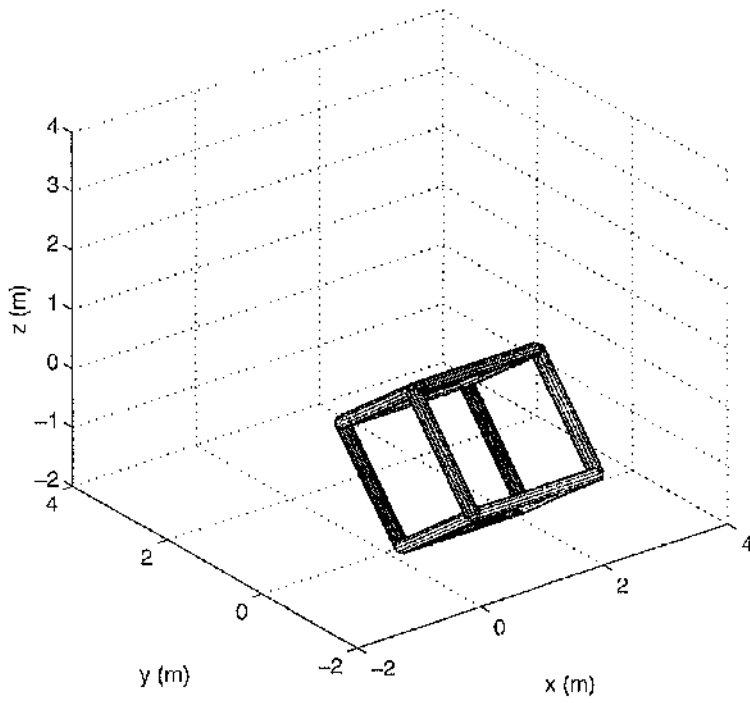


Figure 7.7.a.x: Serial Cube Assembly: Time = 2900 s.

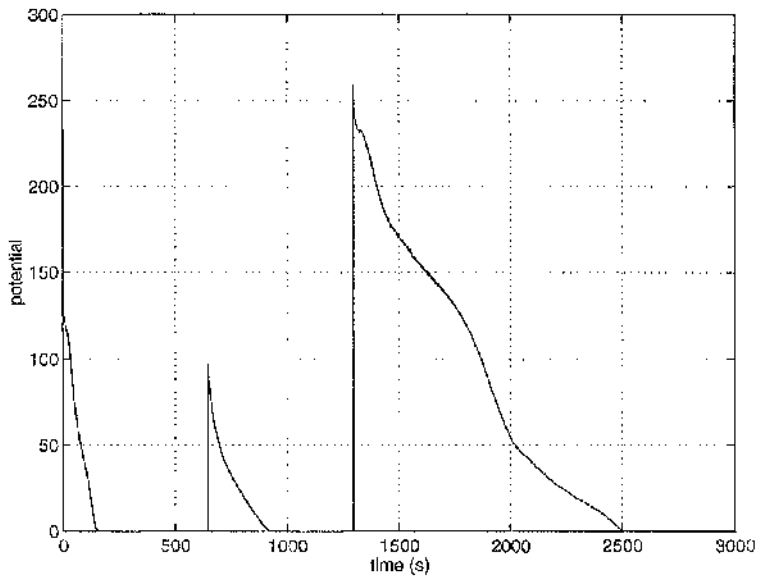


Figure 7.7.b: Potential Function.

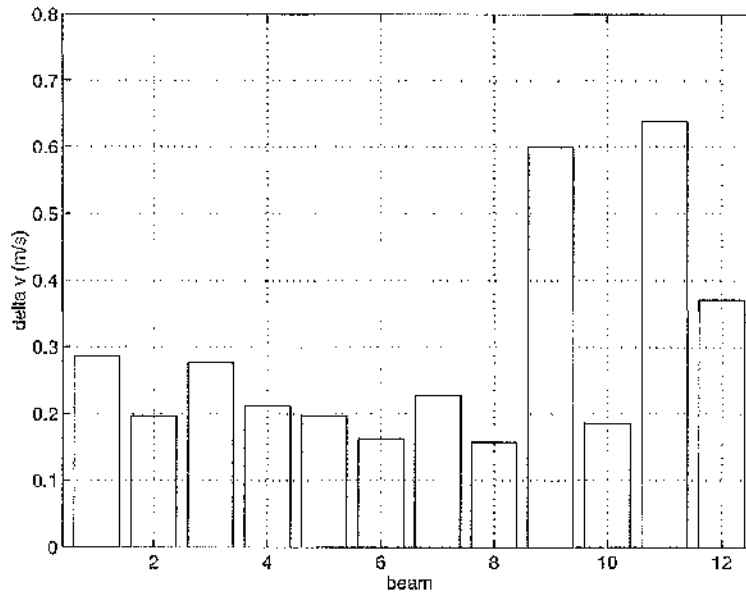


Figure 7.7.c:  $\Delta v$  Cost.

#### 7.4.4 Comparison of Serial and Parallel Cases

The contrast between the serial and parallel assembly of the cube highlights problems and impracticalities associated with both methods. The principal consideration with this analysis is that the resources required to assemble the cube are minimised. Therefore, the topics which must be considered are as follows;

- The total number of controlling vehicles required to assemble the structure.
- The  $\Delta v$  cost of assembly.
- The dexterity and complexity of movement required of the controlling vehicles.

Considering the parallel case, although the assembly time was far less than that of the serial case, the demands on the controlling vehicles were high with multiple operations being carried out simultaneously. If the cube were to be assembled in parallel, the controlling vehicles would find the task of connecting the structure simultaneously more complex than if it were connected together one joint at a time. However the overall  $\Delta v$  cost is considerably lower per vehicle, especially in light of the higher  $\Delta v$  being distributed over fewer vehicles with the serial case. With the parallel case, the results here suggest that a smart beam rather than a distinct controlling vehicle is more practical, as will be discussed later.

In contrast, the serial case does lower the initial resources required for assembly, especially in the area of sensors, communications and dexterity of the controlling vehicle. The practicality of performing a series of simple manoeuvres cannot be ignored. However, the  $\Delta v$  cost of performing these manoeuvres is high. It is possible for the vehicle to perform as much

as three or four operations requiring  $2-4 \text{ m.s}^{-1}$  of  $\Delta v$ . An additional problem which is inherent within the serial method is that the potential function will approach the goal configuration in an exponential manner. Therefore, a cut-off value of potential is introduced whereby the potential never vanishes, but leaves a residual potential from every operation. This residual may accumulate over a number of operations since the total potential is measured over the whole connection set. Therefore, errors are introduced to the structure and later operations may never reach the cut-off potential value.

## 7.5 Carbon 60

Following the successful assembly of the cube, it is now possible to expand the size of the connectivity matrix to include more beam elements and larger structures. As an example of a large assembly problem, the Carbon 60, or *bucky ball* structure shall now be considered. The *bucky ball* structure is a spherical structure consisting of 20 hexagons and 12 pentagons connected together to form a faceted ball. A common example of such a structure is a geodesic dome. Consisting of 90 beams connected together at 60 joint nodes, the ball structure represents the most complex structure examined within this thesis. The derivation of the connectivity matrix, and the large amount of information contained to construct the bucky ball requires a re-examination of the connectivity matrix and the formation of a *Connection Set*.

### 7.5.1 The Connectivity Matrix

For a structure containing 90 beam elements, the connectivity matrix would require a  $90 \times 90$  array. Thus, a matrix containing 8100 elements would be required. This is not practical, especially when considering that only 90 of these elements would contain data and the remainder would be null. Therefore, a more efficient approach is required which will store the connections in an condensed form. One method of storing this information is to consider the co-ordinates of the connections within the matrix, i.e. the connectivity matrix of the square, given in **Equation 7.10**, may be written as

$$G_{\text{Square}} = \{(1,4) \quad (2,1) \quad (3,2) \quad (4,3)\} \quad (7.29)$$

where  $G$  is the connection set of the square and each co-ordinate represents the position of the active joints within the connection matrix in the form  $(i, j)$ .

The bucky ball structure is assembled from 20 hexagons and 12 pentagons connected together at common beams. However, the ball itself may be considered to consist of two cap structures connected together by a joining centre section at common beams, as shown in **Figure 7.8**, viz.

$$\varepsilon_{ij}|_{Bucky} = \left\{ \begin{array}{ccc} \varepsilon_{ij}|_{Cap1} & [\mathbf{0}] & [\mathbf{0}] \\ [\mathbf{0}] & \varepsilon_{ij}|_{Centre} & [\mathbf{0}] \\ [\mathbf{0}] & [\mathbf{0}] & \varepsilon_{ij}|_{Cap2} \end{array} \right\} \quad (7.30)$$

The two cap sections may be assembled from a single pentagon connected to 5 hexagons at common beams. Thus, the derivation of the connectivity matrix for the cap may be expressed as

$$\varepsilon_{ij}|_{Cap} = \varepsilon_{ij}|_{Pentagon} \oplus 5 \times \varepsilon_{ij}|_{Hexagon} \quad (7.31)$$

where the connectivity matrix of the pentagon is given as

$$\varepsilon_{ij}|_{Pentagon} = \left\{ \begin{array}{ccccc} 0 & \mathbf{1} & 0 & 0 & 0 \\ 0 & 0 & \mathbf{1} & 0 & 0 \\ 0 & 0 & 0 & \mathbf{1} & 0 \\ 0 & 0 & 0 & 0 & \mathbf{1} \\ \mathbf{1} & 0 & 0 & 0 & 0 \end{array} \right\} \quad (7.32)$$

and the angle constraints are defined as

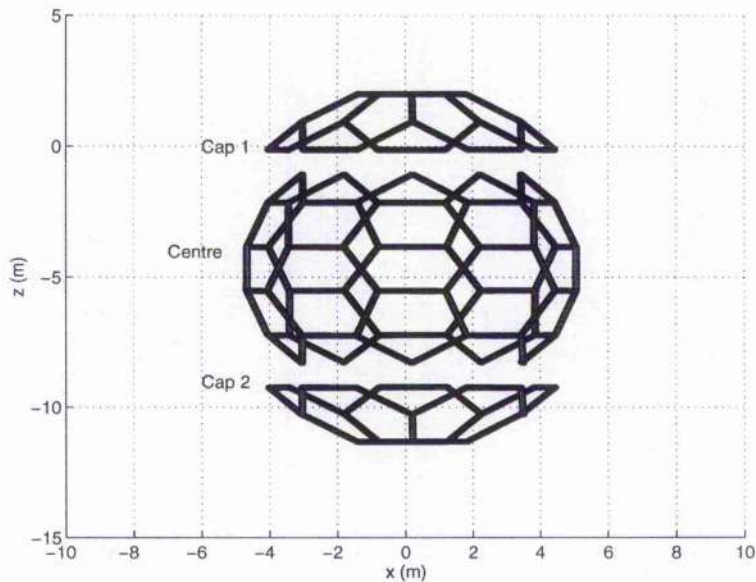


Figure 7.8: Bucky Ball

$$(\bar{\theta}_i, \bar{\phi}_i) = \left( \theta_{i-1} + \frac{2\pi}{5}, 0 \right) \quad (7.33)$$

The connectivity matrix of the hexagon is given as

$$E_{ij} \Big|_{Hexagon} = \begin{pmatrix} 0 & \mathbf{1} & 0 & 0 & 0 & 0 \\ 0 & 0 & \mathbf{1} & 0 & 0 & 0 \\ 0 & 0 & 0 & \mathbf{1} & 0 & 0 \\ 0 & 0 & 0 & 0 & \mathbf{1} & 0 \\ 0 & 0 & 0 & 0 & 0 & \mathbf{1} \\ \mathbf{1} & 0 & 0 & 0 & 0 & 0 \end{pmatrix} \quad (7.34)$$

and the angle constraints are defined as

$$(\bar{\theta}_i, \bar{\phi}_i) = \left( \theta_{i-1} + \frac{\pi}{3}, \bar{\phi} \right) \quad (7.35)$$

where  $\bar{\phi}$  is a variable which constrains the elements to a single plane.

Deriving the connectivity matrix of the cap structure then results in a matrix consisting 25 rows and columns with 625 entries. However, it is simpler to express the connectivity matrix as a connection set, viz.

$$G_{Cap} = \begin{pmatrix} (1,5) & (2,1) & (3,2) & (4,3) & (5,4) \\ (6,1) & (7,2) & (8,3) & (9,4) & (10,5) \\ (11,6) & (12,7) & (13,8) & (14,9) & (15,10) \\ (16,6) & (17,7) & (18,8) & (19,9) & (20,10) \\ (21,11) & (22,12) & (23,13) & (24,14) & (25,15) \end{pmatrix} \quad (7.36)$$

Thus, with a connection set for the two cap sections, the centre section may be derived in a similar fashion. The central section of the bucky ball may itself be assembled from smaller components. Although the full structure consists of 10 pentagons and 10 hexagons connected at common beams, it is possible to connect a single pentagon and hexagon together which may then be tiled to form the complete structure. The connectivity matrix of the pentagon and hexagon structure is derived from

$$E_{ij} \Big|_{Section} = E_{ij} \Big|_{Pentagon} \oplus E_{ij} \Big|_{Hexagon} \quad (7.37)$$

where the two structures are joined at common beams. Thus, the connectivity matrix is given as

$$\varepsilon_{ij}|_{Section} = \begin{pmatrix} 0 & 1 & 0 & 0 & 0 & 0 & 0 & 0 & 0 & 0 \\ 0 & 0 & 1 & 0 & 0 & 0 & 0 & 0 & 0 & 0 \\ 0 & 0 & 0 & 1 & 0 & 0 & 0 & 0 & 0 & 0 \\ 0 & 0 & 0 & 0 & 1 & 0 & 0 & 0 & 0 & 0 \\ 0 & 0 & 0 & 0 & 0 & 1 & 0 & 0 & 0 & 0 \\ 1 & 0 & 0 & 0 & 0 & 0 & 1 & 0 & 0 & 0 \\ 0 & 0 & 0 & 0 & 0 & 0 & 0 & 1 & 0 & 0 \\ 0 & 0 & 0 & 0 & 0 & 0 & 0 & 0 & 1 & 0 \\ 0 & 0 & 0 & 0 & 0 & 0 & 0 & 0 & 0 & 1 \\ 0 & 0 & 0 & 0 & 0 & 1 & 0 & 0 & 0 & 0 \end{pmatrix}$$

(7.38)

The complete centre section of the bucky ball may then be obtained by tiling the section structure into a ring. This may be expressed as

$$\varepsilon_{ij}|_{Centre} = 10 \times \varepsilon_{ij}|_{Section} \quad (7.39)$$

which, when carried out, results in a connectivity matrix of 40 rows and columns. Expressing this as a connection set gives

$$G_{Centre} = \begin{pmatrix} (1,6) & (2,1) & (3,2) & (4,3) & (5,4) & (6,5) & (7,6) \\ (8,7) & (9,8) & (10,9) & (11,1) & (12,11) & (13,12) & (14,13) \\ (15,11) & (16,15) & (17,16) & (18,12) & (19,18) & (20,19) & (21,20) \\ (22,18) & (23,22) & (24,23) & (25,19) & (26,25) & (27,26) & (28,27) \\ (29,25) & (30,29) & (31,30) & (32,26) & (33,32) & (34,33) & (35,34) \\ (36,32) & (37,36) & (38,37) & (39,33) & (40,39) & (41,40) & (42,41) \\ (43,39) & (44,43) & (45,44) & (46,40) & (47,46) & (48,47) & (49,48) \\ (50,46) & (51,50) & (52,51) & (53,47) & (54,53) & (55,54) & (56,55) \\ (57,53) & (58,57) & (59,58) & (60,54) & (60,54) & (62,61) & (63,62) \\ (64,60) & (65,64) & (66,65) & (67,61) & (68,10) & (69,3) & (70,69) \end{pmatrix}$$

(7.40)

The connectivity matrix of the complete bucky ball may then be calculated from **Equation 7.30** and renumbering the beam elements. The resulting matrix may then be expressed by the connection set given in **Equation 7.41**.

$$G_{Bucky} = \left\{ \begin{array}{ccccc} (1,5) & (2,1) & (3,2) & (4,3) & (5,4) \\ (6,1) & (7,2) & (8,3) & (9,4) & (10,5) \\ (11,10) & (12,6) & (13,7) & (14,8) & (15,9) \\ (16,7) & (17,8) & (18,9) & (19,10) & (20,6) \\ (21,16) & (22,17) & (23,18) & (24,19) & (25,20) \\ (26,21) & (27,22) & (28,23) & (29,24) & (30,25) \\ (31,16) & (32,17) & (33,18) & (34,19) & (35,20) \\ (36,26) & (37,27) & (38,28) & (39,29) & (40,30) \\ (41,31) & (42,32) & (43,33) & (44,34) & (45,35) \\ (46,26) & (47,27) & (48,28) & (49,29) & (50,30) \\ (51,41) & (52,42) & (53,43) & (54,44) & (55,45) \\ (56,45) & (57,41) & (58,42) & (59,43) & (60,44) \\ (61,52) & (62,53) & (63,54) & (64,55) & (65,51) \\ (66,65) & (67,61) & (68,62) & (69,63) & (70,64) \\ (71,61) & (72,62) & (73,63) & (74,64) & (75,65) \\ (76,66) & (77,67) & (78,68) & (79,69) & (80,70) \\ (81,72) & (82,73) & (83,74) & (84,75) & (85,71) \\ (86,81) & (87,82) & (88,83) & (89,84) & (90,85) \end{array} \right\} \quad (7.41)$$

The connection angles of the structure need not be explicitly expressed. If the structure is assembled from the 20 hexagons, then the relative positioning of each beam within the structure shall come from its position within the pentagon and hexagon. To assemble a ninety beam structure using a parallel method would require the use of ninety controlling vehicles. This is an unfeasibly large number of vehicles, especially when considering the sensor and communication requirements of a such a large group. However, the assembly process may be simplified considerably if a serial construction is considered. In fact, the construction of the connection set allows the structure to be assembled with a minimum of five controlling vehicles.

### 7.5.2 Results

The assembly of the *bucky ball* structure is carried out using the connection set in **Equation 7.41** and the global potential function given in **Equation 7.26**. Propagating the assembly of the beams, the results are shown in **Figures 7.9**. The convergence of the global potential function is shown in **Figure 7.9.a**. As can be seen, the time of assembly is 3400 s and occurs in 18 stages with the connection set being implemented in groups of 5. The assembly of the structure is shown in the series of plots **Figures 7.9.b**. The plot shows the

assembly of the structure at 500 s intervals. As can be seen, the assembly occurs in groups of five, and the final structure is successfully completed.

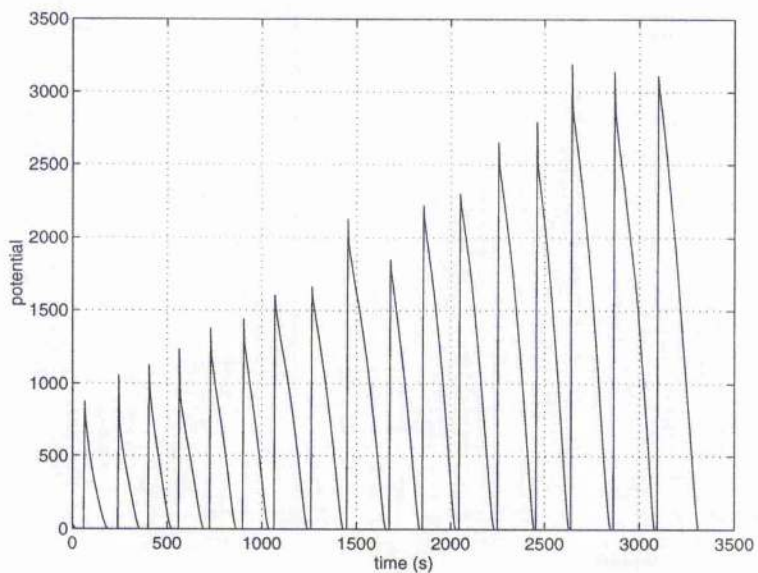


**Figure 7.9.a:** Potential Function.

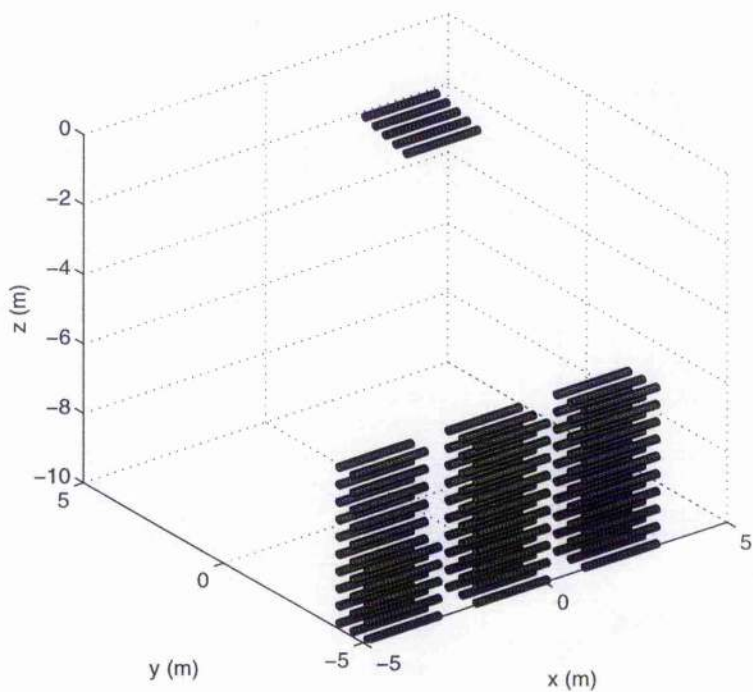


**Figure 7.9.b.i:** Bucky Ball Assembly: Time = 0 s.

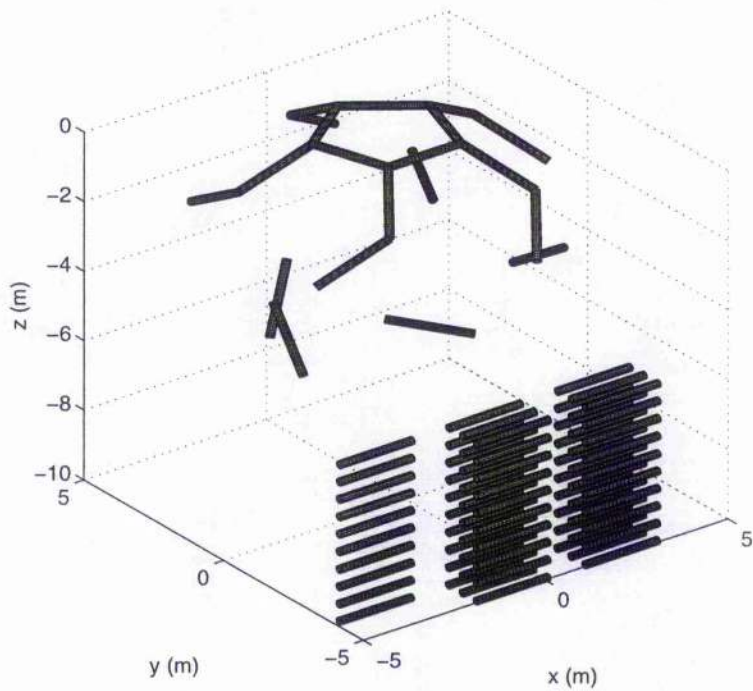


**Figure 7.9.b.ii:** Bucky Ball Assembly: Time = 500 s.

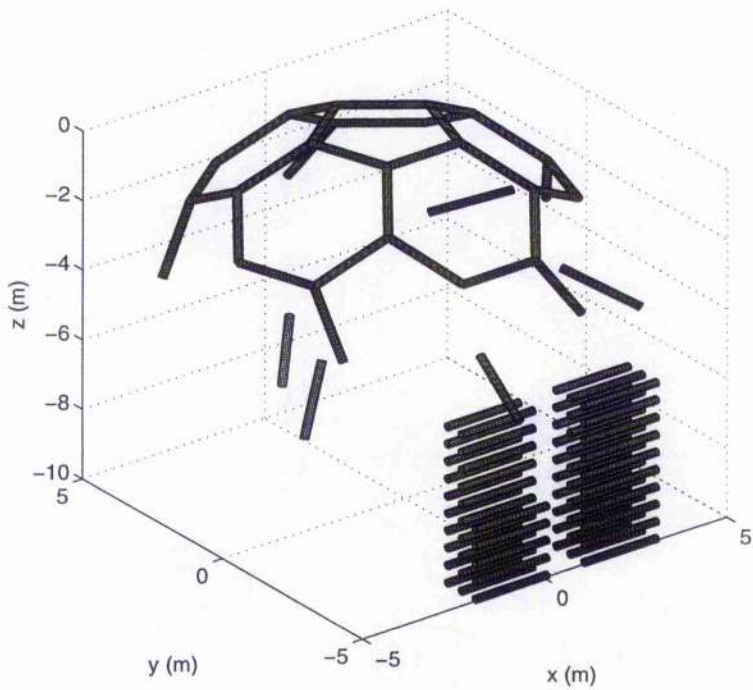


**Figure 7.9.b.iii:** Bucky Ball Assembly: Time = 1000 s.

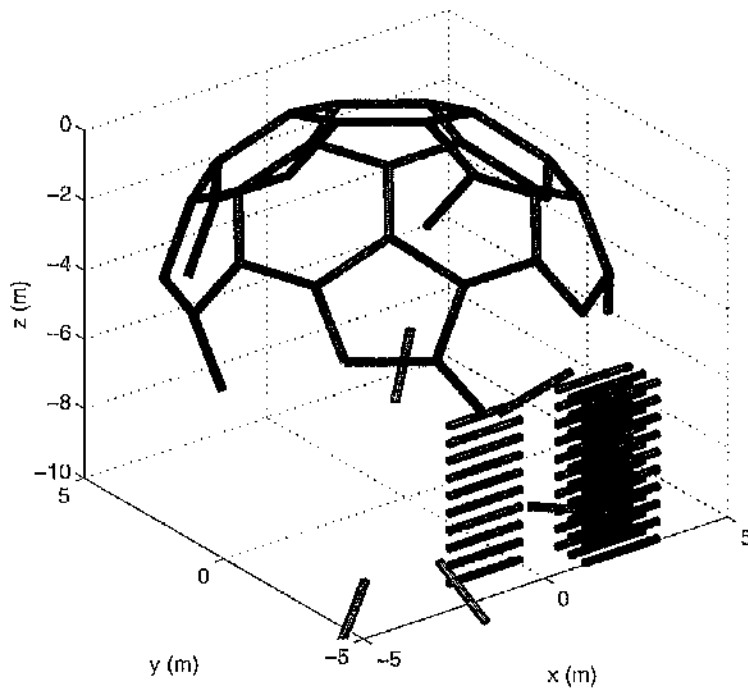


**Figure 7.9.b.iv:** Bucky Ball Assembly: Time = 1500 s.

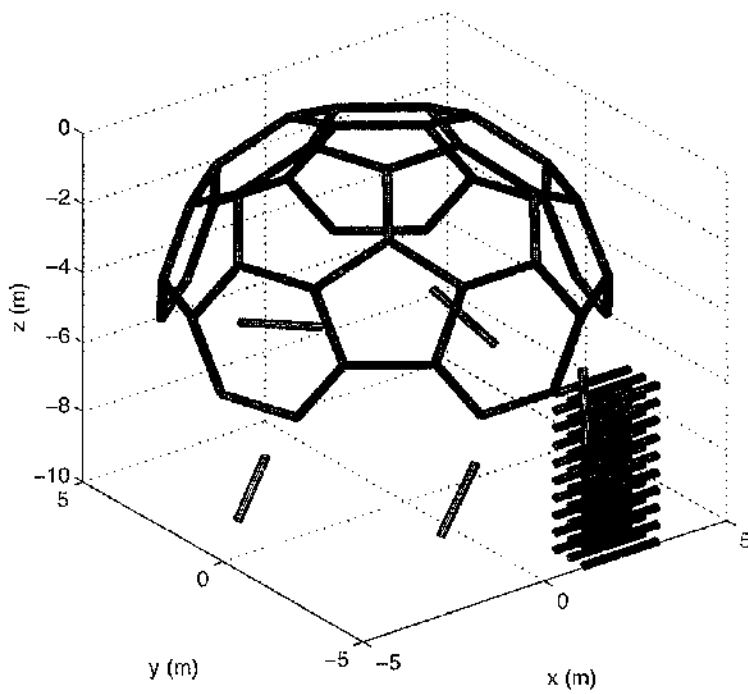


**Figure 7.9.b.v:** Bucky Ball Assembly: Time = 2000 s.

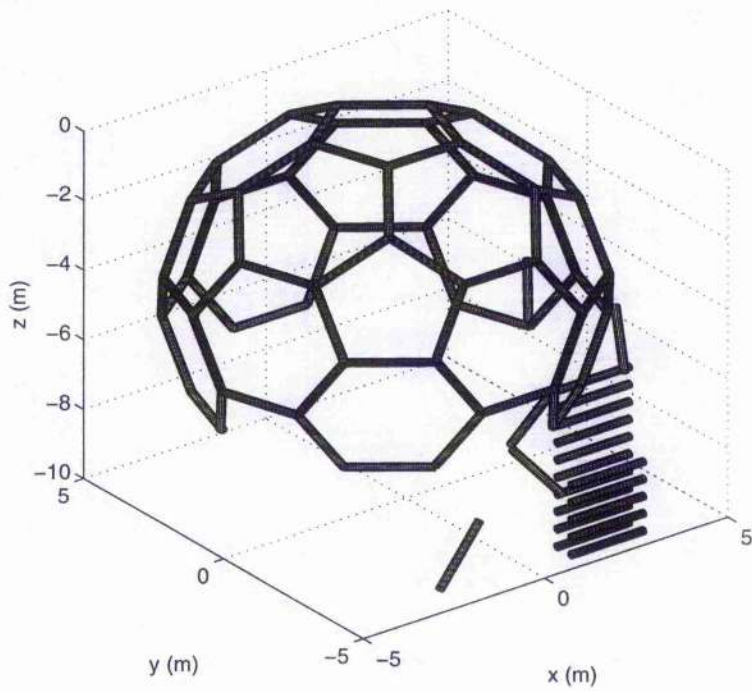


**Figure 7.9.b.vi:** Bucky Ball Assembly: Time = 2500 s.

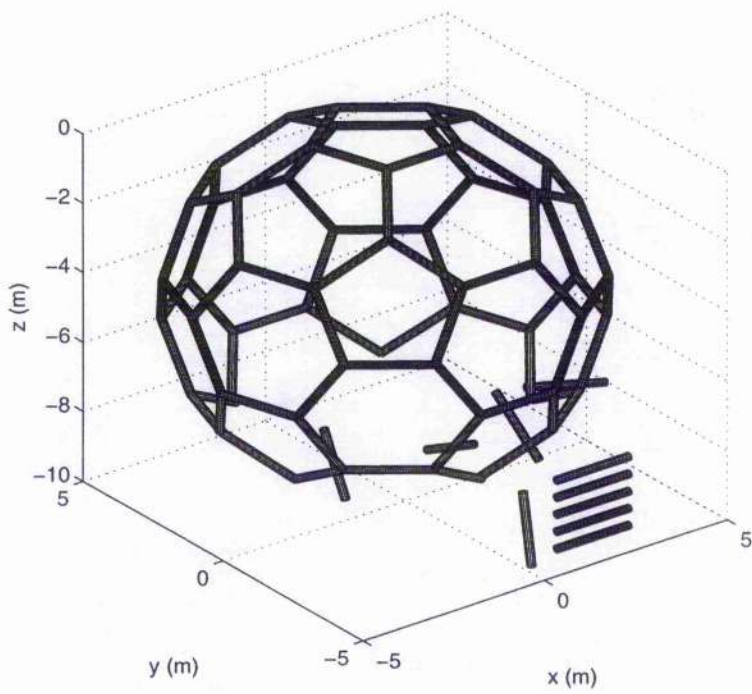


**Figure 7.9.b.vii:** Bucky Ball Assembly: Time = 3000 s.

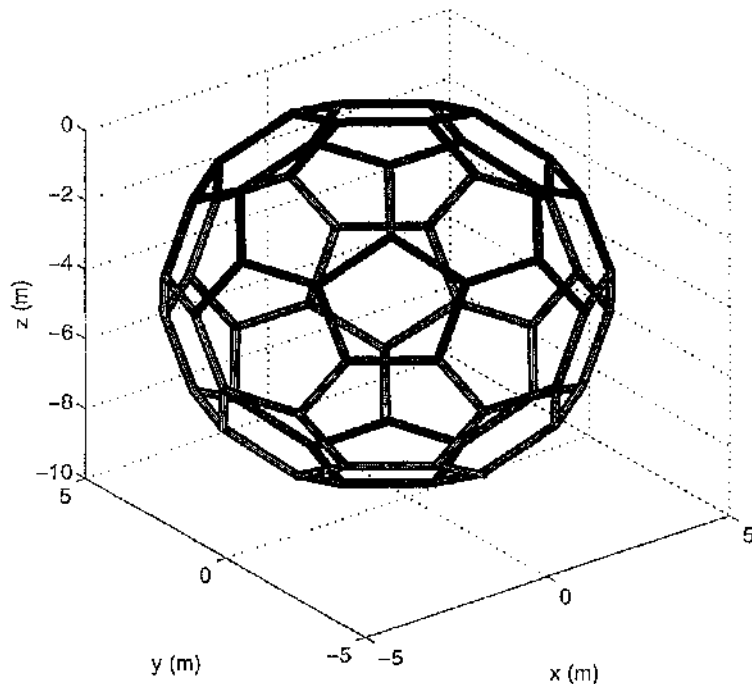


**Figure 7.9.b.viii:** Bucky Ball Assembly; Time = 3250 s.

## 7.6 Variable Structures

Until this point, the application of the potential function method has been to on-orbit assembly. In this section, the method shall again be used to assemble a structure. However, following completion of the structure, the method shall then be used to modify the properties of the structure. For the two cases examined here, firstly, the geometry, and then the topology of the structure shall be altered. For the first case, the orientation of specific beams within the structure shall be modified to alter the overall geometry of the structure. In the second case the structure shall be reconfigured into a new topology.

One of the difficulties which would be encountered when assembling these structures would be the extensive manoeuvring required in proximity to the other beams and vehicles. Although the repulsive potential would ensure separation, the task is made all the more complex by the presence of the controlling vehicles. One method to ease this problem would be to eliminate the controlling vehicles. This may be done by creating a smart beam. A smart beam would include all the thrusters and sensors required to assemble the structure as an integral part of the beam. Therefore, there would be no need for a separate controlling entity. This would obviously be inefficient when consider structures that would be static for long periods of time, however, for adaptive structures they would be ideally suited. This application is considered in more depth in **Chapter 9**.

The application envisaged here is that of the deployment of a supporting structure of a large reflector. As the structure geometry changes, the attached reflector will also begin to

deploy. In the second case, a cube shall be formed which will then be altered to form a twelve sided polygon. The practical application of this would be the transformation of a structure during a mission from a load bearing structure to a sensor array. Such reconfigurable spacecraft may have interesting applications for future planetary missions. For example, the load bearing structure may be required for Earth escape and orbit insertion burns. However, once injected into orbit about the target body, the spacecraft may unfold into a new configuration to maximise the exposed area and sensor attachment points for mapping and remote sensing applications.

### 7.6.1 Variable Geometry: The Connectivity Matrix

The supporting structure of the reflector is identical to that of the cap structure given in Equation 7.36. Constructed from a central pentagon base structure, the base is surrounded by five hexagons which will support the reflector mesh. The orientation of the individual beams, again as with the *bucky ball* comes from the relative positioning of the beams. However, examining Figure 7.10, it can be seen that five radial elements are formed within the structure corresponding to beam elements 6 to 10. These elements are fixed in azimuth, however, it becomes possible to vary the elevation of these beams and the remainder of the structure shall follow as the structure moves to a new equilibrium. It is this property that will allow the structure to be moved from a stowed, folded position to the deployed position. Such stowed position may represent the cruise phase of an interplanetary mission, while the deployed position represents on-orbit operations. Thus, if the elevation of the beams 6 to 10 are to be varied, then the angle potential for these elements becomes

$$V = \frac{1}{2} \sum_{i=6}^{10} (\phi_i - \bar{\phi}) \tag{7.42}$$

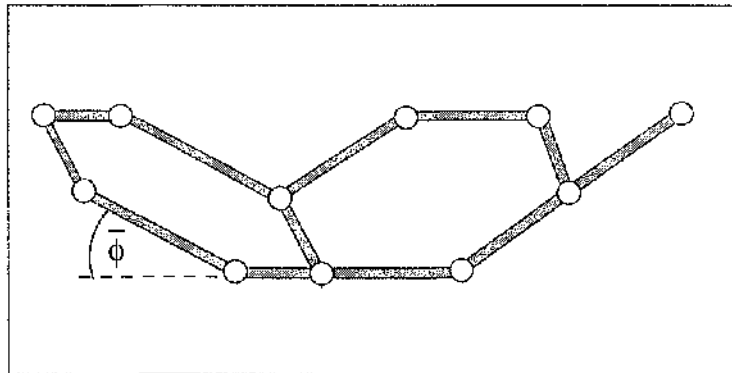


Figure 7.10: Reflector Structure.

where the target elevation may be varied with time, viz.

$$\bar{\phi} = f(t) \tag{7.43}$$

allowing the structure to be moved from the stowed to the deployed position.

### 7.6.2 Variable Geometry: Results

The example is simulated using the global potential function defined in **Equation 7.26** in conjunction with the connection set given in **Equation 7.36** and the target orientations given in **Equation 7.43**. Examining **Figure 7.11.a**, the potential function behaviour is shown with a smooth convergence to the goal. However, if the plot is examined in close detail, as shown in **Figure 7.11.b**, the variation in the potential caused by the variation in the elevation of the beams as the structure is deployed may be clearly seen. The variation in the controlled angle may be clearly seen in **Figure 7.11.c** and, in addition, the variation in the beam elevation as the structure is deployed. The goal elevation of the beams is determined by the function

$$\bar{\phi} = \frac{\lambda}{T + t} \tag{7.44}$$

where  $T$  is the initial deployment time and  $\lambda$  is a constant.

Thus, considering the potential function behaviour, the initial increase in potential following the deployment is caused by the initial rate of change in elevation swamping the global potential function. As the rate of change of elevation decreases, then the potential function may again start to converge. The formation of the structure, and its deployment, may be clearly seen in **Figures 7.11.d**. Considering the physical assembly of this structure, following the initial assembly, no control vehicle intervention would be required. However, a form of smart joint would be required which would be capable of uniformly adjusting the beam elevations. This will be discussed further in **Chapter 9**.

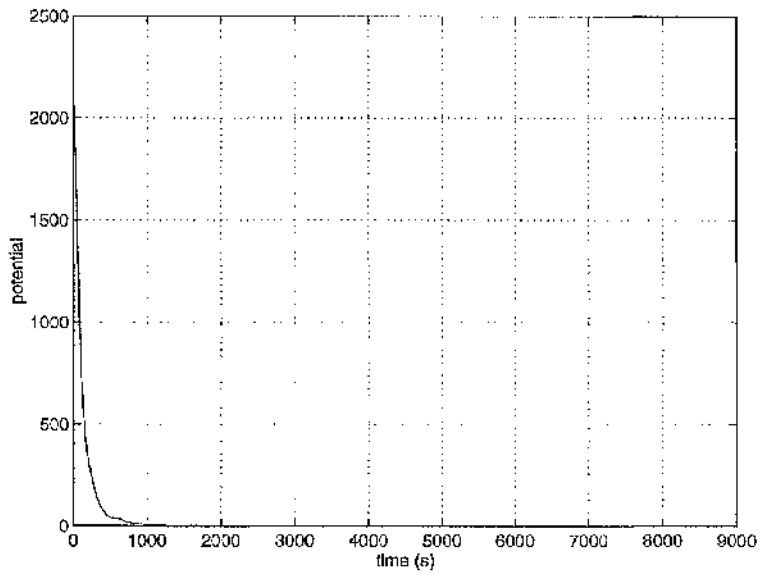


Figure 7.11.a: Potential Function.

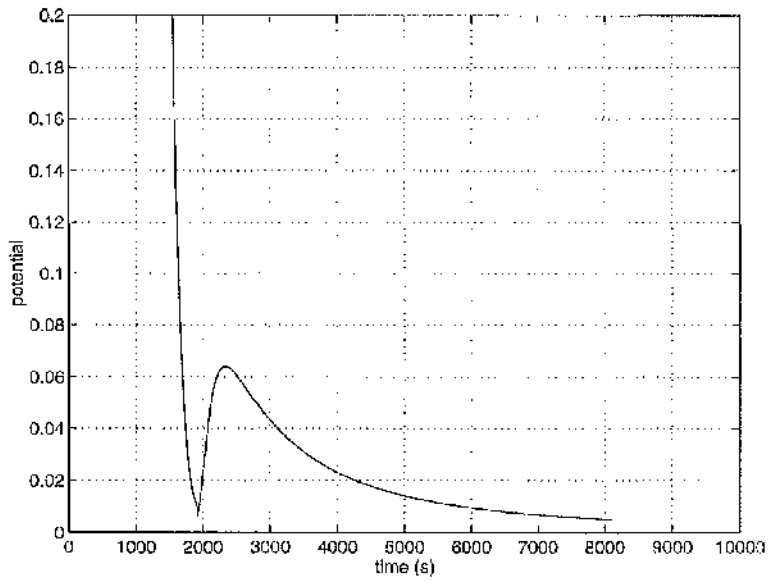


Figure 7.11.b: Potential Function.

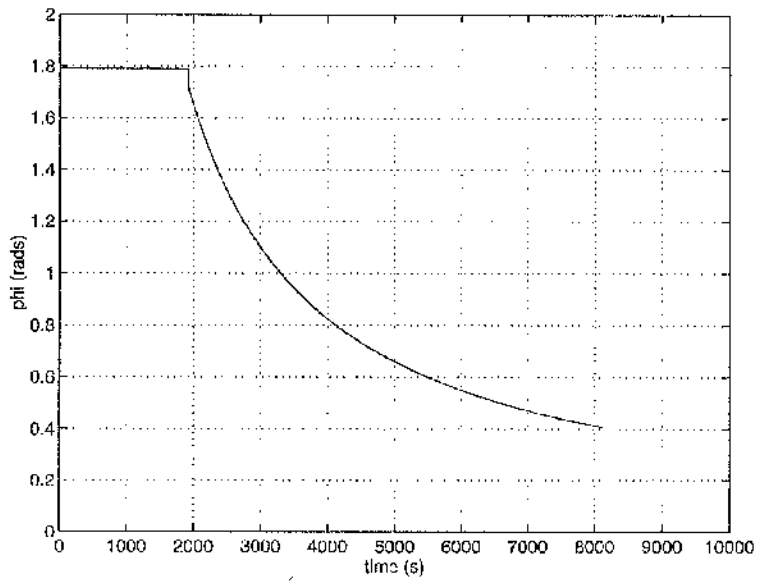


Figure 7.11.c: Controlled Angle.

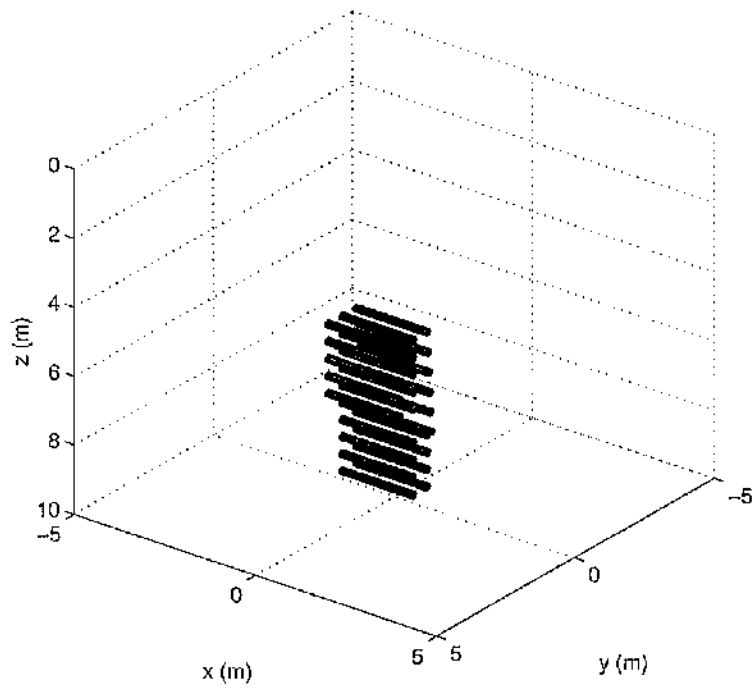


Figure 7.11.d.i: Deployment; Time = 0 s.

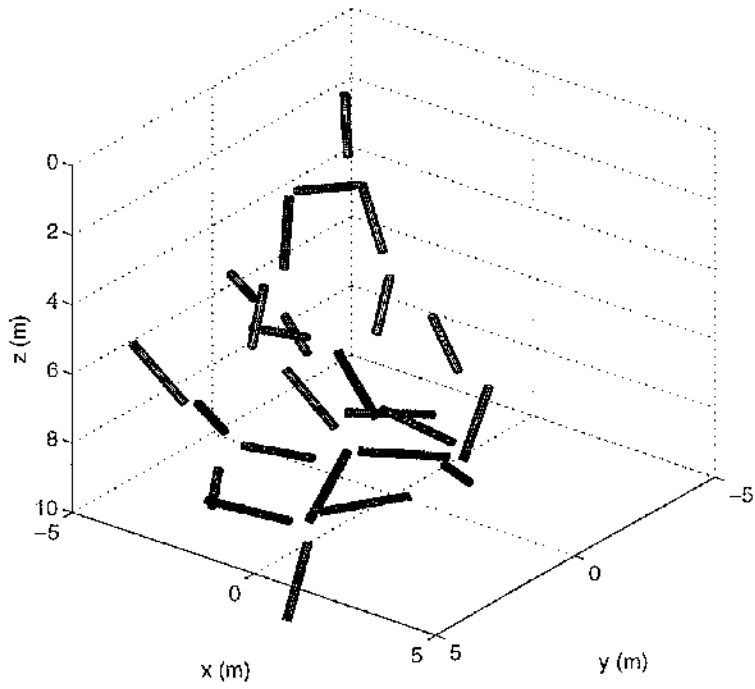


Figure 7.11.d.ii: Deployment: Time = 500 s.

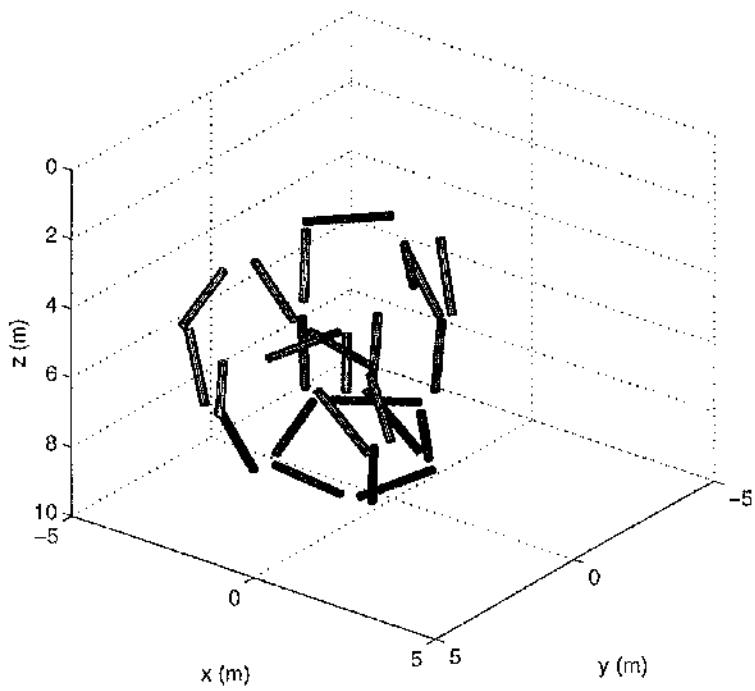


Figure 7.11.d.iii: Deployment: Time = 1000 s.

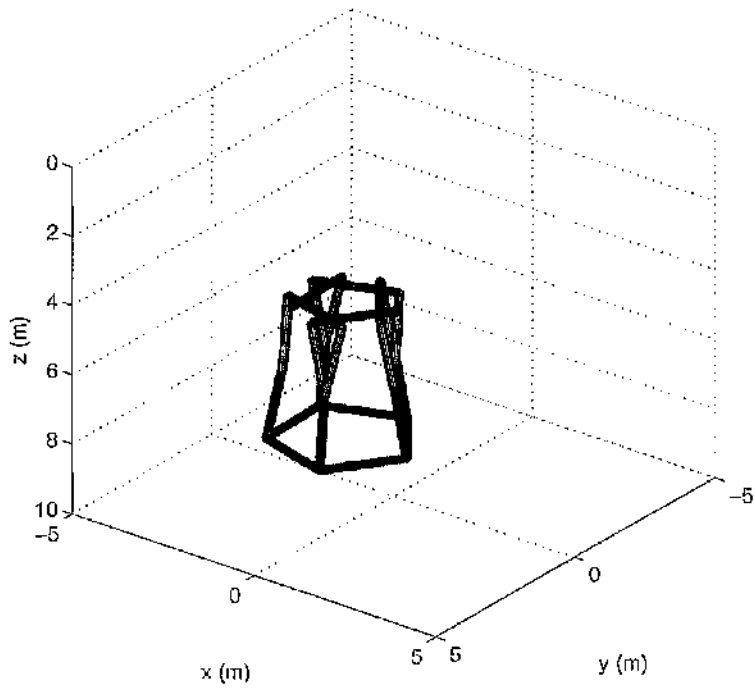


Figure 7.11.d.iv: Deployment: Time = 2000 s.

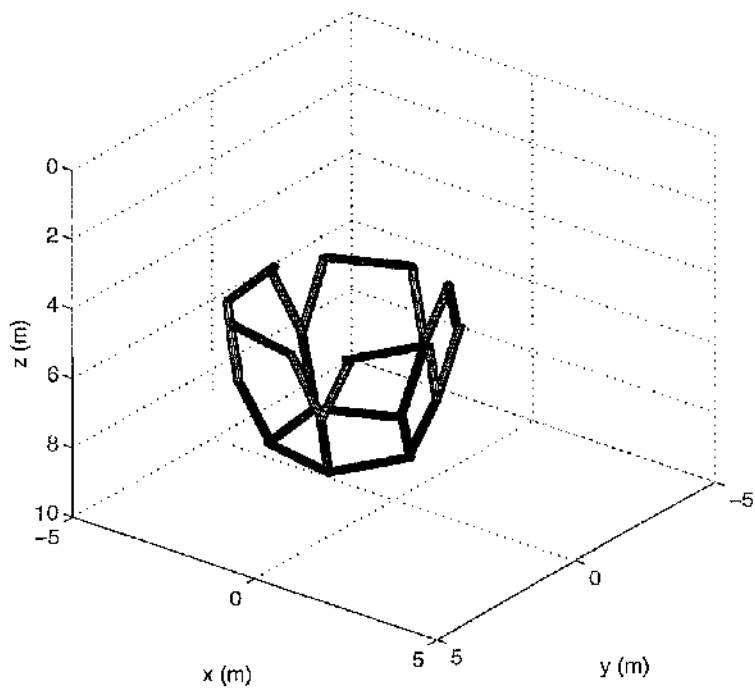


Figure 7.11.d.v: Deployment: Time = 3000 s.

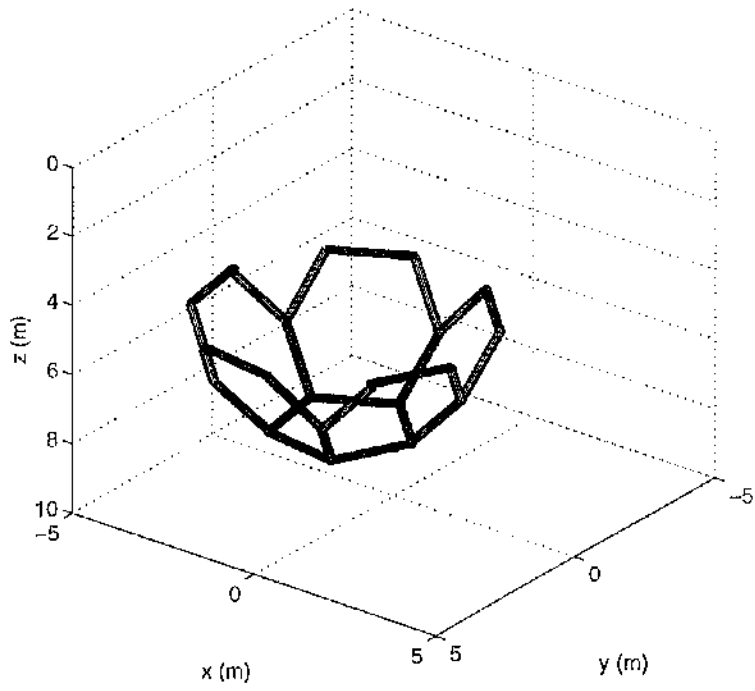


Figure 7.11.d.vi: Deployment: Time = 4000 s.

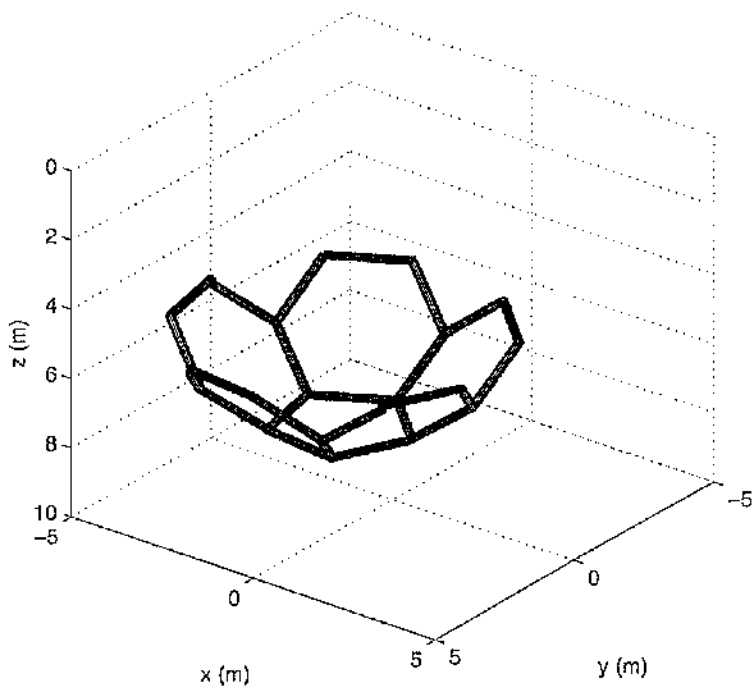


Figure 7.11.d.vii: Deployment: Time = 5000 s.

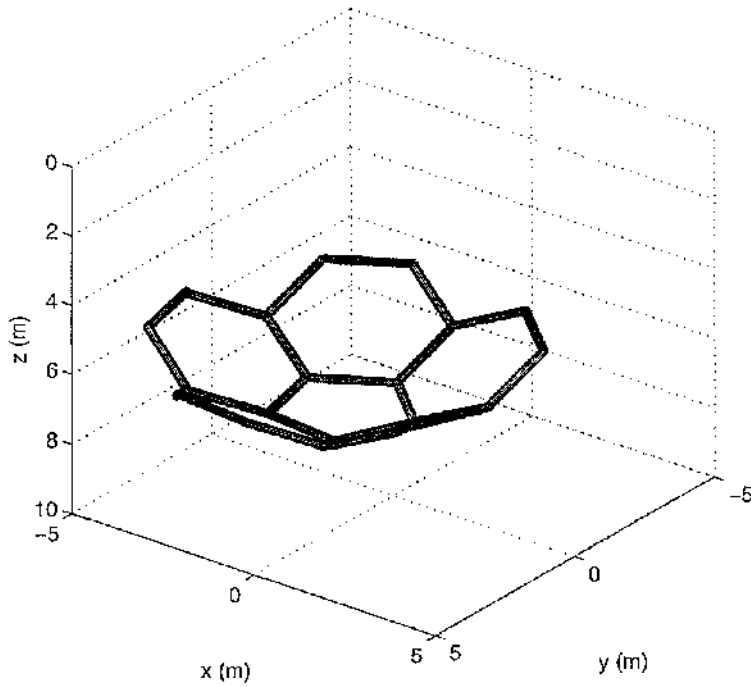


Figure 7.11.d.viii: Deployment: Time = 8000 s.

### 7.6.3 Variable Topology: The Connectivity Matrix

In this example, a set of smart beams will be used to reconfigure the topology of a structure. A cube will be considered as the initial structure and, using potential function methods, will be reconfigured to a polygon. The connectivity matrix of the cube structure from which the goal structure will deploy has been previously defined in Equation 7.10. However, the connectivity matrix of the target structure corresponds to a twelve sided polygon with the connectivity matrix

$$\varepsilon_{ij} = \begin{pmatrix} 0 & 1 & 0 & 0 & 0 & 0 & 0 & 0 & 0 & 0 & 0 & 0 \\ 0 & 0 & 1 & 0 & 0 & 0 & 0 & 0 & 0 & 0 & 0 & 0 \\ 0 & 0 & 0 & 1 & 0 & 0 & 0 & 0 & 0 & 0 & 0 & 0 \\ 0 & 0 & 0 & 0 & 1 & 0 & 0 & 0 & 0 & 0 & 0 & 0 \\ 0 & 0 & 0 & 0 & 0 & 1 & 0 & 0 & 0 & 0 & 0 & 0 \\ 0 & 0 & 0 & 0 & 0 & 0 & 1 & 0 & 0 & 0 & 0 & 0 \\ 0 & 0 & 0 & 0 & 0 & 0 & 0 & 1 & 0 & 0 & 0 & 0 \\ 0 & 0 & 0 & 0 & 0 & 0 & 0 & 0 & 1 & 0 & 0 & 0 \\ 0 & 0 & 0 & 0 & 0 & 0 & 0 & 0 & 0 & 1 & 0 & 0 \\ 0 & 0 & 0 & 0 & 0 & 0 & 0 & 0 & 0 & 0 & 1 & 0 \\ 1 & 0 & 0 & 0 & 0 & 0 & 0 & 0 & 0 & 0 & 0 & 0 \end{pmatrix}$$

(7.45)

The angle potential of the cube has been previously defined in **Section 7.4.2**, however, the target orientation of the polygon is defined as

$$(\bar{\theta}_i, \bar{\phi}_i) = \left( \theta_{i-1} + \frac{\pi}{6}, 0 \right) \quad (7.46)$$

thus forming the polygon in the x-y plane.

#### 7.6.4 Variable Topology: Results

This example is again simulated using the global potential function defined in **Equation 7.26** in conjunction with the connection set for the cube given in **Equation 7.25**, the target orientations given in **Equation 7.27**, the connection set for the polygon given in **Equation 7.45** and the target orientation given in **Equation 7.46**. The potential function of the example is shown in **Figure 7.12.a**. As can be seen, following convergence to the cube structure, the change in connection set results in a marked increase in the potential function. However, following convergence, the structure then reconverges to the second, polygon structure. The physical reconfiguration of the beams may be seen in **Figure 7.12.b** as the cube is formed and then reconfigured.

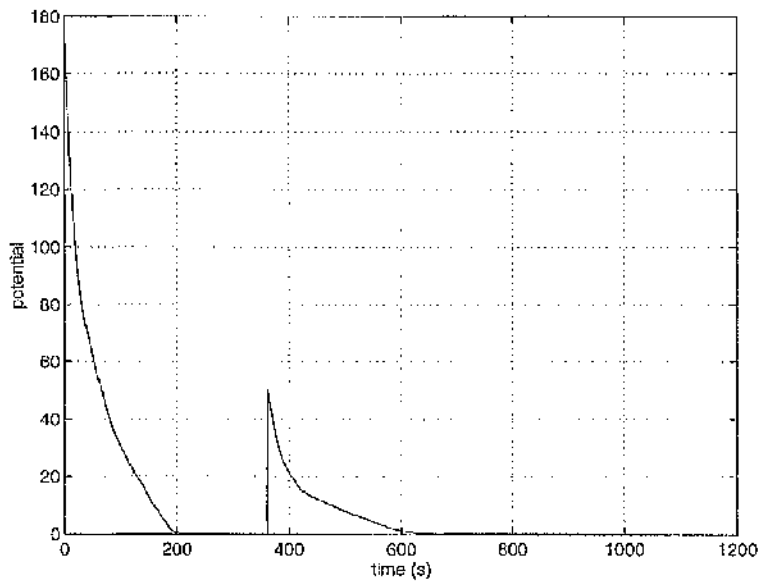


**Figure 7.12.a:** Potential Function.

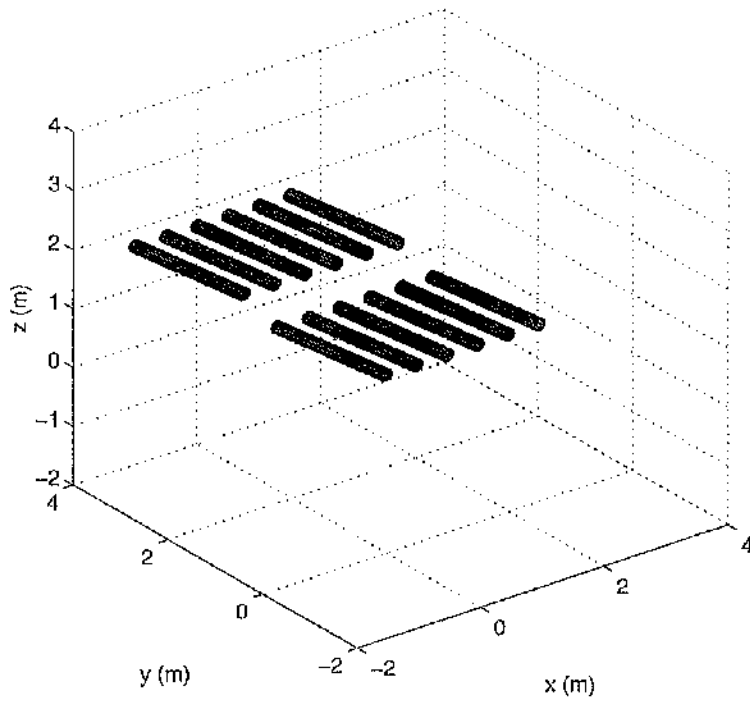


Figure 7.12.b.i: Reconfigure: Time = 0 s.

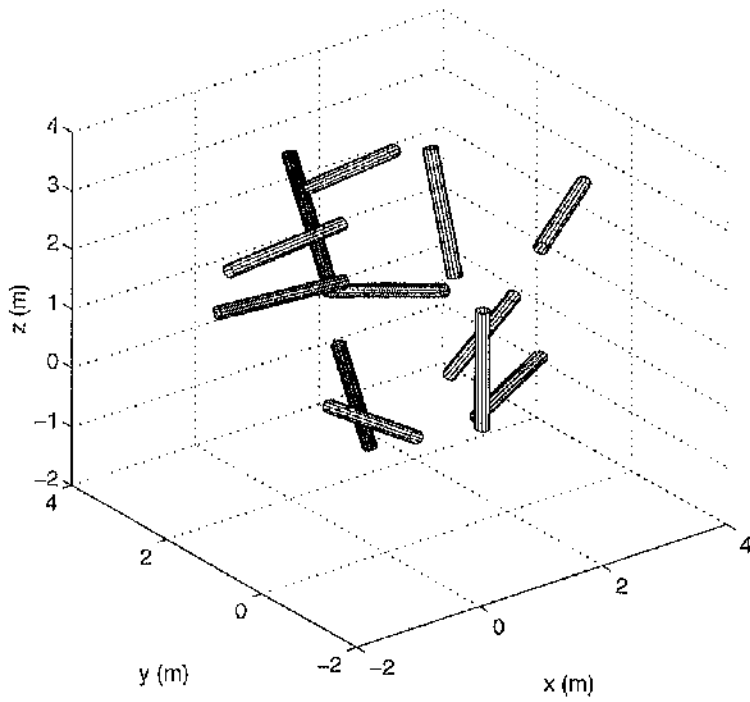


Figure 7.12.b.ii: Reconfigure: Time = 100 s.

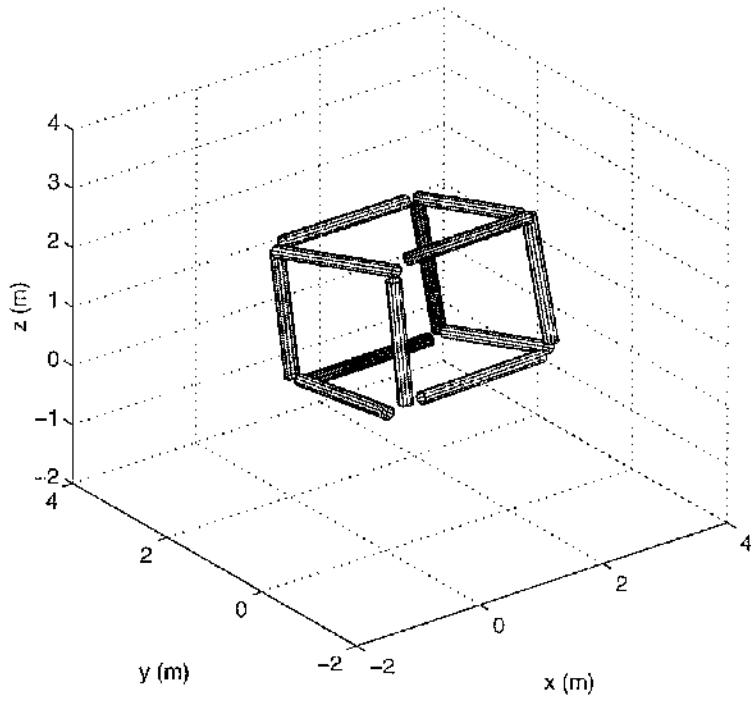


Figure 7.12.b.iii: Reconfigure: Time = 200 s.

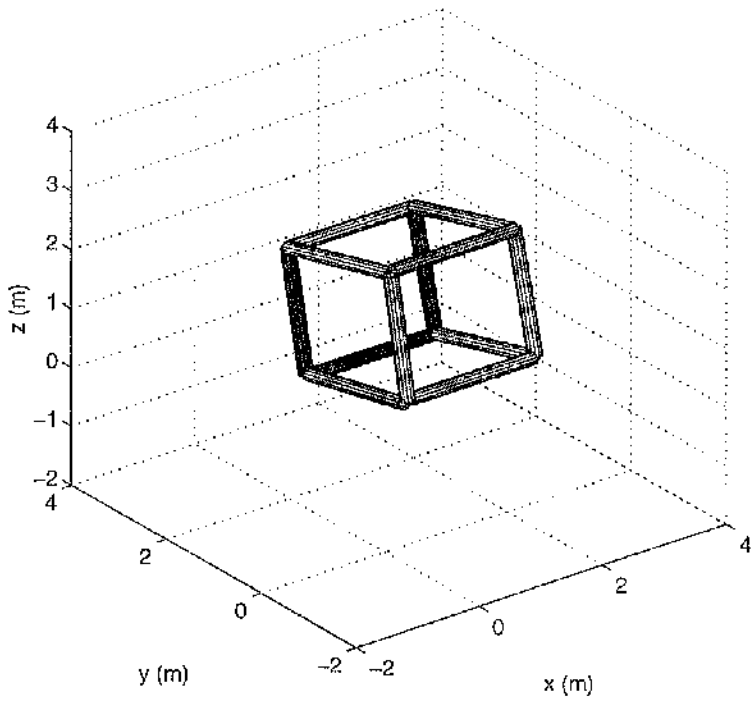


Figure 7.12.b.iv: Reconfigure: Time = 300 s.

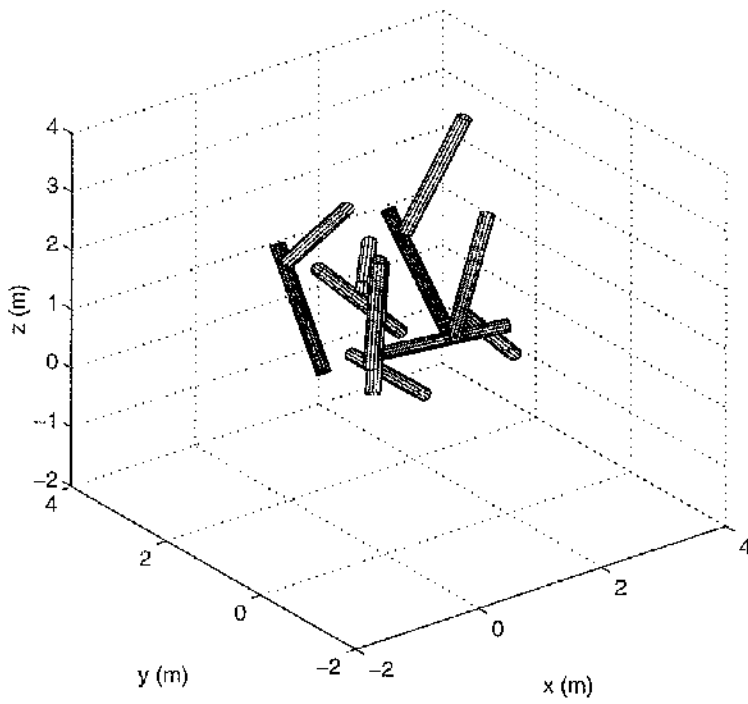


Figure 7.12.b.v: Reconfigure: Time = 400 s.

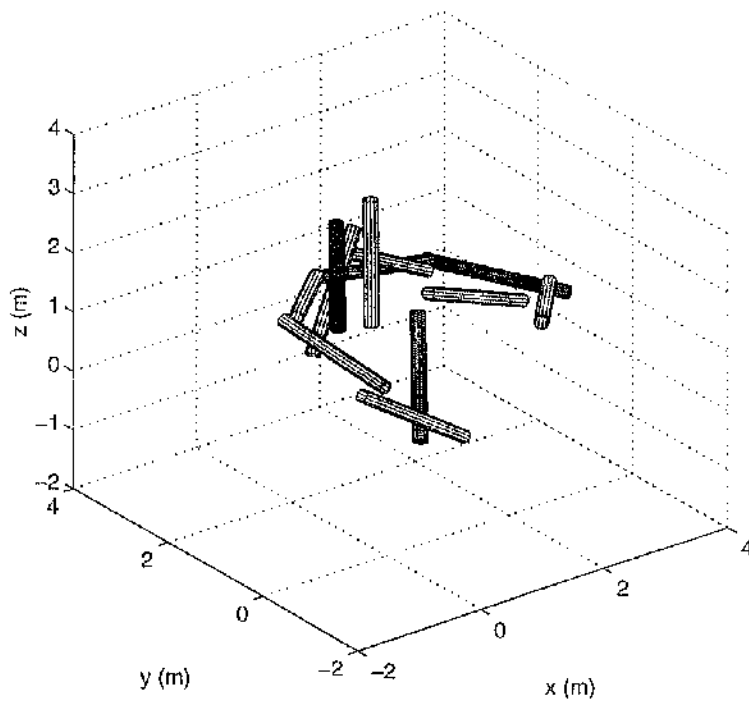


Figure 7.12.b.vi: Reconfigure: Time = 500 s.

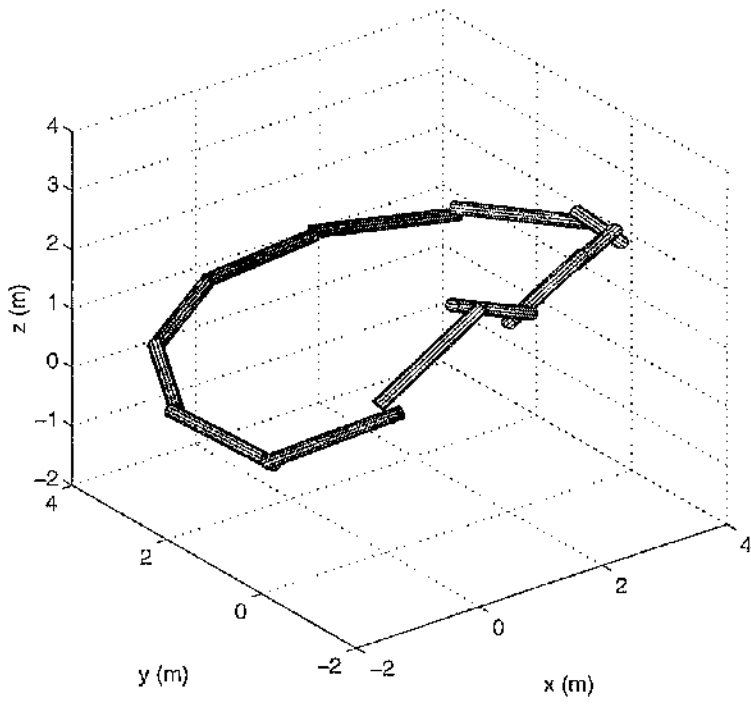


Figure 7.12.b.vii: Reconfigure: Time = 600 s.

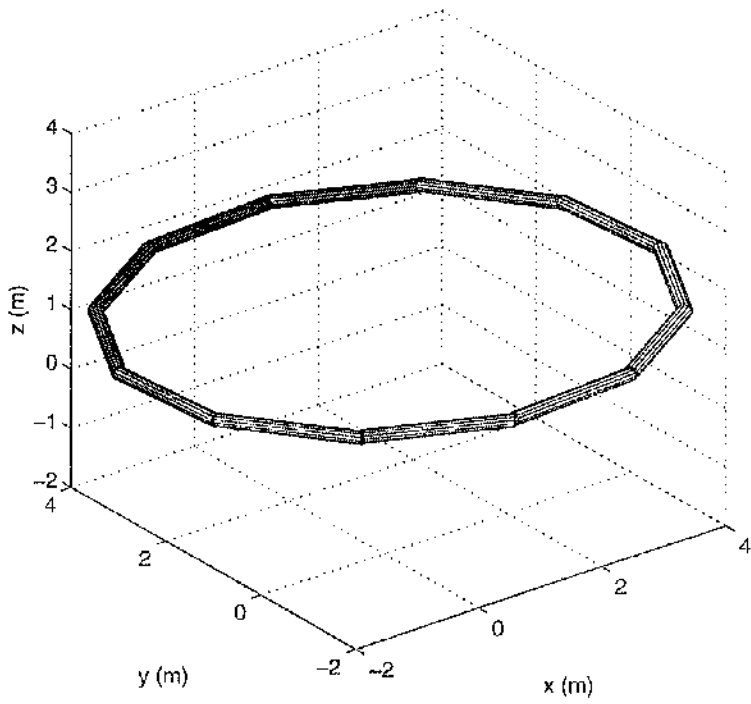


Figure 7.12.b.viii: Reconfigure: Time = 1100 s.

## 7.7 Conclusions

Examining the technique developed, it becomes apparent that for these structures, the expansion of the basic matrices to a Global Connectivity matrix follows a simple set of rules. However, it is the concept that these rules may be applied at all which allows the possibility of a broader, more complex construction strategy. Although the overall assembly process may be complex, this method allows the problem to be analytically broken down into the solution of a set of simpler sub-problems. Therefore, the development of a global potential function and a global connectivity matrix may be considered to be a success. In addition, the concept of a smart joint and beam system lends the method to a new class of smart, and adaptive structures. These reconfigurable structures may have interesting applications for future Earth orbiting and missions.

# Chapter Eight: Control Architecture

*Subsume: Include in a rule, class, category*

Oxford English Dictionary

## 8.1 Introduction

As previously discussed, a structure need not be assembled in a single effort. The implementation of a planned sequence of tasks leads to reduced assembly times and can simplify complex assembly problems. As with terrestrial construction, components can be prefabricated and assembled on site in a pre-planned assembly sequence. As the size and complexity of the structure increases, the required planning sequence also grows. Therefore, a requirement exists for an overall strategy of construction. It is possible to pre-define a construction strategy inherent within the design of the controller architecture. The strategy considered here is that of a *subsumption-type* architecture.

## 8.2 Subsumption

Treating the complete group of assembly vehicles as a *population*, a subsumptive-type architecture becomes possible. If the population is divided into *groups* or *teams* capable of working independently or in conjunction with the other teams, the capability and effectiveness of the population is much greater than by treating the population as a single entity. The relevance of this technique to the assembly method developed here is that the population is no longer dependent upon a single connectivity matrix. In fact, each team may have its own connectivity matrix. In physical terms, the teams will assemble sub-components which will be assembled into the larger goal structure. Thus, the use of teams within the vehicle population allows the advantage of parallel assembly to be combined with the practicality of serial assembly.

The subsumption architecture requires a method of dividing the population of assembly vehicles. In addition, the beam elements required to assemble a structure must be managed, therefore, an overseer is required to manage and react to the whole environment. This may be carried out with the use of a top level controller whose duties are to divide the population into teams, and in addition allocate resources. Future overseer controllers may implement definite strategies. However, for the structures assembled here, the allocation of

resources will be pre-defined. Defining this overseer controller as the *Primary* controller, the assembly of sub-components and resources will be allocated to a set of *Secondary* controllers, thus resulting in a management tree similar to that shown in **Figure 8.1**. This management scheme is best demonstrated by example.

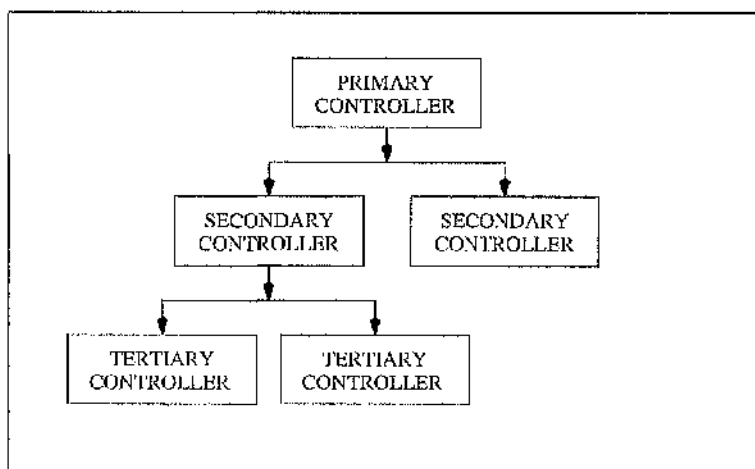


**Figure 8.1:** Subsumption Architecture.

### 8.3 Case Study: Cube Assembly

The cube assemblies carried out in **Section 7.4** demonstrated the practicalities of the structure in both the parallel and serial case. However, as discussed, each method has its advantages and disadvantages. If the subsumption approach is adopted, then the assembly procedure may be broken into two components. The assembly sequence envisaged is shown in **Figure 8.2**. The square base shown in the figure is assembled first. A second more complex table-like structure is then added to the base to form the cube.

#### 8.3.1 Potential Function Definition

Examining the architecture required to assemble the cube, the primary controller is required to task two secondary controllers to assemble the two separate components of the cube. The secondary controller tasked with assembling the base unit utilises the potential function given in **Equation 7.26** with the following connection set

$$\mathbf{G}_{Base} = \{(1,4) \quad (2,1) \quad (3,2) \quad (4,3)\} \quad (8.1)$$

This is the well known connection set associated with the assembly of a square. The primary controller will allocate to the assembly of the base, four beam elements and four controlling vehicles. On completion of the base, these four controlling vehicles will return to the general

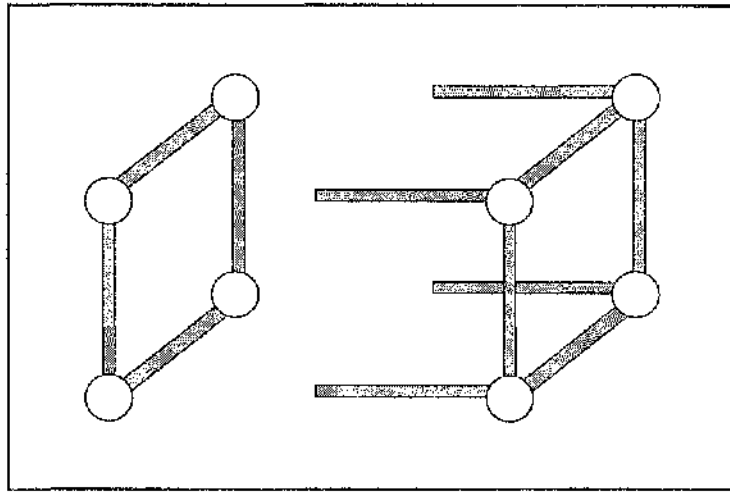


Figure 8.2: Cube Assembly.

population of vehicles for reassignment. In this case reassignment to the secondary controller tasked with building the second table-like structure.

The secondary controller tasked with assembling the table-like structure again will make use of the general potential function given in **Equation 7.26**. The connection set required to assemble the components is given by

$$\mathbf{G}_{Extension} = \left\{ \begin{array}{cccc} (5, \sigma_1) & (6, \sigma_2) & (7, \sigma_3) & (8, \sigma_4) \\ (9, 5) & (10, 6) & (11, 7) & (12, 8) \\ (9, 12) & (10, 9) & (11, 10) & (12, 11) \end{array} \right\} \quad (8.2)$$

where  $\sigma_i$  ( $i = 1 - 4$ ) is the connection points of the secondary structure to the base structure. In this case, the values will be 1, 2, 3, 4. Thus these two connectivity sets complete the full connectivity set as given in **Section 7.4**. The primary controller will assign to the secondary controller eight beams and the corresponding eight controlling vehicles. Thus the total population required to assemble the cube structure is eight vehicles for a total number of twelve beams.

### 8.3.2 Results

The two stages of assembly are apparent when examining the potential shown in **Figure 8.3.a**. The initial stage may be seen to converge to the solution after approximately 500 seconds. The second stage is then activated by the primary controller which perturbs the potential from the equilibrium state. The potential again re-converges to the solution. Thus, the cube structure is constructed successfully. Therefore, it is possible to expand the subsumption architecture to a more ambitious structure, such as load bearing truss.

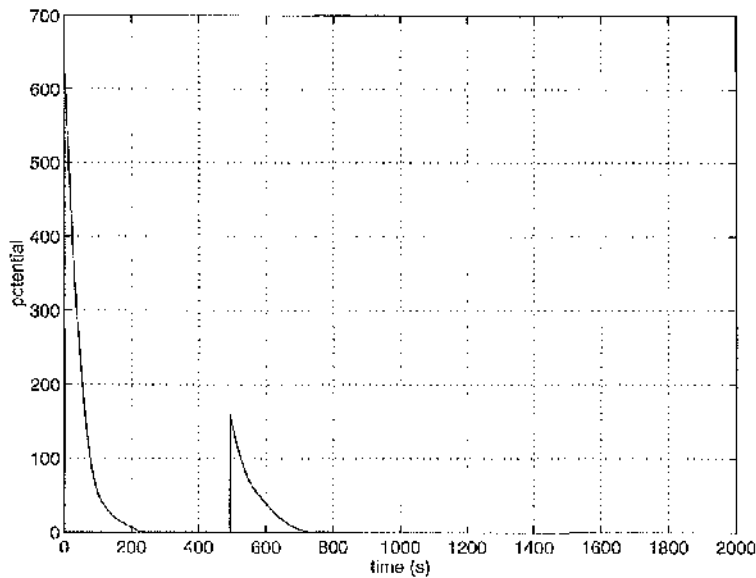


**Figure 8.3.a:** Potential Function.

Examining the series of plots shown in **Figure 8.3.b**, the assembly of the cube proceeds as expected in two stages. It should be noted that an additional quadratic potential has been added to the total potential to position the base unit at the origin. After 1,000 s, the base square is complete and the second table structure assembly has begun. The assembly of the second structure, and thus the final goal structure is completed by 3,000 s. As can be seen, the components are successfully assembled into the goal structure.

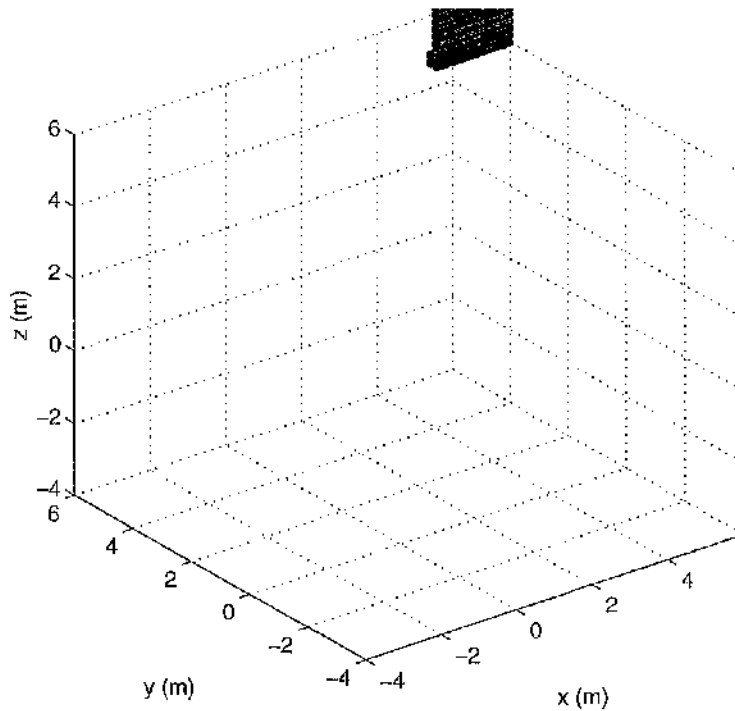


**Figure 8.3.b.i:** Cube Assembly: Time = 0 s.

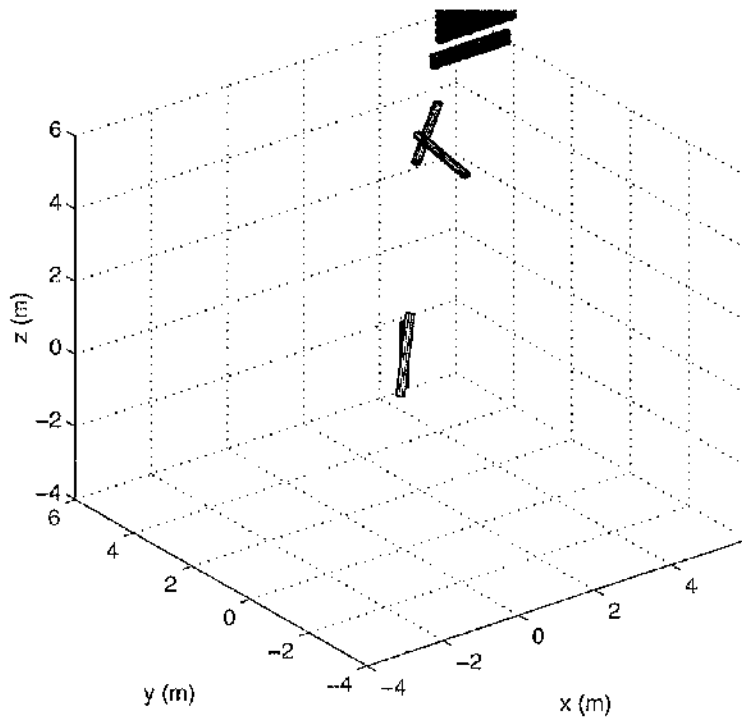


Figure 8.3.b.ii: Cube Assembly: Time = 125 s.

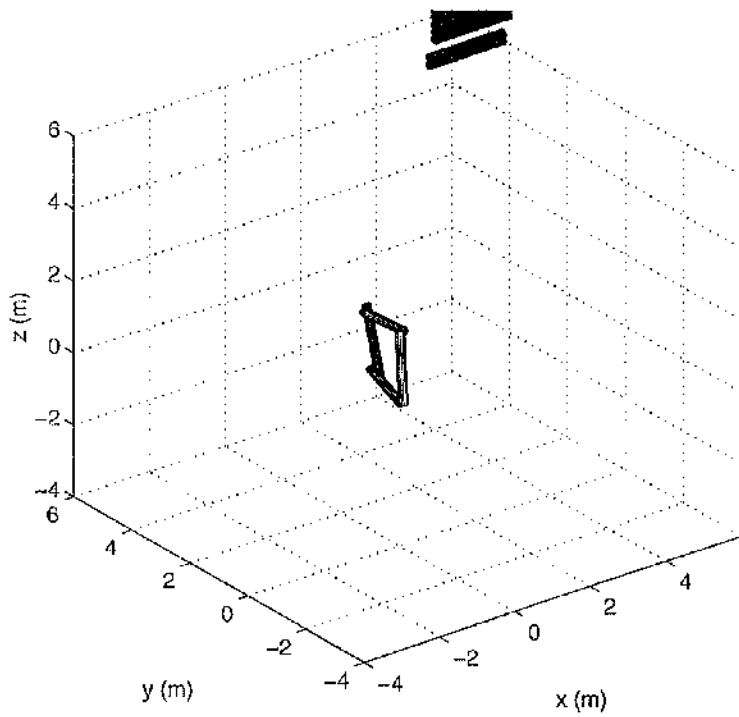


Figure 8.3.b.iii: Cube Assembly: Time = 250 s.

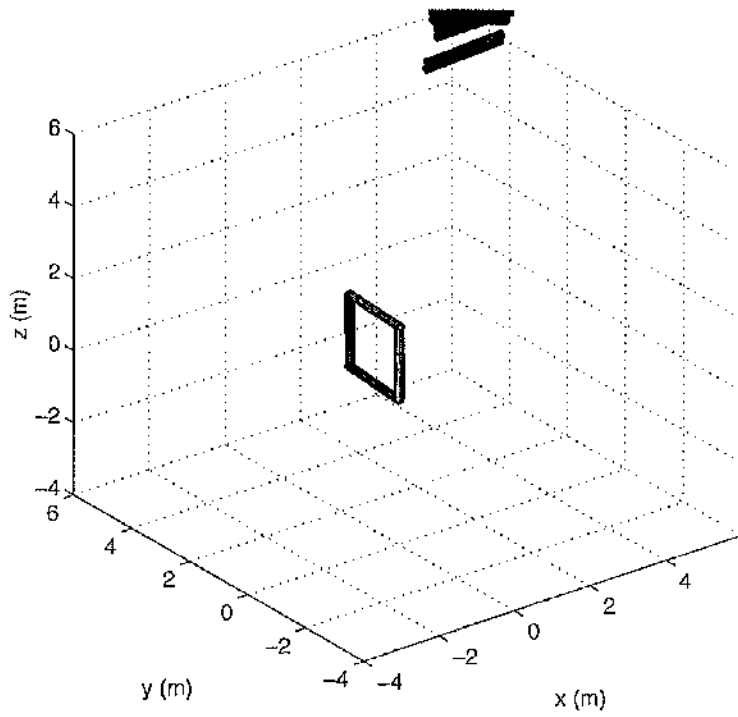


Figure 8.3.b.iv: Cube Assembly: Time = 500 s.

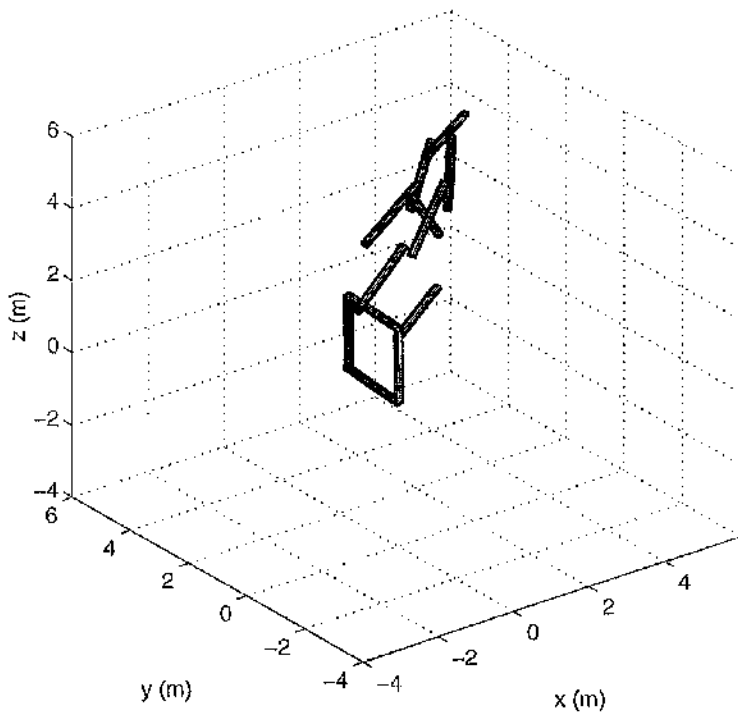


Figure 8.3.b.v: Cube Assembly: Time = 675 s.

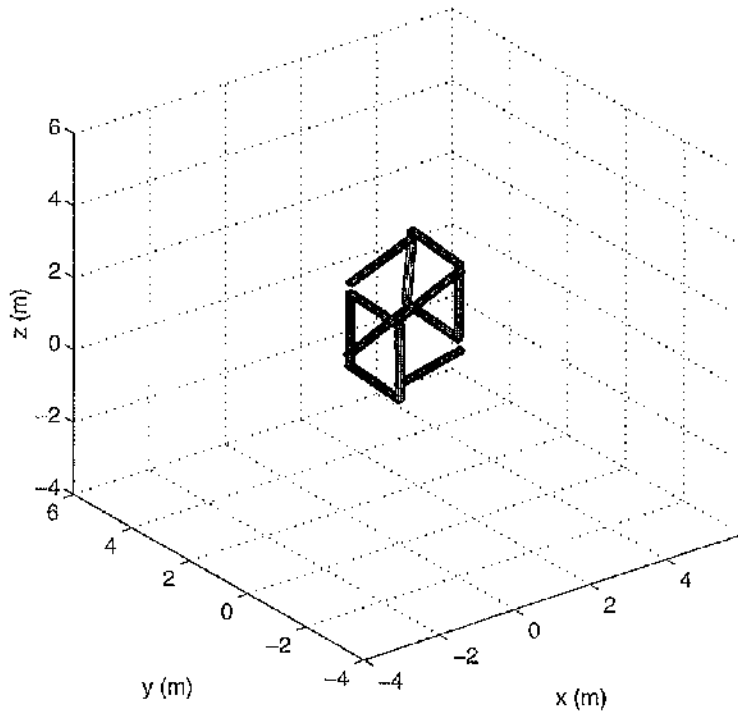


Figure 8.3.b.vi: Cube Assembly: Time = 750 s.

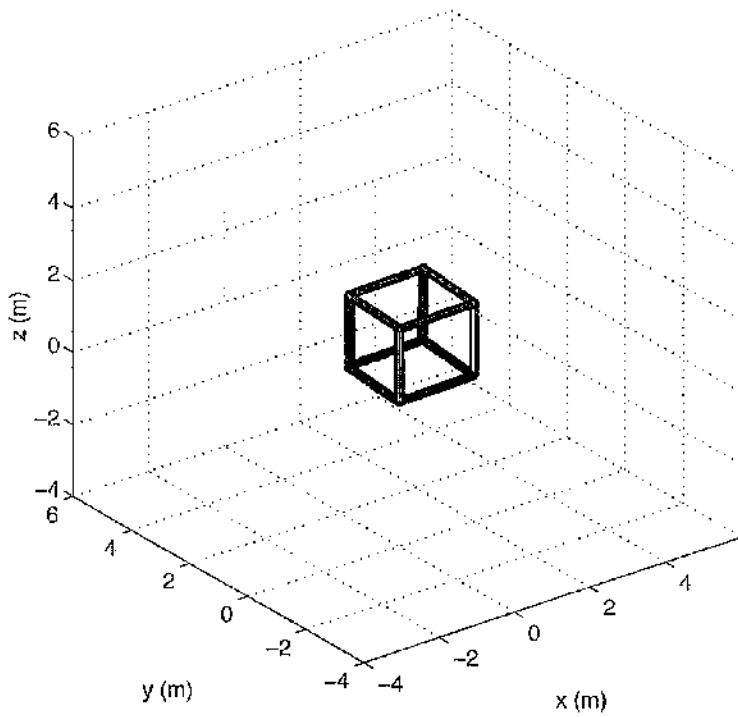
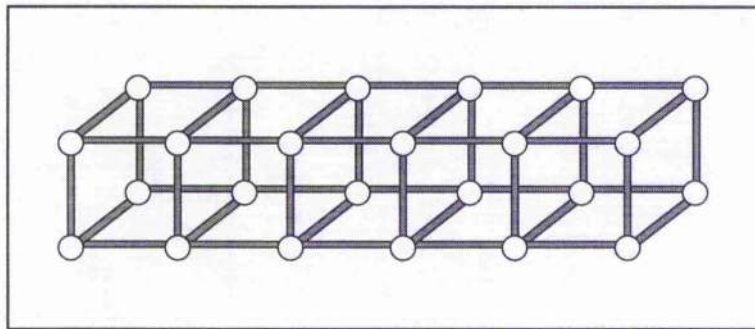


Figure 8.3.b.vii: Cube Assembly: Time = 1850 s.

### 8.4 Case Study: Truss Assembly

The truss structure shown in **Figure 8.4** represents one of the strongest, yet simplest structures in common use. The truss consists of forty four beam elements rigidly connected to form a larger load bearing structure. The assembly sequence for the truss is based upon the cube assembled in **Section 8.3**. Following the assembly of the cube, the table-like structure previously assembled as the second component of the cube may be used to extend the cube in a given direction. Examining **Figure 8.4**, the breakdown of the assembly sequence is shown with the initial base cube being extended.

Considering the architecture required to assemble the truss, initially a primary controller is required which will devolve tasks to a secondary set of controllers. Examining **Figure 8.5**, the architecture is shown with the primary controller controlling two secondary controllers. The secondary controllers are responsible for the assembly of the cube base and the extension structure. An advantage of the subsumption architecture is that the secondary controller responsible for the assembly of the cube is identical in every respect to that of the primary controller used in **Section 8.3**. Therefore it may be stated that any structure previously assembled may be incorporated into another larger structure. Thus, it becomes possible to build a library of validated building block structures which may be quickly and easily assembled into larger, more practical structures.



**Figure 8.4:** Truss Structure.

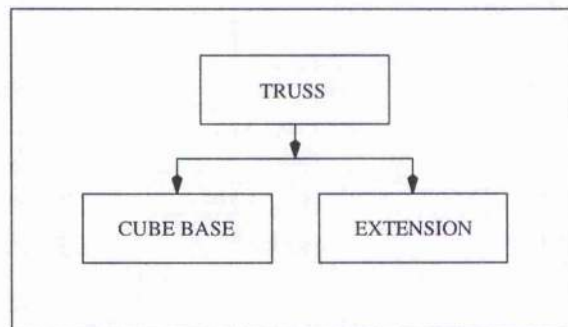


**Figure 8.5:** Truss Controller Architecture.

### 8.4.1 Potential Function Definition

Considering **Figure 8.5**, the architecture required to assemble the truss requires two secondary controllers. The first of the two secondary controllers is the cube controller previously developed. This controller is tasked with extending the cube structure and is very similar to that of the extension unit controller used previously. The only difference is that the connection site of the extension structure must be updated with every extension unit added. The total length of the truss structure envisaged here is five units. Therefore, from the cube, the extension unit controller will add four units with each unit connection set specified by **Equation 8.2** with an updated connection site. Again, considering the population size, the total number of vehicles required to assemble the truss is derived from the largest single task required to assemble the structure, i.e. the extension unit requires eight vehicles for assembly, therefore the total population required to assemble the truss structure is eight vehicles.

### 8.4.2 Results

The addition of the extension structure and the displacement from equilibrium that results may be clearly seen in the behaviour of the global potential, shown in **Figure 8.6.a**. The potential is repeatedly displaced by the activation of the secondary controllers. However, every time a controller is activated and the potential displaced, Lyapunov's theorem guarantees that the potential converges to the goal. Thus the final result is that of the goal structure. The simulation of the assembly problem is shown in **Figures 8.6.b**. The assembly is carried out by eight free-flying vehicles requiring a total time of 5250 s (87.5 minutes). From the simulation, the assembly of the cube structure is clear. From the initial cube structure, the addition of the remaining extension structures can be seen with a finished goal structure of a five bay truss.

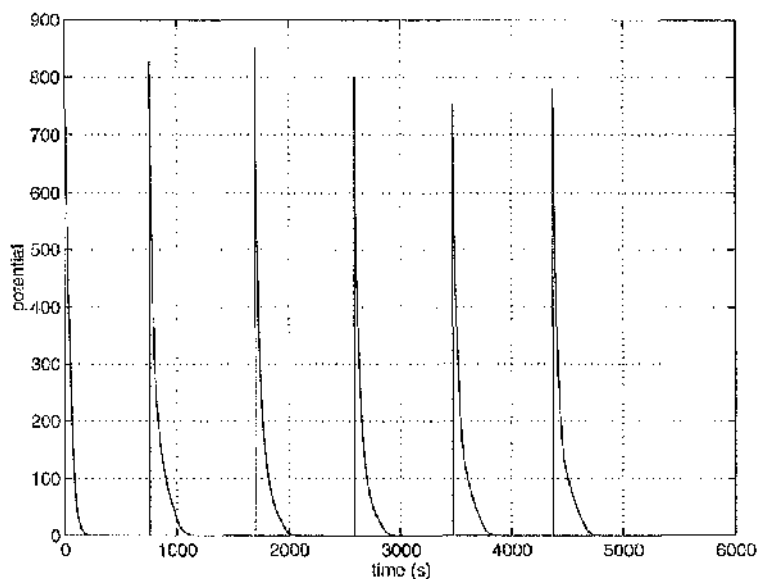


**Figure 8.6.a:** Potential Function.

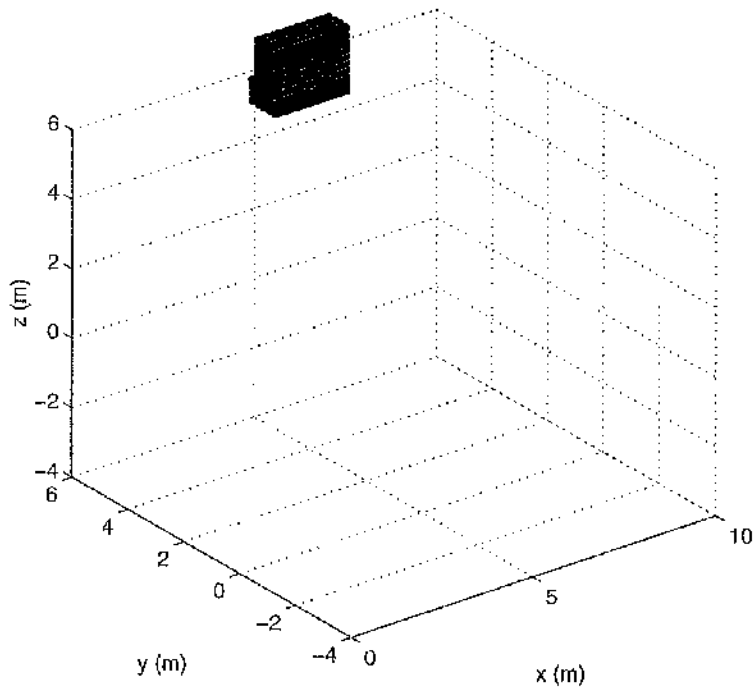


Figure 8.6.b.i: Truss Assembly: Time = 0 s.

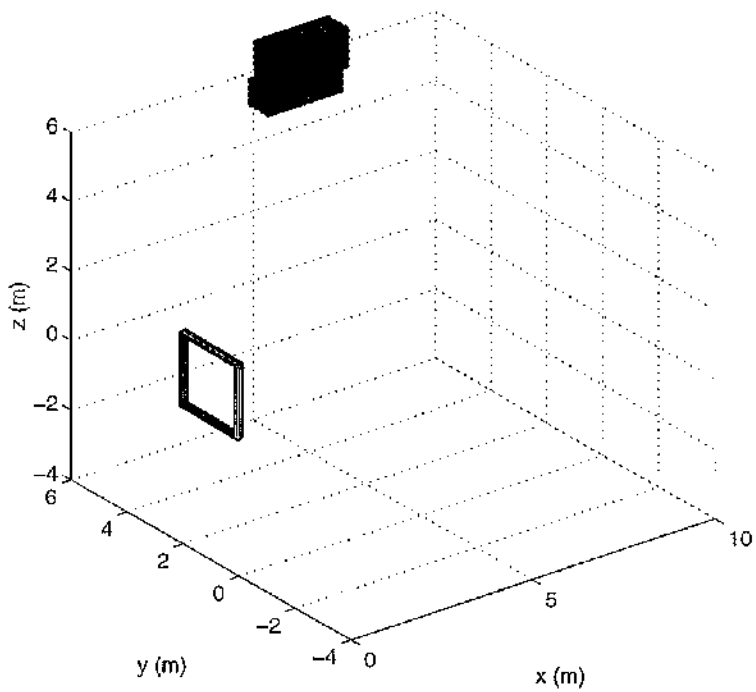


Figure 8.6.b.ii: Truss Assembly: Time = 500 s.

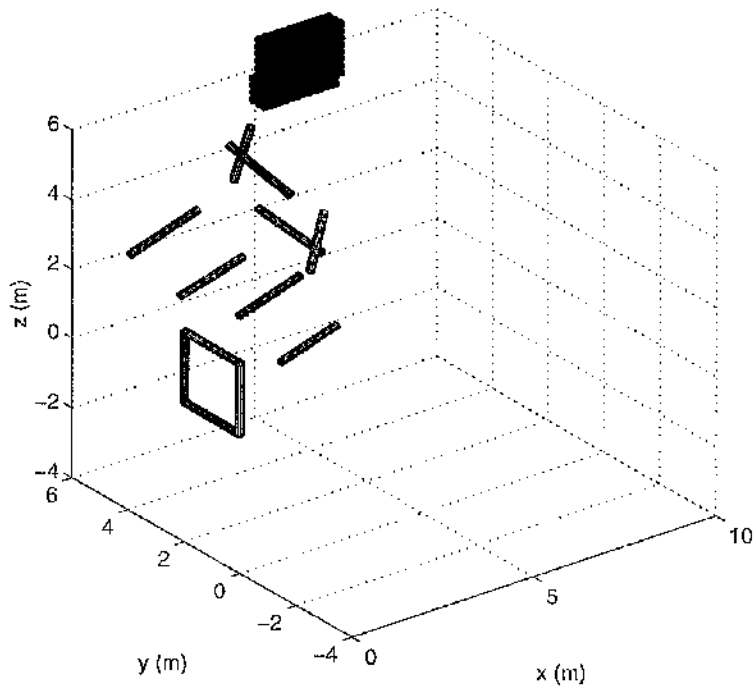


Figure 8.6.b.iii: Truss Assembly: Time = 1000 s.

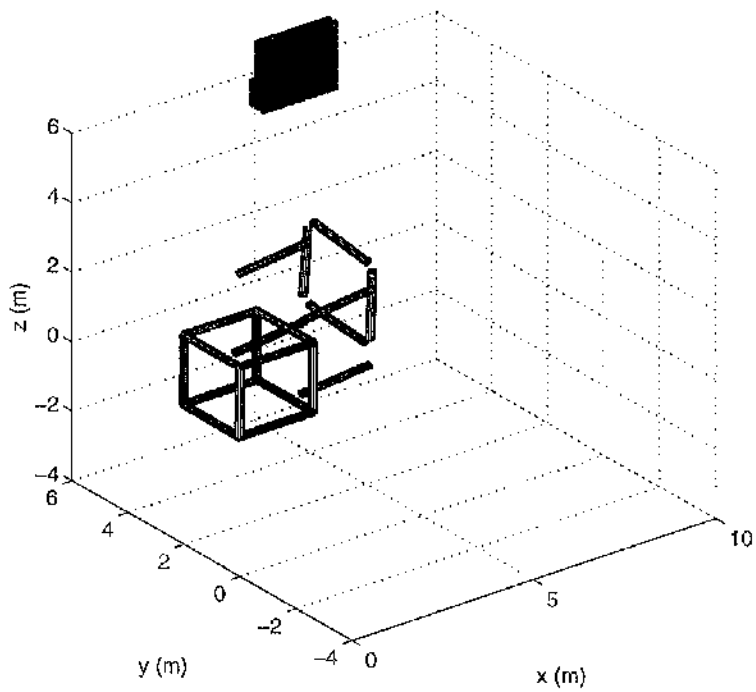
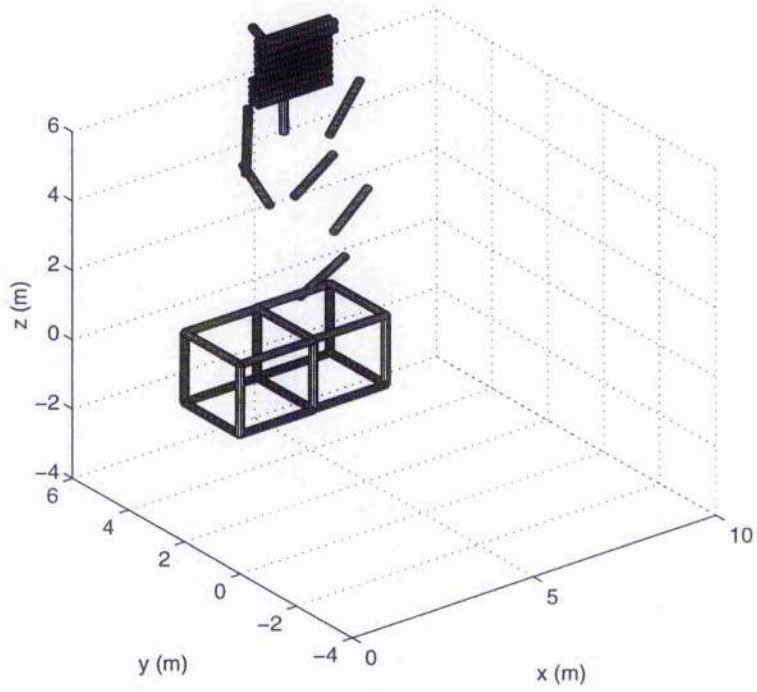
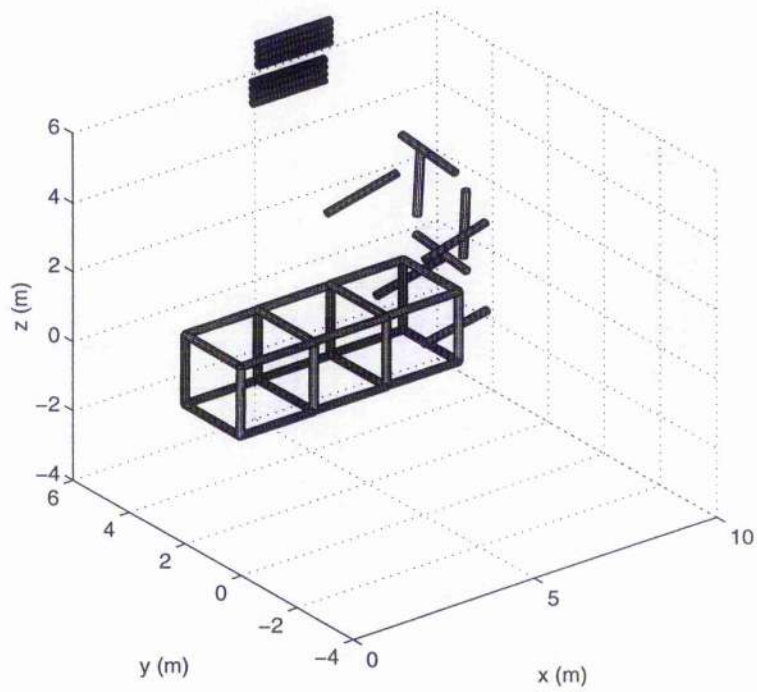


Figure 8.6.b.iv: Truss Assembly: Time = 2000 s.



**Figure 8.6.b.v:** Truss Assembly: Time = 2750 s.



**Figure 8.6.b.vi:** Truss Assembly: Time = 3750 s.

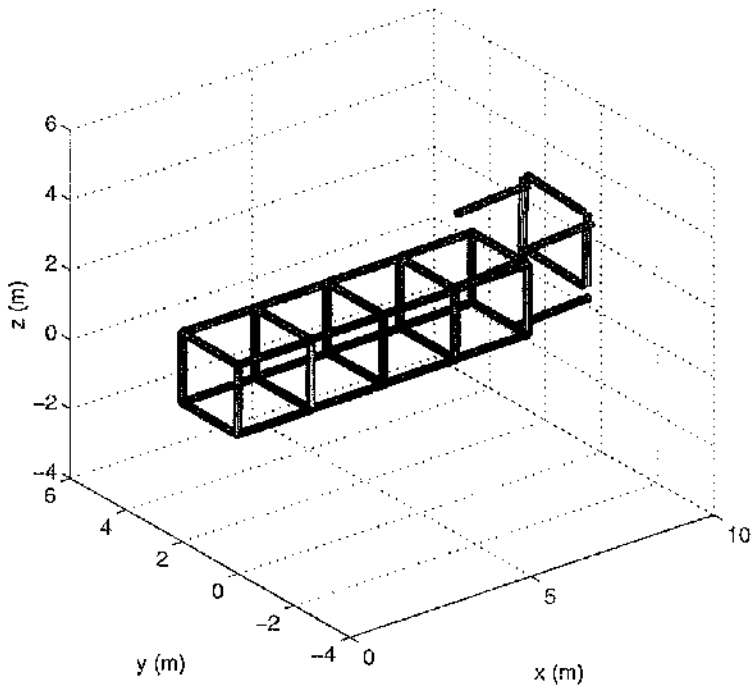


Figure 8.6.b.vii: Truss Assembly: Time = 4750 s.

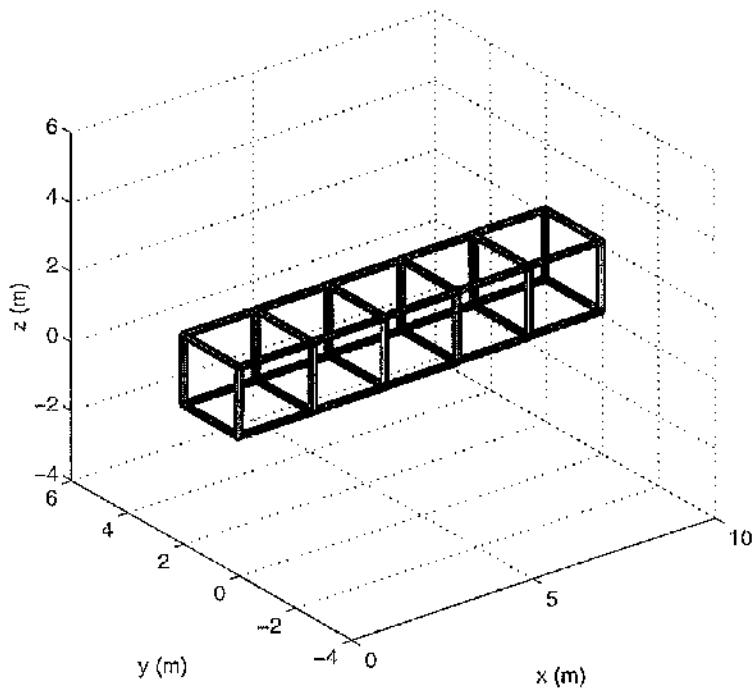


Figure 8.6.b.viii: Truss Assembly: Time = 5295 s.

## 8.5 Case Study: Truss Cube Assembly

The assembly of the cube structure and the subsequent assembly of the truss has demonstrated the use of a subsumption architecture in conjunction with a primary controller. However, each of these structures has made use of a single team of assembly vehicles assembling sub-components in a serial fashion. If a multi-team vehicle population is to be demonstrated, a goal structure must be defined which requires such a population. Such a structure is the truss-cube. A truss-cube, is a simple cube where each edge is assembled not from beams, but from the truss assembly. Thus, it is possible to have individual teams of vehicles assembling individual trusses.

The use of multi-team populations and the subsequent simulation of assembly lends itself to a particular type of simulation. In this case study, each team has been simulated by a separate processor in a cluster of workstations using the *Parallel Virtual Machine* (PVM) environment. Each team's assembly tasks is carried out as normal by an individual processor, however, careful consideration must be given to the information flow between the processor and thus the teams. Therefore, it is possible to have a team operating on two distinct levels. The first level is that within the team, which demands communication between the vehicles pertaining to position and velocity, which may be handled by a single processor. The second level is communication between the team controller and the primary controller regarding task completion and resource allocation. This is dealt with by an overseer processor which communicates with all the processors within the cluster.

Therefore, the use of a parallel computing environment has allowed a realistic simulation of a total population of vehicles performing complex assembly problems. This leads to the definition of sensor and information flow specifications between the teams and individual team members. Currently, for the structure envisaged here, the micro-communications between team members shall be as normal, with full position and velocity information being broadcast to other team members. However, the macro-communications between the teams themselves shall be limited to position information and times of completion for individual tasks. One area not examined here is that of collisions between vehicles on separate teams. However, this is easily circumvented by placing larger repulsive potential spheres around the whole team and broadcasting that information to the remainder of the population as opposed to the broadcasting of position information of each individual team member.

### 8.5.1 Potential Function Development

The potential function used in this example is that given in **Equation 7.26**. As previously described, this potential function will be used within every team to complete the desired tasks. The connection set of every team however, shall be determined by the team primary controller and may differ from team to team. The truss-cube structure envisaged here consists of three hundred and thirty six beam elements. The maximum number of teams

employed shall be six, each consisting of eight members resulting in a total population of forty-eight assembly vehicles. Thus the total number of processors required to simulate assembly is also six. The maximum number of vehicles employed at any given time is forty-eight, with a minimum of four vehicles for the initial base assembly tasks.

The full subsumptive architecture is shown in **Figure 8.7** with the primary truss-cube controller utilising the previously developed truss controllers. The only additional connection set derived for this structure which has not been previously employed has been added to the truss controller to allow two truss elements to join together to form a corner joint. This connection set consists of a truncated extension structure given by

$$\mathbf{G}_{Cap} = \{(1, \sigma_1) \quad (2, \sigma_2) \quad (3, \sigma_3) \quad (4, \sigma_4)\} \quad (8.3)$$

where  $\sigma_i$  ( $i=1 - 4$ ), are the female connection points on the main structure. Thus, using the connecting element, the sides of the cube may be joined and the goal structure assembled.

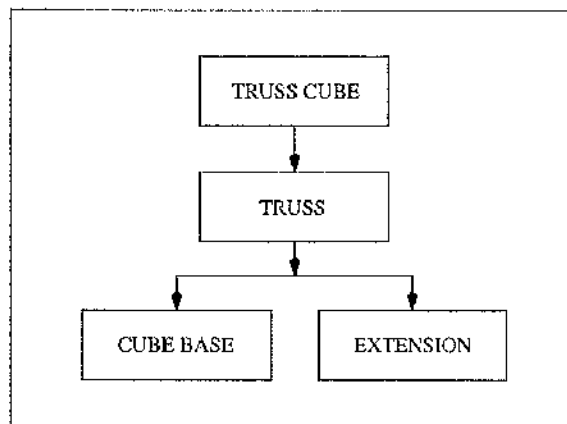


**Figure 8.7:** Truss Cube Controller Architecture.

### 8.5.2 Results

The simulation of the assembly problem is shown in **Figure 8.8**. The assembly was carried out in a total time of 267 minutes. From the simulation of the assembly, the growth of the goal cube structure is clear. The initial base cube structure, the addition of the truss and the growth of the structure in three dimensions are clear.

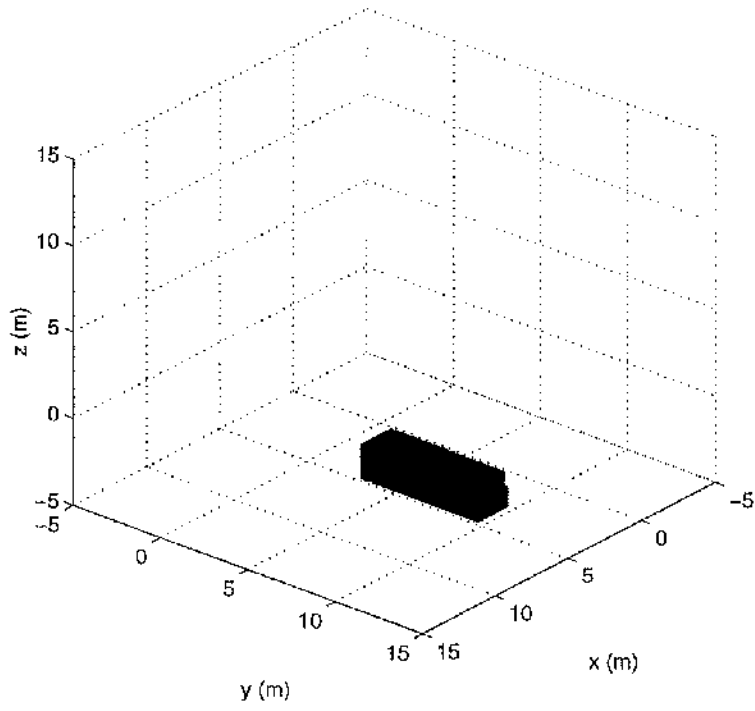


**Figure 8.8.i:** Truss Cube Assembly: Time = 0 s.

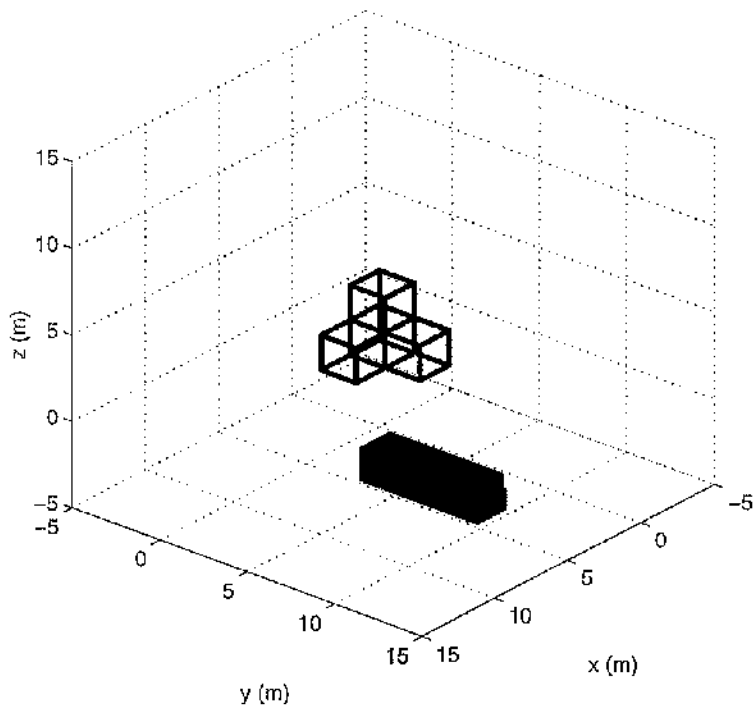


**Figure 8.8.ii:** Truss Cube Assembly: Time = 500 s.

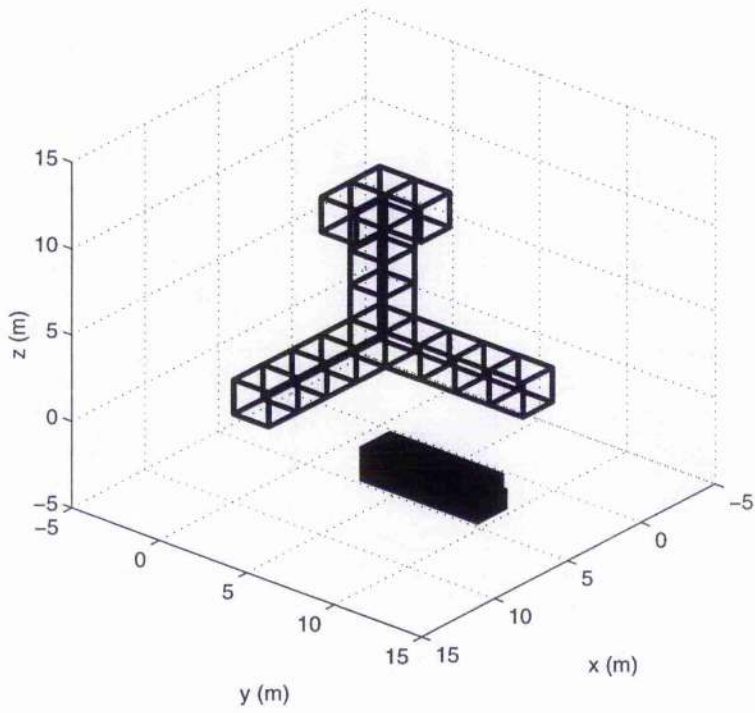


**Figure 8.8.iii:** Truss Cube Assembly: Time = 1000 s.

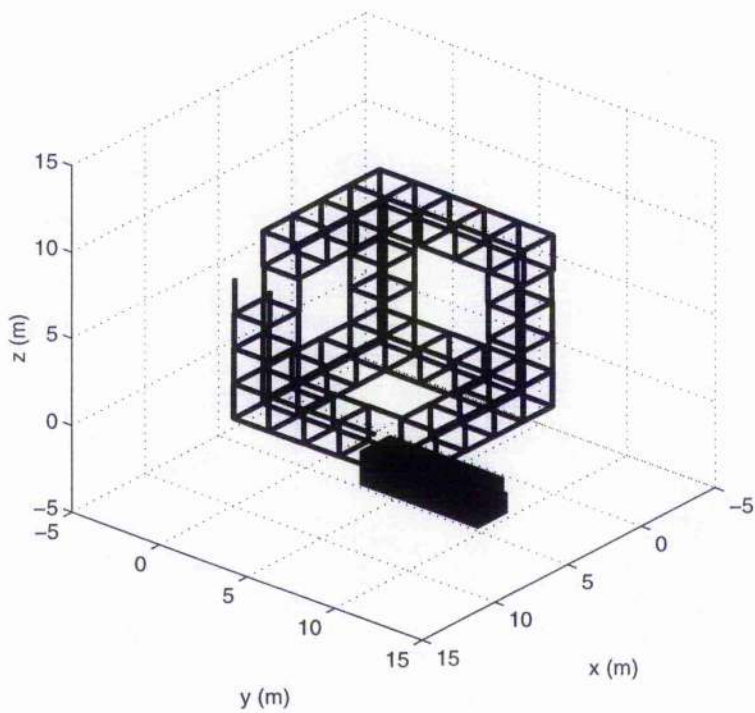


**Figure 8.8.iv:** Truss Cube Assembly: Time = 1500 s.

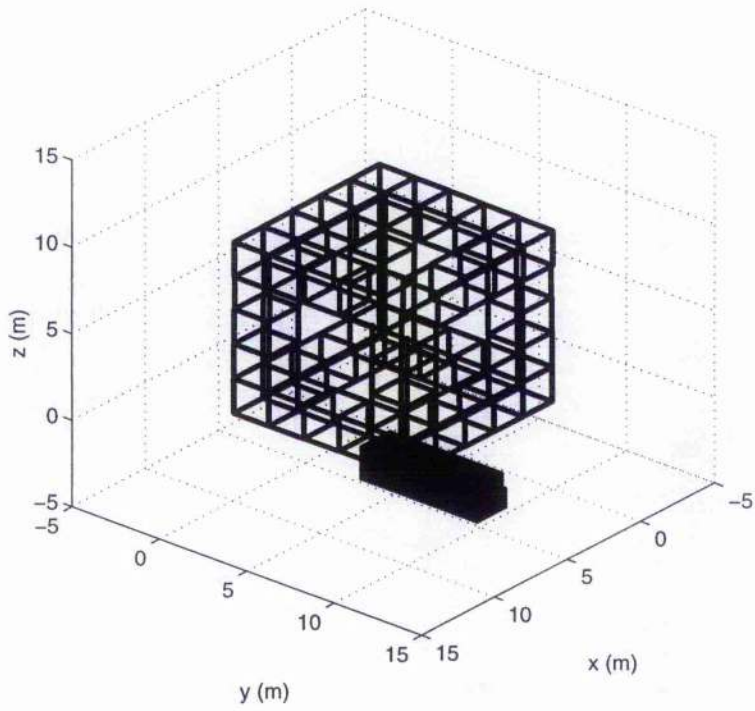


**Figure 8.8.v:** Truss Cube Assembly: Time = 2000 s.

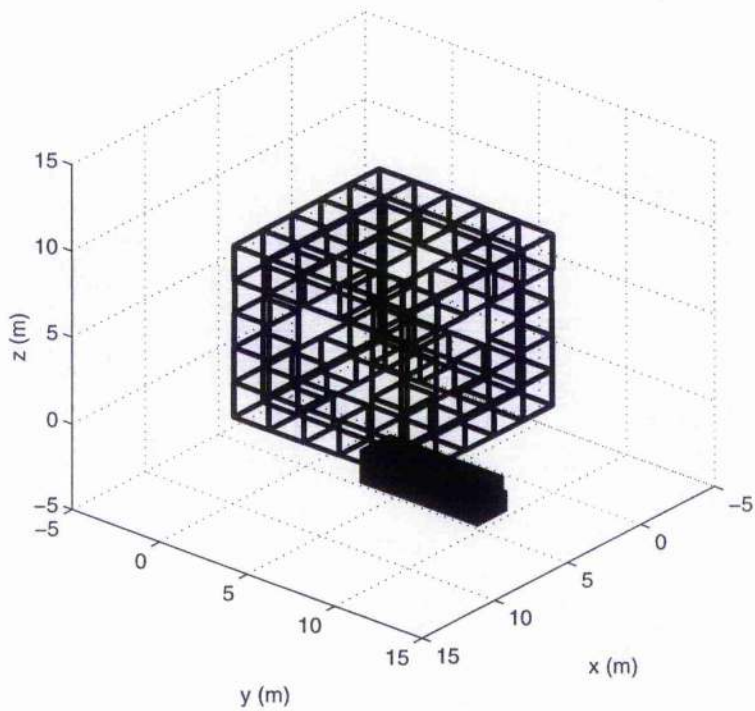


**Figure 8.8.vi:** Truss Cube Assembly: Time = 2230 s.

## 8.6 Informatics

The principal result of the architecture is the development of relatively simple controllers each capable of working co-operatively to assemble complex structures. The scope of this architecture is, in principle, unlimited. Secondary controllers may be called upon in many different scenarios. Also, the controller need only store the connectivity matrix associated with the component it is tasked to assemble. Therefore, any supervising controller need not see the detailed mechanism of assembly, but only requires notification of the completion of a sub-structure.

It also important to note that the only difference in all the controllers presented here is the connectivity matrix, the connection angles and the resources required for a sub-structure. This information may be stored as separate data. It therefore becomes practical to develop a library of data sets associated with specific components. In addition, the formation of the global potential function through a connectivity matrix allows a compact solution to complex assembly problems. Therefore, from high level commands for the assembly of components, the method will reduce this problem to individual actuator commands to manoeuvre the free-flying assembly vehicles into the correct configurations.

## 8.7 Conclusion

Technologically, the greatest requirements on the free-flying vehicles will be in the area of communications and sensors. However, these requirements have been partially addressed with the application of the subsumptive type architecture. With the use of robot teams, communicating only with other team members, the problem then reduces to managing a group of vehicles, rather than the total vehicle population. The implication of applying a subsumption architecture to the truss cube, and its effect on the vehicle requirements, is that each vehicle must interact with a team numbering as much as eight, as opposed to the total population of forty eight.

# Chapter Nine: Conclusions

## 9.1 Review

Initially a review of on-orbit assembly and large space structures was provided in **Chapter 1**. Then, the solution to the two-body problem, and the examination of the relative motion of two spacecraft provided the basis for a model of spacecraft operations on-orbit. The resulting motion and the optimal solution of the two impulse transfer rendezvous was then considered in detail in **Chapter 2**. The development of the equations of relative motion and the resulting linearisation provided the commonly used Clohessy-Wiltshire equations of motion. Furthermore, the development of a closed form solution to these equations provided a method of calculating the  $\Delta v$  required to execute a two-impulse transfer between two arbitrary points. The development of the state transition matrix and the optimisation of the transfer with respect to  $\Delta v$  provided an optimal two-impulse transfer. Thus, any method which manoeuvres a spacecraft between two points may be compared with this optimal value. However, there are drawbacks to the optimisation method. Principally the flexibility of the two-impulse transfer must be called into question when considering the possibility of obstacle avoidance. i.e. the optimisation of a transfer would be compromised if a mid-course correction were required.

An inherently flexible control method was examined in **Chapter 3**. The development of the potential function method from Lyapunov's second method and the application to spacecraft control problems was introduced. The potential function method provided a robust, highly flexible control method which was examined for both attitude and translational control problems. Both of these proved to be satisfactorily controlled by the use of a goal potential. In addition, the application of a control method based on Lyapunov's theorem guaranteed stability and, even for the complex attitude control problem, convergence to the solution was ensured in a smooth manner. The application of the method to the translational problem allowed a comparison between the potential function method and the optimal two impulse transfer  $\Delta v$  cost. Comparing case studies, it was found that the  $\Delta v$  cost of transfer for the potential function method is generally several times greater than the optimal case.

The potential function and the control inputs to the spacecraft may be derived analytically within a self contained control algorithm. In addition, the method is both flexible

and robust allowing path shaping to the goal. The transfer problem was re-examined in **Chapter 4** with the inclusion of obstacles in the environment. To introduce an obstacle into the environment, a region of high potential was added to the goal potential function. Thus, when the spacecraft closes on the obstacle, the potential will begin to increase and the spacecraft will be autonomously deflected. Four methods of defining obstacle potentials were examined. These are the Gaussian, power-law, flat-sided and superquadric obstacle potentials. Of the four, only one method, the flat-sided obstacle potential was unsuccessfully negotiated by the chase vehicle. The remaining three methods created obstacle potentials that, when added to an goal potential, did not generate stable local minima.

The Gaussian obstacle potential offered the best all round performance with regard to computational complexity and accuracy. The ability to exactly define the characteristic dimension of the obstacle and guarantee minimal incursions into that space in conjunction with easily definable parameters made this function more applicable to general problems. The power-law obstacle potential proved to be computationally efficient, however, the sizing of the obstacle proved to be dependent on the index and difficulties were encountered in determining the interface between the goal and obstacle potentials throughout the circumference of the obstacle. The superquadric was by far the most complex of the obstacle potentials with parameters which were obtained from non-linear problems. However, the performance was found to be excellent and very efficient in the use of space since the potential function mapped itself onto the contours of the body. This method would be applicable to complex geometries where there were significant restrictions on movement.

When considering an assembly control problem, the control philosophy must include an examination of multi-body systems. In **Chapter 5**, other forms of potential functions were examined, and more specifically, those which are applied in molecular dynamics to simulate atomic behaviour. The behaviour of large molecules was considered to provide insight to such multi-body system dynamics. The primary consideration when examining these molecules, is the relationship between the potential and stability of the molecule. It was found that, as the potential decreases, the stability of the molecule increases as expected. A potential function based on the bond length between atoms was developed which allowed a twelve atom system to be simulated for convergence and stability. Thus, the application of potential functions to multi-body systems proved to be feasible.

Using multi-body potentials and expanding them to include connection constraints has demonstrated the feasibility of using potential functions to assemble specific structures. In **Chapter 6**, a beam element was defined which allowed a potential function to be developed from the state vectors of the beams. This assembly potential allowed both the parallel and serial assembly of two structures, the triangle and square. The parallel assembly method, which is the assembly of the structure in a single effort, and the serial method, which is the assembly of the structure in stages, were both examined. The advantages and disadvantages of each method were examined and principally, the parallel method was found to be the lesser of the two with regards to the computational demands. However, the demands on the controlling

vehicles rapidly increased with the complexity of the structure. The serial method was also successful with the use of virtual beams and phased application potentials. However, the computational complexity was higher than the parallel method. In contrast, the vehicle demands were uniform throughout the assembly which would be relevant to larger structures.

In addition to the development of a goal potential function, which allowed the assembly of specific structures, a repulsive potential was developed to maintain separation of the beams and prevent collisions throughout the assembly process. However, a contradiction emerged in that the beams must eventually be connected together and in addition separation must be maintained. Therefore, the repulsive potential was expanded to include the scaling of the repulsive potential so that separation was maintained until the beams were in the correct configuration. Once the beams were in the correct configuration, the repulsive potential would vanish, thus allowing convergence to the goal structure.

The development of assembly potential functions and their application has proved successful to the assembly of the triangle and square. In **Chapter 7**, the state vectors of the individual beams were included within a global state vector. This global state vector allowed a global potential function capable of assembling any predetermined structure. Inherent within the global potential function is the information regarding the form of the goal structure. This information takes the form of a connectivity matrix. The development and manipulation of the connectivity matrix was examined. In particular, the manipulation of the matrix during assembly for adaptive structures and deployables. In addition, the use of connectivity matrices has allowed complex problems to be broken down by partitioning elements of the connectivity matrix until the resources were available to complete assembly. Thus, assembly strategies become possible and the emphasis has altered from the development of the potential function to that of the application of the connectivity matrix.

Finally, the use of construction strategies allowed the assembly of the structure in a variety of ways. However, the principal objective of these strategies is to complete the goal structure using the minimum number of control vehicles. The application of a subsumptive type architecture was examined in **Chapter 8**. The subsumptive architecture allows the assembly of large, complex structures by devolving the assembly of sub-components to sub-controllers. The application of sub-controllers has allowed the development of robot teams, communicating only with other team members. Therefore, the communication and sensor problems reduce to the management of a team of vehicles, rather than the total vehicle population, thus simplifying the vehicle design. The delegation of sub-tasks allows the method to multi-task and this was reflected in the parallelisation of the potential function controller so that six independent tasks may be carried out simultaneously.

## 9.2 Mission Statement

The development of the potential function and the objectives of this thesis were developed and refined in **Chapter 1** to produce the mission statement;

*'To provide an on-orbit assembly method which will incorporate a practical and robust algorithm for individual vehicle control within a larger co-operative group. The emphasis shall be on providing a practical application of the control method which will allow further development to a prototype article.'*

In every respect, the development of the potential function has met the objectives within the mission statement, more specifically;

- The computational elements of the control algorithm have improved with development to produce an efficient, flexible control method which may be applied using current computing capabilities.
- The development of test cases to assess the control algorithm performance has allowed application to new and novel applications such as reconfigurable structures and integrated design.
- The use of the global potential function and the connectivity matrix has allowed the application of strategies to simplify the assembly process and vehicle design.

Considering the overall practicality of the method, current results are promising. Especially to the application of the method to areas such as variable topology structures and integrated design.

In **Chapter 7**, the application of smart joints and beams was shown to be highly successful. This technique has proven to be an interesting characteristic of the global potential function and in particular the connectivity matrix. It is believed that this technique offers a capability beyond other spacecraft deployables and structures. Technologically, much work must be carried out in the physical development of the beams and joints and also in areas such as sensor technologies. Some applications of this type of structure have been discussed. However, in areas such as large reflector deployment the use of variable topology structures could significantly reduce the launch mass of the spacecraft as the duplication of components is not required. For example, during the launch and orbit insertion phases of a mission, the spacecraft must withstand large loads. Therefore, the spacecraft structure must be designed to that maximum launch load. However, this is only a small fraction of the total mission duration. Variable topology structures would allow spacecraft design to be more efficient as the spacecraft structure would change to meet the mission demands. For example, a stiff, load bearing truss structure could reconfigure itself into a large reflector on-orbit.

Another element of the potential function method which offers distinct advantages over conventional structures is the integrated design capability. With the development of an accurate simulation in conjunction with an on-orbit assembly package, the design of the structure may be carried out on computer using a CAD package. The potential function method would then simulate the design as it assembled to the goal structure. If the goal structure is acceptable, the connectivity matrix may then be supplied directly to the on-orbit robot assembly team. Thus, the prototyping and assembly of components would proceed at an unprecedented rate, and the design stage of a structure may be minimised.

Thus, in conclusion, this thesis has provided an examination of the application of potential function methods to on-orbit assembly. Although the method has proven to be promising, further study and research is required.

#### 9.4 Recommendations

Any future development of the potential function assembly method can be divided into near term development of the assembly simulation, and the long term development to a physical prototype. With specific regards to the assembly simulation, near term improvements may be made in the areas of;

- **Incorporation of detailed physical properties of the structure:** This includes the development of joint and elastic beam properties. This would allow the evaluation of strategies to develop physical properties, such as to maximise the load bearing capability of a structure, at the top level of the subsumptive architecture.
- **Incorporation of a detailed robot vehicle model:** One possibility is to incorporate developed models of the *Ranger* vehicle. Thus, the modelling of the assembly process would be sufficiently accurate to allow the design of a physical prototype. In addition, models of internal robot systems such as thrusters and sensors will allow accurate modelling of physical translations and rotations of the vehicle thus allowing the development of strategies to minimise the fuel consumption and thus maximise the efficiency of the vehicle operation.
- **Development of a smart beam model:** As discussed previously, the smart beam and joint concept could prove to have interesting applications in spacecraft operations. The reasons for developing an accurate vehicle model are still valid for smart beams.
- **Informatics:** Although the algorithms developed for the calculation of the potential function were successfully parallelised into teams within the subsumption architecture, the parallelisation of individual controlling vehicles is required. Thus, accurate modelling of the information flow and the sensor and communication requirements of the controlling vehicles may be developed.

In conclusion, the development of the potential function method and its application to on-orbit assembly has proven to be promising. Although much work would be required to develop a physical prototype, there is significant near-term simulation tasks to be considered which will lead to this ultimate goal.

## References

- 1 Parrish J.C., Akin D.L., *The Ranger Telerobotic Flight Experiment: Mission, Technologies, and Programmatics*, Proc. of RCE II, Albuquerque, NM, pp. 136-142, June, 1996.
- 2 *History of Space Exploration*, <http://nauts.com/histpace/histpace.html>. Last Visited December 1997.
- 3 *The Race to the Moon - A Chronology*, <http://khandu.unl.edu/~nikku/moonrace.html>. Last Visited December 1997.
- 4 Riley D.R. et al., *Comparison of Results of Two Simulations Employing full-size Visual Cues for Pilot Controlled Gemini-Agena Docking*, NASA TN D-3687, Langley, November 1966.
- 5 Long E.R. Jr, Pennington J.E. and Deal P.L., *Remote Pilot-Controlled Docking with Television*, NASA TN D-3044, Langley, October 1965.
- 6 Mikulas M.M. Jr, Thomson M., *State of the Art and Technology Needs for Large Space Structures*, Flight-Vehicle Materials, Structures, and Dynamics - Assessment and Future Directions, ASME, pp. 173-238, 1994.
- 7 Akin D.L., *EASE Experimental Assembly of Structures in EVA: Overview of Selected Results*, SSL 12-86, MIT, August 1986.
- 8 Akin D.L., Bowden M.L., *EVA Capabilities for the Assembly of Larger Space Structures*, MIT Space Systems Laboratory IAF 82-393, October 1982.
- 9 Akin D.L., Mills R.A. and Bowden M.L., *Final Report on the Structural Assembly Demonstration Experiment (SADE)*, MIT Space Systems Laboratory Report 16-87, July 1987.
- 10 Bowden M.L., *Progress Report on the Structural assembly Demonstration Experiment*, SSL Report 2-83, MIT, January 1983.
- 11 Rhodes M.D., Will R.W., and Quach C., *Baseline Tests of an Autonomous Telerobotic System for Assembly of Space Truss Structures*, NASA TP-3448, Langley, July 1994.

- 12 Doggett W.R., *A Guidance Scheme for Automated Tetrahedral Truss Structure Assembly Based on Machine Vision*, NASA TP-3601, Langley, November 1996.
- 13 Rhodes M.D., Will R.W., and Quach C.C., *Verification Tests of Automated Robotic Assembly of Space Truss Structures*, J. Spacecraft and Rockets, Vol.32, No. 4, July-August 1995.
- 14 Herstrom C.J. et al., *Software Design for Automated Assembly of Truss Structures*, NASA TP-3198, Langley, June 1992.
- 15 Allen C.L., *An Expert System Executive for Automated Assembly of Large Space Structures*, NASA TM-4487, Langley, November 1993.
- 16 Homem-de-Mello L.S., *Automatic Planning in Robotic Applications*, AIAA, 'Telerobotics and Robotics in Space, Progress in Astronautics and Aeronautics, Vol. 161, Chap 7, 1990.
- 17 Dorsey J.T., Sutter T.R., and Wu K.C., *Structurally Adaptive Space Crane Concept for Assembling Space Systems on Orbit*, NASA TP-3307, Langley, November 1992.
- 18 Wu K.C., Sutter T.R., *Structural Analysis of three Space Crane Articulated Truss Joint Concepts*, NASA TM-4373, Langley, May 1992.
- 19 Sutter T.R. et al., *Structural Characterisation of a First Generation Articulated Truss Joint for Space Crane Application*, NASA TM-4371, Langley, June 1992.
- 20 Furness T., *Act of Faith*, Flight International, June 11-17, pp. 52-54, 1997.
- 21 Stofan A.J., *Preparing for the Future*, Aerospace America, pp. 16-22, September 1987.
- 22 Foley T.M., *Engineering the Space Station*, Aerospace America, pp. 26-32, October 1996.
- 23 Gates R.E., *International Space Station (ISS) Assembly Sequence Planning*, Proc. of RCE II, Albuquerque, NM, pp. 435 - 442, June 1-6, 1996.
- 24 Hunt T., *Overview of the International Space Station Extra Vehicular Robotics verification*, Proc. of RCE II, Albuquerque, NM, pp. 502 - 508, June 1-6, 1996.
- 25 Briggs W., Mapar J., and O' Donnell J., *Robot Utilisation Opportunities for the International Space Station Alpha*, NASA Contract NAS5-32539, Goddard Space Flight Center, May 1995.
- 26 McSpadden J., Chang K., *Review of the Solar Power Satellite*, Proc. of RCE II, Albuquerque, NM, pp. 254 - 259, June 1-6, 1996.
- 27 Glaser P.E., *Evolution of the Satellite Solar Power Station (SSPS) Concept*, J. Spacecraft and Rockets, Vol. 13, No. 9, pp. 573-576, September 1996.
- 28 Miller K.H., *Solar Power Satellite Construction Concepts*, NAS915196: Solar Power Satellite System Definition Study, 1977.
- 29 Mankins J.C., *The Space Solar Power Option*, Aerospace America, pp. 31-36, May 1997.

- 30 Ignatiev A., Freundlich A., *The Production of Photovoltaic Devices in Space*, Proc. of RCE II, Albuquerque, NM, pp. 287 - 292, June 1-6, 1996.
- 31 Christiansen C.B., Camstock D.A., Mankins J.C., *The Economics of Space Solar Power*, Proc. of RCE II, Albuquerque, NM, pp. 260 - 268, June 1-6, 1996.
- 32 Akin D.L., *Quantifying Human Performance in Space Operations*, SSL Report 23-86, MIT, October 1986.
- 33 Heard W.L. et al., *Tests of an Alternate Mobile Transporter and Extravehicular Activity Assembly Procedure for the Space Station Freedom Truss*, NASA TP-3245, Langley, October 1992.
- 34 Watson J. et al., *Mobile Transporter Concept for Extravehicular Activity Assembly of Future spacecraft*, J. Spacecraft and Rockets, Vol. 29, No.4, July-August, 1992.
- 35 Coppa A., *Robotic Assembly of Truss Beams for Large Space Structures*, J. Spacecraft and Rockets, Vol. 32, No. 4, July-August 1995.
- 36 Bush H.G., Mikulas M.M. Jr., and W.L. Heard Jr., *Some Design Considerations for Large Space Structures*, AIAA Journal, Vol. 16, No. 4, pp. 352-359, April 1978.
- 37 Davis W.T., King C.B., *Packaging, Development, and on-Orbit Assembly Options for Large Geostationary Spacecraft*, NASA TP-3088, Langley, July 1991.
- 38 *STS-77, Press Kit Spartan 207/IAE*, <http://titania.osf.hq.nasa.gov/shuttle/sts77/spartan.html>. Last Visited December 1997.
- 39 *Inflatable Antenna Kit*, [http://www.jpl.nasa.gov/iae/iae\\_index.html](http://www.jpl.nasa.gov/iae/iae_index.html). Last Visited December 1997.
- 40 Snead J.M., *Building Large Space Bases in Low Earth Orbit*, Proc. of RCE II, Albuquerque, NM, pp. 367 - 377, June 1-6, 1996.
- 41 Snead J.M., *Space Infrastructure Planning*, Proc. of RCE II, Albuquerque, NM, pp. 360 - 366, June 1-6, 1996.
- 42 Garibotti J.F., Cwiertny A.J. Jr and Johnson R. Jr., *On-Orbit Fabrication and Assembly of Large Space Structural Sub-Systems*, Acta Astronautica, Vol. 7, pp. 847-865, 1980.
- 43 Matsue T., Wakabayashi Y., *Investigation of On-Orbit Servicing Robot*, Proc. of RCE II, Albuquerque, NM, pp. 533 - 539, June 1-6, 1996.
- 44 Weisbin C.R., Lavery D., *NASA Rover and Telerobotics Technology Program*, IEEE Robotics and Automation Magazine, December 1994.
- 45 Weisbin C.R., *Rover and Telerobotics Technology Program: Accomplishments and Technology Transfer*, NASA JPL, 1995.
- 46 Sanderson E., *BAT Report*, SSL Report, Space Systems Laboratory, University of Maryland, 1986.

- 47 David L., *Robots for all Reasons*, Aerospace America, pp. 30-35, September 1995.
- 48 Sanner R.M., Slotine J.E., *Stable Adaptive Control of Robot Manipulators Using Neural Networks*, Neural Computation, Vol 7, No. 4, 1995.
- 49 Sanner R.M., Slotine J.E., *Structurally Dynamic Wavelet Networks for Adaptive Control of Robotic Systems*, Proc. IEEE Conf. Decision and Control, New Orleans, 1995.
- 50 Cohen R., Akin D.L., *Development of an Interchangeable End Effector Mechanism for the Ranger Telerobotic Vehicle*, Space Systems Laboratory, University of Maryland, 1995.
- 51 Vance E.E. *Control of Free-Floating and Free-Flying Manipulators with Uncertainty*, Thesis Proposal, Space Systems Laboratory, U. of Maryland, February 1996.
- 52 Kuester S.P., Lane J.C., *Interface Design Issues of the Ranger Telerobotics Flight Experiment*, SAE Technical Paper Series 951522, 1995.
- 53 Bon B., Seraji H., *Obstacle Detection for the Ranger Telerobotic Flight Experiment*, Proc. IEEE Conf. on Robotics and Automation, 1996.
- 54 Bon B., Seraji H., *On-Line Collision Avoidance for the Ranger Telerobotic Flight Experiment*, Proc. IEEE Conf. on Robotics and Automation, 1996.
- 55 Williams T., Tanygin S., *Trajectory Issues Affecting Propulsion System Sizing and Operations of Orbital Inspection Vehicles*, AIAA 96-3648, AIAA/AAS Astrodynamics Specialist Conference, San Diego, CA, USA, July 1996.
- 56 Balaram J., Hayati S., and Volpe R., *Multi-Sensor Inspection Telerobot*, Proc. Int. Symposium on Robotics and Automation, Maui, Hawaii 1994.
- 57 Volpe R., McAfee D., *A Robotic Lighting System for Solar Illumination Simulation*, IEEE Int. Conf. on Robotics and Automation, San Diego, 1994.
- 58 Volpe R., Balaram J., *Technology for Robotic Surface Inspection in Space*, Proc. AIAA/NASA Conf. on Intelligent Robots in Field, Factory, Service, and Space, Houston, Texas, 1994.
- 59 Colavita M.M. et al, *Separated Spacecraft Interferometer Concept for the Millennium Project*, SPIE Vol. 28, No. 07, pp. 51-58, 1996.
- 60 Volpe R., Ivlev R., *A Survey and Experimental Evaluation of Proximity Sensors for Space Robotics*. Proc. IEEE International Conference on Robotics and Automation, 1994.
- 61 Warren, C.W., *Global Path Planning Using Artificial Potential Functions*, Proc. IEEE Int. Conf. Robotics and Automation, Scottsdale, AZ, pp. 316-321, May 1989.
- 62 McInnes C.R., *Potential Function Methods for Autonomous Spacecraft Guidance and Control*, AAS 95-447, AAS/AIAA Astrodynamics Specialist Conference, Halifax, NS, Canada, August 1995.

- 63 McInnes C.R., *Autonomous Proximity Manoeuvring Using Artificial Potential Functions*, ESA Journal, Vol. 17, pp. 159-169, 1994.
- 64 McInnes C.R., *Large Angle Slew Manoeuvres with Autonomous Sun Vector Avoidance*, J. Guidance , Control and Dynamics, Vol.17, No.4, pp. 875-877, 1994.
- 65 McInnes C.R., *Terminal Descent to the Lunar Surface with Terrain Constraints*, University of Glasgow, Dept. of Aerospace Eng. Report 9414, 1994.
- 66 McInnes C.R., *Autonomous Ring Formation for a Constellation of Satellites*, University of Glasgow, Dept. of Aerospace Eng. Report 9426, 1994.
- 67 McInnes C.R., *Autonomous Rendezvous using Artificial Potential Functions*, J. Guidance , Control and Dynamics, Vol.18, No.2, pp. 237-241, 1995.
- 68 Wang P.K.C., *Automatic Assembly of Space Stations*, Proc. NASA/ACC Workshop on Identification and Control of Flexible Space Structures, San Diego, CA, June, pp. 67 - 101, 1984.
- 69 Wang P.K.C., *Interaction Dynamics of Multiple Mobile Robots with Simple Navigation Strategies*, J. of Robotic Systems, Vol 6, No.1, 1989.
- 70 Wang P.K.C., *Navigation Strategies for Multiple Autonomous Mobile Robots Moving in Formation*, J. of Robotic Systems, Vol. 8, No. 2, 1991.
- 71 Wang P.K.C., *Interaction Dynamics of Multiple Autonomous Mobile Robots in Bounded Spatial Domains*, Int. J. of Control, Vol. 50, No. 4, pp. 2109-2124, October 1989.
- 72 Wang P.K.C., Hadacgh F.Y., *Co-ordination and Control of Multiple Microspacecraft Moving in Formation*, J. Astronautical Sciences, Vol. 44, No. 3, pp.315-355, July-September 1996.
- 73 St. John-Olcayto E., McInnes C.R., *Applicability of Potential Function Method to Path Constrained Manoeuvre*, ESTEC Contract 11478/95/NL/JQ/SC, Technical Report #2, October 1996.
- 74 Bay J.S., *Design of the 'Army-Ant' Co-operative Lifting Robot*, IEEE Robotics and Automation Magazine, March 1995.
- 75 Niwa H., *Self-Organising Dynamic Module of Fish Schooling*, J. Theoretical Biology, Vol. 171, pp. 123-136, 1994.
- 76 Noreils F.R., Chatila R.G., *Plan Execution Monitoring and Control Architecture for Mobile Robots*, IEEE Trans. on Robotics and Automation, Vol. 11, No. 2, April 1995.
- 77 Brooks R.A., *A Robust Layered Control System for a Mobile Robot*, IEEE trans. Robotics and Automation, Vol. RA-2, No.1, pp. 14-23, 1986.
- 78 Daviss B., *Adaptable Robots*, New Scientist, pp. 33-35, 4 January 1997.

- 79 Gottschlich S., Ramos C., and Lyons D., *Assembly and Task Planning: A Taxonomy*, IEEE Robotics and Automation Magazine, September 1994.
- 80 Hamernik T.A., Garcia E., and Stech D., *Optimal Placement of Damped Struts Using Simulated Annealing*, J. Spacecraft and Rockets, Vol. 32, No. 4, July-August, 1995.
- 81 Cheney E.W., Kinkaid D., *Numerical Techniques*, Brooks/Cole, 1985.
- 82 W.H. Clohessy, R.S. Wiltshire, Terminal Guidance System for Satellite Rendezvous, J. Aerospace Science, Vol 27, No. 9, pp. 653-674, 1960.
- 83 Ed. Chobotov V., *Orbital Mechanics*, AIAA Education Series, 1988.
- 84 Kalman R.E., Bertram J.E., *Control System Analysis & Design Via the Second Method of Lyapunov Part I: Continuous Systems*, Trans. ASME, Vol. 82, pp. 371-393, June 1960.
- 85 Kalman R.E., Bertram J.E., *Control System Analysis & Design Via the Second Method of Lyapunov Part II: Discrete Systems*, Trans. ASME, Vol. 82, pp. 394-400, June 1960.
- 86 Grantham W.J., Chingcuanco A.O., *Lyapunov Steepest Descent Control of Constrained Linear Systems*, IEEE. Trans. Automatic Control, Vol. 29, No. 8, August 1984.
- 87 Rimon E., Koditschek D.E., *Exact Robot Navigation Using Artificial Potential Functions*, IEEE Trans. on Robotics and Automation, Vol. 8, No.5, October 1992.
- 88 Volpe R., *Techniques for Collision Prevention, Impact Stability, and Force Control by Space Manipulators*, Telerobotics and Robotics in Space, Progress in Astronautics and Aeronautics, Vol. 161, Chap 8, 1992.
- 89 Barr A.H., *Superquadrics and Angle Preserving Transformations*, IEEE Computer Graphics and Applications, Vol.1, No.1, pp. 11-23, January 1981.
- 90 Volpe R., Khosla P., *Manipulator Control with Superquadric Artificial Potential Functions: Theory and Experiments*, IEEE Trans. Systems, Man and Cybernetics, Vol. 20, No. 6, Nov/Dec 1990.
- 91 Wright S., Zhang Y., *A Superquadratic Infeasible-Interior-Point Method for Linear Complementary Problems.*, Research Report YZ94-03, Dept. Mathematics and Statistics, UMBC, 1994.
- 92 Burkert U., Allinger N.L., *Molecular Mechanics*, American Chemical Society, No. 177, 1982.
- 93 Flores T.P., Moss D.S., *Simulating the Dynamics of Macromolecules*, Molecular, Dynamics and Structure, MacMillan, pp. 1-26, 1991.
- 94 Drexler K.E., *Nanosystems, Molecular Machinery, Manufacturing and Computation*, Wiley, 1992.
- 95 McInnes C.R., *Distributed Control of Manoeuvring Vehicles for On-Orbit Assembly*, Dept. of Aerospace Eng., University of Glasgow, Dept. Report 9502, 1995.

- 96 McQuade F., McInnes C.R., *Distributed Control for On-Orbit Assembly*, AAS 95-446, AAS/AIAA Astrodynamics Specialist Conference, Halifax, NS, Canada, August 1995.
- 97 McQuade F., McInnes C.R., *Co-operative Control for the Fabrication of Extended Structures in Space*, AIAA 96-3590, AIAA/AAS Astrodynamics Specialist Conference, San Diego, CA, USA, July 1996.
- 98 McQuade F., McInnes C.R., *Distributed Control for Serial Assembly in Space*, Proc. 5th International Conference of Space '96, Vol. 2, pp. 1169-1175, 1996.

